

Syracuse University

SURFACE

Dissertations - ALL

SURFACE

August 2017

The detection and parameter estimation of binary black hole mergers

Christopher Michael Biver
Syracuse University

Follow this and additional works at: <https://surface.syr.edu/etd>



Part of the [Physical Sciences and Mathematics Commons](#)

Recommended Citation

Biver, Christopher Michael, "The detection and parameter estimation of binary black hole mergers" (2017). *Dissertations - ALL*. 791.
<https://surface.syr.edu/etd/791>

This Dissertation is brought to you for free and open access by the SURFACE at SURFACE. It has been accepted for inclusion in Dissertations - ALL by an authorized administrator of SURFACE. For more information, please contact surface@syr.edu.

ABSTRACT

In this dissertation we study gravitational-wave data analysis techniques for binary neutron star and black hole mergers. During its first observing run, the Advanced Laser Interferometer Gravitational-wave Observatory (Advanced LIGO) reported the first, direct observations of gravitational waves from two binary black hole mergers. We present the results from the search for binary black hole mergers which unambiguously detected the binary black hole mergers. We determine the effect of calibration errors on the detection statistic of the search. Since the search is not designed to precisely measure the astrophysical parameters of the binary neutron star and black hole mergers, we use Bayesian methods to develop a new parameter estimation analysis. We demonstrate the performance of the analysis on the binary black hole mergers detected during Advanced LIGO's first observing run. We use the parameter estimation analysis to assess the ability of gravitational-wave observatories to observe a gap in the black hole mass distribution between $52 M_{\odot}$ and $133 M_{\odot}$ due to pair-instability supernovae. Finally, we use simulated signals added to the Advanced LIGO detectors to validate the search and parameter estimation analyses used to publish the detection of the astrophysical events.

**THE DETECTION AND PARAMETER
ESTIMATION OF BINARY BLACK HOLE
MERGERS**

By

Christopher M. Biwer

B.S. Applied Mathematics and Physics, University of Wisconsin-Milwaukee

DISSERTATION

SUBMITTED IN PARTIAL FULFILLMENT OF THE REQUIREMENTS

FOR THE DEGREE OF

DOCTOR OF PHILOSOPHY IN PHYSICS

Syracuse University

August 2017

Copyright © 2017 Christopher M. Biwer
All rights reserved.

Preface

The work presented in this thesis stems from my participation in the LIGO Scientific Collaboration (LSC). This work does not reflect the scientific opinion of the LSC and it was not reviewed by the collaboration.

Chapter 2 is based on material from

B .P. Abbott *et al.*, “Binary Black Hole Mergers in the First Advanced LIGO Observing Run,” *Phys. Rev. X* 6, 041015 (2016)

Chapter 6 is based on material from

C. Biwer *et al.*, “Validating gravitational-wave detections: The Advanced LIGO hardware injection system,” *Phys. Rev. D* 95, 062002 (2017)

Acknowledgments

First, I would like to express my gratitude and thanks to my advisor Duncan Brown. I have had the opportunity to work on a diverse set of projects and to learn from his broad knowledge of the detectors and gravitational-wave astronomy. He has been an excellent advisor and I am grateful for his mentorship.

I have thoroughly enjoyed working with the Syracuse University Gravitational-wave Group. The breadth of expertise and the friendliness of this group has made it an exceptional environment to work. I would like to thank Peter Saulson who has always presented great pedagogy, and Stefan Ballmer for sharing his extensive knowledge of the detectors. I have frequently sought the help of Ryan Fisher over the past few years, and I am thankful for his willingness to help me with the many problems I have brought to him. I would like to give a special thanks to Ian Harry for his mentorship, and especially his patience. He taught me so much my first couple of years at Syracuse. Thanks to Ben Lackey and Laura Nuttall for their insight, comments, and collaboration on much of my work. I am thankful to have had the opportunity to work and share an office with TJ Massinger and Alex Nitz; they have set a high standard to aspire to. I have had a lot of help on many projects, and I would like to especially thank Larne Pekowsky, Soumi De, Daniel Finstad, Steven Reyes, Swetha Bhagwat, David Kelley, and Peter Couvares for all their contributions and time.

Thanks to everyone from the PyCBC Group, the Hardware Injection Group, the Calibration Group, and the Hanford observatory that have shared their knowledge with me. Collin Capano has helped me accomplish so much these past few months, and I am extremely appreciative of all his comments and contributions. I am glad to have received the exceptional guidance of Eric Thrane, Mike Landry, and David Shoemaker. I would like to thank my fellow Fellows: Marissa Walker, Evan Goetz,

Elli King, Miquel Oliver, Jordan Palamos, and Vinnie Roma. It was a pleasure serving with you all at the Hanford observatory during the first observing run. For their help on various projects I would like to thank: Stuart Anderson, Joe Betzwieser, Miriam Cabero, Craig Cahillane, Mykyta Hulko, Sudarshan Karki, Jeff Kissel, Andy Lundgren, Duncan Macleod, Adam Mullavey, Keith Riles, Jamie Rollins, Rick Savage, Josh Smith, John Veitch, and Salvo Vitale.

I would like to thank my committee members Duncan Brown, Liviu Movilenau, Carl Rosenzweig, Matt Rudolph, Peter Saulson, and Will Wyle for taking the time to review my dissertation.

Finally, I would like to thank my parents. They have done so much for my brothers and me, and I owe so much to them.

to Mom and Pops

Contents

Preface	iv
Acknowledgments	v
List of Tables	xii
List of Figures	xxvi
1 Introduction	1
1.1 Gravitational waves and binary black hole mergers	1
1.2 Advanced LIGO	3
1.3 Advanced LIGO’s first observing run	5
2 The detection of binary black hole mergers in Advanced LIGO’s first observing run	8
2.1 Introduction	8
2.2 Matched filter	9
2.3 Template bank	10
2.4 Data conditioning	12
2.5 Signal-consistency test	12
2.6 Significance measurement	14
2.7 Data selection	16
2.8 Results	17
2.9 Conclusions	20
3 The impact of calibration errors on the detection of binary black hole mergers in Advanced LIGO data	33

3.1	Introduction	33
3.2	Models of the sensing function and actuation function	37
3.3	Simulating calibration errors in Advanced LIGO data	39
3.4	Derivation of the impact of calibration errors on the matched-filter signal-to-noise ratio	42
3.5	Impact of calibration errors on the matched-filter signal-to-noise ratio of GW150914	49
3.6	Impact of calibration errors on the matched-filter signal-to-noise ratio of binary neutron star and black hole mergers with a total mass up to 100 M_{\odot}	50
3.7	Impact of calibration errors on the detection statistic of GW150914	51
3.8	Impact of calibration errors on the detection statistic of a simulated 30-30 M_{\odot} binary black hole merger	53
3.9	Conclusions	53
4	A parameter estimation pipeline for binary neutron star and black hole mergers in Advanced LIGO data	73
4.1	Introduction	73
4.2	Likelihood	75
4.3	Priors	78
4.4	Ensemble Markov-chain Monte Carlo sampling	84
4.5	emcee sampling algorithm	87
4.6	kombine sampling algorithm	89
4.7	The state of parameter estimation pipelines in Advanced LIGO's first and second observing runs	91
4.8	Parameter estimation of binary black hole mergers from Advanced LIGO's first observing run	93
4.9	Conclusions	97
5	The capability of gravitational-wave observatories to probe the black hole mass gap due to pair-instability supernovae	104
5.1	Introduction	104
5.2	Methods	105
5.3	Results	108

5.4	Conclusions	110
6	The Advanced LIGO hardware injection system	120
6.1	Introduction	120
6.2	Hardware injection procedure	122
6.3	Binary black hole merger hardware injections	128
6.4	Loud hardware injections for detector characterization	136
6.5	Conclusions	137
7	A pipeline for validating the Advanced LIGO hardware injection state information	139
7.1	Introduction	139
7.2	Hardware injection state information	140
7.3	Pipeline topology	145
7.4	Conclusions	145
8	Conclusions	148
	Bibliography	151

List of Tables

1	Table of measured time-dependent calibration parameter values for analysis time on September 15, 2015. The 90% percentile is the interval that contains 90% of the total samples. The change in the cavity pole frequency Δf_c is offset from the measured value of 341 Hz.	50
2	Table of measured time-dependent calibration parameter values for analysis time on September 14 and September 15, 2015. The 90% percentile is the interval that contains 90% of the total samples. The change in the cavity pole frequency Δf_c is offset from the measured value of 341 Hz.	52
3	Table of measured time-dependent calibration parameter values for analysis time on January 19 and January 20, 2016. The 90% percentile is the interval that contains 90% of the total samples. The change in the cavity pole frequency Δf_c , optical spring frequency Δf_s , and inverse dimensionless quality factor ΔQ^{-1} are offset from their measured values of 360 Hz, 6.9 Hz and 0.05 respectively.	53

4	Table of model parameters. Note that not all waveform models include every parameter, and may only be valid for particular choices of mass and spin parameters. Spin parameters are expressed in spherical coordinates where $\theta_i^p = \frac{\pi}{2}$ is aligned with the angular momentum of the binary. Some models may choose to use mass or spin parameters that are functions of the component masses and spins as well. In this convention, $\iota = -\frac{\pi}{2}$ corresponds to a face-on binary (line of sight parallel to binary angular momentum), $\iota = 0$ corresponds to an edge-on binary (line of sight perpendicular to binary angular momentum), and $\iota = \frac{\pi}{2}$ corresponds to a face-away binary (line of sight anti-parallel to binary angular momentum).	75
5	Table of inferred astrophysical parameters using PyCBC Inference for GW150914, GW151226, and LVT151012. Multiply the detector-frame parameters by $(1 + z)$ to convert to the source-frame, where z is redshift.	103

List of Figures

1	A schematic of the layout of an Advanced Laser Interferometer Gravitational-Wave Observatory (Advanced LIGO) detector from Ref. [1].	4
2	The left panel shows the amplitude spectral densities $\sqrt{S(f)}$ of the total strain noise in units of strain per $\sqrt{\text{Hz}}$, and the recovered signals of GW150914, GW151226, and LVT51012. The relative amplitudes can be related to the matched-filter signal-to-noise ratio of the signal. The right panel shows the 90% credible regions of the LIGO Hanford signal reconstructions from a coherent Bayesian analysis using a non-precessing spin waveform model [2].	7
3	The four-dimensional search parameter space covered by the template bank shown projected into the component-mass plane, where $m_1 > m_2$. The lines bound mass regions with different limits on the dimensionless aligned-spin parameters χ_1 and χ_2 . Each point indicates the position of a template in the bank. The markers indicate the best-matching template waveform for each event. Since the template bank includes a diverse set of waveforms, we search regions of the bank separately; this is discussed in Sec. 2.6. The green region corresponds to binary neutron stars, the red region corresponds to neutron star-black hole binaries, and the blue region corresponds to binary black holes.	21
4	The whitened gravitational-wave strain time series at the time of GW150914. The left panel shows the Hanford data and the right panel shows the Livingston data. The gravitational-wave strain is whitened with the amplitude spectral density to remove the strong instrumental lines seen in Fig. 2. In this figure, an additional 43-300 Hz bandpass filter was applied to the whitened time series.	22

5	The whitened gravitational-wave strain time series at the time of GW151226. The left panel shows the Hanford data and the right panel shows the Livingston data. The gravitational-wave strain is whitened with the amplitude spectral density to remove the strong instrumental lines seen in Fig. 2. In this figure, an additional 43-800 Hz bandpass filter was applied to the whitened time series.	22
6	The whitened gravitational-wave strain time series at the time of LVT151011. The left panel shows the Hanford data and the right panel shows the Livingston data2. The gravitational-wave strain is whitened with the amplitude spectral density to remove the strong instrumental lines seen in Fig. 2. In this figure, an additional 43-400 Hz bandpass filter was applied to the whitened time series.	23
7	The results from the search for binary black hole mergers in Advanced LIGO’s first observing run. The result for signals with chirp mass $\mathcal{M} > 1.74M_{\odot}$ (the chirp mass of a $m_1 = m_2 = 2M_{\odot}$ binary) and $f_{\text{peak}} > 100$ Hz are shown. Here we show the histogram of the detection statistic $\hat{\rho}$. GW150914 is the most significant event in the data and is more significant than any background event in the data. GW150914 is identified with a significance $> 5 \sigma$	24
8	The results from the search for binary black hole mergers in Advanced LIGO’s first observing run. The result for signals with chirp mass $\mathcal{M} > 1.74M_{\odot}$ (the chirp mass of a $m_1 = m_2 = 2M_{\odot}$ binary) and $f_{\text{peak}} > 100$ Hz are shown. This histogram shows the mapping between the detection statistic and the false-alarm rate, p-value, and significance.	25
9	The results from the search for binary black hole mergers in Advanced LIGO’s first observing run with GW150914 removed. Here we show the histogram of the detection statistic $\hat{\rho}$. GW151226 is identified as the most significant event remaining in the data. GW151226 is more significant than the remaining background in the analysis with a significance $> 5 \sigma$. The third most significant event in the search, LVT151012, is identified with a significance of 1.7σ . The significance obtained for LVT151012 is not greatly affected by including or removing background contributions from GW150914 and GW151226.	26

10	The matched-filter signal-to-noise ratio $\rho(t)$ (blue), detection statistic $\hat{\rho}_c(t)$ (purple), and signal-consistency test value $\chi_r^2(t)$ (green) versus time using the best-matching template at the time of GW150914. The top plot shows the Hanford detector (H1) and the bottom plot shows the Livingston detector (L1).	27
11	The matched-filter signal-to-noise ratio $\rho(t)$ (blue), detection statistic $\hat{\rho}_c(t)$ (purple), and signal-consistency test value $\chi_r^2(t)$ (green) versus time using the best-matching template at the time of GW151226. The top plot shows the Hanford detector (H1) and the bottom plot shows the Livingston detector (L1).	28
12	The matched-filter signal-to-noise ratio $\rho(t)$ (blue), detection statistic $\hat{\rho}_c(t)$ (purple), and signal-consistency test value $\chi_r^2(t)$ (green) versus time using the best-matching template at the time of LVT151012. The top plot shows the Hanford detector (H1) and the bottom plot shows the Livingston detector (L1).	29
13	The results from the search for binary black hole mergers in Advanced LIGO's first observing run with GW150914 removed. The result for signals with chirp mass $\mathcal{M} > 1.74M_\odot$ (the chirp mass of a $m_1 = m_2 = 2M_\odot$ binary) and $f_{\text{peak}} > 100$ Hz are shown. This histogram shows the mapping between the detection statistic and the false-alarm rate, p-value, and significance.	30
14	A spectrogram of the whitened gravitational-wave strain time series from Figure 4. The left panel shows the Hanford data and the right panel shows the Livingston data at the time of GW150914.	31
15	A spectrogram of the whitened gravitational-wave strain time series from Figure 5. The left panel shows the Hanford data and the right panel shows the Livingston data at the time of GW151226.	31
16	A spectrogram of the whitened gravitational-wave strain time series from Figure 6. The left panel shows the Hanford data and the right panel shows the Livingston data at the time of LVT151012.	32

17	A schematic of the feedback loop that controls the differential arm length ΔL_{free} and calibration from Ref. [3]. The sensing function C , digital filters D , and actuation function A are the components of the feedback loop. Models of the sensing function $C^{(\text{model})}$ and actuation function $A^{(\text{model})}$ are used to calibrate the error signal d_{err} and control signal d_{ctrl} to obtain the gravitational-wave strain h . $x_{\text{T}}^{(\text{PC})}$ represents sinusoidal excitations at select frequencies called calibration lines. Calibration lines are used to monitor time-dependent changes in the sensing and actuation functions.	36
18	A schematic of the quadruple pendulum system from Ref. [3]. There is an independent pendulum system which is used to generate reaction forces on each mass of the test mass pendulum.	40
19	The fractional amplitude error $\delta\mathcal{A}(f, t)/\mathcal{A}(f, t)$ and phase error $\delta\phi(f, t)$ as $\Re\kappa_{\text{tst}}$ and $\Im\kappa_{\text{tst}}$ varied. Here, we use the model from the calibration epoch beginning on January 3, 2017, during Advanced LIGO's second observing run.	55
20	The fractional amplitude error $\delta\mathcal{A}(f, t)/\mathcal{A}(f, t)$ and phase error $\delta\phi(f, t)$ as $\Re\kappa_{\text{pu}}$ and $\Im\kappa_{\text{pu}}$ are varied. Here, we use the model from the calibration epoch beginning on January 3, 2017, during Advanced LIGO's second observing run.	56
21	The fractional amplitude error $\delta\mathcal{A}(f, t)/\mathcal{A}(f, t)$ and phase error $\delta\phi(f, t)$ as κ_{C} and Δf_{c} are varied. Here, we use the model from the calibration epoch beginning on January 3, 2017, during Advanced LIGO's second observing run.	57
22	The fractional amplitude error $\delta\mathcal{A}(f, t)/\mathcal{A}(f, t)$ and phase error $\delta\phi(f, t)$ as Δf_{s} and ΔQ^{-1} are varied. Here, we use the model from the calibration epoch beginning on January 3, 2017, during Advanced LIGO's second observing run.	58

23	Variation in the matched-filter signal-to-noise ratio ρ when $\Re\kappa_{\text{tst}}$ and $\Im\kappa_{\text{tst}}$ are adjusted for GW150914. The best-fit waveform parameters from the search results reported in Ref. [4] were used to generate the template waveform to calculate ρ . The blue curve was computed using the initial calibration and the orange curve was computed using the final calibration from Advanced LIGO's first observing run. The black histogram represents the measured values of the time-dependent calibration parameters for times used in the analysis on September 14, 2015.	59
24	Variation in the matched-filter signal-to-noise ratio ρ when $\Re\kappa_{\text{pu}}$ and $\Im\kappa_{\text{pu}}$ are adjusted for GW150914. The best-fit waveform parameters from the search results reported in Ref. [4] were used to generate the template waveform to calculate ρ . The blue curve was computed using the initial calibration and the orange curve was computed using the final calibration from Advanced LIGO's first observing run. The black histogram represents the measured values of the time-dependent calibration parameters for times used in the analysis on September 14, 2015.	60
25	Variation in the matched-filter signal-to-noise ratio ρ when κ_C and Δf_c are adjusted for GW150914. The best-fit waveform parameters from the search results reported in Ref. [4] were used to generate the template waveform to calculate ρ . The blue curve was computed using the initial calibration and the orange curve was computed using the final calibration from Advanced LIGO's first observing run. The black histogram represents the measured values of the time-dependent calibration parameters for times used in the analysis on September 14, 2015. The change in the cavity pole frequency Δf_c is offset from the measured value of 341 Hz.	61
26	The difference from the nominal value that corresponds to a match [5] of 0.99 which is a 1% loss in the matched-filter signal-to-noise ratio. Smaller differences corresponds to a steeper quadratic dependence. . .	62

27	The difference from the nominal value that corresponds to a match [5] of 0.99 which is a 1% loss in the matched-filter signal-to-noise ratio. Smaller differences corresponds to a steeper quadratic dependence. . .	63
28	The difference from the nominal value that corresponds to a match [5] of 0.99 which is a 1% loss in the matched-filter signal-to-noise ratio. Smaller differences corresponds to a steeper quadratic dependence. . .	64
29	The difference from the nominal value that corresponds to a match [5] of 0.99 which is a 1% loss in the matched-filter signal-to-noise ratio. Smaller differences corresponds to a steeper quadratic dependence. . .	65
30	Variation in the detection statistic $\hat{\rho}$ when the time-dependent calibration parameters are adjusted for GW150914. The best-fit waveform parameters from the search results reported in Ref. [4] were used to generate the template waveform to calculate $\hat{\rho}$. The blue solid curve represents $\hat{\rho}$ averaged over 16 noise realizations in Advanced LIGO's first observing run. The orange dashed curve is a quadratic fit, and it represents the approximate behavior of $\hat{\rho}$ for a large population of simulated signals. The maximum $\hat{\rho}$ recovered over all 16 noise realizations is denoted as $\hat{\rho}_{\max}$. The black histogram represents the measured values of the time-dependent calibration parameters for times used in the analysis on September 14 and September 15, 2015.	66
31	Variation in the detection statistic $\hat{\rho}$ when the time-dependent calibration parameters are adjusted for GW150914. The best-fit waveform parameters from the search results reported in Ref. [4] were used to generate the template waveform to calculate $\hat{\rho}$. The blue solid curve represents $\hat{\rho}$ averaged over 16 noise realizations in Advanced LIGO's first observing run. The orange dashed curve is a quadratic fit, and it represents the approximate behavior of $\hat{\rho}$ for a large population of simulated signals. The maximum $\hat{\rho}$ recovered over all 16 noise realizations is denoted as $\hat{\rho}_{\max}$. The black histogram represents the measured values of the time-dependent calibration parameters for times used in the analysis on September 14 and September 15, 2015.	67

32	<p>Variation in the detection statistic $\hat{\rho}$ when the time-dependent calibration parameters are adjusted for GW150914. The best-fit waveform parameters from the search results reported in Ref. [4] were used to generate the template waveform to calculate $\hat{\rho}$. The blue solid curve represents $\hat{\rho}$ averaged over 16 noise realizations in Advanced LIGO's first observing run. The orange dashed curve is a quadratic fit, and it represents the approximate behavior of $\hat{\rho}$ for a large population of simulated signals. The maximum $\hat{\rho}$ recovered over all 16 noise realizations is denoted as $\hat{\rho}_{\max}$. The black histogram represents the measured values of the time-dependent calibration parameters for times used in the analysis on September 14 and September 15, 2015. The change in the cavity pole frequency Δf_c is offset from the measured value of 341 Hz.</p>	68
33	<p>Variation in the detection statistic $\hat{\rho}$ when the time-dependent calibration parameters are adjusted for a non-spinning 30-30 M_{\odot} binary black hole merger simulated signal. The blue solid curve represents $\hat{\rho}$ averaged over 16 noise realizations in Advanced LIGO's second observing run. The orange dashed curve is a quadratic fit, and it represents the approximate behavior of $\hat{\rho}$ for a large population of simulated signals. The maximum $\hat{\rho}$ recovered over all 16 noise realizations is denoted as $\hat{\rho}_{\max}$. The black histogram represents the measured values of the time-dependent calibration parameters for times used in the analysis on January 19 and January 20, 2017.</p>	69
34	<p>Variation in the detection statistic $\hat{\rho}$ when the time-dependent calibration parameters are adjusted for a non-spinning 30-30 M_{\odot} binary black hole merger simulated signal. The blue solid curve represents $\hat{\rho}$ averaged over 16 noise realizations in Advanced LIGO's second observing run. The orange dashed curve is a quadratic fit, and it represents the approximate behavior of $\hat{\rho}$ for a large population of simulated signals. The maximum $\hat{\rho}$ recovered over all 16 noise realizations is denoted as $\hat{\rho}_{\max}$. The black histogram represents the measured values of the time-dependent calibration parameters for times used in the analysis on January 19 and January 20, 2017.</p>	70

35	Variation in the detection statistic $\hat{\rho}$ when the time-dependent calibration parameters are adjusted for a non-spinning 30-30 M_{\odot} binary black hole merger simulated signal. The blue solid curve represents $\hat{\rho}$ averaged over 16 noise realizations in Advanced LIGO's second observing run. The orange dashed curve is a quadratic fit, and it represents the approximate behavior of $\hat{\rho}$ for a large population of simulated signals. The maximum $\hat{\rho}$ recovered over all 16 noise realizations is denoted as $\hat{\rho}_{\max}$. The black histogram represents the measured values of the time-dependent calibration parameters for times used in the analysis on January 19 and January 20, 2017. The change in the cavity pole frequency Δf_c is offset from the measured values of 360 Hz.	71
36	Variation in the detection statistic $\hat{\rho}$ when the time-dependent calibration parameters are adjusted for a non-spinning 30-30 M_{\odot} binary black hole merger simulated signal. The blue solid curve represents $\hat{\rho}$ averaged over 16 noise realizations in Advanced LIGO's second observing run. The orange dashed curve is a quadratic fit, and it represents the approximate behavior of $\hat{\rho}$ for a large population of simulated signals. The maximum $\hat{\rho}$ recovered over all 16 noise realizations is denoted as $\hat{\rho}_{\max}$. The black histogram represents the measured values of the time-dependent calibration parameters for times used in the analysis on January 19 and January 20, 2017. The change in the optical spring frequency Δf_s , and inverse dimensionless quality factor ΔQ^{-1} are offset from their measured values of 6.9 Hz and 0.05 respectively.	72
37	An ensemble of 5,000 Markov chains while estimating the source-frame component mass of the larger black hole m_1^{src} . Initially the Markov chains are distributed according to the prior and as the Markov chains advance they converge.	94
38	The Gelman-Rubin convergence statistic (Point Scale Reduction Factor) for an ensemble of 5,000 Markov chains while estimating the source-frame component mass of the larger black hole m_1^{src} . The red dashed line corresponds to 1 which indicates the ensemble has converged.	95

39	The posterior probability density function of the source-frame primary mass m_1^{src} and secondary mass m_2^{src} for GW150914 (blue), GW151226 (orange), and LVT151012 (green).	97
40	the posterior probability density function of mass ratio $q = m_1/m_2$ where $m_1 > m_2$, and effective spin χ_{eff} for GW150914 (blue), GW151226 (orange), and LVT151012 (green).	98
41	The posterior probability density function (PDF) of distance for GW150914 (blue), GW151226 (orange), and LVT151012 (green).	99
42	The posterior probability density functions of the dimensionless spin magnitude as a function of the polar spin angle. The first row shows GW150914, the second row shows GW151226, and the third row shows LVT151012.	100
43	The sky localization of GW150914 in celestial coordinates.	101
44	The sky localization of GW151226 in celestial coordinates.	101
45	The sky localization of LVT151012 in celestial coordinates.	102
46	The amplitude spectral density of Advanced LIGO and Advanced Virgo at design sensitivity [6].	107
47	The component masses m_1^{src} and m_2^{src} of all 2,407 simulated signals colored by the effective spin χ_{eff} . The dashed magenta lines represent the PISN mass gap between $52 M_{\odot}$ and $113 M_{\odot}$	108
48	Histogram of the simulated signals' median network signal-to-noise ratio (SNR) from the posterior distributions. The solid red histogram represents the simulated signals with their distance distributed uniformly in the logarithm. The dashed purple histogram represents the simulated signals with $m_1 = 52 M_{\odot}$. The dashed-dotted green histogram represents the simulated signals with $m_1 = 133 M_{\odot}$. The solid blue histogram represents the 832 simulated signals with their network SNR distributed around 29. The dashed orange histogram represents the 832 simulated signals from the blue histogram with their distance scaled by a factor of 2.	111

49	The 90% credible interval of the source-frame primary mass m_1^{src} versus the m_1^{src} used to generate the simulated signal. The dashed magenta lines represent the PISN mass gap between $52 M_\odot$ and $113 M_\odot$. The dashed gray line represent the 1:1 ratio which is an exact match. Simulated signals with either m_1^{src} or m_2^{src} not recovered in the 90% credible interval are colored gray.	112
50	The 90% credible interval of the source-frame secondary mass m_2^{src} versus the m_2^{src} used to generate the simulated signal. The dashed magenta lines represent the PISN mass gap between $52 M_\odot$ and $113 M_\odot$. The dashed gray line represent the 1:1 ratio which is an exact match. Simulated signals with either m_1^{src} or m_2^{src} not recovered in the 90% credible interval are colored gray.	113
51	The 90% credible interval of m_1^{src} from simulated signals generated with m_1^{src} outside the PISN mass gap versus the median network signal-to-noise ratio (SNR) from the posterior distributions. The points are colored by effective spin χ_{eff} . The dashed magenta lines represent the PISN mass gap between $52 M_\odot$ and $113 M_\odot$. Simulated signals with either m_1^{src} or m_2^{src} not recovered in the 90% credible interval are colored gray.	114
52	The 90% credible interval of redshift z for simulated signals generated with m_1^{src} outside the PISN mass gap ($52 < m_1^{\text{src}} < 133$) but recovered with $52 < m_1^{\text{src}} < 133$	115
53	The fraction of simulated signals generated in the mass bin that have their 90% credible interval for the primary mass m_1^{src} contained entirely inside the PISN mass gap; this is labeled as ξ_1^{in} . Results for simulated signals recovered with a median network SNR ≤ 22 . The dashed magenta lines represent the PISN mass gap between $52 M_\odot$ and $113 M_\odot$	116

54	The fraction of simulated signals generated in the mass bin that have their 90% credible interval for the primary mass m_1^{src} contained entirely inside the PISN mass gap; this is labeled as ξ_1^{in} . Results for simulated signals recovered with a median network SNR > 22 . The dashed magenta lines represent the PISN mass gap between $52 M_\odot$ and $113 M_\odot$	117
55	The fraction of simulated signals generated in the mass bin that have their 90% credible interval for the secondary mass m_2^{src} contained entirely inside the PISN mass gap; this is labeled as ξ_2^{in} . Results for simulated signals recovered with a median network SNR ≤ 22 . The dashed magenta lines represent the PISN mass gap between $52 M_\odot$ and $113 M_\odot$	118
56	The fraction of simulated signals generated in the mass bin that have their 90% credible interval for the secondary mass m_2^{src} contained entirely inside the PISN mass gap; this is labeled as ξ_2^{in} . Results for simulated signals recovered with a median network SNR > 22 . The dashed magenta lines represent the PISN mass gap between $52 M_\odot$ and $113 M_\odot$	119
57	Block overview of the Advanced LIGO hardware injection system. Time series for transient and continuous-wave injections are generated and sent to the photon calibrator (PCAL). The signal modulates the laser power of the photon calibrator to displace the end test mass (ETM) in a way that mimics a gravitational wave (GW) passing through the detector. The optical follower servo has its own pick-off of the light that is sent towards the ETM indicated by a dashed line. The gravitational-wave strain of the detector is analyzed and checked for consistency by the analysis' developers. A photodetector that receives the light reflected from the test mass is used to monitor and verify the injected signal.	124

58	<p>The maximum displacement of an ETM using the photon calibrator (blue). For the sinusoidal force induced by sinusoidally power modulated laser beams, $F = mA$ implies that the induced displacement is given by $x = -F/(m\omega)^2$. The dashed blue curve indicates that the fidelity of the induced displacements degrades above 1kHz due to the need to roll off the inverse actuation filters to maintain stability near the Nyquist frequency. The maximum displacement of the ETM required for two optimally-oriented compact binary waveforms that contain an inspiral, merger, and ringdown are shown for reference. A 3-30 M_\odot binary at 100 Mpc (yellow) and 1.4-1.4 M_\odot binary at 100 Mpc (red) were generated using the SEOBNRv2 approximant [7]. Note that the required displacement for the 1.4-1.4 M_\odot binary exceeds the maximal photon calibrator displacement at high frequencies. . . .</p>	132
59	<p>A comparison of the signal-to-noise ratio ρ from software injections and the recovered signal-to-noise ratio of the hardware injection. Parameters for the hardware injections were drawn from the posterior distributions for GW150914 (circles) and GW151226 (triangles). The software injection ρ is the mean and 1σ error from the recovery of 50 software injections filtered with the injected waveform near the time of the injection. The threshold on ρ is indicated by the gray region. The arrows indicate the coherent injection affected by a nearby noise transient.</p>	133
60	<p>PyCBC χ_r^2 statistic versus matched-filter signal-to-noise ratio ρ for each detector. Software injections are represented as pluses that are colored by false-alarm rate. The false-alarm rate is calculated using the time-slide algorithm described in [8]. The gravitational-wave events GW150914 and GW151226 are shown as stars. Hardware injections for GW150914 and GW151226 are represented as boxes. These are coherent software and hardware injections, therefore the H1 and L1 plots are dependent on each other. Single-detector background distributions (black dots) are plotted; there was a threshold applied indicated by the gray region. Lines of constant detection statistic $\hat{\rho}$ are shown (gray dashed lines); plotted are $\hat{\rho} = \{8, 10, 14, 20\}$.</p>	134

61	The 90% confidence interval skymaps for two hardware injection (red and green) and GW151226 (magenta). The skymaps are shown in Earth-bound coordinates. H+ and L+ mark the Hanford and Livingston sites, and H- and L- indicate antipodal points; H-L and L-H mark the poles of the line connecting the two detectors (the points of maximal time delay). The two hardware injections are chosen to be representative of an average event (green) and a sub-threshold event (red). We notice how all sky maps have support near the same ring of equal time delay between the two Advanced LIGO detectors.	135
62	Posterior probability density functions (PDF) for the chirp mass inferred from GW151226 hardware injections. The true value has been removed to center all distributions around zero. Hardware injections with very low signal-to-noise ratio show large width and in one case bimodality. The bimodal distribution comes from the injection at GPS time 1136588346 which is also shown in Fig. 61.	137
63	Block diagram depicting the flow of state information about the hardware injection during Advanced LIGO's first observing run. A team of hardware injectors schedule hardware injections using <code>tinj</code> and upload entries to the Gravitational-wave Event Candidate Database (GraCEDb). The scheduling program <code>tinj</code> transmits the hardware injection time-domain waveform data to the controls system. The controls system stores the injected time series into excitation channels and the state of the inverse actuation filters to the switch channels. The Online Data Characterization (ODC) system monitors these channels in the controls systems and produces bit vectors that indicate if a hardware injection has occurred. The Data Monitoring Tool receives the ODC bit vectors and records them to the data files that low-latency searches read and the segment database that offline searches query for state information about the hardware injection system.	141

64	The hardware injection ODC bit vector for the Hanford detector on January 16, 2016. At the top, the 0-th bit is the summary bit that describes if the hardware injection system is operating in its nominal state. Green indicates that it is. Bits 1 through 6 indicate that the filters, filter gains, and switches are in their nominal state. Bits 7 and 8 indicate that the continuous hardware injections are active. Bits 9 through 13 describe when and what type of transient injection was injected throughout the day. At the bottom is a bit time series that indicates if the detector was observing; green indicates that the detector was observing and red indicates that the detector was not observing.	143
65	The state of each hardware injection segment in the segment database for the Hanford detector on January, 16, 2016. This plot shows that the continuous hardware injections were active the entire day, there were seven burst hardware injections, and there was one compact binary coalescence hardware injection. At the bottom is a bit time series that indicates if the detector was observing; green indicates that the detector was observing and red indicates that the detector was not observing.	144
66	Block diagram of the pipeline. The observing run is split into n 2048 s segments. The ODC bit vector channels, the low-latency ODC bit vector channel, and switch channels use bitmasks to check the state of individual bits in each 2048 s segment. There are h ODC bit vector channels that are searched with i bitmasks, the low-latency ODC bit vector is searched with j bitmasks, and there are k switch channel that are searched with l bitmasks. There are m excitation channels that are searched for non-zero samples in each 2048 s. There are s segment names queried in the segment database. The list of events found in each 2048 s segments are concatenated and combined with the schedule file and GraCEDb entries to find coincidences. A results table is rendered at the end that lists all coincidences.	147

Chapter 1

Introduction

1.1 Gravitational waves and binary black hole mergers

In 1915, Albert Einstein published the theory of General Relativity, a geometric description of gravitation that generalizes Newtonian mechanics and special relativity. One year later, Einstein predicted the existence of gravitational waves [9, 10] which are wave solutions to the linearized Einstein field equations. These solutions imply that as a gravitational wave passes it changes the distance between free falling objects. Einstein realized that the amplitude of gravitational waves would be too small to be detected by contemporary experiments. The very existence of gravitational waves was debated for several decades as it was thought that they may be an unphysical effect of changing coordinates. Einstein began to accept that gravitational waves are real in 1936 [11], but it was not until 1957 at the Chapel Hill conference that the existence of gravitational waves became widely accepted [12, 13].

The amplitude of gravitational waves is small and the most promising observable sources are of astrophysical origin which produce fractional changes in length less than 10^{-21} . Massive objects moving at relativistic velocities can generate detectable gravitational waves; examples include binary neutron star and black holes mergers. There are several proposed channels of stellar evolution that allow black holes to form binaries and coalesce within the Hubble time. These formation channels include classical isolated binary evolution in low-metallicity environments [14, 15, 16], dynamical formation in dense stellar environments [17, 18, 19, 20, 21], homogenous chemical evolution in rapidly rotating binaries [22, 23, 24], and binaries of Population

III stars [25, 26]. Binary neutron star and black holes lose energy through gravitational waves which causes the two compact-objects to spiral in towards each other. At the merger, the component masses in a binary neutron star and black hole mergers will reach relativistic velocities and their mass will be converted into gravitational energy and travel outward as gravitational waves [27]. After the merger, the final black hole oscillates, still emitting gravitational waves, before settling down to a stationary Kerr black hole.

Advances in waveform modeling over the last century have provided accurate models of the gravitational waveforms radiated by binary neutron star and black hole mergers. In 1916, Karl Schwarzschild published a solution of the field equations [28] for the geometry of spacetime around an uncharged, spherically-symmetric, and non-rotating body. This solution was later understood to describe a black hole [29, 30]. In 1963, Roy Kerr generalized Schwarzschild's solution to describe rotating black holes [31], and Phillip Peters and Jon Matthews used the Einstein quadrupole formula to determine the gravitational wave emission from stars in Keplerian orbits [32]. Quasinormal modes [33, 34, 35] were later used to model the ringdown of the final resultant black hole. Further studies of higher-order post-Newtonian calculations [36], analytical studies of relativistic two-body dynamics [37, 38], and advances in numerical relativity [39, 40, 41] led to the waveform models [42, 43, 44, 45] used in the search [46] and parameter estimation [47] of binary black hole mergers.

In 1975, Russell Hulse and Joseph Taylor [48] found PSR-B1913+16 which is a binary neutron star where one of the neutron stars emits a collimated electromagnetic jet that aligns with the line of sight with Earth. Subsequent observations of its energy loss by Taylor and Joel Weisberg [49] provided compelling evidence for the the existence of gravitational waves. Taylor and Weisberg showed that the decay of the binary's orbital period matches the expected orbital decay due to energy loss from the emission of gravitational waves.

Binary black hole mergers had not been observed prior to September 14, 2015; however, several black hole candidates in binaries with ordinary stars (main sequence stars, white dwarfs, or evolved main sequence stars) have been identified through X-ray observations [50, 51, 52].

1.2 Advanced LIGO

The first experiments designed to detect gravitational waves began in the 1960s using resonant mass detectors [53] and an international network of cryogenic resonant mass detectors was constructed [54]. In 1956, Felix Pirani suggested gravitational waves are observable if you compare the spacetime positions of nearby masses with light [55], and interferometric detectors were suggested in the 1960s [56] and the 1970s [57]. Interferometric detectors showed potential for higher sensitivity to gravitational waves than resonant mass detectors [58] which led to proposals for a network of interferometric gravitational-wave detectors [59, 60, 61, 62].

Construction of the first-generation interferometric gravitational-wave detectors began in the 1990s including TAMA 300 [63], GEO 600 [64], the Laser Interferometer Gravitational-Wave Observatory (Initial LIGO) [65], and Virgo [66]. Initial LIGO was a network of two interferometric gravitational-wave detectors located in Hanford, WA, and Livingston, LA [65]. Initial LIGO and Virgo conducted joint observing runs from 2002 to 2010 which set an upper limit on the rate of binary black hole mergers [67, 68, 69, 70, 71].

In September 2015, the Advanced Laser Interferometer Gravitational-Wave Observatory (Advanced LIGO) began observing after a major upgrade targeting a tenfold improvement in sensitivity over the initial LIGO detectors [72]. The detectors were not operating at design sensitivity. However, both detectors reached an instrument noise 3-4 times lower than the Initial LIGO detectors in their most sensitive frequency band between 100 Hz and 300 Hz, and several orders of magnitude at lower frequencies [73].

A schematic of one of the Advanced LIGO observatories [74] is shown in Figure 1. A beam of light from a laser is passed through electro-optic modulators which introduce radio-frequency sidebands into the beam's optical field. The beam then passes through the input mode cleaner which rejects higher-order optical modes of the beam; only the TEM00 mode which has a Gaussian intensity profile is transmitted. Then, the beam is transmitted through the power recycling mirror, is split by a beamsplitter, and is directed down the two 4 km arms of the interferometer. Half of the light from the beam is directed toward one input test mass and half of the light from the beam is directed toward the other input test mass. Gravitational waves cause differential

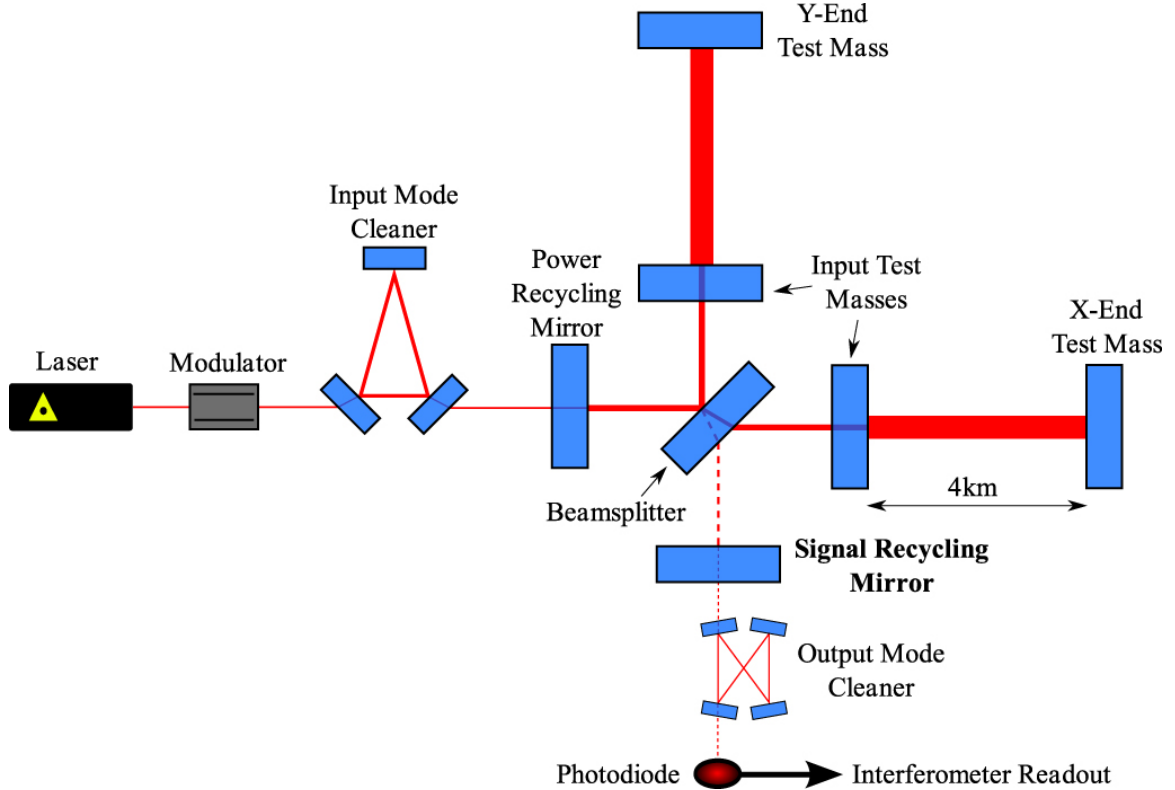


Figure 1 : A schematic of the layout of an Advanced Laser Interferometer Gravitational-Wave Observatory (Advanced LIGO) detector from Ref. [1].

changes in the length of the arm cavities which results in a difference in the path a beam travels in each arm. This causes a phase difference between the beams in the two arms which introduces two sidebands offset from the laser's carrier frequency. If there is a gravitational wave signal in the recombined beam, then a small amount of light is directed toward and transmitted through the signal recycling cavity. The output mode cleaner removes higher-order optical modes, isolates the TEM₀₀ mode, and removes the radio-frequency sidebands. The gravitational wave sidebands have a low frequency offset from the laser frequency such that they are allowed to transmit through the output mode cleaner. The signal transmitted from the output mode cleaner is read out on a photodiode. The photodiode measures power, and therefore it witnesses the beat frequencies between the beam optical field and gravitational-wave sideband. The power measured from the photodiode is used as the gravitational-wave readout port.

1.3 Advanced LIGO’s first observing run

Advanced LIGO’s first observing run began on September 12, 2015, and concluded on January 19, 2016. During the first observing run, the detectors were sensitive to gravitational waves over a range of frequencies from 30 Hz up to several kHz [73]. This frequency band covers the frequencies of gravitational waves emitted during the late inspiral, merger, and ringdown of binary neutron star and stellar-mass binary black hole mergers. Advanced LIGO observed two binary black hole mergers (GW150914 and GW151226) and a detection candidate (LVT151012) in its first observing run [74, 75].

The PyCBC search unambiguously identified the two binary black hole mergers and the candidate event [76, 77] in Advanced LIGO’s first observing run. This search uses matched filtering which correlates the data from each detector with a bank of template waveforms that model the gravitational waves generated from binary neutron star and black hole mergers [46]. The first event, called GW150914, was observed on September 14, 2015, at 09:50:45 UTC [76], and the second event, called GW151226, was observed on December 26, 2015, at 03:38:53 UTC [77]. Both of these signals were observed with a statistical significance greater than 5σ . A third candidate event called LVT151012 is consistent with a binary black hole merger. LVT151012 was observed on October 12, 2015, at 09:54:43 UTC with a significance $\lesssim 2 \sigma$ [76]. Although LVT151012 is not significant enough to claim an unambiguous detection, an analysis to constrain the rate of binary black hole mergers in the Universe found the probability that LVT151012 is of astrophysical origin is 87% [2, 78].

Advanced LIGO’s searches for binary black hole mergers are designed to identify astrophysical signals with high significance; however they are not designed to provide measurements of the parameters of the detected sources. For example, the template bank [79] is discretized which results in a sub-optimal measurement of the masses and spins. The astrophysical parameters from a binary black hole may lie between points in the discretized template bank and not directly at one of the points in the bank. In this case, we lose a fraction of signal-to-noise ratio; however, we construct our templates banks such that there is enough overlap between the astrophysical signal and nearby points in the template bank to limit the loss to $< 3\%$ [80, 81, 82, 83]. Therefore, follow-up analyses that use Bayesian inference methods must be used to

estimate the astrophysical parameters of binary black hole mergers after the search has identified a candidate event [84, 75, 47]. This Bayesian framework makes it possible to construct an estimate of the posterior probability density functions of astrophysical parameters that describe a given model.

The Advanced LIGO detectors’ noise budget is comprised of fundamental noise, technical noise, and environmental noise. Fundamental noise such as thermal noise or quantum noise determine the ultimate sensitivity of the detector [85, 86]. Technical noise sources include the electronics and feedback loops used to control the position of the test masses [85]. Examples of environmental noise include seismic motion or magnetic fields [85, 87]. In the left panel of Fig. 2, for both detectors we show the amplitude spectral density $\sqrt{S(f)}$ of the total strain noise calibrated in units of strain per $\sqrt{\text{Hz}}$ [3] for a typical time during Advanced LIGO’s first observing run. Overlaid on the noise curves of the detectors are the waveforms of GW150914, GW151226, and LVT151012. Since the amplitude of the majority of gravitational-wave sources will be comparable to the noise background [88], and compact-objects can be modeled, then it is natural to use matched filtering to distinguish signals from the noise background [89]. The expected matched-filter signal-to-noise ratio ρ of a signal $h(t)$ in a detector can be expressed as [2]

$$\rho^2 = \int_0^\infty \frac{\left(2|\tilde{h}(f)|\sqrt{f}\right)^2}{S_n(f)} d\ln(f), \quad (1.1)$$

where $\tilde{h}(f)$ is the Fourier transform of the signal. Writing it in this form motivates the normalization of the waveform plotted in Fig. 2, where the area between the signal and noise curves is indicative of the matched-filter signal-to-noise ratio of the events.

The gravitational-wave signal from a binary black hole merger has a characteristic “chirp” time-frequency evolution that increases in frequency and amplitude as the black holes spiral inwards. The corresponding time series of GW150914, GW151226, and LVT151012 are plotted in the right panel of Fig. 2 to visualize the difference in duration of the signals in the Advanced LIGO frequency band, as well as their amplitude measured in strain in the left panel. The amplitude of the signal is maximum at the merger, after which it decays rapidly as the final black hole rings down to equilibrium. In the frequency domain, the amplitude decreases with frequency during inspiral, as the signal spends a greater number of cycles at lower frequencies.

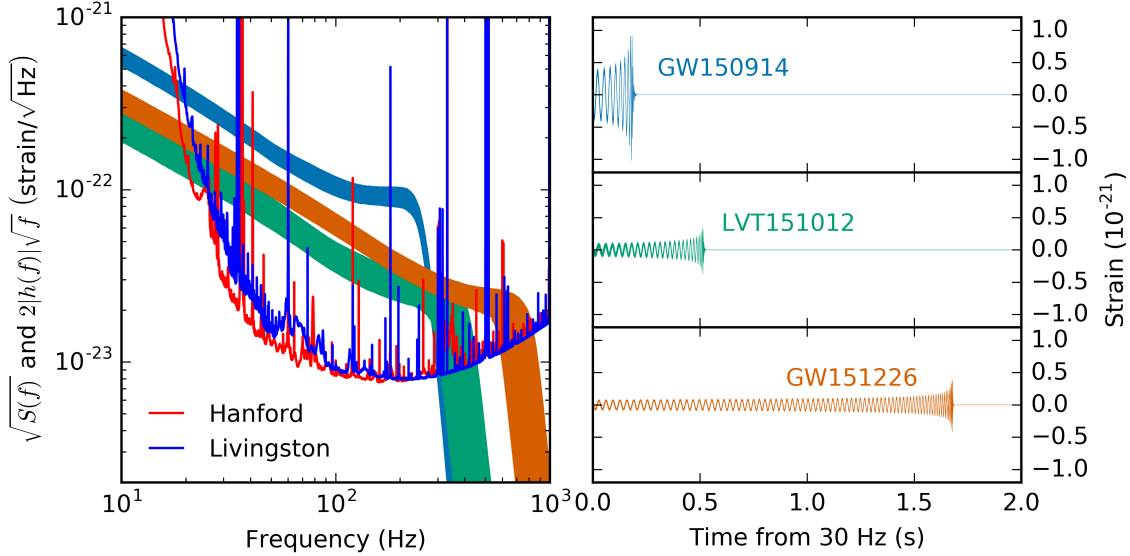


Figure 2 : The left panel shows the amplitude spectral densities $\sqrt{S(f)}$ of the total strain noise in units of strain per $\sqrt{\text{Hz}}$, and the recovered signals of GW150914, GW151226, and LVT51012. The relative amplitudes can be related to the matched-filter signal-to-noise ratio of the signal. The right panel shows the 90% credible regions of the LIGO Hanford signal reconstructions from a coherent Bayesian analysis using a non-precessing spin waveform model [2].

This is followed by a slower falloff during merger and then a step decrease during the ringdown. The amplitude of GW150914 is significantly larger than the other two events, and at the time of the merger, the gravitational-wave signal lies well above the noise. GW151226 has a lower amplitude but sweeps across the entire frequency band up to nearly 800 Hz as shown in Fig. 2. GW150914 lasts only a few cycles, while LVT51012 and GW151226 have lower amplitudes but persist in the Advanced LIGO band longer.

Chapter 2

The detection of binary black hole mergers in Advanced LIGO's first observing run

2.1 Introduction

The purpose of the PyCBC search [79, 46, 90] is to identify gravitational-wave signals from binary neutron star and black hole mergers and measure the statistical significance of candidate events [46]. We expect the amplitude of the majority of gravitational-wave sources is comparable to the noise background [88], therefore signal processing techniques are required to identify candidate events. Even for loud sources, the statistical significance of candidate detections must be empirically measured since there it is not possible to shield the detectors from gravitational waves and no theoretical model of the detector noise exists. Even if it were possible to shield the detectors from gravitational-wave sources and accumulate a distribution of noise, then the observations of background time would need to be split with the time observing astrophysical sources. In addition, we would need to block gravitational-wave signals from the detector and observe for 5.0×10^6 years in order to obtain the same limit on the false-alarm rate reported in the search here. Therefore, we measure the distribution of noise events in the search for assigning the statistical significance of candidate events.

We present the details and results of the PyCBC search for stellar-mass binary

black hole mergers. Section 2.2 describes how the search identifies candidate events and Sec. 2.3 describes the parameter space that was searched during Advanced LIGO’s first observing run. Sections 2.4 and 2.5 explain the additional steps that are taken to mitigate the impact of noise transients on the significance of candidate events. We explain how the search assesses the statistical significance of candidate events in Sec. 2.6. In Sec. 2.7 we provide an overview of the Advanced LIGO detectors during their first observing run, as well as the data used for the search. Section 2.8 presents the results from the PyCBC search for binary black hole mergers in Advanced LIGO’s first observing run. Details of the two gravitational-wave events GW150914 and GW151226, and the candidate event LVT151012 are discussed in Sec. 2.8. Finally, we summarize the results of the search for binary black hole mergers in Sec. 6.5.

2.2 Matched filter

Since the parameters of astrophysical signals are not known in advance, each detector’s gravitational-wave strain time series is correlated with a discrete bank of binary black hole merger waveforms [46]; the construction of this template bank is described in Sec. 2.3. Numerical and analytical waveform modeling [91, 92, 38, 42, 43] provides accurate models of the waveforms from binary black hole mergers. These waveforms depend sensitively on the astrophysical parameters of the binary black hole merger such as the masses and spins of the black holes.

The correlation operation is referred to as match filtering. In match filtering, the data and waveform are correlated in the frequency domain and the product is weighted by the noise in the detector. The matched filter is the optimal linear filter for the detection of a known waveform in stationary, Gaussian noise [93]. The matched-filter signal-to-noise ratio (SNR) $\rho(t)$ for each waveform and each detector’s data as a function of time is calculated according to [94]

$$\rho^2(t) = [\langle s(t)|h_c(t)\rangle^2(t) + \langle s(t)|h_s(t)\rangle^2(t)] , \quad (2.1)$$

where the correlation is defined by

$$\langle s(t)|h(t)\rangle(t) = 4\Re \int_0^\infty \frac{\tilde{s}(f)\tilde{h}^*(f)}{S_n(f)} e^{2\pi ift} df , \quad (2.2)$$

and where $h_c(t)$ and $h_s(t)$ are the normalized orthogonal sine and cosine parts of the template waveform. $s(t)$ is the gravitational-wave strain from the detector and

$\tilde{s}(f)$ is used to denote the Fourier transform of the time domain quantity $s(t)$. Here, $S_n(f)$ denotes the one-sided average power spectral density of the detector noise. The waveform components $h_c(t)$ and $h_s(t)$ are normalized such that the expected value of $\langle s(t)|h_i(t)\rangle^2(t) = 1$ in stationary, Gaussian noise [95].

A local maximum in the $\rho(t)$ time series which exceeds a matched-filter SNR threshold of 5.5 is called a trigger. Triggers may be caused by astrophysical signals or noise in the data, and there may be several points in the $\rho(t)$ time series that exceed the threshold value. However, the $\rho(t)$ time series from a real signal in Gaussian noise would have a single narrow peak. Therefore a maximum of one trigger is stored in each 1 s window of the matched-filter SNR time series. The threshold and window size were chosen to limit the number of triggers stored from noise transients, while also making sure that no detectable binary black hole mergers are excluded. In addition to the time of the trigger, we store the parameters of the template waveform and the result from the signal consistency test that helps distinguish astrophysical signals from noise transients; the signal consistency test is described in Sec. 2.5.

2.3 Template bank

Each template waveform in the bank is characterized by the masses and spins of the two black holes. In the post-Newtonian expansion, at leading order the phase evolution during the inspiral depends on the chirp mass \mathcal{M} of the binary [32, 27, 96]

$$\mathcal{M} \equiv \frac{(m_1 m_2)^{3/5}}{(m_1 + m_2)^{1/5}}, \quad (2.3)$$

where m_1 and m_2 are the masses of the two compact-objects. At subsequent orders in the post-Newtonian expansion, the phase evolution depends predominately on the asymmetric mass ratio [97]

$$\eta = \frac{m_1 m_2}{(m_1 + m_2)^2}, \quad (2.4)$$

and the effective spin [98, 99, 100, 101, 102, 103]

$$\chi_{\text{eff}} = \frac{m_1 \chi_1 + m_2 \chi_2}{m_1 + m_2}, \quad (2.5)$$

where χ_i is the component of the black hole's angular momentum aligned with the direction of the orbital angular momentum, \vec{L} , of the binary which is given by [47, 84]

$$\chi_i = \frac{c}{G m_i^2} \vec{S}_i \cdot \hat{L}. \quad (2.6)$$

Here, \vec{S}_i is the spin of the black hole where $i = \{1, 2\}$, c is the speed of light, and G is the gravitational constant. We restrict this template bank to circular binaries since the loss in energy and angular momentum from gravitational waves will circularize the orbit by the time the binaries enter the Advanced LIGO frequency band [27]. We use template waveforms where the spin of each black hole is aligned (or anti-aligned) with the orbital angular momentum of the binary. These waveforms can recover systems with spins misaligned with the angular momentum of the binary, which will exhibit orbital precession, with good sensitivity over much of the parameter space [104]. In principle, black hole spins can lie anywhere in the range from $\chi_i = -1$ (maximal and anti-aligned) to $\chi_i = 1$ (maximal and aligned); however, in practice, waveform models do not produce valid waveforms for all spins.

The choice of parameters for the templates depends on the shape of the power spectrum of the detector noise [46]. The average noise power spectral density of the Advanced LIGO detectors was measured over the period September 12 to September 26, 2015. The harmonic mean of these noise spectra from the two detectors was used to place a single template bank that was employed for the duration of Advanced LIGO’s first observing run [46]. The templates are placed using a combination of geometric and stochastic methods [80, 81, 82, 83] such that the loss in matched-filter SNR caused by the discrete nature of the template bank is $<3\%$.

The template bank used in Advanced LIGO’s first observing run includes template waveforms with individual masses from $1 M_\odot$ to $99 M_\odot$ and a total mass less than $100 M_\odot$. The template bank assumes that the spins of the two compact objects are aligned with the orbital angular momentum. We limit the spin magnitude to less than 0.9895 which is the region over which the reduced-order SEOBNRv2 waveform model [42, 43] used in the search is able to generate valid template waveforms. This waveform model includes the inspiral, merger, and ringdown of gravitational-waves emitted from aligned (or anti-aligned) binary black holes using the effective-one body approach [38]. The 249,077 template waveforms used to cover the parameter space in Advanced LIGO’s first observing run are shown in Fig. 3.

The template bank does include template waveforms for binary neutron star and neutron star-black hole mergers. Results from the searches for binary neutron star and neutron star-black hole mergers obtained with the PyCBC search are reported in Ref. [105] and are not discussed here.

2.4 Data conditioning

The PyCBC search includes a data conditioning step prior to correlating the data from each detector with the template bank. The gravitational-wave strain time series is high-pass filtered such that the frequency content below 30 Hz is suppressed. In addition, loud and short instrumental transients are excised from the data by applying an inverse-Tukey window function that smoothly transitions the time series to zero [46]. This is different than detector characterization and data quality studies which identify noise transients and poor quality data prior to beginning the match filtering analysis. The data removed from detector characterization is discussed in Section 2.7.

Here, we describe how noise transients are identified in the data conditioning step. An initial identification of large excursions in the gravitational-wave strain time series are identified by whitening the time series and comparing the magnitude of each sample against a threshold value. The procedure was tuned by modifying the threshold value and adjusting the width of the window function to remove data around each transient. Samples within a time window of ± 0.5 s are clustered together, then for every sample with a whitened strain time series value greater than 100 an inverse-Tukey window is centered at the time of the loudest sample in the cluster. A whitened strain time series value of 100 is much larger than the typical value of the magnitude in Gaussian noise and also larger than the value expected from any gravitational-wave signal from binaries at astrophysical distances with masses and spins within our search space.

Figures 4, 5, and 6 show the whitened gravitational-wave time series for GW150914, GW151226, and LVT151012 respectively. We see that the whitened strain amplitudes are much lower than the threshold value set to 100.

2.5 Signal-consistency test

The search implements a signal-consistency test [106] to distinguish between astrophysical signals and non-Gaussian noise transients that were not excised from the data during the data conditioning step. The χ^2 signal-consistency test quantifies whether the signal power in a number of non-overlapping frequency bands is consistent with

that expected from the waveform template [106]. The χ^2 signal-consistency test is defined as

$$\chi_r^2 = \frac{p}{2p-2} \sum_{i=2}^p \left[\rho_i - \frac{\rho}{p} \right]^2, \quad (2.7)$$

where p denotes the number of frequency bands and ρ_i is the matched-filter SNR in the i -th frequency band. The frequency bands are constructed such that the expected signal power in each band is equal. For data containing only Gaussian noise, or Gaussian noise and a signal exactly matching the template waveform, the expected value of this statistic will be 1. For data containing non-Gaussian artifacts, or a signal not matching well with the template waveform, this value will be elevated.

The number of frequency bands p used to compute the χ^2 signal-consistency test [106] was optimized using data from the first month of Advanced LIGO's first observing run. An improved background rejection was found when adopting the following, template-dependent expression for the number of frequency bands

$$p = 1.75 \times \left[\frac{f_{\text{peak}}}{1 \text{ Hz}} - 60 \right]^{1/2}, \quad (2.8)$$

where f_{peak} is the frequency corresponding to the maximum amplitude of the template waveform using the models described in Ref. [42], and p is rounded to the nearest integer. This choice was adopted for the full analysis of Advanced LIGO's first observing run, where all waveforms have peak frequencies greater than 60 Hz.

If the detector noise was Gaussian it would be sufficient to use the matched filter signal-to-noise ratio to rank the significance of events. Since our data contains non-Gaussian transients, we use a detection statistic which is a combination of the matched-filter SNR and the χ^2 signal-consistency test value. For a single-detector trigger, the detection statistic $\hat{\rho}$ is defined as

$$\hat{\rho} = \begin{cases} \rho [(1 + (\chi_r^2)^3)/2]^{-1/6}, & \text{if } \chi_r^2 > 1, \\ \rho, & \text{if } \chi_r^2 \leq 1. \end{cases} \quad (2.9)$$

The functional form of $\hat{\rho}$ was empirically determined comparing noise triggers and simulated signals. In Chapter 6 we present a study that shows how this choice of detection statistic discriminates between noise triggers and astrophysical signals.

2.6 Significance measurement

Candidate events must be coincident between the detectors. Only Hanford-Livingston trigger pairs that occur within ± 15 ms window of each other are considered as possible candidate events. The 15 ms window is determined by the 10 ms intersite propagation time plus 5 ms for uncertainty in accurately determining the measured arrival time of weak signals. The search assesses the significance of all coincident Hanford-Livingston trigger pairs.

Each Hanford-Livingston coincidence is ranked with a network detection statistic $\hat{\rho}_c$, defined as the quadrature sum of the detection statistic $\hat{\rho}$ in each observatory

$$\hat{\rho}_c = \sqrt{\sum_{i=1}^N \hat{\rho}_i^2}, \quad (2.10)$$

where $\hat{\rho}_i$ is the detection statistic in the i -th detector calculated using Equation 2.9.

The significance of a candidate event is determined by comparing the detection statistic $\hat{\rho}_c$ to the search background. The rate of background events as a function of $\hat{\rho}_c$ is estimated from the data by repeating the analysis after artificially time-shifting the triggers from one detector relative to the other [46]. Time shifts in multiples of 100 ms were performed in Advanced LIGO's first observing run. The 100 ms time shift is ~ 3 times larger than the autocorrelation length of the waveforms in the template bank, therefore time shifts do not find coincidences between triggers associated with the same event. From this we are able to determine the rate at which detector noise produces events with a detection statistic value equal to or higher than the candidate event; this is called the false-alarm rate (FAR).

The results from the search are a list of candidate events with each candidate event assigned a FAR and a p-value. The p-value describes the probability of observing another signal from noise alone that has a detection statistic greater than or equal to a candidate event's detection statistic $\hat{\rho}_c^*$ given the background distribution [46]. We can write the p-value as [46]

$$\text{p-value} = p(\geq 1 \text{ above } \hat{\rho}_c^* | N_b) = \sum_{N_e} p(\geq 1 \text{ above } \hat{\rho}_c^* | N_e, N_b) p(N_e | N_b), \quad (2.11)$$

where N_e is the number of candidates events and N_b is the number of background events. The p-value is the product of $p(\geq 1 \text{ above } \hat{\rho}_c^* | N_e, N_b)$ which is the probability

that at least one candidate events is louder than $\hat{\rho}_c^*$ given the number of candidate events and background events, and $p(N_e|N_b)$ which is the probability of the number of candidate events given the number of background events. We can find expressions for both of these probabilities. First, we find an expression for $p(\geq 1 \text{ above } \hat{\rho}_c^*|N_e, N_b)$ which is the probability that at least one candidate events is louder than $\hat{\rho}_c^*$. For a single candidate event, the probability that one random coincident noise event lies above $\hat{\rho}_c^*$ is [46]

$$p(\hat{\rho}_c \geq \hat{\rho}_c^*|N_e = 1, N_b) = \frac{1 + n_b^*(\hat{\rho}_c^*)}{1 + N_b}, \quad (2.12)$$

where $n_b(\hat{\rho}_c^*)$ is the number of background triggers greater than or equal to $\hat{\rho}_c^*$. Therefore, the probability that no candidate event out of N_e candidate events are above this threshold $\hat{\rho}_c^*$ is

$$p(\text{none above } \hat{\rho}_c^*|N_e = 1, N_b) = \left[1 - \frac{1 + n_b^*(\hat{\rho}_c^*)}{1 + N_b}\right]^{N_e}. \quad (2.13)$$

And the probability that at least one candidate event is above $\hat{\rho}_c^*$ is the complement which is equal to

$$p(\geq 1 \text{ above } \hat{\rho}_c^*|N_e = 1, N_b) = 1 - \left[1 - \frac{1 + n_b^*(\hat{\rho}_c^*)}{1 + N_b}\right]^{N_e}. \quad (2.14)$$

Equation 2.14 can be substituted into Equation 2.11. Now, we model the coincident noise events as a Poisson distribution, where the probability $p(N_e|N_b)$ of the number of candidate events N_e given the number of background events N_b is [46]

$$p(N_e|N_b) \equiv p(N_e|\mu) = \mu^{N_e} \frac{e^{-\mu}}{N_e!}, \quad (2.15)$$

where $\mu = N_b T/T_b$ is the Poisson rate, and T is the amount of time observed and T_b is the amount of background time in the analysis. In Ref. [46] it has been shown that Equations 2.14 and 2.15 can be substituted into Equation 2.11 and simplified to obtain

$$\text{p-value} = 1 - e^{-\text{FAR } T}, \quad (2.16)$$

where FAR is the false-alarm rate and T is the amount of time observed.

A small p-value tells us that our hypothesis (the candidate event is due to noise) may not explain our observation. If we assume a Gaussian probability density function for our observation of candidate events due to Gaussian noise, then the p-value can

be related to the significance quoted in terms of σ . To find the significance we can integrate the one-tailed area under the standard normal curve according to [4]

$$\text{significance} = -\sqrt{2} \operatorname{erf}^{-1}(1 - (1 - \text{p-value})^2), \quad (2.17)$$

where $\operatorname{erf}^{-1}(x)$ is the inverse error function. Candidates events with a low FAR have a high significance and are identified as possible gravitational-wave signals.

In Advanced LIGO's first observing run, there were 46.1 days of coincident data that was searched for candidate events; the triggers during these times are time-shifted to acquire an equivalent of 5.0×10^6 years of background time analyzed in Advanced LIGO's first observing run. This amount of background time allows us to measure the FAR of a candidate event down to $6.0 \times 10^{-7} \text{ yr}^{-1}$.

The distribution of background noise events over $\hat{\rho}_c$ can vary strongly as a function of the template waveform. To account for this variation, the parameter space is divided into several regions which are treated as independent searches [46, 107]. Each coincident trigger is assigned a FAR based on the background distribution in the region containing the coincidence and incorporating a trials factor equal to the number of regions. We split the parameter space into three regions defined by (i) $\mathcal{M} < 1.74 M_\odot$, (ii) $\mathcal{M} \geq 1.74 M_\odot$ and $f_{\text{peak}} \geq 100 \text{ Hz}$, and (iii) $\mathcal{M} \geq 1.74 M_\odot$ and $f_{\text{peak}} < 100 \text{ Hz}$. In Section 2.8 we present the results from region (iii) which covers the parameter space of binary black hole mergers.

2.7 Data selection

The analysis from September 12, 2015, to January 19, 2016, contains a total coincident analysis time of 51.5 days accumulated when both detectors were operating in their normal state. Prior to measuring the significance of the coincident trigger, the non-coincident, single-detector triggers are reviewed to identify data with excess noise. When an interval of data with excessive noise is identified, the contaminated data are removed from the analysis data set, if a systematic instrumental condition without any regard for the presence of gravitational wave signals can be found [87]. The removal of data with excessive noise treats all data equally and has the chance to remove real gravitational-wave signals as well [87]. If the cause of the noise can be determined, then it is fixed as soon as possible. Data from either detector with

excessive noise typically contains non-stationary and non-Gaussian features in the form of noise transients of varying durations [87, 108].

Longer duration noise transients, such as non-stationary behavior in the interferometer noise, are not very detrimental to the PyCBC search as they occur on a time scale that is much longer than any waveform in the template bank. However, shorter duration artifacts can pollute the noise background distribution [85, 87]. In particular, above 30 Hz the Advanced LIGO detectors are sensitive to only the final few cycles of inspiral plus merger of higher mass binaries which makes their analysis more susceptible to noise transients. Many of these artifacts have distinct signatures [1] visible in data channels from the larger number of sensors used to monitor instrumental or environmental disturbances at each observatory site [109]. After applying this data quality process [87] the remaining coincident analysis time in Advanced LIGO’s first observing run is 48.6 days.

The search analyzes stretches of data longer than a minimum duration to ensure that the detectors are operating stably and that there is enough data to perform the match filtering operation. In Advanced LIGO’s first observing run, the minimum duration was 2048 s and this choice reduced the available data of 48.6 days to 46.1 days.

2.8 Results

Figure 7 shows the results from the search for binary black hole mergers using template waveforms with $\mathcal{M} \geq 1.74 M_{\odot}$ and $f_{\text{peak}} < 100$ Hz. The figure shows the observed distribution of events as well as the background distribution used to assess the significance. There are three events that lie above the estimated background: GW150914, GW151226, and LVT151012. All three of these are consistent with binary black hole merger signals and the templates that produced the highest significance for each event are indicated in Fig. 3. Figure 8 shows the mapping between the detection statistic from Fig. 7 and the FAR, p-value, and significance.

The search’s signal-consistency test shows no sign that GW150914, GW151226, or LVT151012 are noise transients. The matched-filter SNR $\rho(t)$, detection statistic $\hat{\rho}(t)$, and signal-consistency test value $\chi_r^2(t)$ time series for the best-matching template at the time of GW150914, GW151226, and LVT151015 are shown in Figures 10, 11,

and 12 respectively. For astrophysical signals that match the template waveform we expect that $\hat{\rho} \approx \rho$. Figures 10, 11, and 12 shows for both detectors the matched-filter SNR and detection statistic time series peak as the gravitational waves from each event passes through the detector. Checks of the instrumental data reveal no data quality issues at the times of the events [87].

All other observed events are consistent with the noise background for the search. A follow-up of the coincident events with $\hat{\rho}_c \approx 9$ suggests that they are likely due to noise fluctuations or poor data quality, rather than a population of weaker gravitational-wave signals.

GW150914 was observed on September 14, 2015, at 09:50:45 UTC with a combined matched-filter SNR of 23.7 and a detection statistic $\hat{\rho}_c = 22.7$. GW150914 is the most significant event in the analysis as shown in Figure 7. We can only calculate a limit on the FAR for GW150914 since there are no background events with significance equal to or greater than GW150914. Using the time-shift method to estimate the background distribution we limit the FAR of GW150914 to be $< 6.0 \times 10^{-7} \text{ yr}^{-1}$. This corresponds to a p-value of $7.5 \times 10^{-8} \text{ yr}^{-1}$ or a significance of $> 5.3 \sigma$.

Figure 7 shows that at high significance the background distribution is dominated by the presence of GW150914 in the data. Since we can limit GW150914's significance to be $> 5.3 \sigma$ we are confident it is an astrophysical signal. Once an event has been confidently identified as an astrophysical signal, we remove triggers associated with it from the background in order to get an accurate estimate of the noise background for the lower amplitude events. In Fig. 9 we show the search results with GW150914 removed from both the foreground and background distributions. Figure 13 shows the mapping between the detection statistic from Figure 13 and the FAR, p-value, and significance with GW150914 removed from both the foreground and background distributions.

GW151226 was identified as the second most significant event with a a combined matched-filter SNR of 13.0 and a detection statistic $\hat{\rho}_c = 12.8$. GW151226 was observed on December 26, 2015, at 03:38:53 UTC. After the removal of GW150914 from the background, now GW151226 is the most significant event that contributes to the background distribution. GW151226 is more significant than all background events as well. Since GW151226 is more significant than all the background events, we cannot measure its significance; however, we limit the FAR to be $< 6.0 \times 10^{-7} \text{ yr}^{-1}$.

This corresponds to a p-value of $7.5 \times 10^{-8} \text{ yr}^{-1}$ or a significance of $> 5.3 \sigma$.

We continue removing signals from the background distribution as long as the event is more significant than all the background triggers. The background distribution for events less significant than GW151226 are not dominated by the presence of GW150914 or GW151226. Therefore, the removal of GW151226 has no significant effect on assessing the significance of events with a $\hat{\rho}_c$ less than GW151226.

The third most significant event in Advanced LIGO’s first observing run is LVT151012 observed on October 12, 2015, at 09:54:43 UTC. It was observed with a combined matched-filter SNR of 9.7 and detection statistic $\hat{\rho}_c = 9.7$. The matched-filter SNR of this event is considerably lower than GW150914 and GW151226, and the FAR of LVT151012 is 1 per 2.7 years. This corresponds to a p-value of 0.045 or a significance of 1.7σ . Removing the triggers associated with GW150914 or GW151226 from the background does not have a large effect on the significance of LVT151012.

At the significance of LVT151012, we do not confidently claim this event as a gravitational-wave signal. This is why we assigned this candidate event a designation beginning with “LVT” (for LIGO-Virgo trigger) instead of “GW” (for gravitational wave). However, it is more likely to be a gravitational-wave signal than noise transient based on our estimate for the rate of gravitational-wave signals. Detector characterization studies have not identified an instrumental or environmental source for this candidate event [108] and the signal-consistency test shows no signs it is a noise transient.

Heavier chirp masses and closer distances increase the amplitude of the gravitational-wave signal from binary black hole mergers. The combination of the chirp mass, distance, and orientation of GW150914 [110] produces a signal that accumulates a loud matched-filter SNR over ~ 0.2 s in the Advanced LIGO frequency band. This makes GW150914 easily visible in the data. Figure 14 shows a whitened spectrogram where the time-frequency evolution of the signal in both detectors’ data is visible. GW151226 is located at approximately the same distance as GW150914 but has a lower chirp mass [77], therefore GW151226 accumulates a lower matched-filter SNR in the Advanced LIGO frequency band over a longer duration. Similarly if LVT151012 is an astrophysical signal, its distance is further and its chirp mass is less than GW150914 [76] which reduces our ability to visualize a distinct signature in the data. Whitened spectrograms of GW151226 and LVT151012 are shown in Figures 15

and 16. Neither GW151226 or LVT151012 can easily be seen in the data. This emphasizes the need for a matched-filter search that can detect distant or lower-mass binaries that are not easily be visualized in the data.

2.9 Conclusions

The PyCBC search employs matched filtering which correlates Advanced LIGO data with binary neutron star and black hole merger waveforms given by models based on general relativity. The search detected two stellar-mass binary black hole mergers with a significance $> 5 \sigma$ and another candidate event that is likely to be a binary black hole merger. The signals from Advanced LIGO's first observing run have several astrophysical implications, as well as being the first, direct observations of gravitational waves. The detection of GW150914 and GW151226 confirm the existence of binary black holes and stellar-mass black holes with masses $> 25 M_{\odot}$.

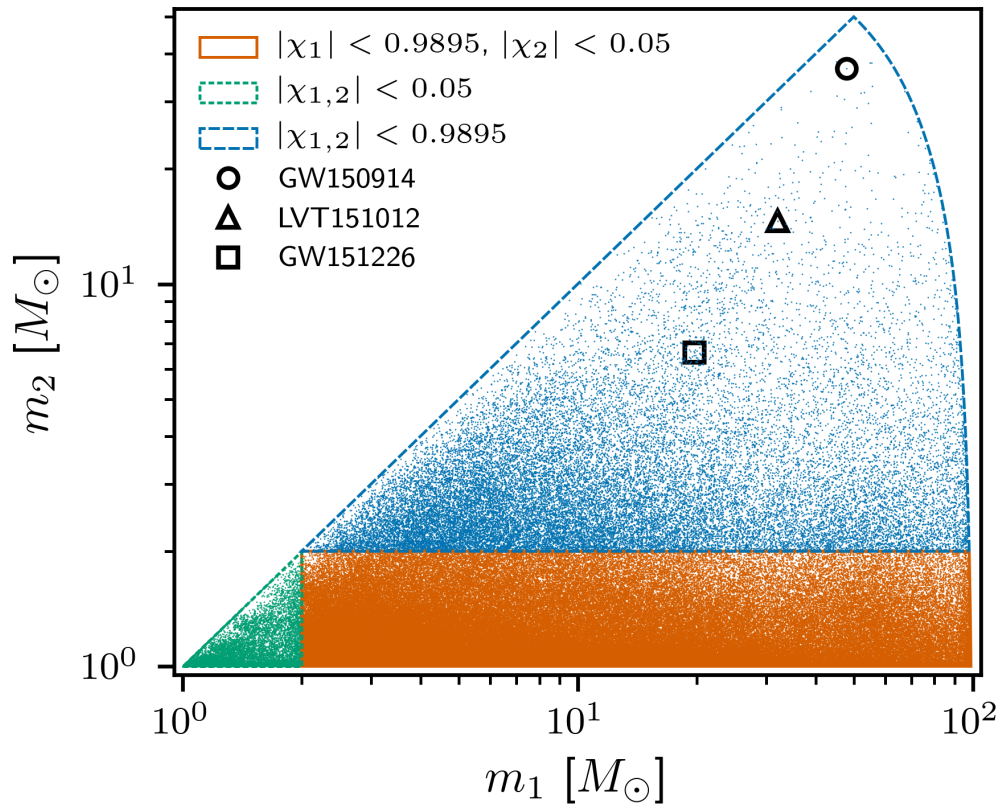


Figure 3 : The four-dimensional search parameter space covered by the template bank shown projected into the component-mass plane, where $m_1 > m_2$. The lines bound mass regions with different limits on the dimensionless aligned-spin parameters χ_1 and χ_2 . Each point indicates the position of a template in the bank. The markers indicate the best-matching template waveform for each event. Since the template bank includes a diverse set of waveforms, we search regions of the bank separately; this is discussed in Sec. 2.6. The green region corresponds to binary neutron stars, the red region corresponds to neutron star-black hole binaries, and the blue region corresponds to binary black holes.

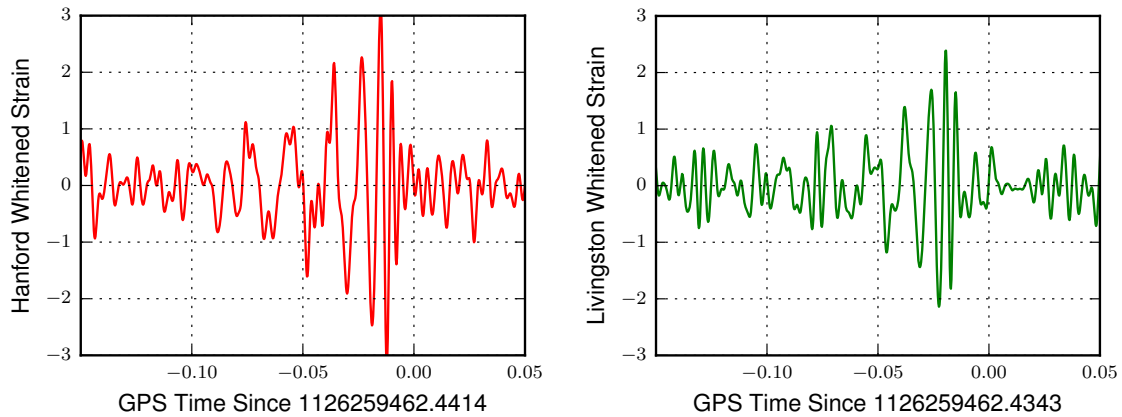


Figure 4 : The whitened gravitational-wave strain time series at the time of GW150914. The left panel shows the Hanford data and the right panel shows the Livingston data. The gravitational-wave strain is whitened with the amplitude spectral density to remove the strong instrumental lines seen in Fig. 2. In this figure, an additional 43-300 Hz bandpass filter was applied to the whitened time series.

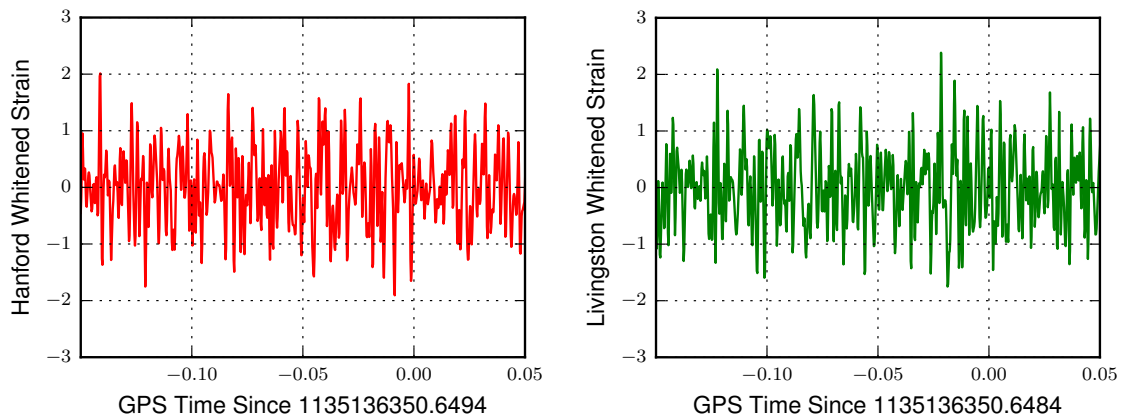


Figure 5 : The whitened gravitational-wave strain time series at the time of GW151226. The left panel shows the Hanford data and the right panel shows the Livingston data. The gravitational-wave strain is whitened with the amplitude spectral density to remove the strong instrumental lines seen in Fig. 2. In this figure, an additional 43-800 Hz bandpass filter was applied to the whitened time series.

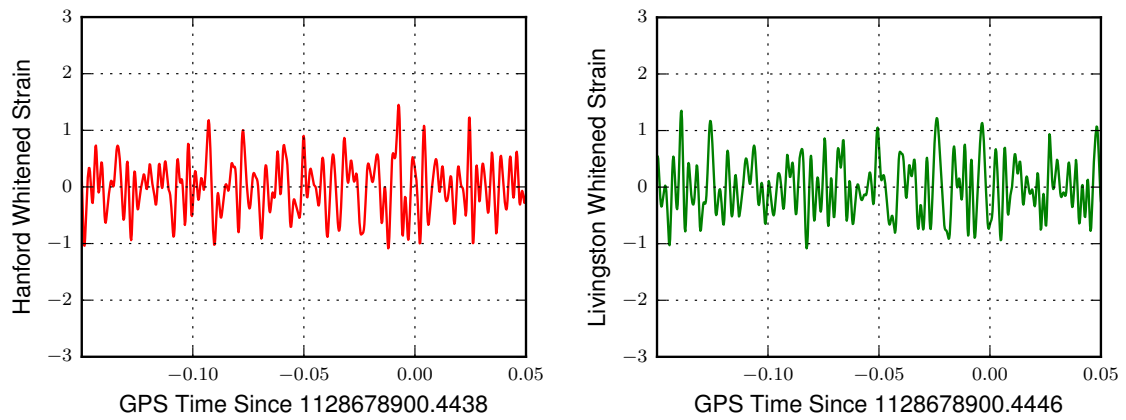


Figure 6 : The whitened gravitational-wave strain time series at the time of LVT15101. The left panel shows the Hanford data and the right panel shows the Livingston data2. The gravitational-wave strain is whitened with the amplitude spectral density to remove the strong instrumental lines seen in Fig. 2. In this figure, an additional 43-400 Hz bandpass filter was applied to the whitened time series.

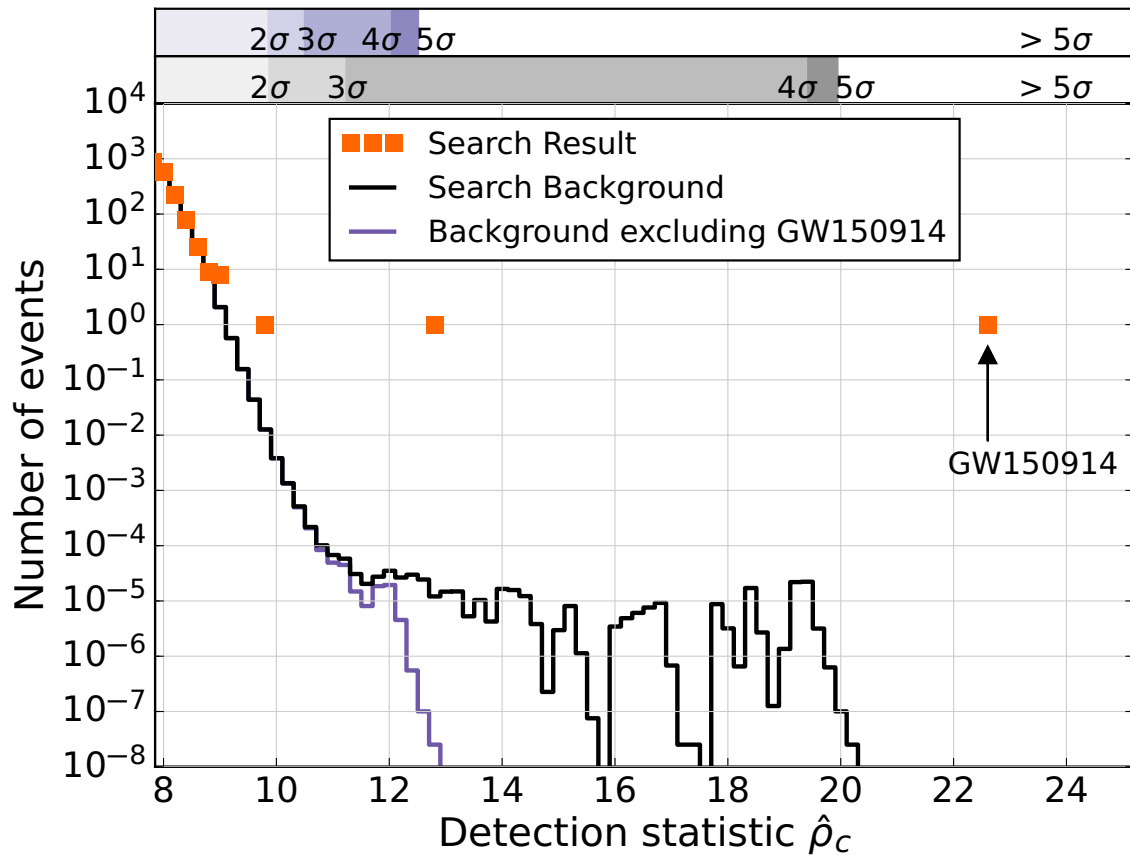


Figure 7 : The results from the search for binary black hole mergers in Advanced LIGO's first observing run. The result for signals with chirp mass $\mathcal{M} > 1.74M_{\odot}$ (the chirp mass of a $m_1 = m_2 = 2M_{\odot}$ binary) and $f_{\text{peak}} > 100$ Hz are shown. Here we show the histogram of the detection statistic $\hat{\rho}$. GW150914 is the most significant event in the data and is more significant than any background event in the data. GW150914 is identified with a significance $> 5\sigma$.

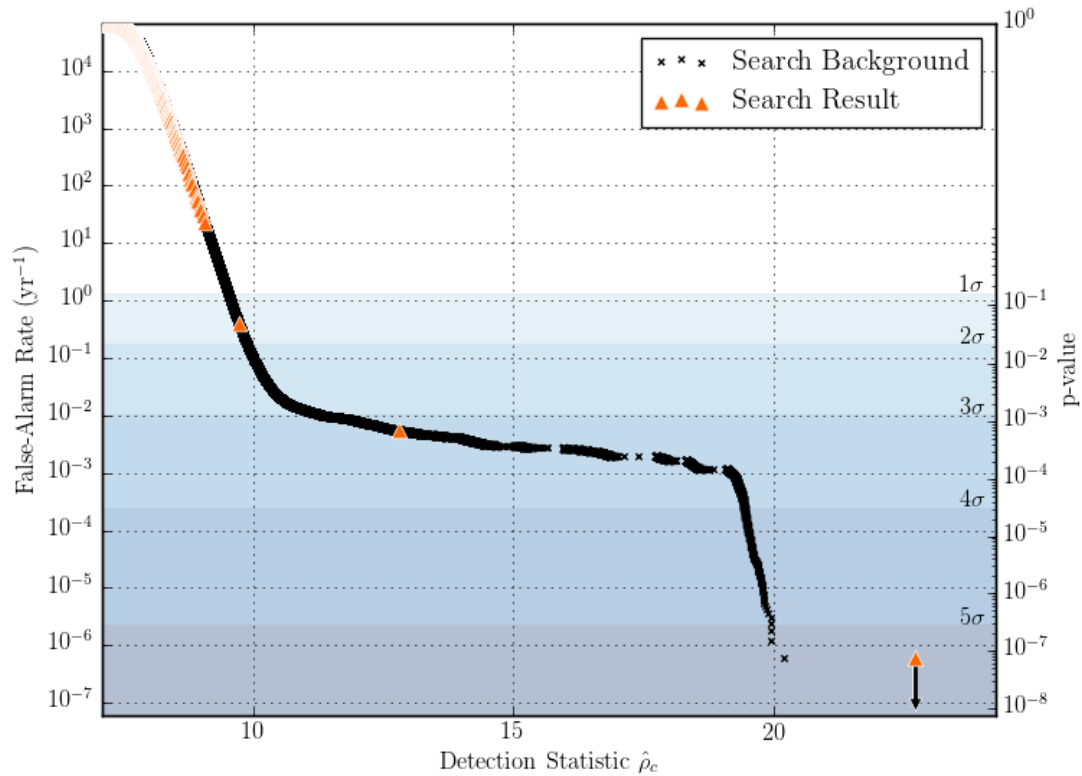


Figure 8 : The results from the search for binary black hole mergers in Advanced LIGO’s first observing run. The result for signals with chirp mass $\mathcal{M} > 1.74M_{\odot}$ (the chirp mass of a $m_1 = m_2 = 2M_{\odot}$ binary) and $f_{\text{peak}} > 100$ Hz are shown. This histogram shows the mapping between the detection statistic and the false-alarm rate, p-value, and significance.

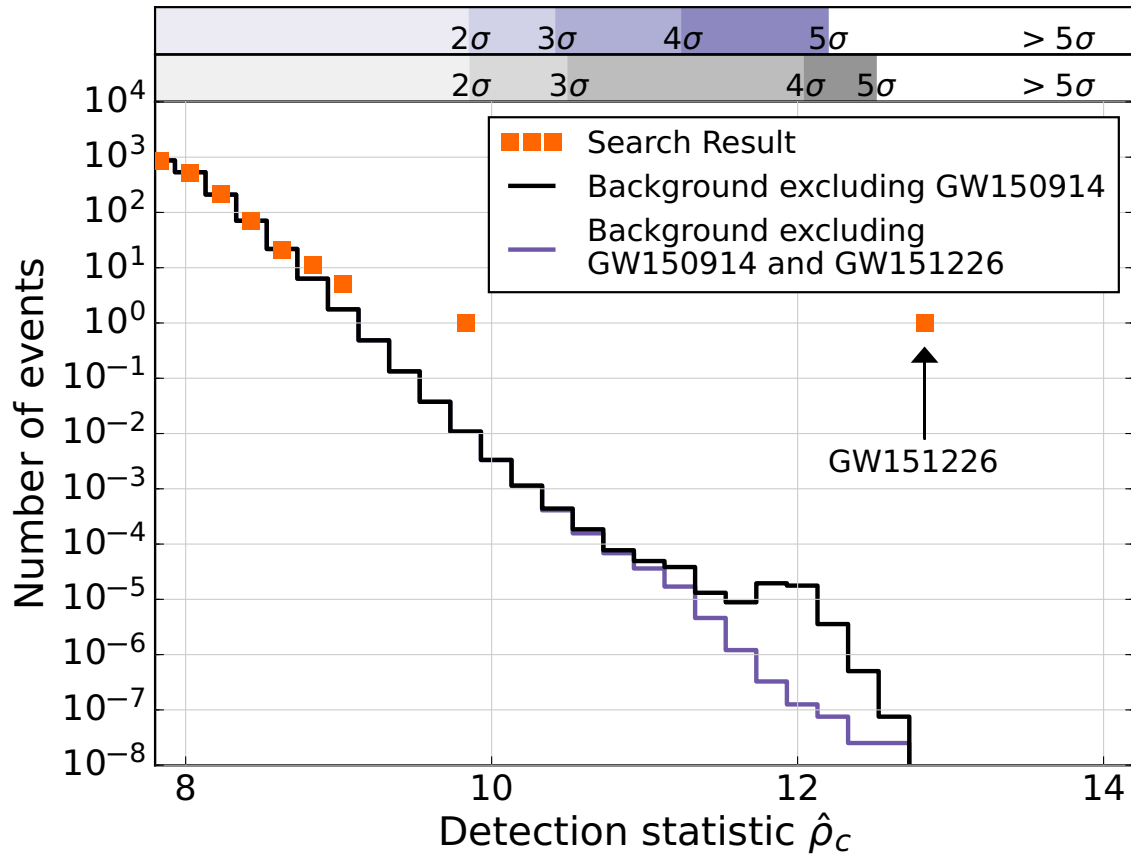


Figure 9 : The results from the search for binary black hole mergers in Advanced LIGO’s first observing run with GW150914 removed. Here we show the histogram of the detection statistic $\hat{\rho}$. GW151226 is identified as the most significant event remaining in the data. GW151226 is more significant than the remaining background in the analysis with a significance $> 5\sigma$. The third most significant event in the search, LVT151012, is identified with a significance of 1.7σ . The significance obtained for LVT151012 is not greatly affected by including or removing background contributions from GW150914 and GW151226.

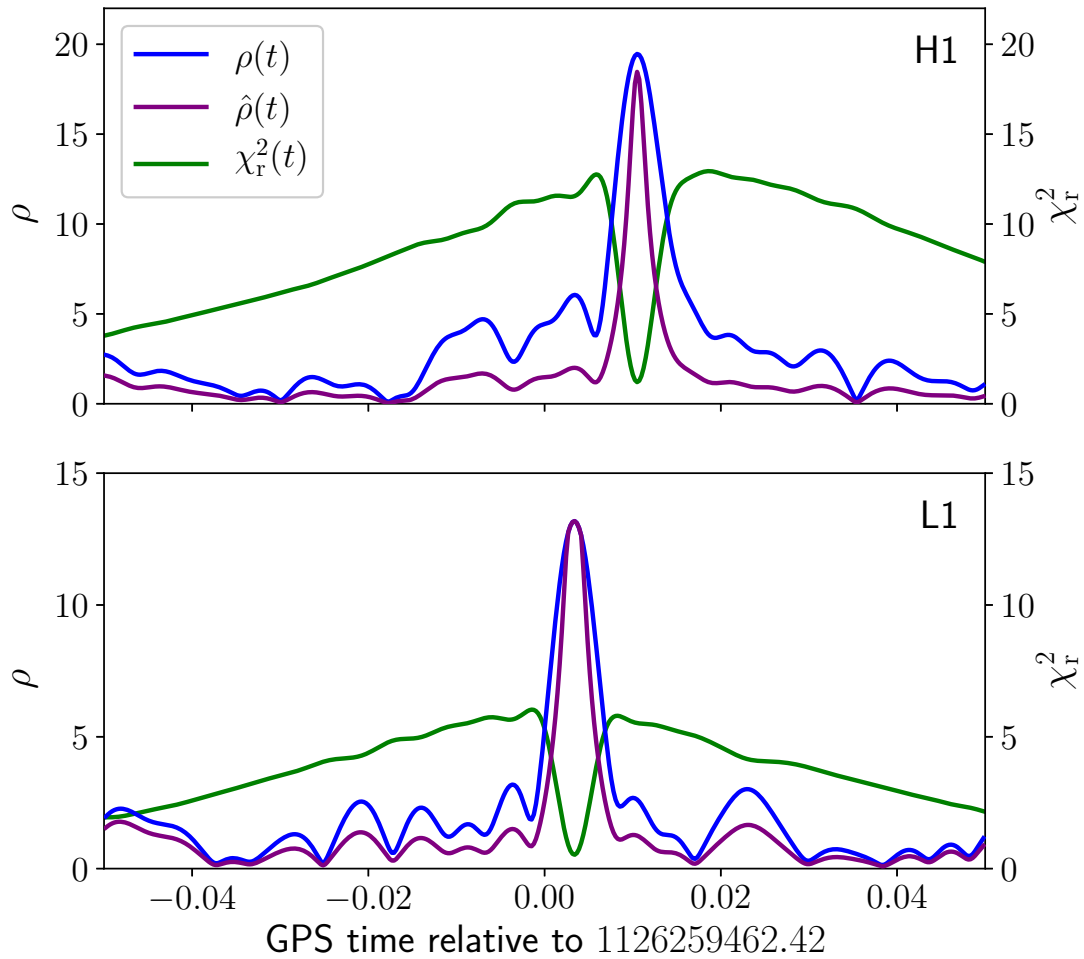


Figure 10 : The matched-filter signal-to-noise ratio $\rho(t)$ (blue), detection statistic $\hat{\rho}_c(t)$ (purple), and signal-consistency test value $\chi_r^2(t)$ (green) versus time using the best-matching template at the time of GW150914. The top plot shows the Hanford detector (H1) and the bottom plot shows the Livingston detector (L1).

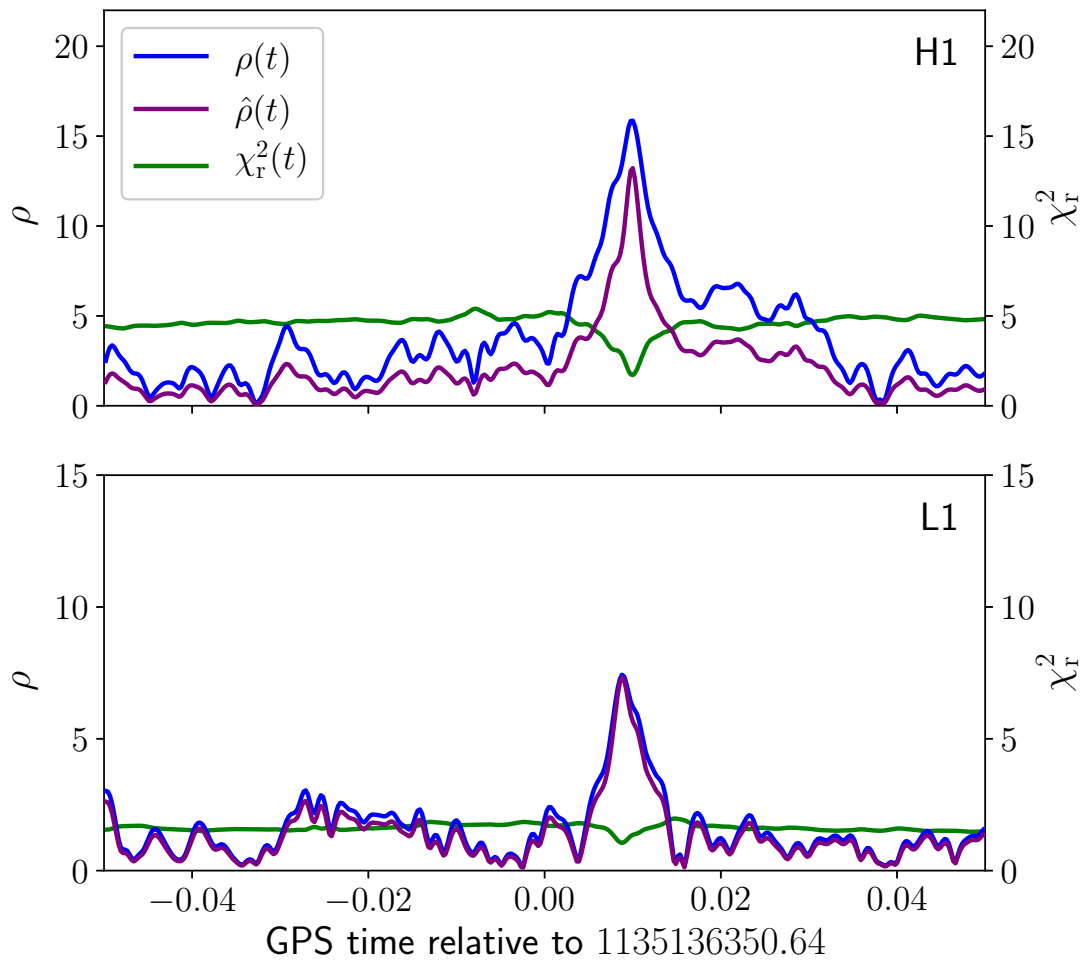


Figure 11 : The matched-filter signal-to-noise ratio $\rho(t)$ (blue), detection statistic $\hat{\rho}_c(t)$ (purple), and signal-consistency test value $\chi_r^2(t)$ (green) versus time using the best-matching template at the time of GW151226. The top plot shows the Hanford detector (H1) and the bottom plot shows the Livingston detector (L1).

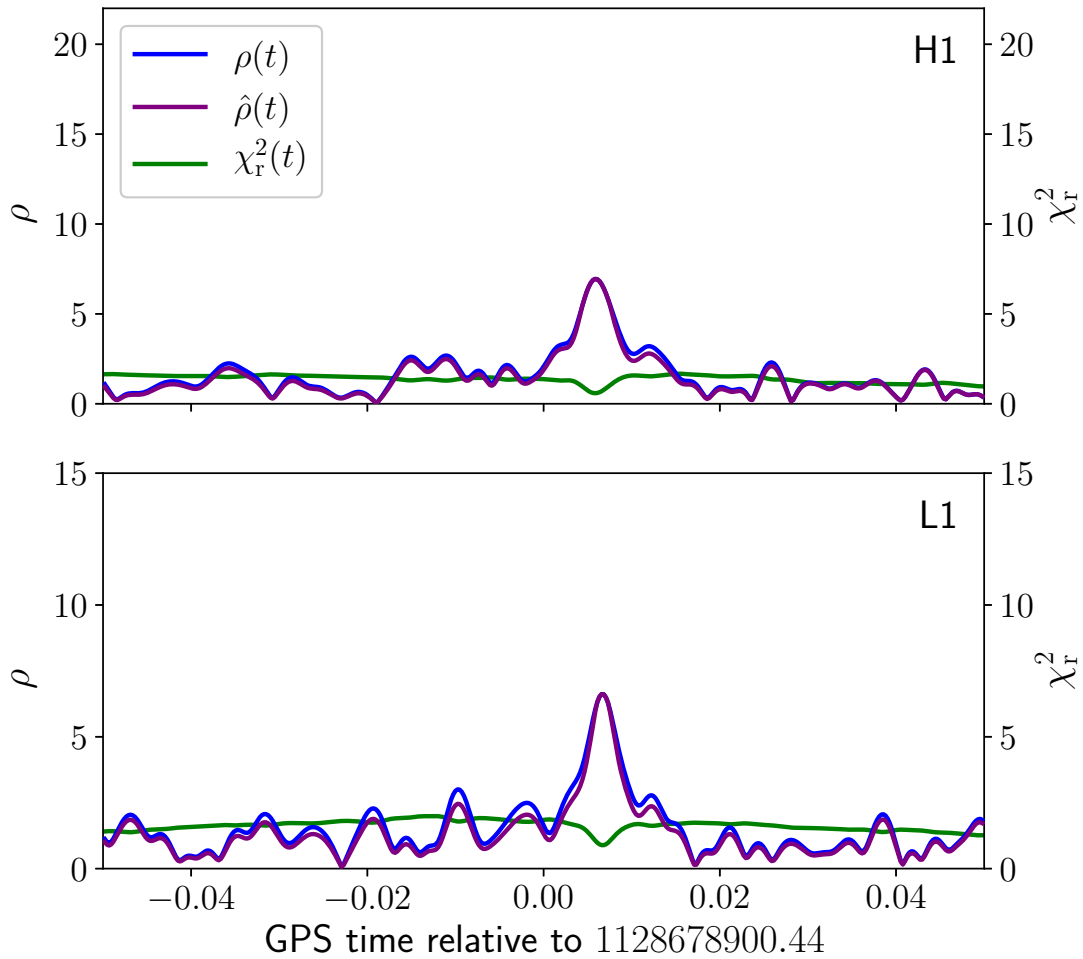


Figure 12 : The matched-filter signal-to-noise ratio $\rho(t)$ (blue), detection statistic $\hat{\rho}_c(t)$ (purple), and signal-consistency test value $\chi_r^2(t)$ (green) versus time using the best-matching template at the time of LVT151012. The top plot shows the Hanford detector (H1) and the bottom plot shows the Livingston detector (L1).

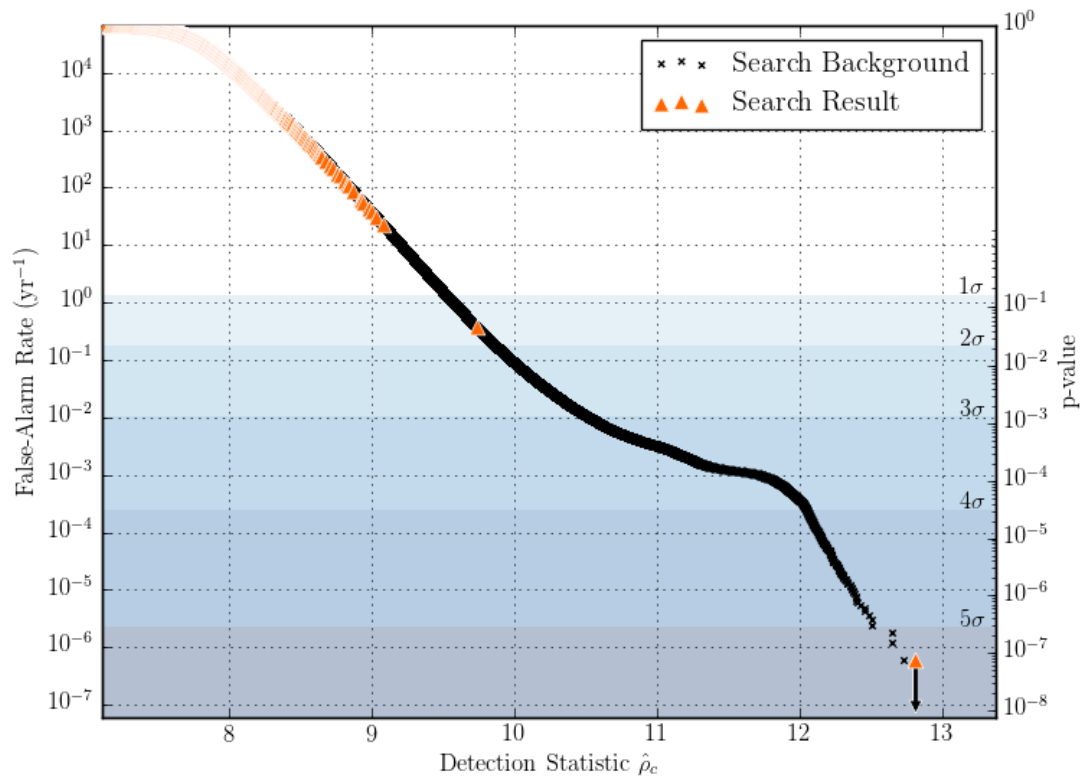


Figure 13 : The results from the search for binary black hole mergers in Advanced LIGO's first observing run with GW150914 removed. The result for signals with chirp mass $\mathcal{M} > 1.74M_{\odot}$ (the chirp mass of a $m_1 = m_2 = 2M_{\odot}$ binary) and $f_{\text{peak}} > 100$ Hz are shown. This histogram shows the mapping between the detection statistic and the false-alarm rate, p-value, and significance.

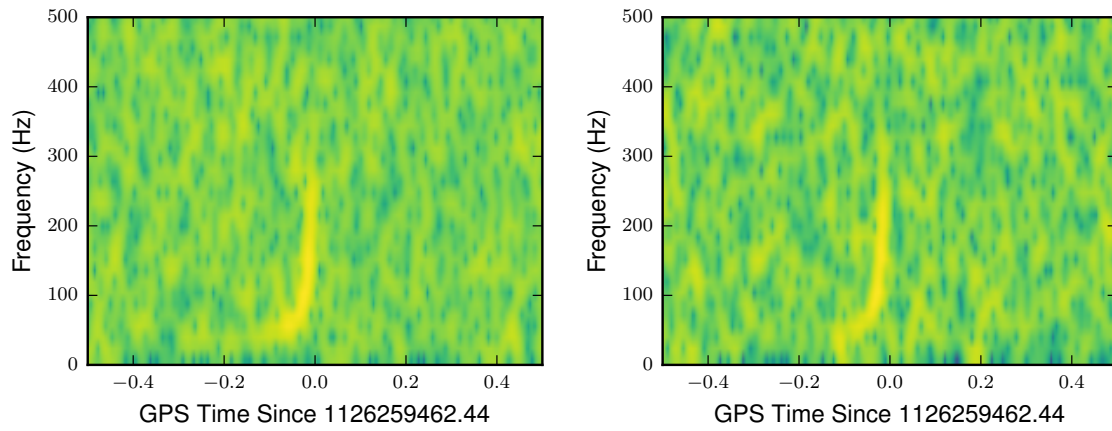


Figure 14 : A spectrogram of the whitened gravitational-wave strain time series from Figure 4. The left panel shows the Hanford data and the right panel shows the Livingston data at the time of GW150914.

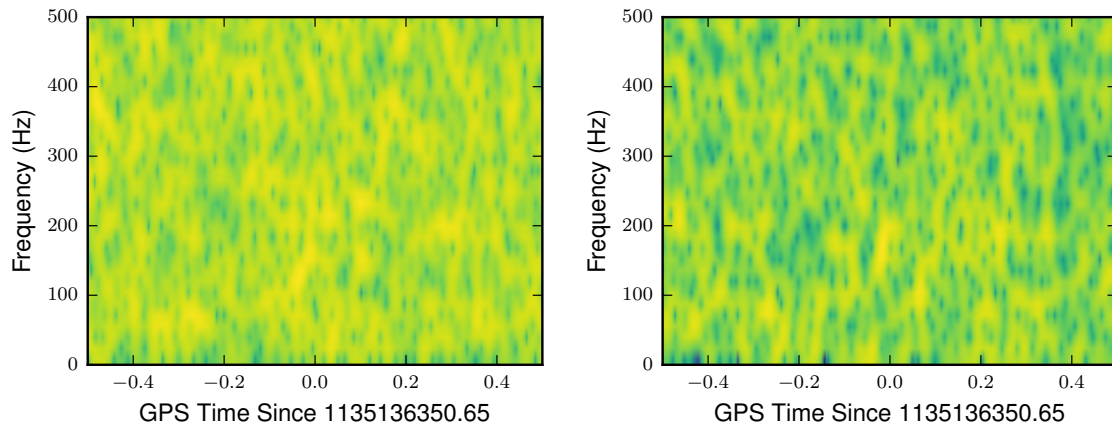


Figure 15 : A spectrogram of the whitened gravitational-wave strain time series from Figure 5. The left panel shows the Hanford data and the right panel shows the Livingston data at the time of GW151226.

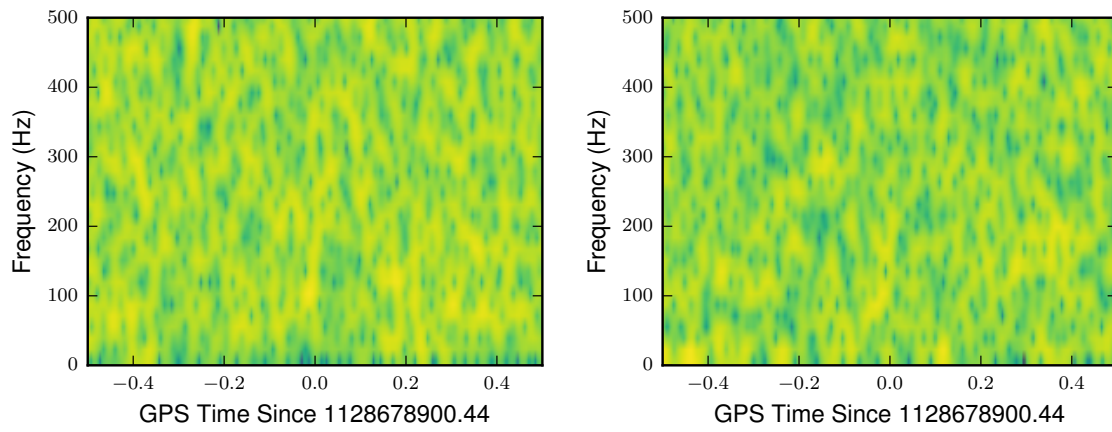


Figure 16 : A spectrogram of the whitened gravitational-wave strain time series from Figure 6. The left panel shows the Hanford data and the right panel shows the Livingston data at the time of LVT151012.

Chapter 3

The impact of calibration errors on the detection of binary black hole mergers in Advanced LIGO data

3.1 Introduction

The detection of astrophysical sources such as binary black hole mergers with Advanced LIGO requires the detectors' data to be calibrated properly [111]. Searches for binary neutron star and black hole mergers use matched filtering to correlate the calibrated gravitational-wave strain data with a bank of templates [112, 46]. Calibration errors directly affect the uncertainty in the gravitational-wave strain analyzed by the PyCBC search. The uncertainty in the gravitational-wave strain could reduce the matched-filter signal-to-noise ratio [113, 114]. Previous studies have shown that the loss in the matched-filter signal-to-noise ratio and the loss in the detection statistic [46] in the PyCBC search have a quadratic relation with respect to calibration errors [113, 114, 4].

We can show that these calibration errors that reduce the matched-filter signal-to-noise ratio will adversely affect the sensitive volume of a search as well as the detection rate. The detection rate R which can be characterized as

$$R = \frac{N}{VT} \sim \frac{1}{D^3}, \quad (3.1)$$

where N is the number of detections, V is the sensitive volume of the search which

depends on the cube of the horizon distance D averaged over all sky positions and binary orientations [115], and T is the time observed. For a single detector, the horizon distance is defined as the distance at which an optimally-oriented, overhead source can be detected with an optimal matched-filter signal-to-noise ratio ρ equal to 8 [115], where the optimal matched-filter signal-to-noise ratio is

$$\rho = \sqrt{4\Re \int_0^\infty \frac{|\tilde{h}(f)|^2}{S(f)} df}, \quad (3.2)$$

where $\tilde{h}(f)$ is the frequency-domain gravitational waveform, $S(f)$ is the power spectral density, and \Re denotes the real part of a complex number. Here, we see the calibration errors that reduce the matched-filter signal-to-noise lowers the horizon distance which reduces the detection rate [116]. Therefore its important that Advanced LIGO's calibration is accurate since a significant deviation from the correct calibration could cause a loss in signal-to-noise ratio that will reduce the detection rate of binary neutron star and black hole mergers.

Advanced LIGO measures variations in differential arm length $\Delta L_{\text{free}} = L_x - L_y$ between its two arms caused by gravitational waves [74]. A feedback loop controls the error signal between the laser frequency and the resonant frequency of the arm cavities which is referred to as locking the arm cavities [74, 3]. Figure 17 depicts the feedback loop that controls the differential displacement of the detector's arms ΔL_{free} which sends the error signal $d_{\text{err}}(t)$ through a set of digital filters to produce a control signal $d_{\text{ctrl}}(t)$, and then the control signal is sent to the actuator systems which displace the test masses [117, 3]. In Advanced LIGO the mirrors act as freely falling test masses that detect gravitational waves [117, 3].

The searches for binary black hole mergers analyze a calibrated gravitational-wave strain $h(t)$ which is the fractional variation in the Advanced LIGO differential arm length defined as

$$h(t) \equiv \frac{\Delta L_{\text{free}}(t)}{L}, \quad (3.3)$$

where L is the length of the arms.

We can derive an expression for $h(t)$ from the feedback loop in Figure 17. In Figure 17 we see that

$$\Delta L_{\text{res}}(t) = \Delta L_{\text{free}}(t) - \Delta L_{\text{ctrl}}(t), \quad (3.4)$$

where $\Delta L_{\text{ctrl}}(t)$ is the control displacement applied to physically move the test masses in opposition of the differential displacement and $\Delta L_{\text{res}}(t)$ is the residual displacement that is the difference between $\Delta L_{\text{free}}(t)$ and $\Delta L_{\text{ctrl}}(t)$. Therefore, we can find an expression for $\Delta L_{\text{free}}(t)$ from the feedback loop in Figure 17 which gives us

$$Lh(t) = \Delta L_{\text{free}}(t) = \Delta L_{\text{res}}(t) + \Delta L_{\text{ctrl}}(t) \quad (3.5)$$

$$= \frac{1}{C^{(m)}(f, t)} d_{\text{err}}(t) + A^{(m)}(f, t) d_{\text{ctrl}}(t), \quad (3.6)$$

where f is the gravitational-wave frequency, t is the time, $C^{(m)}(f, t)$ is a model of the sensing function that describes the response of the detector to changes in the arm lengths, and $A^{(m)}(f, t)$ is a model of the actuation function that describes the motion of the test mass when driven by the control signal $d_{\text{ctrl}}(t)$. Here, we write the sensing and actuation functions as dependent on frequency and time because they consist of frequency domain functions with time-dependent coefficients. This formulation of $\Delta L_{\text{free}}(t)$ is convenient since the digital filters have already been applied to $d_{\text{ctrl}}(t)$. The calibration of the gravitational-wave strain is depicted on the right side of Figure 17.

Both $C^{(m)}(f, t)$ and $A^{(m)}(f, t)$ are generated from measurements that have uncertainties and systematic errors. From Equations 3.3 and 3.5 we see that uncertainties and systematic errors in these models and model parameters directly impact the uncertainties and systematic errors of the calibrated gravitational-wave strain. These errors can reduce the signal-to-noise ratio of astrophysical signals as previously discussed.

One source of systematic errors while calibrating the gravitational-wave strain is time-dependent drift of the state of the detector from the state described by the model of the sensing and actuation functions [118]. The time dependence of the sensing function is due to changes in the alignment and thermal state of the detectors' optics [118]. Slow variations in the charging of actuators introduce time-dependent changes to the actuation functions [118]. Advanced LIGO tracks these time-dependent variations by monitoring the response of the error signal from the differential arm length error servo to injected signals [118]. Applying the time-dependent correction factors improves systematic errors in the magnitude of the reconstructed differential arm length by several percent [118].

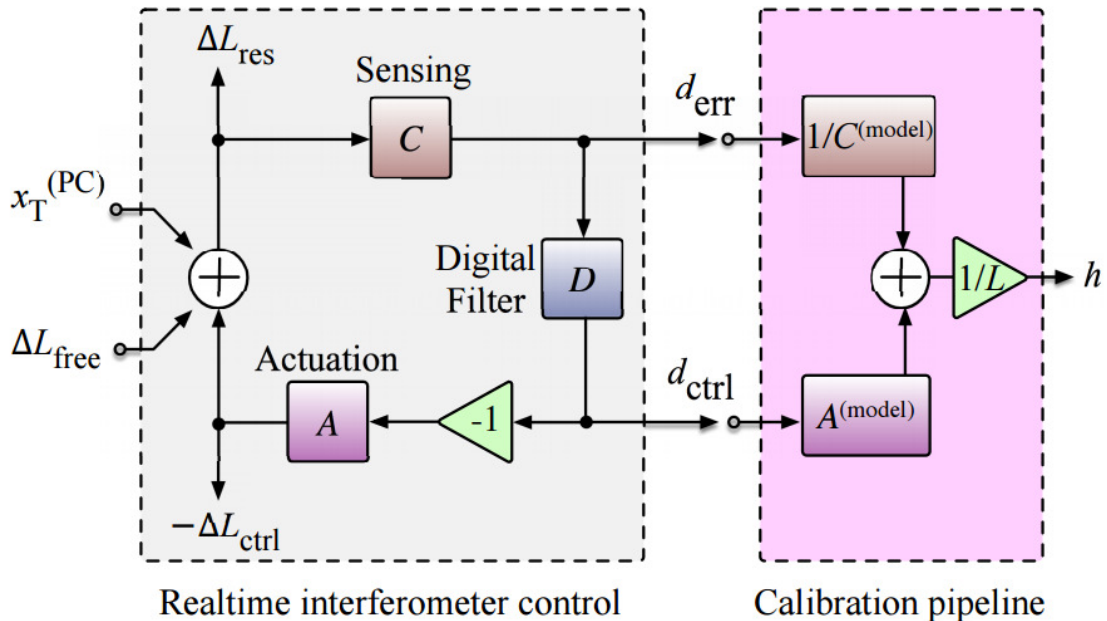


Figure 17 : A schematic of the feedback loop that controls the differential arm length ΔL_{free} and calibration from Ref. [3]. The sensing function C , digital filters D , and actuation function A are the components of the feedback loop. Models of the sensing function $C^{(model)}$ and actuation function $A^{(model)}$ are used to calibrate the error signal d_{err} and control signal d_{ctrl} to obtain the gravitational-wave strain h . $x_T^{(PC)}$ represents sinusoidal excitations at select frequencies called calibration lines. Calibration lines are used to monitor time-dependent changes in the sensing and actuation functions.

This chapter describes the impact of time-dependent calibration errors on the detection of binary neutron star and black hole mergers. We demonstrate their impact with real and simulated signals analyzed by the PyCBC search [79, 46, 90]. Section 3.3 describes the Advanced LIGO calibration and our method for simulating calibration errors in Advanced LIGO data. This is the same method used to initially evaluate the impact of calibration errors on the detection of GW150914 in Ref. [4]. We consider the impact of the time-dependent calibration parameters in the calibration on the matched-filter signal-to-noise ratio of binary neutron star and black hole mergers with masses up to $100 M_{\odot}$ in Sec. 3.4. In Sections 3.7 and 3.8 we present results from evaluating the impact of these temporal variations on the PyCBC detection statistic [46]. Finally, Sec. 3.9 summarizes the impact of time-dependent calibration errors on the detection of binary neutron star and black hole mergers in Advanced LIGO.

3.2 Models of the sensing function and actuation function

Models of the sensing function and actuation function are used to calibrate the gravitational wave strain as shown in Figure 17. These models compensate for the temporal variations in the sensing and actuation functions [118]. In this section, we describe how Advanced LIGO incorporates temporal corrections into the models of the sensing function and actuation function.

The frequency dependence of $C(f, t)$ and $A(f, t)$ is periodically measured to update the models of the sensing and actuation functions. Observing runs are divided into calibration epochs which correspond to times between these measurements. At the start time t_0 of a calibration epoch, the frequency-dependence of $C(f, t)$ and $A(f, t)$ are modeled such that $C(f, t_0) = C_0^{(m)}(f)$ and $A(f, t_0) = A_0^{(m)}(f)$. The digital filter $D(f) = D_0(f)$ is a known, exact function but $D(f)$ is manually changed from time to time to improve the performance of the detector. $C_0^{(m)}(f)$, $A_0^{(m)}(f)$, and $D_0(f)$ are unchanged throughout a calibration epoch. The drift from $C_0^{(m)}(f)$ and $A_0^{(m)}(f)$ at the start of the calibration epoch is monitored by actuating the test masses at specific frequencies called calibration lines [111] which are used to update time-dependent calibration parameters in the sensing and actuation functions [118].

The sensing function $C(f, t)$ converts the residual test mass differential displacement $\Delta\tilde{L}_{\text{res}}(f)$ to the digitized error signal $\tilde{d}_{\text{err}}(f)$ representing the laser power fluctuation at the gravitational-wave readout port. The sensing function includes the detector's response converting differential displacement to the laser power fluctuation at the readout port which is determined by the arm cavity test mass reflectivities, the reflectivity of the signal recycling mirror, the length of the arm cavities, and the length of the signal recycling cavity [3]. In addition, the sensing function includes the response of the photodiodes and their analog readout electronics, and effects from the digitization of the signal from the photodiodes [76].

The Advanced LIGO calibration uses a model of the sensing function $C^{(m)}(f, t)$ that models a signal-recycled Fabry-Perot interferometer [119]. The model from Ref. [119] has been simplified to a single coupled cavity pole system [120]. The signal recycling cavity is detuned and during Advanced LIGO's first observing run, there was a small, unintentional offset of the detuning phase [120]. This is likely due to an offset in the angular control of the signal recycling mirror and this detuning

induces an optical anti-spring [120]. We include corrections for the optical anti-spring in the model of the sensing function which is [3, 120]

$$C^{(m)}(f, t) = C_{\text{res}}(f) \left[\frac{\kappa_C(t)}{1 + i \frac{f}{f_c(t)}} \right] \left[\frac{f^2}{f^2 - i \frac{f_s(t)}{Q(t)} f + f_s^2(t)} \right], \quad (3.7)$$

where $C_{\text{res}}(f)$ is the time-independent residual of the sensing function which is given by

$$C_{\text{res}}(f) = C_0(f) \left[1 + i \frac{f}{f_c(t_0)} \right] \left[\frac{f^2 - i \frac{f_s(t_0)}{Q(t_0)} f + f_s^2(t_0)}{f^2} \right]. \quad (3.8)$$

The drift in the sensing function is described by a real gain $\kappa_C(t)$ and cavity pole frequency $f_c(t)$. In this chapter we consider data from both Advanced LIGO's first and second observing runs. In Advanced LIGO's second observing run, the the optical spring frequency $f_s(t)$ and the dimensionless quality factor $Q(t)$ of the signal recycling cavity [74] were tracked but not compensated for; however, we include $f_s(t)$ and $Q(t)$ in our model while analyzing data from Advanced LIGO's second observing run. The term including $f_s(t)$ and $Q(t)$ is omitted while analyzing data from Advanced LIGO's first observing run.

The interferometer differential arm length is controlled by actuating on the quadruple suspension system of the test masses. Each of suspension systems consists of four coupled pendulums [3, 121] which isolates the test masses from motion that is not suppressed by the isolation system [3, 121]. There is an independent pendulum system that hangs beside the test mass. This pendulum system is used to generate reaction forces on each mass of the test mass pendulum. A diagram of one of these suspension systems is shown in Fig. 18. The contributions to the actuation function $A(f, t)$ from three lowest stages in the suspension system are modeled in $A^{(m)}(f, t)$. The upper-intermediate stage actuators are dominant below 5 Hz, the penultimate stage actuators are dominant between 5 Hz and 20 Hz, and the test stage actuator are dominant above 20 Hz [118]. The actuation from the top mass in the pendulum system is negligible compared to the three masses that hang below it. Therefore, the model actuation function $A^{(m)}(f, t)$ is decomposed into the sum of these three components: the actuation of the test mass $A_{\text{tst}}^{(m)}(f, t)$, the actuation of the penultimate mass $A_{\text{pu}}^{(m)}(f, t)$, and the actuation of the upper-intermediate mass $A_{\text{uim}}^{(m)}(f, t)$. The

actuation function model is

$$A^{(m)}(f, t) = \kappa_{tst}(t)A_{tst,0}^{(m)}(f) + \kappa_{pu}^{(m)}(t)(A_{pu,0}^{(m)}(f) + A_{uim,0}^{(m)}(f)). \quad (3.9)$$

The drift in the actuation function is parameterized by the complex gain in the actuation of the test mass $\kappa_{tst}(t)$ and another complex gain which is the combination of the actuation of the penultimate mass and the upper-intermediate mass $\kappa_{pu}(t)$.

The nominal values for the time-dependent gains are $\kappa_C(t_0) = 1$, $\kappa_{tst}(t_0) = 1$, and $\kappa_{pu}(t_0) = 1$. Prior to a calibration epoch $f_c(t_0)$, $f_s(t_0)$, and $Q(t_0)$ are measured. During the observing run these parameters will vary from their nominal values. For example, $\kappa_{tst}(t)$ drifts from 1 due to electrostatic charging of the test mass [118]. $\kappa_C(t)$ and $f_c(t)$ vary due to changes in the alignment and thermal state of the interferometer optics, and thermally distorted mirrors can result in optical mode mismatch between the arm cavities and the signal recycling cavity [118].

3.3 Simulating calibration errors in Advanced LIGO data

In this section, we present the method we use to simulate calibration errors in Advanced LIGO data for our studies examining the impact of systematic errors from time-dependent variations in $C^{(m)}(f, t)$ and $A^{(m)}(f, t)$ on the detection of binary neutron star and black hole mergers. Although the Advanced LIGO calibration is done in the time-domain, we simulate calibration errors in the frequency-domain. Since the matched-filter calculation is done in the frequency-domain its more convenient to adjust the calibration in the frequency domain as well. Equation 3.5 can be rewritten in terms of just the differential arm length error signal using the relation $\tilde{d}_{ctrl}(f) = D(f)\tilde{d}_{err}(f)$ [117] where $D(f)$ are the set of known digital filters in the detectors and $\tilde{d}_{ctrl}(f)$ denotes the Fourier transform of the time series $d_{ctrl}(t)$. The differential displacement arm length along the two arms becomes

$$\Delta\tilde{L}_{free}(f) = R(f, t)\tilde{d}_{err}(f), \quad (3.10)$$

where $R(f, t)$ is the response function of the detector. $R(f, t)$ is given by

$$R(f, t) = \frac{1 + G(f, t)}{C^{(m)}(f, t)}, \quad (3.11)$$

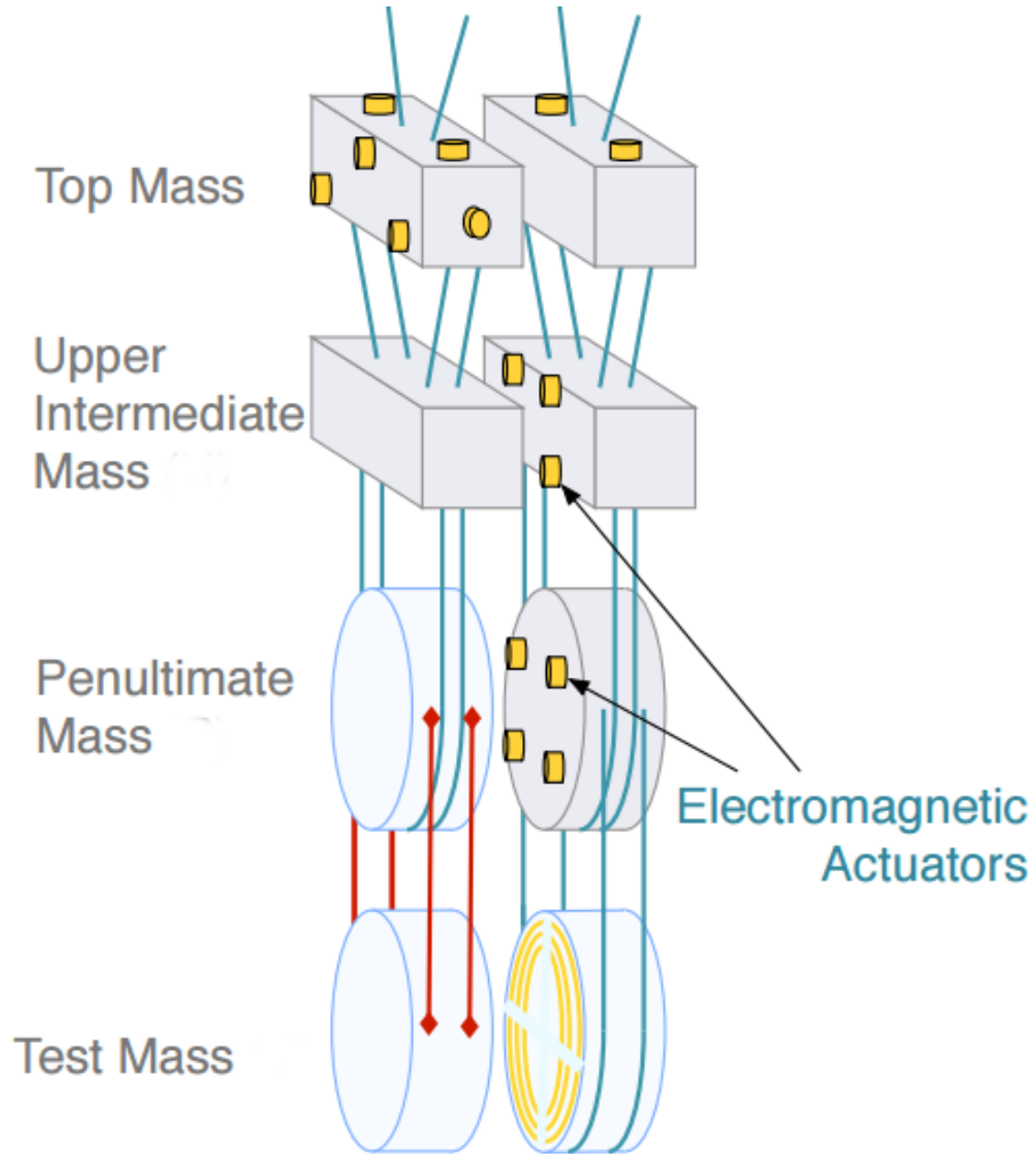


Figure 18 : A schematic of the quadruple pendulum system from Ref. [3]. There is an independent pendulum system which is used to generate reaction forces on each mass of the test mass pendulum.

where $G(f, t)$ is the open loop transfer function which is given by

$$G(f, t) = C^{(m)}(f, t)D_0(f)A^{(m)}(f, t). \quad (3.12)$$

If we insert the models for the sensing function from Equation 3.8 and the model for the actuation function from Equation 3.9, then the time evolution of the response

functions is modeled as

$$R(f, t) = \frac{1}{\kappa_C(t)C_{\text{res}}(f)} \left[1 + i \frac{f}{f_c(t)} \right]^{-1} \left[\frac{f^2 - i \frac{f_s(t)}{Q(t)} f + f_s^2(t)}{f^2} \right]^{-1} + D_0(f) [\kappa_{tst}(t)A_{tst,0}(f) + \kappa_{pu}(t)(A_{pu,0}(f) + A_{uim,0}(f))] . \quad (3.13)$$

The response function from Equation 3.13 will have systematic and measurement uncertainties from $C_0(f)$ and $A_0(f)$ as well as time-dependent drift. At time t , this can be expressed as the relation between the response function with no errors from the amplitude or phase $R_t(f)$ and the response function that includes errors from the amplitude and phase $R_m(f)$. We use the subscript t to denote the ‘‘true’’ value (without calibration errors), and the subscript m to denote the ‘‘measured’’ value which contains calibration errors. We define $R_t(f)$ in polar form as

$$R_t(f) = A(f)e^{i\phi(f)}, \quad (3.14)$$

where $A(f)$ is the amplitude of the response function and $\phi(f)$ is the phase of the response function. We define $R_m(f)$ in polar form as

$$R_m(f) = [A(f) + \delta A(f)] e^{i[\phi(f) + \delta\phi(f)]} \quad (3.15)$$

$$= A(f) \left[1 + \frac{\delta A(f)}{A(f)} \right] e^{i\phi(f)} e^{i\delta\phi(f)}, \quad (3.16)$$

where $\delta A(f)$ is the change in the amplitude of the response function due to errors and $\delta\phi(f)$ is the change in the phase of the response function due to errors. The amplitude $A(f)$ and phase $\phi(f)$ in Equations 3.14 and 3.15 are equivalent. The relation between $R_t(f)$ and $R_m(f)$ is the error function $K(f)$ which is defined in polar form as

$$K(f) = \frac{R_t(f)}{R_m(f)} = \left[1 + \frac{\delta A(f)}{A(f)} \right] e^{i\delta\phi(f)}. \quad (3.17)$$

In Figures 19, 20, 21, and 22 we show the fractional amplitude error $\delta A(f)/A(f)$ and phase error $\phi(f)$ as each time-dependent calibration parameter is varied. The model from the calibration epoch beginning on January 3, 2017, during Advanced LIGO’s second observing run was used to generate these results.

We simulate calibration errors by multiplying the frequency-domain gravitational-wave strain $\tilde{h}(f)$ from the detector by the error function $K(f, t) = R_m(f, t)/R_t(f, t)$ such that

$$\tilde{h}'(f) = R_m(f, t)\tilde{d}_{err}(f) = K(f, t)\tilde{h}(f), \quad (3.18)$$

where $\tilde{h}'(f)$ is the gravitational-wave strain with simulated calibration errors.

3.4 Derivation of the impact of calibration errors on the matched-filter signal-to-noise ratio

Changes in the response function alter the amplitude and phase of the gravitational-wave strain which reduces the match between the template waveform and the astrophysical signal in the calibrated data. Mismatches between the matched-filter template waveform and the calibrated gravitational-wave strain from the detectors reduces the recovered matched-filter signal-to-noise ratio. Therefore, calibration errors which are introduced through the response function impact the matched-filter signal-to-noise ratio used in the PyCBC search. In this section, we follow the method from Ref. [122] to derive the change in the expectation value of the optimal matched-filter signal-to-noise ratio $\langle \delta\rho \rangle$ from errors in the response function's amplitude and phase. This derivation has two steps: we express the change in the optimal matched-filter signal-to-noise ratio $\delta\rho$ in terms of the amplitude error $\delta A(f)$ and phase error $\delta\phi(f)$ of the response function, and then we find the expectation of value $\langle \delta\rho \rangle$. The optimal matched-filter signal-to-noise ratio ρ is defined as

$$\rho = \frac{\langle \tilde{s}(f) | \tilde{h}(f) \rangle}{\sqrt{\langle \tilde{h}(f) | \tilde{h}(f) \rangle}}, \quad (3.19)$$

where $\tilde{s}(f)$ is the gravitational-wave strain, $\tilde{h}(f)$ is the gravitational waveform template that matches the astrophysical waveform, and the inner product $\langle \tilde{s}(f) | \tilde{h}(f) \rangle$ is defined as

$$\langle \tilde{s}(f) | \tilde{h}(f) \rangle = 4\Re \int_0^\infty \frac{\tilde{s}(f)\tilde{h}^*(f)}{S(f)} df, \quad (3.20)$$

where $S(f)$ is the power spectral density defined as

$$\frac{1}{2}\delta(f - f')S(f) = \langle \tilde{n}_t(f)\tilde{n}_t^*(f') \rangle. \quad (3.21)$$

The change in the optimal matched-filter signal-to-noise ratio $\delta\rho$ is defined as

$$\delta\rho = \rho_m - \rho_t \quad (3.22)$$

$$= \frac{\langle \tilde{s}_m(f) | \tilde{h}(f) \rangle_m}{\sqrt{\langle \tilde{h}(f) | \tilde{h}(f) \rangle_m}} - \frac{\langle \tilde{s}_t(f) | \tilde{h}(f) \rangle_t}{\sqrt{\langle \tilde{h}(f) | \tilde{h}(f) \rangle_t}}, \quad (3.23)$$

where the inner products from Equation 3.22 are

$$\langle \tilde{s}_t(f) | \tilde{h}(f) \rangle_t = 4\Re \int_0^\infty \frac{\tilde{s}_t(f) \tilde{h}^*(f)}{S_t(f)} df, \quad (3.24)$$

and

$$\langle \tilde{s}_m(f) | \tilde{h}(f) \rangle_m = 4\Re \int_0^\infty \frac{\tilde{s}_m(f) \tilde{h}^*(f)}{S_m(f)} df. \quad (3.25)$$

The subscript t indicates that we use a gravitational-wave strain calibrated from a response function with no errors in the amplitude or phase, and the subscript m indicates that we use a gravitational-wave strain calibrated from a response function with errors in the amplitude and phase. Therefore, $\tilde{s}_t(f)$ and $S_t(f)$ represent an ideal, error-free, calibrated gravitational-wave strain and power spectral density respectively, while $\tilde{s}_m(f)$ and $S_m(f)$ represent a calibrated gravitational-wave strain and power spectral density from the detectors which will contain uncertainties and errors in the response function at some level.

The first step in this derivation is to express $\delta\rho$ in terms of the amplitude error and the phase error from the response function. In Equation 3.22, the errors from the response function are introduced into $\delta\rho$ through $\tilde{s}_m(f)$ and $S_m(f)$. Therefore, we need to find expressions for $\tilde{s}_m(f)$ and $S_m(f)$ in terms of the amplitude error $\delta A(f)$ and phase error $\delta\phi(f)$ of the response function. Neither $\tilde{s}_t(f)$ or $S_t(f)$ have any error from the response function so they do not depend on $\delta A(f)$ or $\delta\phi(f)$. We can use the relation between the response function with no errors $R_t(f)$ and the response function with errors in the amplitude and phase $R_m(f)$ from Equations 3.14, 3.15, and 3.17 to find expressions for $\tilde{s}_m(f)$ and $S_m(f)$ in terms of $A(f)$, $\phi(f)$, $\delta A(f)$, $\delta\phi(f)$, $\tilde{s}_t(f)$, and $S_t(f)$. The expressions for $\tilde{s}_m(f)$ and $S_m(f)$ can then be substituted into Equation 3.22 to find the dependence of $\delta\rho$ on $\delta A(f)$ and $\delta\phi(f)$. The expression for

$\tilde{s}_m(f)$ can be found using Equation 3.14 and 3.15 which gives

$$\tilde{s}_m(f) = R_m(f)\tilde{d}_{\text{err}}(f) \quad (3.26)$$

$$= A(f) \left[1 + \frac{\delta A(f)}{A(f)} \right] e^{i\phi(f)} e^{i\delta\phi(f)} \tilde{d}_{\text{err}}(f) \quad (3.27)$$

$$= \left[1 + \frac{\delta A(f)}{A(f)} \right] e^{i\delta\phi(f)} \tilde{s}_t(f) \quad (3.28)$$

$$= K(f)\tilde{s}_t(f). \quad (3.29)$$

Now, we need to find $S_m(f)$ in terms of $\delta A(f)$ and $\delta\phi(f)$ as well. The gravitational-wave strain $\tilde{s}_t(f)$ is composed of noise $\tilde{n}_t(f)$ and the astrophysical signals $\tilde{h}(f)$ such that

$$\tilde{s}_t(f) = \tilde{n}_t(f) + \tilde{h}(f) = K(f)\tilde{s}_m(f), \quad (3.30)$$

and the single-sided power spectral density $S_t(f)$ is defined as

$$\frac{1}{2}\delta(f - f')S_t(f) = \langle \tilde{n}_t(f)\tilde{n}_t^*(f') \rangle. \quad (3.31)$$

We can use Equations 3.30 and 3.31 to find the single-sided power spectral density calculated from the response function with errors in the amplitude and phase $S_m(f)$ which is defined as

$$\frac{1}{2}\delta(f - f')S_m(f) = \langle \tilde{n}_m(f)\tilde{n}_m^*(f') \rangle \quad (3.32)$$

$$= \langle K(f)\tilde{n}_t(f)K^*(f)\tilde{n}_t^*(f') \rangle \quad (3.33)$$

$$= |K(f)|^2 \langle \tilde{n}_t(f)\tilde{n}_t^*(f') \rangle, \quad (3.34)$$

where $\tilde{n}_m(f) = K(f)\tilde{n}_t(f)$. Therefore, we can rewrite $S_m(f)$ as

$$S_m(f) = |K(f)|^2 S_t(f) = \left[1 + \frac{\delta A(f)}{A(f)} \right]^2 S_t(f). \quad (3.35)$$

Now, we have expressions for $\tilde{s}_m(f)$ and $S_m(f)$ in terms of $\delta A(f)$ and $\delta\phi(f)$. We can substitute Equations 3.24, 3.25, 3.26, and 3.35 into Equation 3.22, and we find the

dependence of $\delta\rho$ on $\delta A(f)$ and $\delta\phi(f)$ is

$$\delta\rho = \frac{4\Re \int_0^\infty \frac{e^{i\delta\phi} \tilde{s}_t(f) \tilde{h}^*(f)}{\left[1 + \frac{\delta A(f)}{A(f)}\right] S_t(f)} df}{\sqrt{4\Re \int_0^\infty \frac{|\tilde{h}(f)|^2}{\left[1 + \frac{\delta A(f)}{A(f)}\right]^2 S_t(f)} df}} - \frac{4\Re \int_0^\infty \frac{\tilde{s}_t(f) \tilde{h}^*(f)}{\left[1 + \frac{\delta A(f)}{A(f)}\right]^2 S_t(f)} df}{\sqrt{4\Re \int_0^\infty \frac{|h|^2}{\left[1 + \frac{\delta A(f)}{A(f)}\right]^2 S_t(f)} df}} \quad (3.36)$$

$$= 2 \left[\frac{\Re \int_0^\infty \frac{e^{i\delta\phi} \tilde{s}_t(f) \tilde{h}^*(f)}{\left[1 + \frac{\delta A(f)}{A(f)}\right] S_t(f)} df}{\sqrt{\Re \int_0^\infty \frac{|\tilde{h}(f)|^2}{\left[1 + \frac{\delta A(f)}{A(f)}\right]^2 S_t(f)} df}} - \sqrt{\Re \int_0^\infty \frac{\tilde{s}_t(f) \tilde{h}^*(f)}{\left[1 + \frac{\delta A(f)}{A(f)}\right] S_t(f)} df} \right]. \quad (3.37)$$

The dependence of the expectation value of the change in the optimal matched-filter signal-to-noise ratio $\langle\delta\rho\rangle$ on $\delta A(f)$ and $\delta\phi(f)$ can easily be found from Equation 3.36 since it removes the dependence on $\tilde{s}_t(f)$. Here, we will show that the expectation value of the gravitational-wave strain $\langle\tilde{s}_t(f)\rangle = \tilde{h}(f)$. In stationary, Gaussian noise $\langle\tilde{s}_t(f)\rangle$ is

$$\langle\tilde{s}_t(f)\rangle = \langle\tilde{n}_t(f)\rangle + \langle\tilde{h}(f)\rangle \quad (3.38)$$

$$= 0 + \tilde{h}(f), \quad (3.39)$$

where $\langle\tilde{h}(f)\rangle = \tilde{h}(f)$ since the astrophysical signal is not a random process and the expectation value of stationary, Gaussian noise in the time-domain $n_t(t)$ has the expectation value $\langle n_t(t)\rangle = \mu$ where μ is the mean of $n_t(t)$; however, for simplicity, we set $\mu = 0$ since we are only interested in determining the leading order dependence of $\langle\delta\rho\rangle$ on $\delta A(f)$ and $\delta\phi(f)$. Therefore, $\langle\tilde{n}_t(f)\rangle = 0$. Now, we can substitute Equation 3.38 into $\delta\rho$ from Equation 3.36 and find the expectation value which is

$$\langle\delta\rho\rangle = \langle\rho_m\rangle - \langle\rho_t\rangle \quad (3.40)$$

$$= 2 \left[\frac{\int_0^\infty \frac{\cos(\delta\phi(t)) |\tilde{h}(t)|^2}{\left[1 + \frac{\delta A(f)}{A(f)}\right] S_t} df}{\sqrt{\int_0^\infty \frac{|\tilde{h}(t)|^2}{\left[1 + \frac{\delta A(f)}{A(f)}\right]^2 S_t} df}} - \sqrt{\int_0^\infty \frac{|\tilde{h}(t)|^2}{S_t} df} \right], \quad (3.41)$$

where we use the identity

$$\Re e^{\pm i\theta} = \Re [\cos(\theta) + i \sin(\theta)] = \cos(\theta). \quad (3.42)$$

In order to determine the leading order dependence of $\langle\delta\rho\rangle$ on δA and $\delta\phi$ we will simplify each term in Equation 3.40 separately, and then evaluate $\langle\delta\rho\rangle$. We denote

the three terms in $\langle \delta\rho \rangle$ from Equation 3.40 as

$$X_1 = \int_0^\infty \frac{\cos(\delta\phi)|h_t|^2}{\left[1 + \frac{\delta A(f)}{A(f)}\right] S_t} df, \quad (3.43)$$

and

$$X_2 = \sqrt{\int_0^\infty \frac{|h_t|^2}{\left[1 + \frac{\delta A(f)}{A(f)}\right]^2 S_t} df}, \quad (3.44)$$

and

$$X_3 = \sqrt{\int_0^\infty \frac{|h_t|^2}{S_t} df}, \quad (3.45)$$

such that

$$\langle \delta\rho \rangle = 2 \left[\frac{X_1}{X_2} - X_3 \right]. \quad (3.46)$$

First, we simplify X_1 . We find that

$$X_1 = \int_0^\infty \frac{\cos(\delta\phi)|h_t|^2}{\left[1 + \frac{\delta A(f)}{A(f)}\right] S_t} df \quad (3.47)$$

$$= \int_0^\infty \frac{|h_t|^2}{S_t} \left[1 - \frac{1}{2!}(\delta\phi)^2 + \mathcal{O}((\delta\phi)^4) \right] \left[1 - \frac{\delta A}{A} + \left(\frac{\delta A}{A} \right)^2 + \mathcal{O}((\delta A(f))^3) \right] df \quad (3.48)$$

$$\approx \int_0^\infty \frac{|h_t|^2}{S_t} \left[1 - \frac{1}{2}(\delta\phi)^2 - \frac{\delta A}{A} + \left(\frac{\delta A}{A} \right)^2 \right] df, \quad (3.49)$$

where we use the Taylor expansions

$$\cos(x) = 1 - \frac{1}{2!}x^2 + \mathcal{O}(x^4), \quad (3.50)$$

and

$$(1+x)^{-1} = 1 - x + x^2 + \mathcal{O}(x^3). \quad (3.51)$$

Since X_1 was the only term in $\langle \delta\rho \rangle$ with dependence on $\delta\phi$, we see from Equation 3.47 that $\langle \delta\rho \rangle$ has a quadratic dependence on changes in the phase of the response function. We will have to evaluate X_1 , X_2 , and X_3 to determine the dependence of $\langle \delta\rho \rangle$ on $\delta A(f)$

since all three terms depend on $\delta A(f)$. Now, we simplify X_2 which is

$$X_2^2 = \int_0^\infty \frac{|h_t|^2}{\left[1 + \frac{\delta A(f)}{A(f)}\right]^2 S_t} df \quad (3.52)$$

$$= \int_0^\infty \frac{|h_t|^2}{S_t} \left[1 - 2\frac{\delta A}{A} + 3\left(\frac{\delta A}{A}\right)^2 + \mathcal{O}((\delta A(f))^3) \right] df \quad (3.53)$$

$$\approx \int_0^\infty \frac{|h_t|^2}{S_t} \left[1 - 2\frac{\delta A}{A} + 3\left(\frac{\delta A}{A}\right)^2 \right] df, \quad (3.54)$$

where we use the Taylor expansion

$$(1 + x)^{-2} = 1 - 2x + 3x^2 + \mathcal{O}(x^3). \quad (3.55)$$

We do not need to simplify X_3 since it is a term within X_1 from Equation 3.47. Therefore, for brevity later, we define the three terms within X_1 , X_2 , and X_3 as

$$x_0 = \int_0^\infty \frac{|h_t^2|}{S_t} df, \quad (3.56)$$

and

$$x_1 = \int_0^\infty \frac{|h_t^2| \frac{\delta A}{A}}{S_t} df, \quad (3.57)$$

and

$$x_2 = \int_0^\infty \frac{|h_t|^2 \left(\frac{\delta A}{A}\right)^2}{S_t} df. \quad (3.58)$$

We write X_1 as

$$X_1 \approx x_0 + x_1, \quad (3.59)$$

and we write X_2 as

$$\begin{aligned} X_2 &\approx (x_0 - 2x_1 + 3x_2)^{-1/2} = x_0^{1/2} \left[1 - 2\frac{x_1}{x_0} + 3\frac{x_2}{x_0} \right]^{-1/2} \quad (3.60) \\ &\approx x_0^{-1/2} \left[1 - \frac{1}{2} \left(-2\frac{x_1}{x_0} + 3\frac{x_2}{x_0} \right) + \mathcal{O} \left(\left(-2\frac{x_1}{x_0} + 3\frac{x_2}{x_0} \right)^3 \right) \right] \quad (3.61) \end{aligned}$$

$$\approx x_0^{1/2} \left[1 + \frac{x_1}{x_0} \right], \quad (3.62)$$

where we used the Taylor expansion

$$(1 + x)^{-1/2} = 1 - \frac{1}{2}x + \frac{3}{8}x^2 + \mathcal{O}(x^3). \quad (3.63)$$

Finally, we see that X_3 can be written as

$$X_3 = x_0^{1/2}. \quad (3.64)$$

Now, we can find the dependence of $\langle \delta\rho \rangle$ on δA which is given by

$$\langle \delta\rho \rangle \approx 2 \left[x_0^{-1/2} [x_0 - x_1] \left[1 + \frac{x_1}{x_0} \right] - x_0^{1/2} \right] = 2 \left[x_0^{1/2} \left[1 - \left(\frac{x_1}{x_0} \right)^2 \right] - x_0^{1/2} \right] \quad (3.65)$$

$$= -2 \left[\frac{x_1}{x_0} \right]^2 \quad (3.66)$$

$$= \mathcal{O} \left(\left(\frac{\delta A(f)}{A(f)} \right)^2 \right). \quad (3.67)$$

Therefore, $\langle \delta\rho \rangle$ has quadratic dependence on both changes in the amplitude and phase of the response function.

Now that we know the dependence of $\langle \delta\rho \rangle$ on the amplitude error and phase error from the response function we can set requirements on the calibration errors that limit loss in the detection rate. Since the matched-filter signal-to-noise ratio is inversely proportional to the distance and the detection rate is proportional to volume of the Universe which is observed by the detector, then we can find a relation between the loss in the matched-filter signal-to-noise ratio and the detection rate. For example, the template banks used in the PyCBC search are placed such that there is not more than a 3.5% loss in the matched-filter signal-to-noise ratio [79]. Therefore, a 3.5% loss in the matched-filter signal-to-noise ratio corresponds to a fractional loss in the detection rate equal to $1 - (1 - 0.035)^3 = 0.1$ or 10%. We can use this to set required bounds on the response function such that the loss in the detection rate is not greater than 10%. This limit on the loss in the detection rate requires in the most extreme cases where all the error only comes from the amplitude or phase which corresponds to

$$\left(\frac{\delta A(f)}{A(f)} \right)^2 \leq 0.035, \quad (3.68)$$

and

$$(\delta\phi(f))^2 \leq 0.035. \quad (3.69)$$

Therefore, the requirement on the amplitude error and phase error to limit the loss in the detection rate to 10% is $\delta A(f)/A(f) \leq 19\%$ and $\delta\phi(f) \leq 0.19$ rad = 11 degrees.

3.5 Impact of calibration errors on the matched-filter signal-to-noise ratio of GW150914

In Figures 23, 24, and 25 we show the change in the matched-filter signal-to-noise ratio ρ for GW150914 when each time-dependent calibration parameter is varied. We adjusted only one time-dependent calibration parameter to quantify the decrease in ρ for each parameter separately. We present the results from the Hanford detector; however, we observe similar results in both the Hanford and Livingston detectors. We omit results for $f_s(t)$ and $Q(t)$ since these parameters were not tracked during Advanced LIGO's first observing run. The waveform used in the matched-filter calculation was generated with the reduced-order SEOBNRv2 waveform model [42, 43] using the best-fit parameters that the search reported for GW150914 in Ref. [4]; the component masses m_1 and m_2 are $47.93 M_\odot$ and $36.60 M_\odot$, and the component dimensionless spins [47] χ_1^z and χ_2^z aligned with the angular momentum of the binary are 0.96 and -0.90. The loss in the matched-filter signal-to-noise ratio depends quadratically on the calibration parameters.

We include results from two calibrations of H1 data between 30 Hz and 2048 Hz. The initial calibration called C01 was used in Ref. [4] to show the impact of calibration errors on the detection of GW150914, and in Figures 23, 24, and 25 we present results using the final calibrated gravitational-wave strain data called C02. The final calibrated data includes time-dependent corrections for the sensing and actuation functions.

Figures 23, 24, and 25 include histograms of the measured calibration parameters for 2048 s on September 14, 2015, which encompasses the time of GW150914. These parameters are found to typically deviate from their nominal values by less than $\sim 5\%$. Table 3.5 shows the minimum, maximum, and median of the measured calibration parameters shown in these figures. Overall, the errors from typical measured values of the time-dependent calibration parameters lead to a 1% loss in the matched-filter signal-to-noise ratio. Therefore, even if these temporal variations in the sensing and actuation functions were not modeled, then the errors from the calibration would not have a significant impact on the matched-filter signal-to-noise ratio of GW150914.

Parameter (Units)	Minimum	Maximum	Median (90% Percentile)
$\Re\kappa_{\text{tst}}$	1.029	1.043	$1.037^{+0.004}_{-0.005}$
$\Im\kappa_{\text{tst}}$	-0.021	-0.008	$-0.013^{+0.004}_{-0.006}$
$\Re\kappa_{\text{pu}}$	1.029	1.043	$1.037^{+0.004}_{-0.005}$
$\Im\kappa_{\text{pu}}$	-0.028	-0.010	$-0.020^{+0.008}_{-0.005}$
κ_C	0.990	1.006	$0.997^{+0.005}_{-0.005}$
Δf_c (Hz)	-9.807	7.021	$-1.393^{+7.097}_{-7.211}$

Table 1 : Table of measured time-dependent calibration parameter values for analysis time on September 15, 2015. The 90% percentile is the interval that contains 90% of the total samples. The change in the cavity pole frequency Δf_c is offset from the measured value of 341 Hz.

3.6 Impact of calibration errors on the matched-filter signal-to-noise ratio of binary neutron star and black hole mergers with a total mass up to $100 M_\odot$

To assess the impact of time-dependent calibration errors for a range of masses and spins we generate a population of simulated signals and calculate the match [5] as we vary each time-dependent calibration parameter separately. The match is the maximum overlap of two waveforms marginalized over time and phase [5] which represents the fraction of the optimal matched-filter signal-to-noise ratio [115] of the frequency-domain signal $\tilde{h}_t(f)$ captured by the template waveform $\tilde{h}_m(f)$. Here, the loss is due to calibration errors and we defined the match as

$$\text{Match} = \max_{t, \phi} \langle \tilde{h}_t(f) | \tilde{h}_m(f) \rangle, \quad (3.70)$$

where the inner product is defined as

$$\langle \tilde{h}_t(f) | \tilde{h}_m(f) \rangle = 4\Re \int_0^\infty \frac{\tilde{h}_t(f) \tilde{h}_m^*(f)}{S_n(f)} df, \quad (3.71)$$

where $S_n(f)$ is the one-sided average power spectral density of the detector.

We generate 200 simulated binary neutron star mergers with both m_1 and m_2 between $1 M_\odot$ and $2 M_\odot$, 200 simulated neutron star-black hole mergers with m_1 between $2 M_\odot$ and $99 M_\odot$ and m_2 between $1 M_\odot$ and $2 M_\odot$, and 1100 simulated binary black hole mergers with m_1 and m_2 between $2 M_\odot$ and $99 M_\odot$. The limit on the dimensionless spins of the component masses match the search space in Ref. [75]

which is informed by radio and X-ray observations of compact-object binaries. We limit the dimensionless spin of masses $< 2 M_{\odot}$ to 0.05 which is higher than the shortest observed pulsar period observed in a double neutron star system [123]. For masses $> 2 M_{\odot}$ the spin magnitude is limited to 0.9895 which is the upper limit of our ability to generate valid template waveforms at high spins with the SEBONRv2 waveform model [42].

Figures 26, 27, 28, and 29 shows the difference from each time-dependent calibration parameter's nominal value that corresponds to a 1% loss in the matched-filter SNR. The analysis that produces Figures 26, 27, 28, and 29 uses the calibration model from the calibration epoch beginning January 3, 2017, in Advanced LIGO's second observing run and includes $f_s(t)$ and $Q(t)$. Figures 26, 27, 28, and 29 shows that all time-varying calibration parameters lose $>1\%$ matched-filter SNR beyond the typical observed values of the time-dependent calibration parameters during the calibration epoch. The search uses template banks that limit the loss in the matched-filter signal-to-noise ratio due to the discrete nature of the bank to $<3\%$ [80, 81, 82, 83]. For typical measured values of the time-dependent calibration parameters, we see the loss in matched-filter signal-to-noise ratio from uncertainty in the calibration is less than the loss in matched-filter signal-to-noise ratio from the discretization of the template bank.

3.7 Impact of calibration errors on the detection statistic of GW150914

In Advanced LIGO's first observing run the PyCBC search used a detection statistic [46] $\hat{\rho}$ that weights the matched-filter signal-to-noise ratio ρ by a signal consistency test χ^2 [106]. The detection statistic $\hat{\rho}$ is defined as

$$\hat{\rho} = \rho \left[\frac{1}{2} \left(1 + \left(\frac{\chi^2}{n_{\text{dof}}} \right)^3 \right) \right]^{-1/6}, \quad (3.72)$$

where the number of degrees of freedom is determined by the number of equal-power frequency bins p by $n_{\text{dof}} = 2p - 2$ [106]. From Equation 3.72 we see that the decrease in matched-filter signal-to-noise ratio from calibration errors examined in Sec. 3.4 will affect the detection statistic.

Parameter (Units)	Minimum	Maximum	Median (90% Percentile)
$\Re\kappa_{\text{tst}}$	1.027	1.049	$1.037^{+0.004}_{-0.005}$
$\Im\kappa_{\text{tst}}$	-0.024	-0.005	$-0.013^{+0.004}_{-0.005}$
$\Re\kappa_{\text{pu}}$	1.027	1.049	$1.037^{+0.004}_{-0.005}$
$\Im\kappa_{\text{pu}}$	-0.032	-0.005	$-0.018^{+0.006}_{-0.007}$
κ_C	0.986	1.032	$1.002^{+0.021}_{-0.009}$
Δf_c (Hz)	-5.785	9.011	$1.889^{+3.470}_{-4.196}$

Table 2 : Table of measured time-dependent calibration parameter values for analysis time on September 14 and September 15, 2015. The 90% percentile is the interval that contains 90% of the total samples. The change in the cavity pole frequency Δf_c is offset from the measured value of 341 Hz.

The method described in Section 3.3 is used to assess the impact of temporal variations in the calibration. We generate simulated signals, add them to the gravitational-wave strain from the detector, and then adjusting the gravitational-wave strain with artificial values of the time-dependent calibration parameters. The simulated signals use the same gravitational waveform which is generated with the parameters of the best-fit template waveform for GW150914. We add the gravitational waveform into 16 different noise realizations from Advanced LIGO’s first observing run on September 14, and September 15, 2015. These two days were chosen so we could sample noise realizations around the time GW150914. In Figures 30, 31, and 32, we show the results for variations in $\kappa_C(t)$, $f_c(t)$, $\Re\kappa_{\text{tst}}(t)$, $\Im\kappa_{\text{tst}}(t)$, $\Re\kappa_{\text{pu}}(t)$, and $\Im\kappa_{\text{pu}}(t)$. Large amplitude noise due to fluctuations in the boundaries of the χ^2 bins used in the χ^2 calculation dominates over any trend due to the artificially varied time-dependent calibration parameters. We fit a quadratic curve to the ensemble of 16 simulated signals. For extreme variations in these parameters the loss in the expectation value of $\hat{\rho}$ can be as much as 20%; however, as shown by the histograms, these parameters rarely deviate by more than 5% from their nominal values. Table 3.7 shows the minimum, maximum, and median values for the time-dependent calibration parameters during these times. For this range of values, the loss in the expectation value of $\hat{\rho}$ is less than 3%. Since in practice the detection statistic is used to calculate sensitive volume of the PyCBC search, then the loss in the detection rate due to calibration errors is less than 10%.

Parameter (Units)	Minimum	Maximum	Median (90% Percentile)
$\Re\kappa_{\text{tst}}$	1.002	1.010	$1.006^{+0.002}_{-0.002}$
$\Im\kappa_{\text{tst}}$	-0.008	-0.004	$-0.006^{+0.001}_{-0.001}$
$\Re\kappa_{\text{pu}}$	1.002	1.010	$1.006^{+0.002}_{-0.002}$
$\Im\kappa_{\text{pu}}$	-0.001	0.012	$0.008^{+0.002}_{-0.008}$
κ_C	1.019	1.056	$1.035^{+0.013}_{-0.010}$
Δf_c (Hz)	-18.206	-2.583	$-12.981^{+7.317}_{-3.331}$
Δf_s (Hz)	-0.737	2.676	$1.337^{+0.750}_{-1.204}$
ΔQ^{-1}	-0.490	0.356	$-0.083^{+0.184}_{-0.203}$

Table 3 : Table of measured time-dependent calibration parameter values for analysis time on January 19 and January 20, 2016. The 90% percentile is the interval that contains 90% of the total samples. The change in the cavity pole frequency Δf_c , optical spring frequency Δf_s , and inverse dimensionless quality factor ΔQ^{-1} are offset from their measured values of 360 Hz, 6.9 Hz and 0.05 respectively.

3.8 Impact of calibration errors on the detection statistic of a simulated 30-30 M_\odot binary black hole merger

The results from Section 3.8 do not include corrections for time-dependent changes in the signal recycling cavity. In Figures 33, 34, 35, and 36 we show the results from a simulated non-spinning, 30-30 M_\odot in 16 noise realizations from Advanced LIGO's second observing run on January 19 and January 20, 2017, which includes results for $f_s(t)$ and $Q(t)$. For typical values of $f_s(t)$ and $Q(t)$ the expectation value of loss in $\hat{\rho}$ is less than 3% as well. The minimum, maximum, and median of the measured calibration parameters for these times are listed in Table 3.8.

3.9 Conclusions

We present the method used for simulating calibration errors in Advanced LIGO data to assess the impact of time-dependent calibration errors for GW150914. The model considers the impact of calibration errors from temporal drift in the Advanced LIGO sensing and actuation functions.

We use this method to show the impact of time-dependent calibration errors on GW150914 using the final Advanced LIGO calibration. We show the loss in the

matched filter signal-to-noise ratio is quadratic when the time-dependent calibration parameters are varied, and they account for a 1% loss in signal-to-noise ratio for typical measured values of the parameters. Over the same range of values, the expectation value of the detection statistic was found to lose up to 3% from the quadratic fit. Extreme temporal variations may cause up to a 20% loss in the detection statistic; however, the time-dependent calibration parameters are tracked and do not deviate from the nominal values this much. Therefore, under normal operating conditions, calibration errors from the time-dependent variations would not have strongly impact the detection of signals like GW150914.

Using a population of simulated signals with total mass up to $100 M_{\odot}$, we find that the loss in matched-filter signal-to-noise ratio due to time-dependent calibration errors is $<1\%$.

For Advanced LIGO's second observing run we extended our models to include corrections for temporal drift in the signal recycling cavity. We examined the loss in the matched-filter signal-to-noise ratio for a population of simulated binary neutron star, neutron star-black hole, and binary black hole mergers. We found that the loss in signal-to-noise ratio from calibration errors is less than the loss from the discretization of the template bank. Finally, we show the loss in detection statistic from temporal drift in the signal recycling cavity spring frequency and dimensionless quality factor for a non-spinning 30-30 M_{\odot} binary black hole merger. We found for typical measured values of the signal recycling cavity parameters the loss was up to 3% which is similar to the other time-dependent calibration parameters.

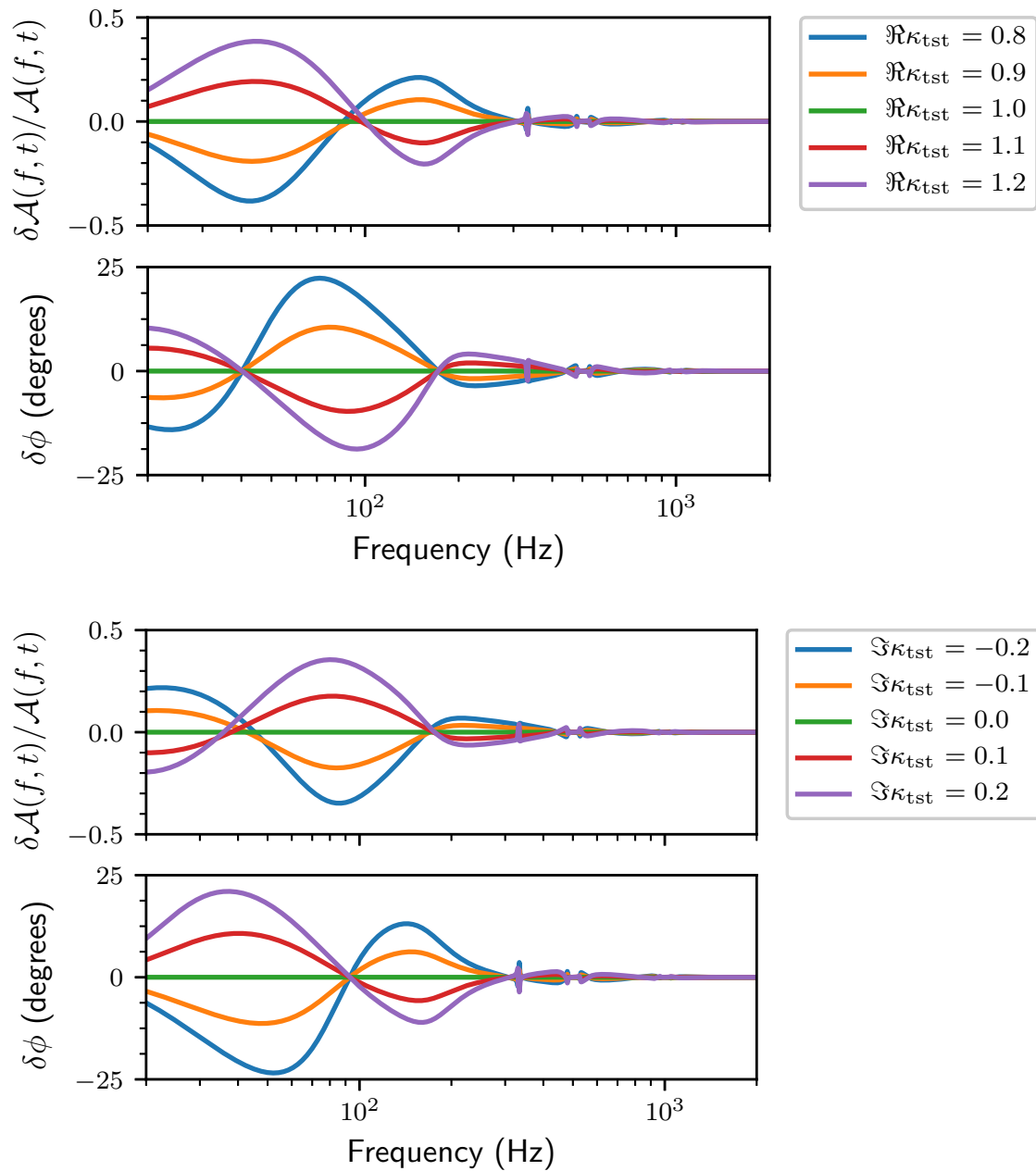


Figure 19 : The fractional amplitude error $\delta\mathcal{A}(f,t)/\mathcal{A}(f,t)$ and phase error $\delta\phi(f,t)$ as $\Re\kappa_{tst}$ and $\Im\kappa_{tst}$ varied. Here, we use the model from the calibration epoch beginning on January 3, 2017, during Advanced LIGO's second observing run.

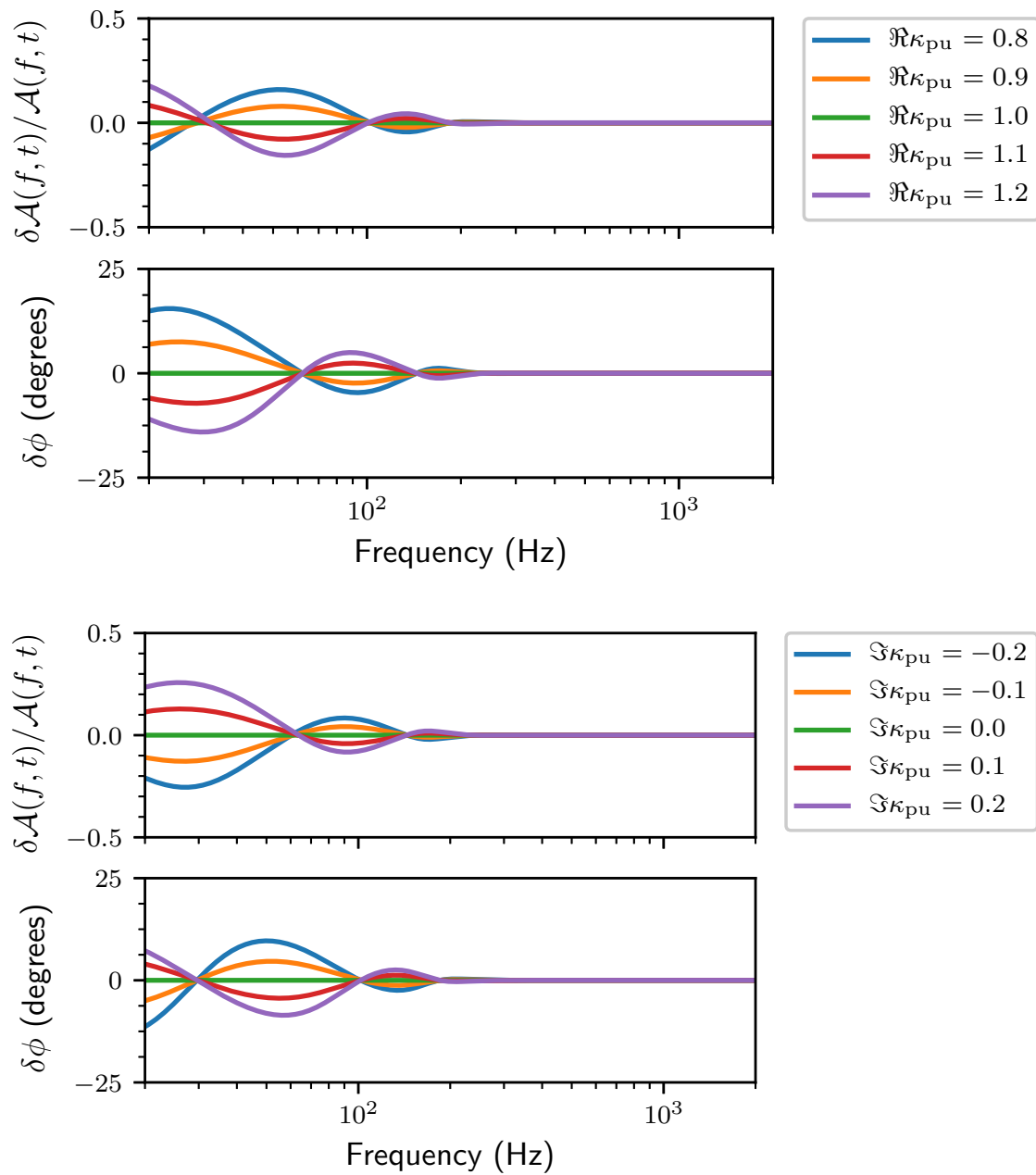


Figure 20 : The fractional amplitude error $\delta\mathcal{A}(f,t)/\mathcal{A}(f,t)$ and phase error $\delta\phi(f,t)$ as $\Re\kappa_{\text{pu}}$ and $\Im\kappa_{\text{pu}}$ are varied. Here, we use the model from the calibration epoch beginning on January 3, 2017, during Advanced LIGO's second observing run.

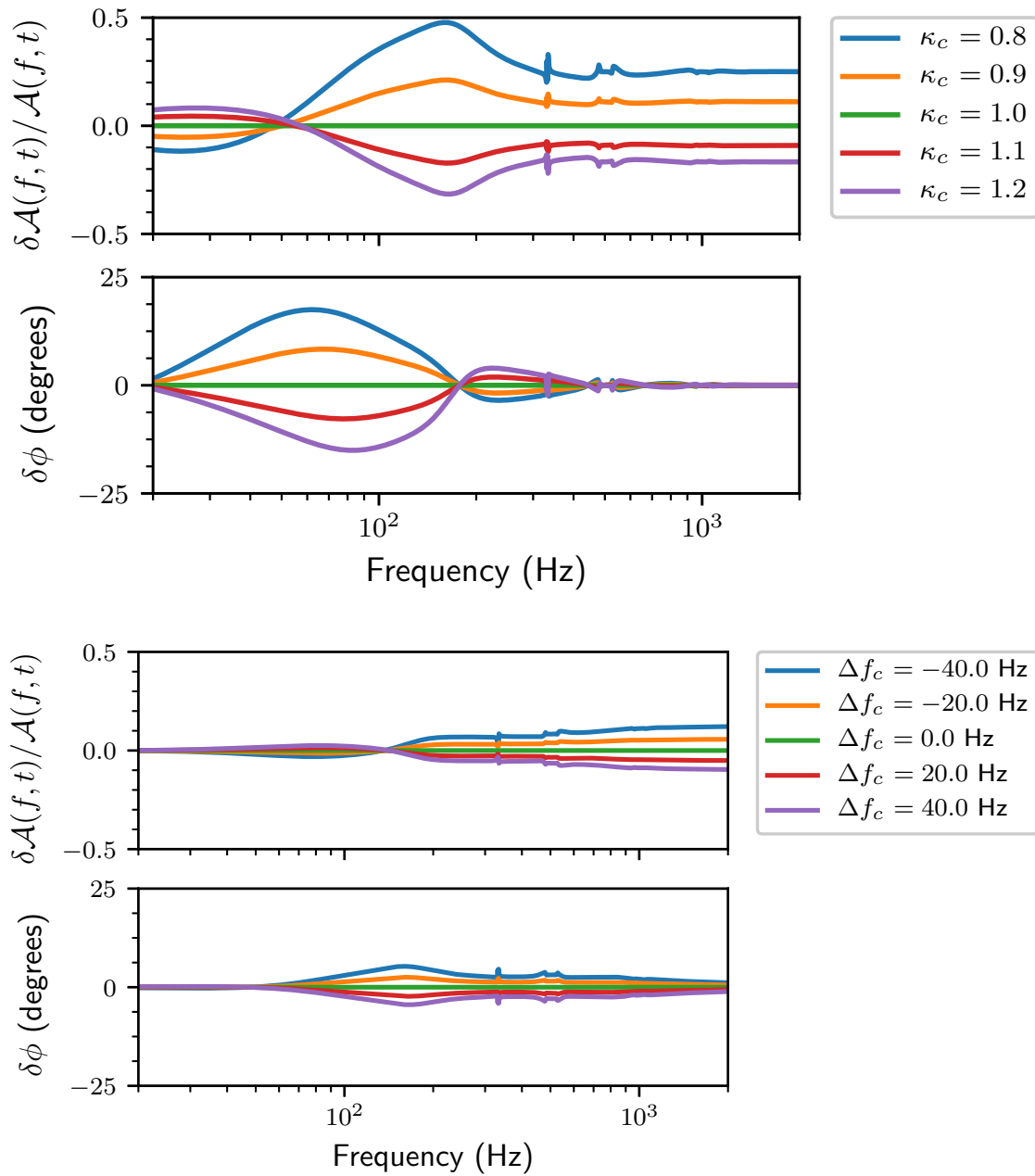


Figure 21 : The fractional amplitude error $\delta\mathcal{A}(f, t)/\mathcal{A}(f, t)$ and phase error $\delta\phi(f, t)$ as κ_C and Δf_c are varied. Here, we use the model from the calibration epoch beginning on January 3, 2017, during Advanced LIGO's second observing run.

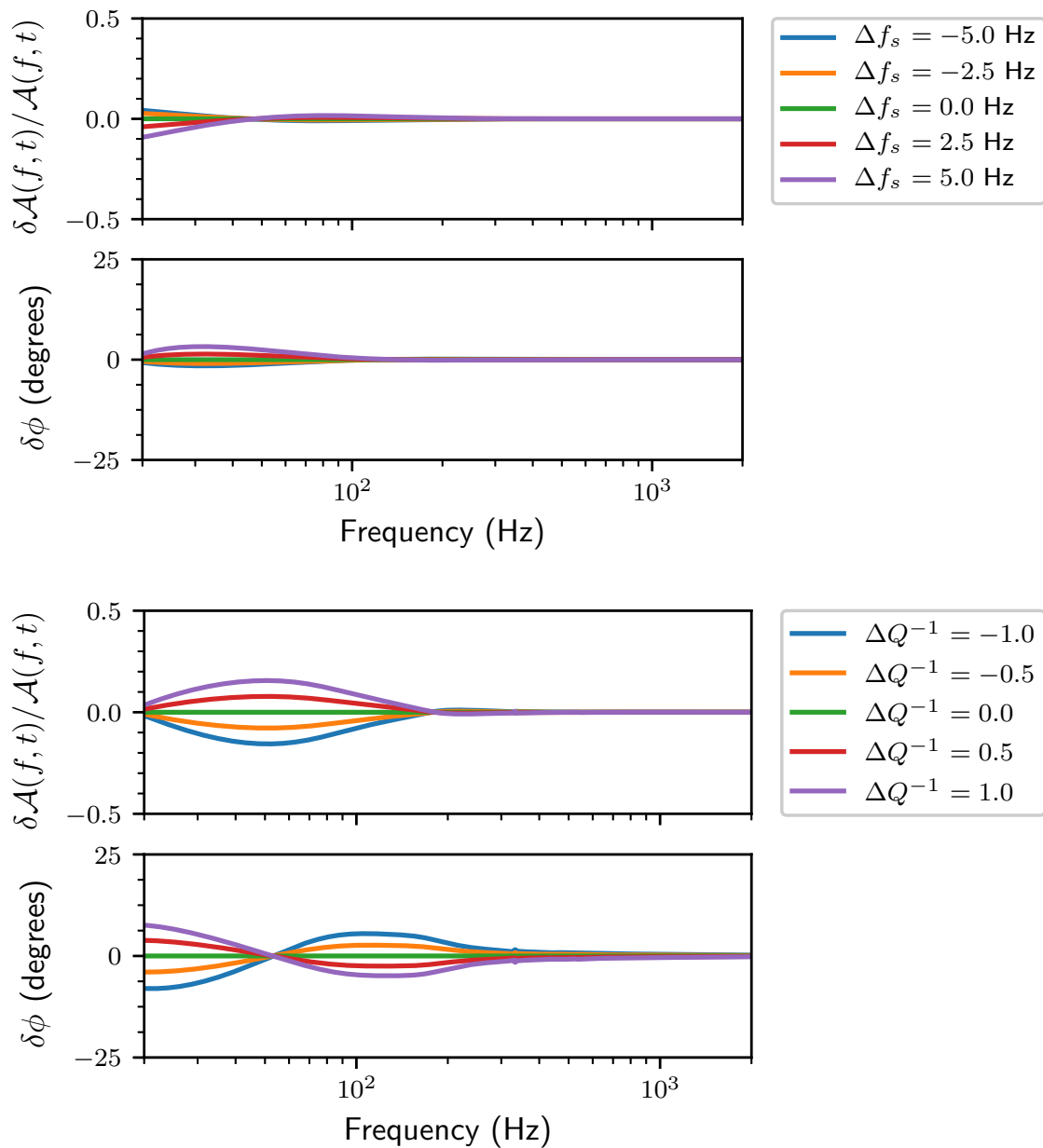


Figure 22 : The fractional amplitude error $\delta\mathcal{A}(f,t)/\mathcal{A}(f,t)$ and phase error $\delta\phi(f,t)$ as Δf_s and ΔQ^{-1} are varied. Here, we use the model from the calibration epoch beginning on January 3, 2017, during Advanced LIGO's second observing run.

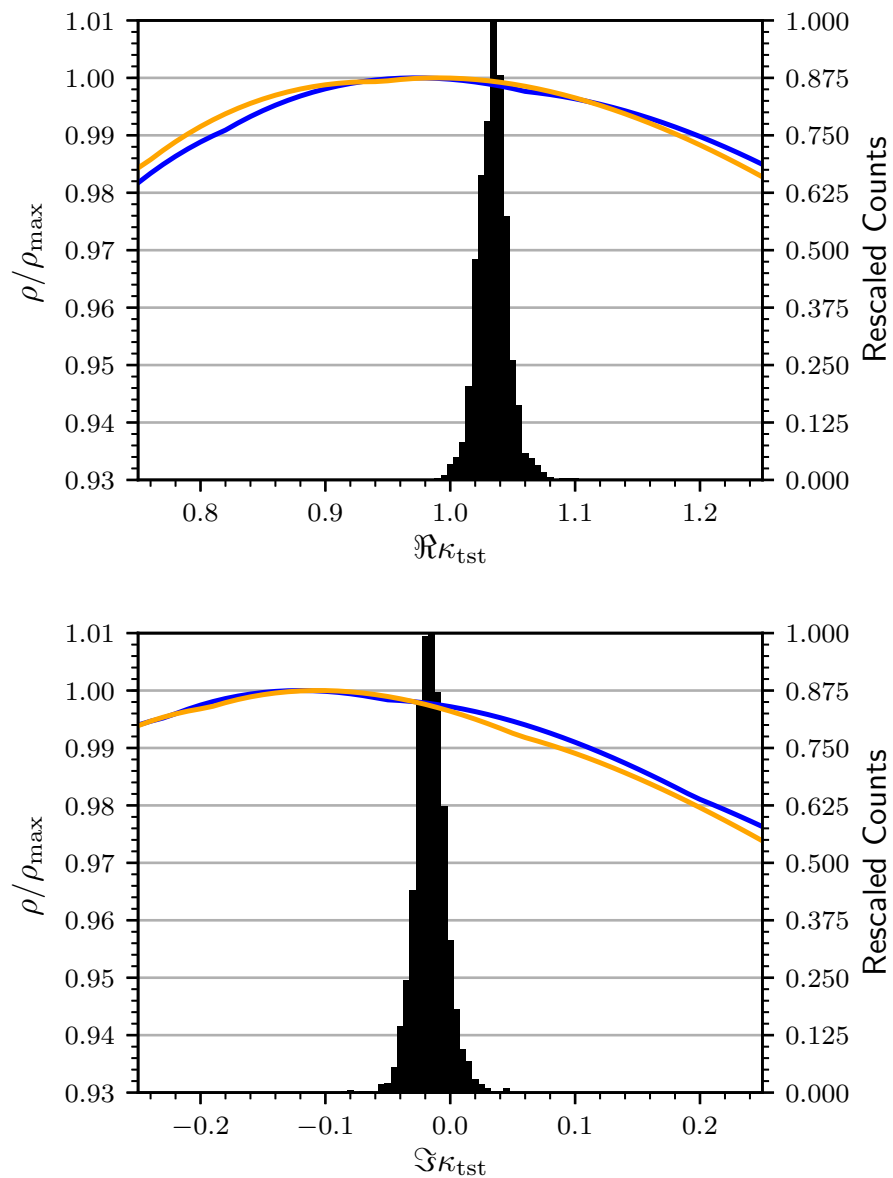


Figure 23 : Variation in the matched-filter signal-to-noise ratio ρ when $\Re\kappa_{\text{tst}}$ and $\Im\kappa_{\text{tst}}$ are adjusted for GW150914. The best-fit waveform parameters from the search results reported in Ref. [4] were used to generate the template waveform to calculate ρ . The blue curve was computed using the initial calibration and the orange curve was computed using the final calibration from Advanced LIGO's first observing run. The black histogram represents the measured values of the time-dependent calibration parameters for times used in the analysis on September 14, 2015.

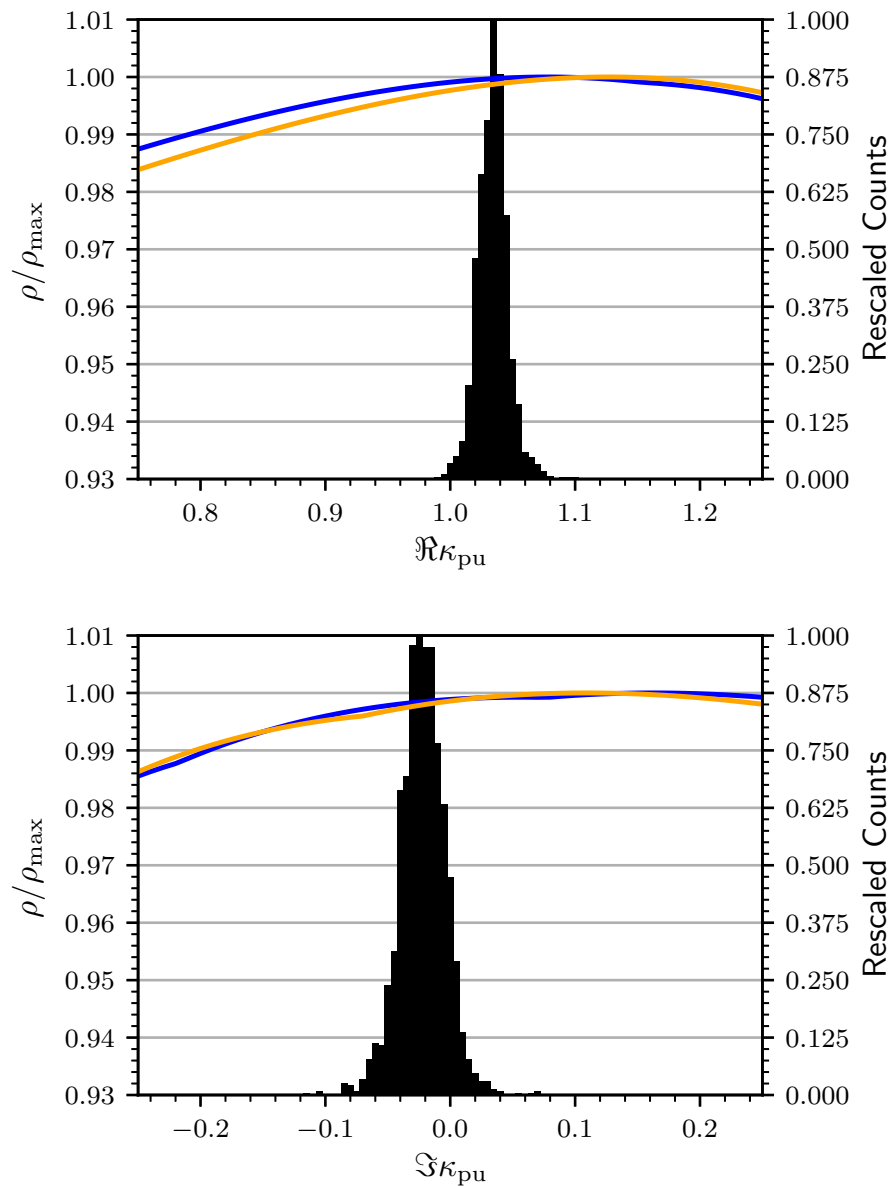


Figure 24 : Variation in the matched-filter signal-to-noise ratio ρ when $\Re\kappa_{\text{pu}}$ and $\Im\kappa_{\text{pu}}$ are adjusted for GW150914. The best-fit waveform parameters from the search results reported in Ref. [4] were used to generate the template waveform to calculate ρ . The blue curve was computed using the initial calibration and the orange curve was computed using the final calibration from Advanced LIGO's first observing run. The black histogram represents the measured values of the time-dependent calibration parameters for times used in the analysis on September 14, 2015.

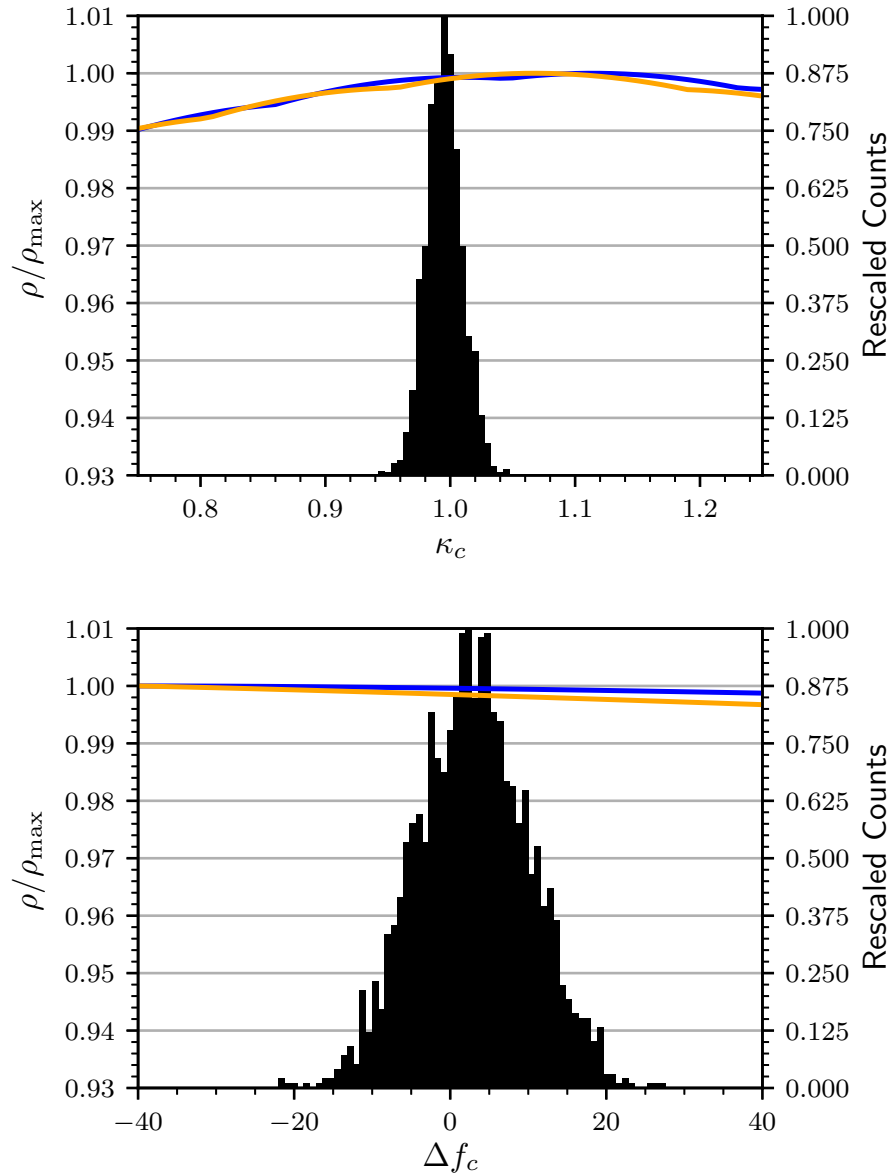


Figure 25 : Variation in the matched-filter signal-to-noise ratio ρ when κ_C and Δf_c are adjusted for GW150914. The best-fit waveform parameters from the search results reported in Ref. [4] were used to generate the template waveform to calculate ρ . The blue curve was computed using the initial calibration and the orange curve was computed using the final calibration from Advanced LIGO's first observing run. The black histogram represents the measured values of the time-dependent calibration parameters for times used in the analysis on September 14, 2015. The change in the cavity pole frequency Δf_c is offset from the measured value of 341 Hz.

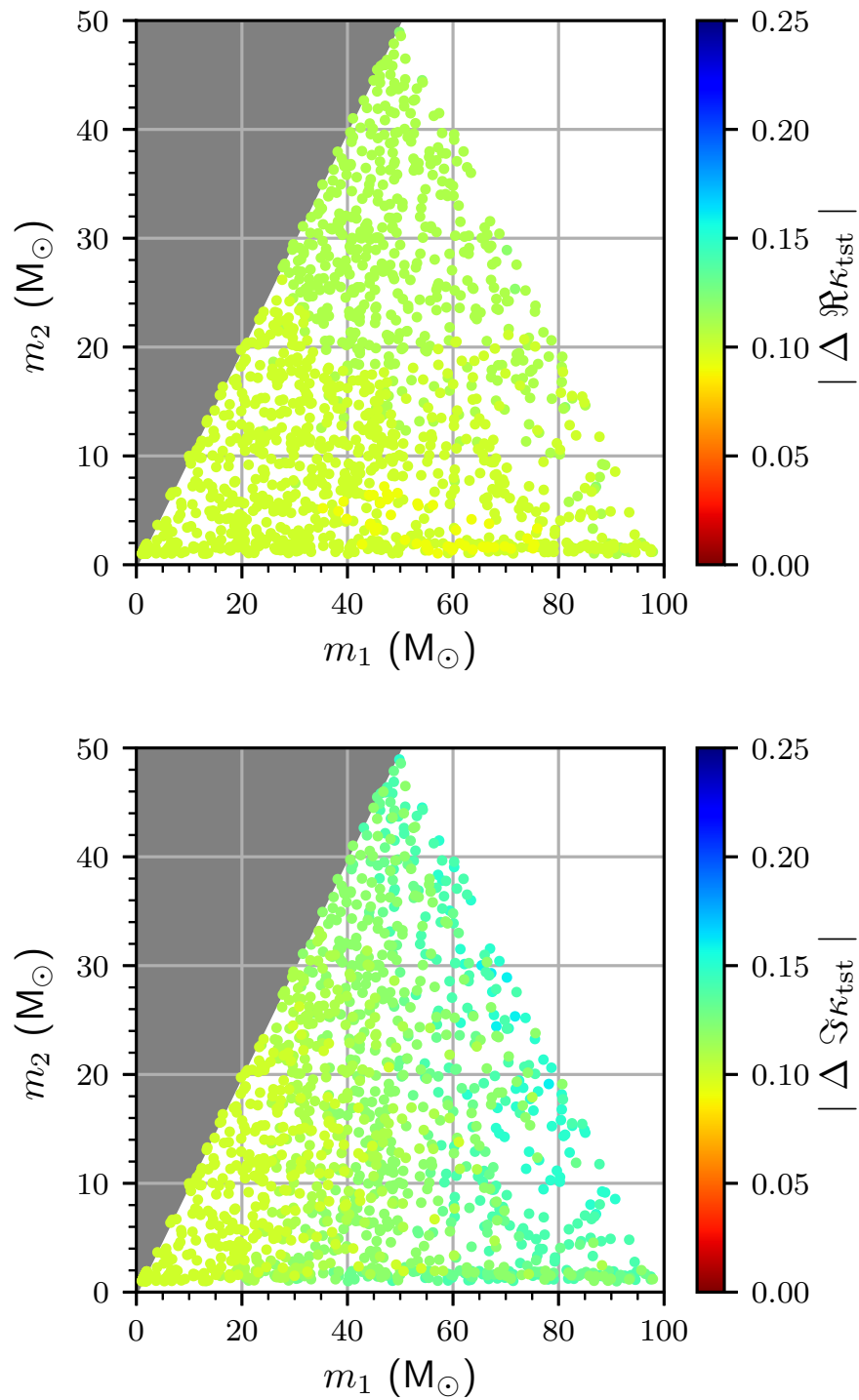


Figure 26 : The difference from the nominal value that corresponds to a match [5] of 0.99 which is a 1% loss in the matched-filter signal-to-noise ratio. Smaller differences corresponds to a steeper quadratic dependence.

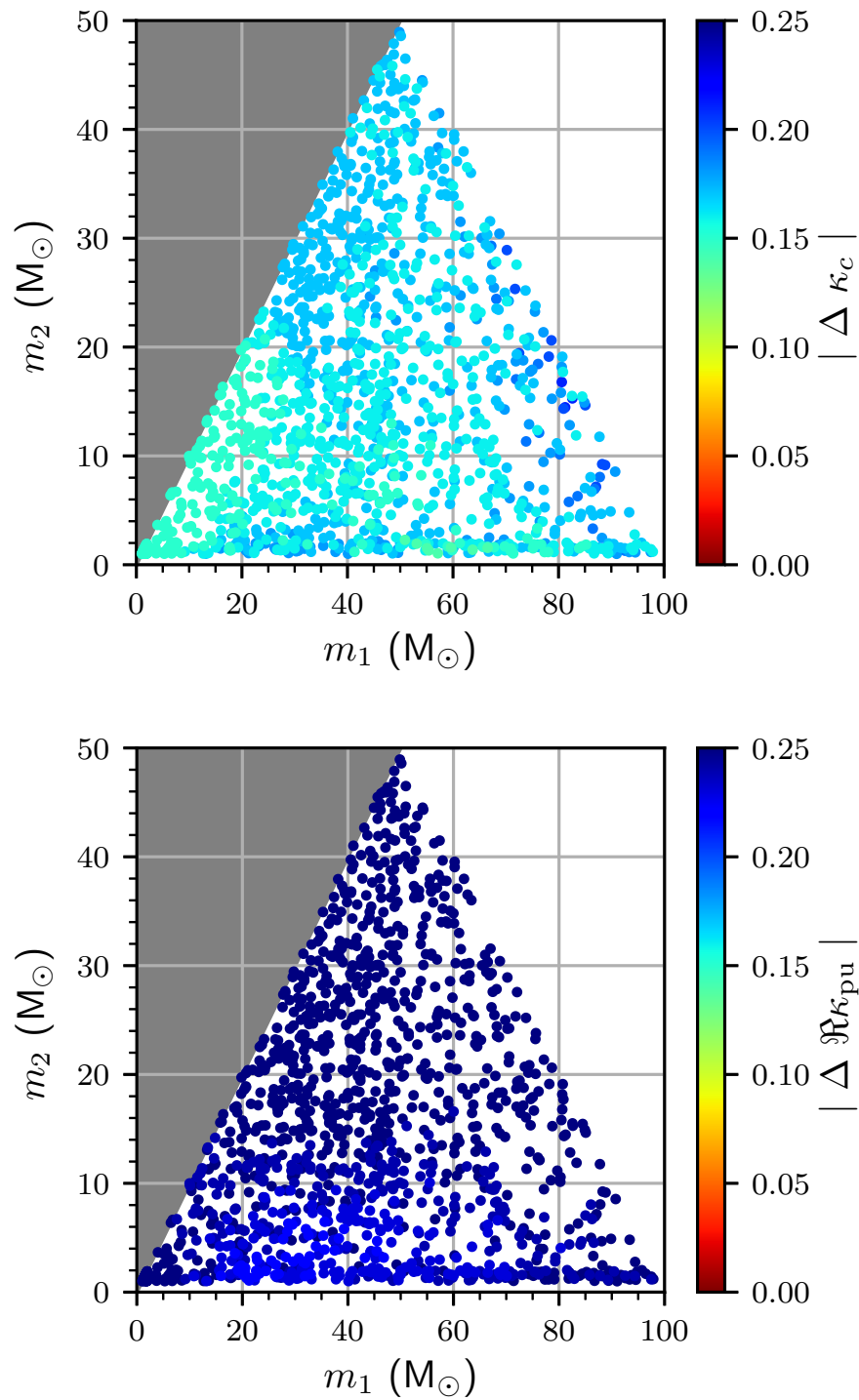


Figure 27 : The difference from the nominal value that corresponds to a match [5] of 0.99 which is a 1% loss in the matched-filter signal-to-noise ratio. Smaller differences corresponds to a steeper quadratic dependence.

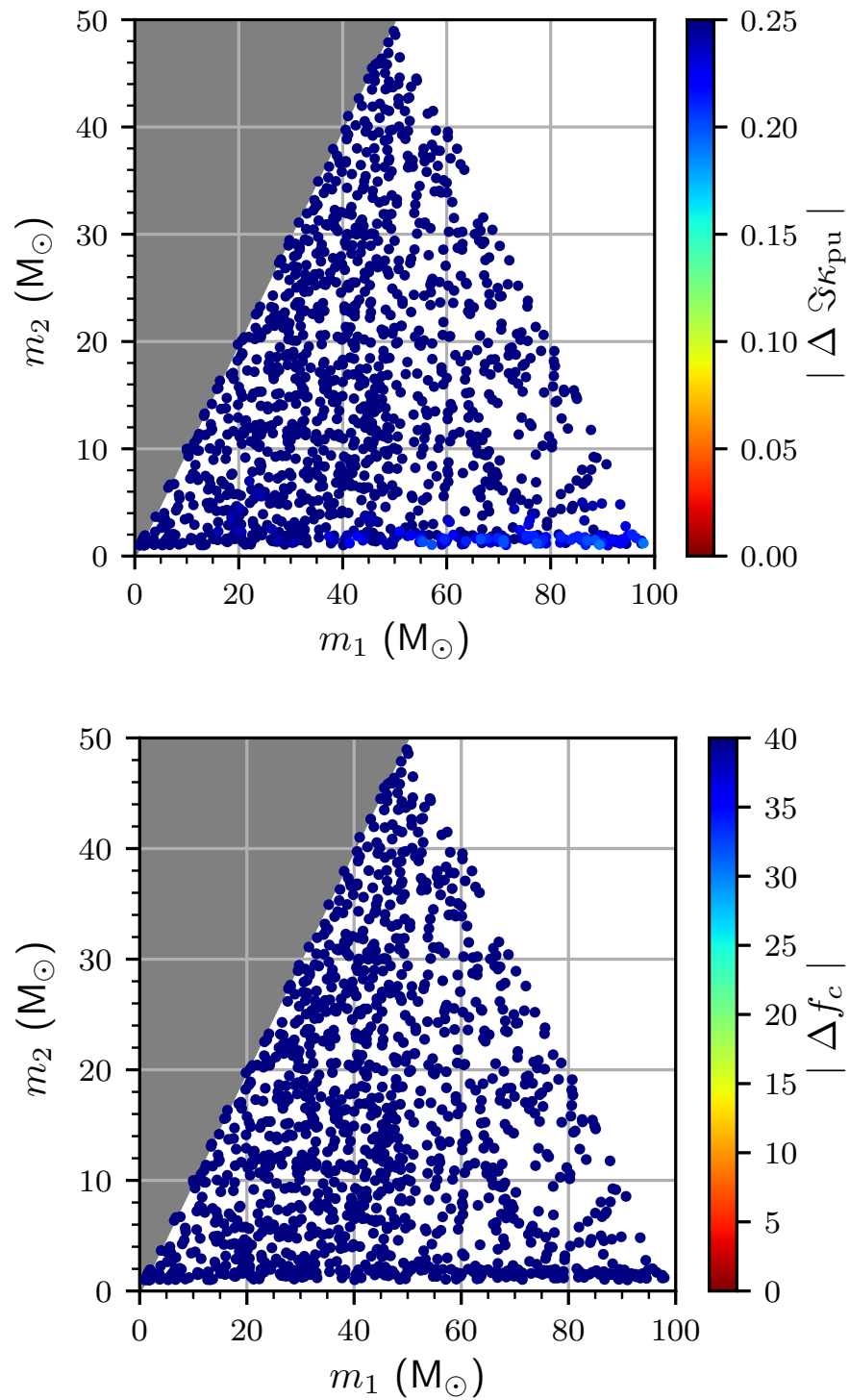


Figure 28 : The difference from the nominal value that corresponds to a match [5] of 0.99 which is a 1% loss in the matched-filter signal-to-noise ratio. Smaller differences corresponds to a steeper quadratic dependence.

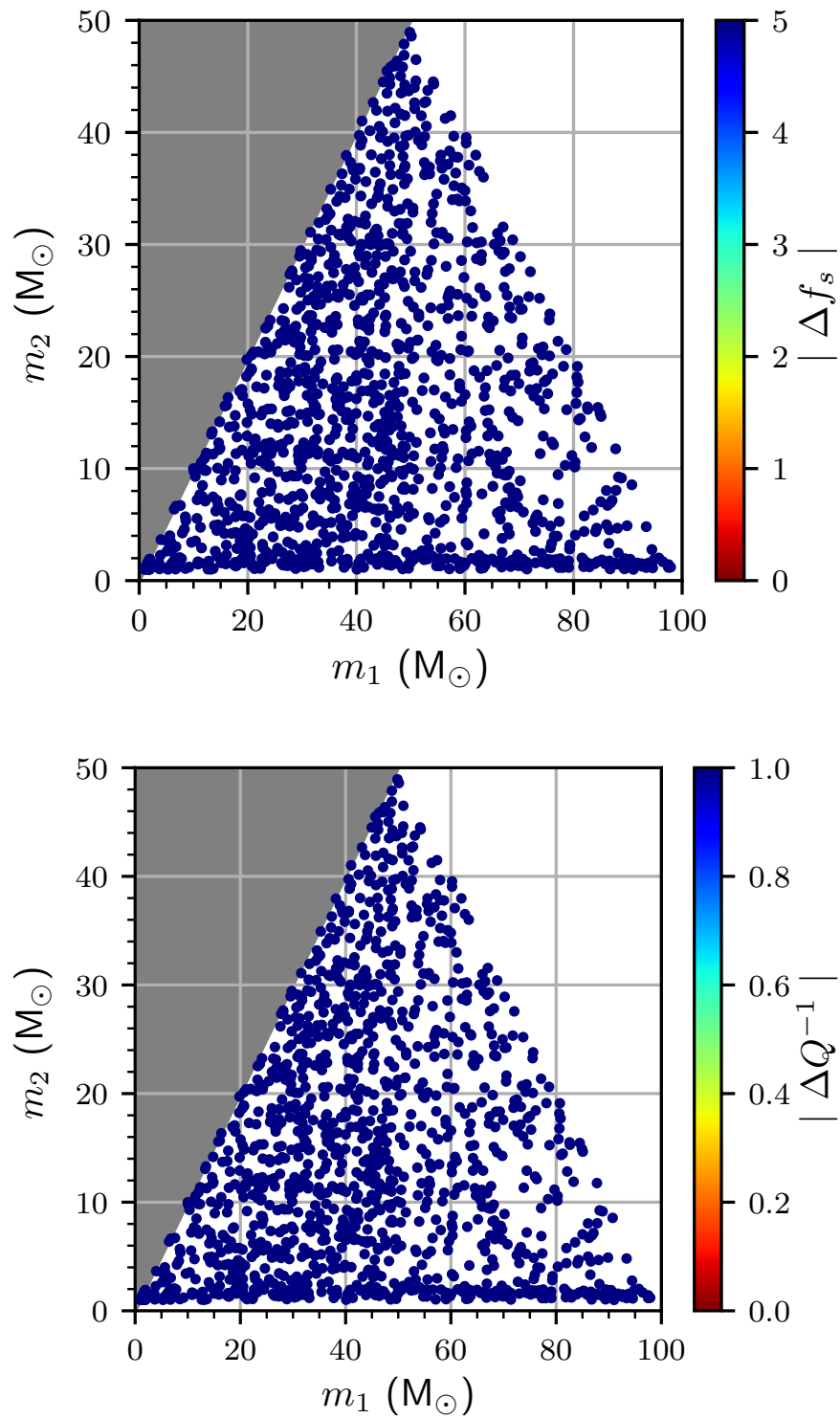


Figure 29 : The difference from the nominal value that corresponds to a match [5] of 0.99 which is a 1% loss in the matched-filter signal-to-noise ratio. Smaller differences corresponds to a steeper quadratic dependence.

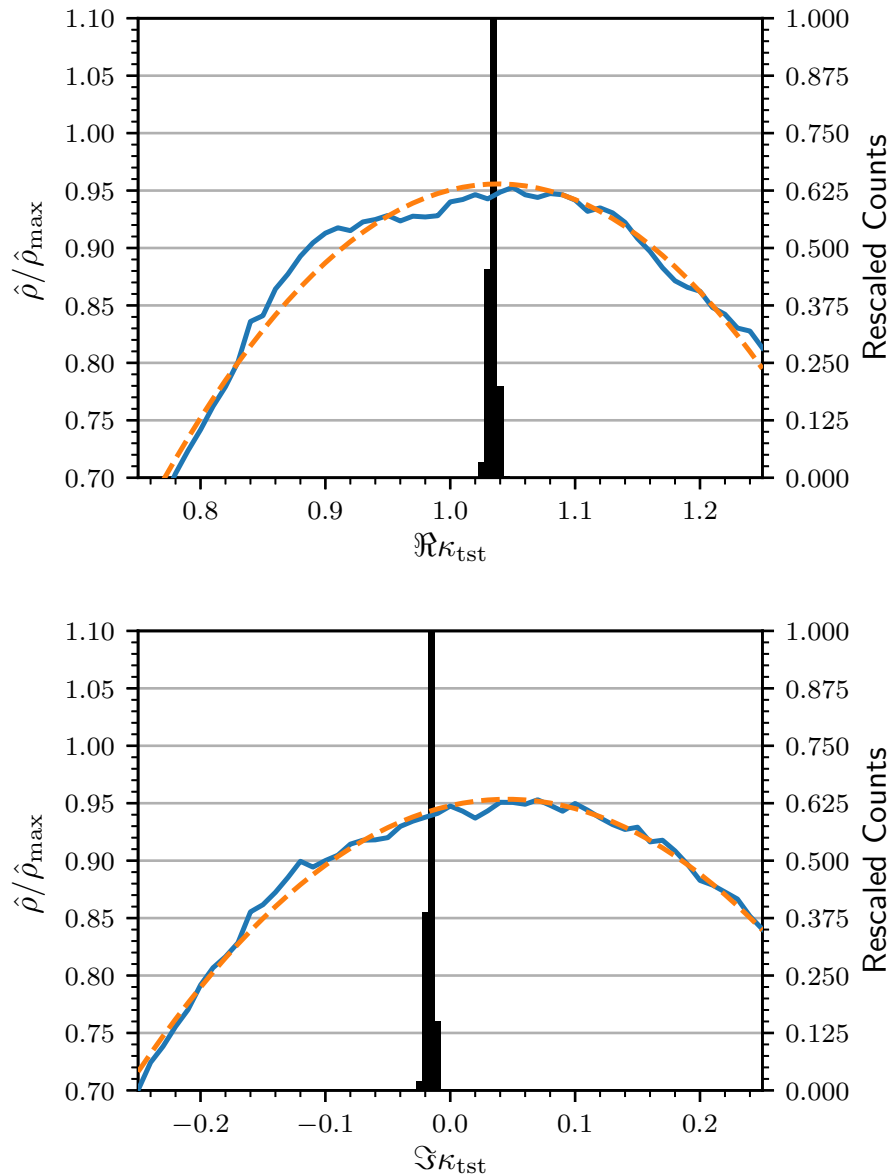


Figure 30 : Variation in the detection statistic $\hat{\rho}$ when the time-dependent calibration parameters are adjusted for GW150914. The best-fit waveform parameters from the search results reported in Ref. [4] were used to generate the template waveform to calculate $\hat{\rho}$. The blue solid curve represents $\hat{\rho}$ averaged over 16 noise realizations in Advanced LIGO's first observing run. The orange dashed curve is a quadratic fit, and it represents the approximate behavior of $\hat{\rho}$ for a large population of simulated signals. The maximum $\hat{\rho}$ recovered over all 16 noise realizations is denoted as $\hat{\rho}_{\max}$. The black histogram represents the measured values of the time-dependent calibration parameters for times used in the analysis on September 14 and September 15, 2015.

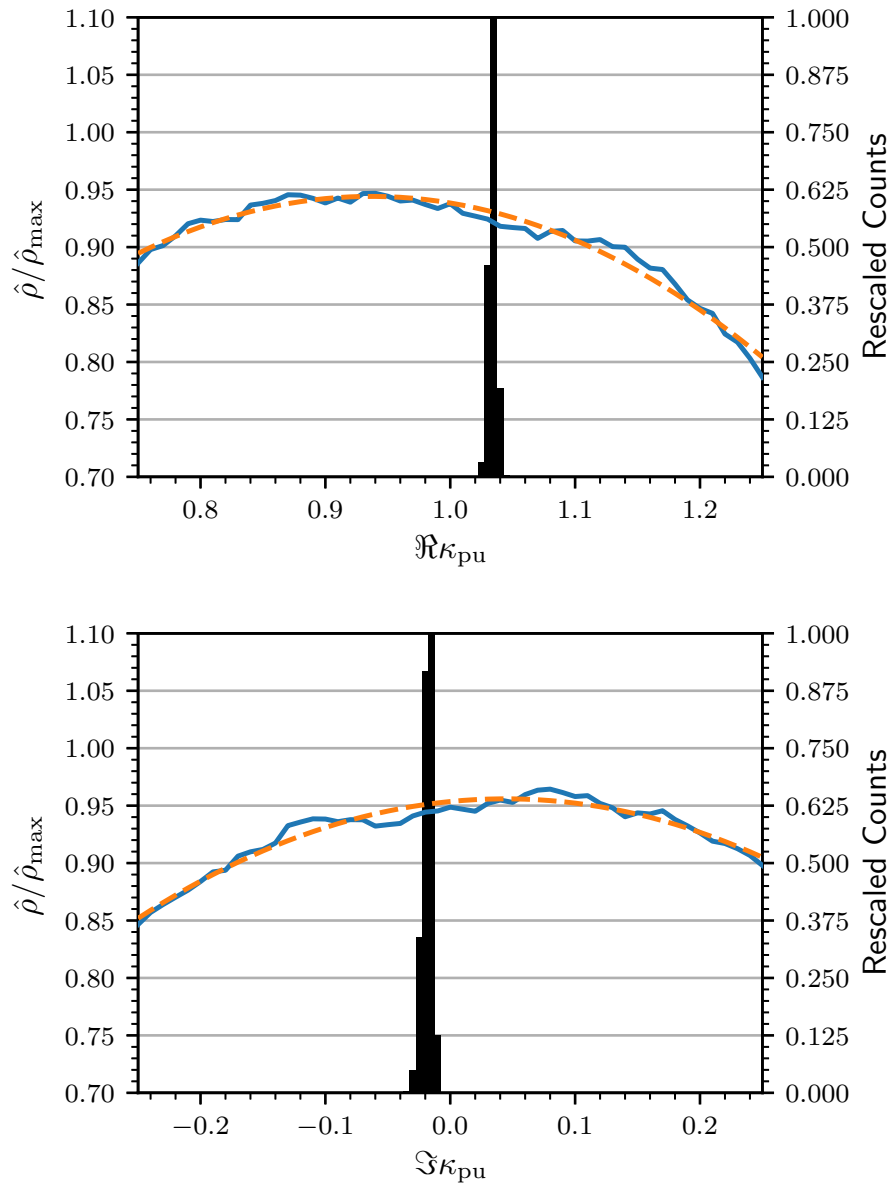


Figure 31 : Variation in the detection statistic $\hat{\rho}$ when the time-dependent calibration parameters are adjusted for GW150914. The best-fit waveform parameters from the search results reported in Ref. [4] were used to generate the template waveform to calculate $\hat{\rho}$. The blue solid curve represents $\hat{\rho}$ averaged over 16 noise realizations in Advanced LIGO's first observing run. The orange dashed curve is a quadratic fit, and it represents the approximate behavior of $\hat{\rho}$ for a large population of simulated signals. The maximum $\hat{\rho}$ recovered over all 16 noise realizations is denoted as $\hat{\rho}_{\max}$. The black histogram represents the measured values of the time-dependent calibration parameters for times used in the analysis on September 14 and September 15, 2015.

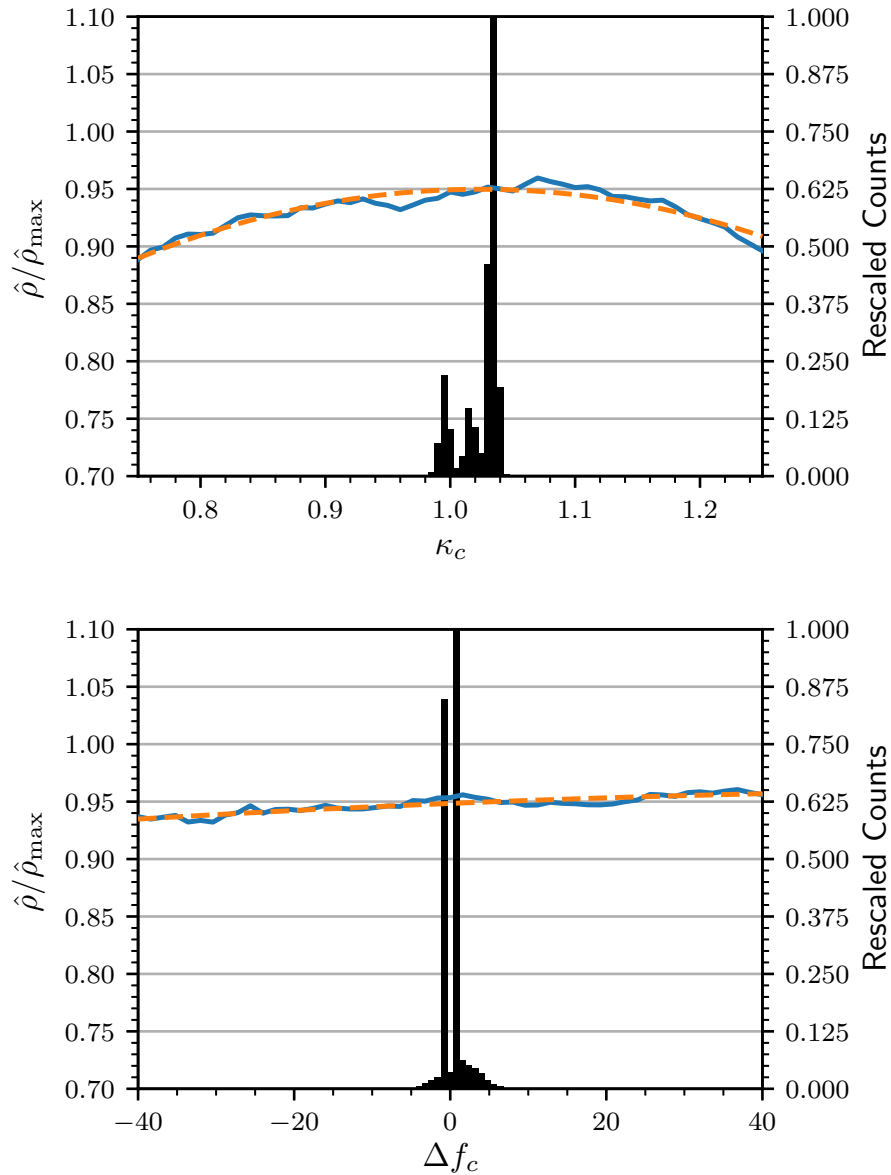


Figure 32 : Variation in the detection statistic $\hat{\rho}$ when the time-dependent calibration parameters are adjusted for GW150914. The best-fit waveform parameters from the search results reported in Ref. [4] were used to generate the template waveform to calculate $\hat{\rho}$. The blue solid curve represents $\hat{\rho}$ averaged over 16 noise realizations in Advanced LIGO's first observing run. The orange dashed curve is a quadratic fit, and it represents the approximate behavior of $\hat{\rho}$ for a large population of simulated signals. The maximum $\hat{\rho}$ recovered over all 16 noise realizations is denoted as $\hat{\rho}_{\max}$. The black histogram represents the measured values of the time-dependent calibration parameters for times used in the analysis on September 14 and September 15, 2015. The change in the cavity pole frequency Δf_c is offset from the measured value of 341 Hz.

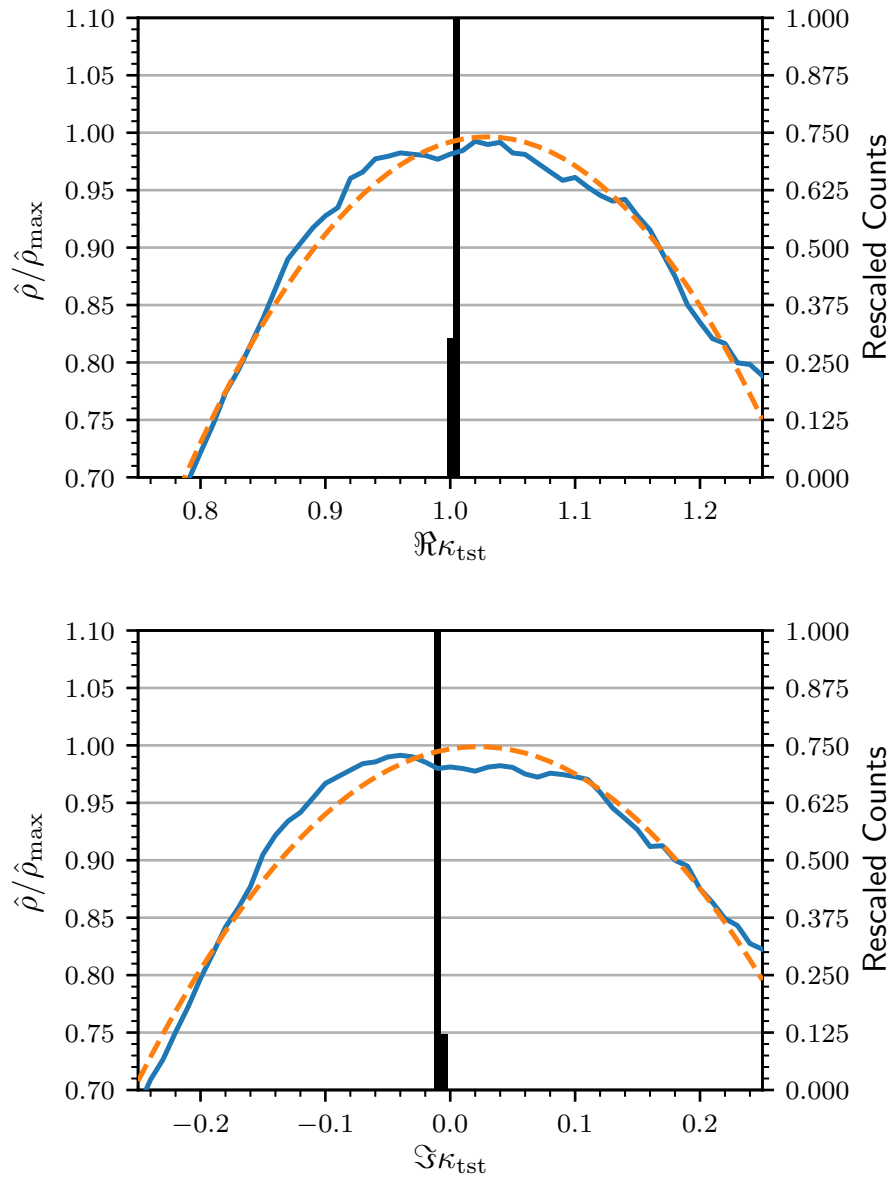


Figure 33 : Variation in the detection statistic $\hat{\rho}$ when the time-dependent calibration parameters are adjusted for a non-spinning 30-30 M_{\odot} binary black hole merger simulated signal. The blue solid curve represents $\hat{\rho}$ averaged over 16 noise realizations in Advanced LIGO's second observing run. The orange dashed curve is a quadratic fit, and it represents the approximate behavior of $\hat{\rho}$ for a large population of simulated signals. The maximum $\hat{\rho}$ recovered over all 16 noise realizations is denoted as $\hat{\rho}_{\text{max}}$. The black histogram represents the measured values of the time-dependent calibration parameters for times used in the analysis on January 19 and January 20, 2017.

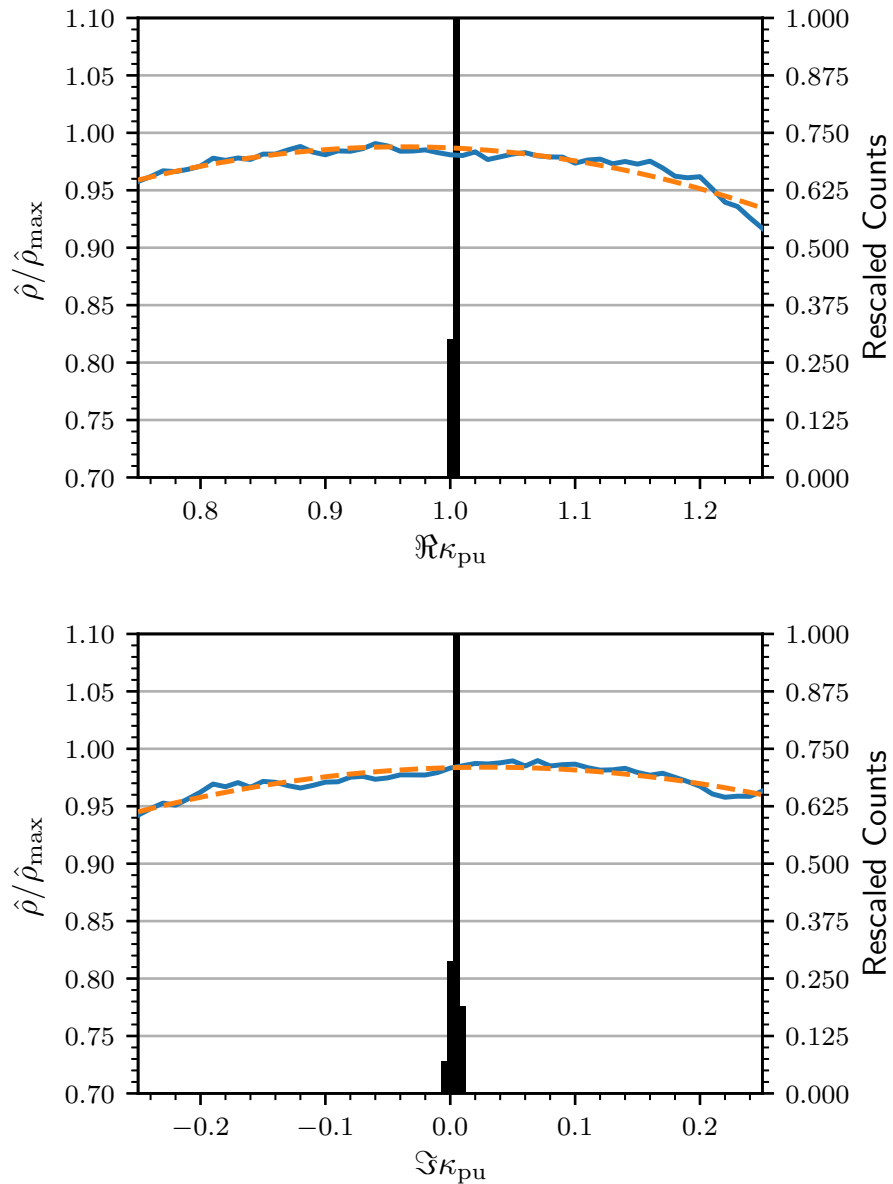


Figure 34 : Variation in the detection statistic $\hat{\rho}$ when the time-dependent calibration parameters are adjusted for a non-spinning 30-30 M_{\odot} binary black hole merger simulated signal. The blue solid curve represents $\hat{\rho}$ averaged over 16 noise realizations in Advanced LIGO's second observing run. The orange dashed curve is a quadratic fit, and it represents the approximate behavior of $\hat{\rho}$ for a large population of simulated signals. The maximum $\hat{\rho}$ recovered over all 16 noise realizations is denoted as $\hat{\rho}_{\max}$. The black histogram represents the measured values of the time-dependent calibration parameters for times used in the analysis on January 19 and January 20, 2017.

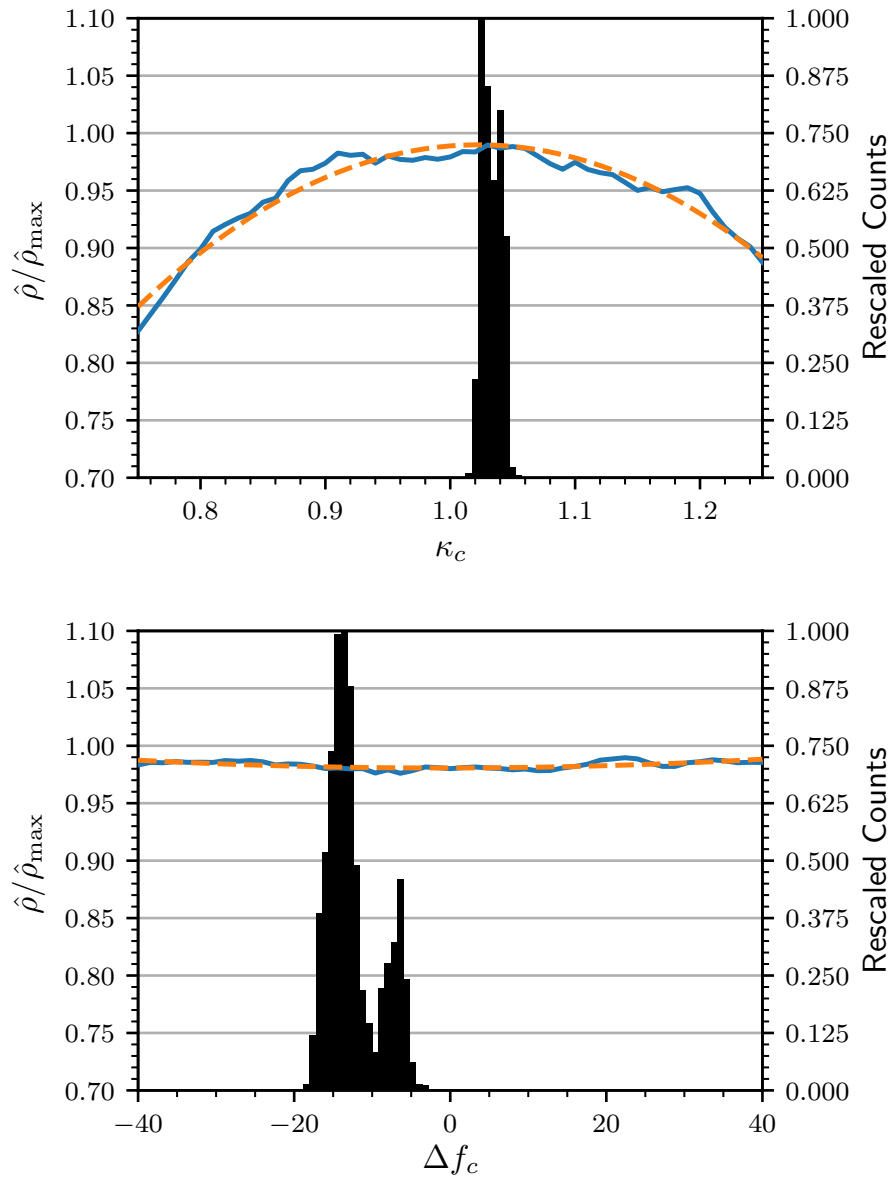


Figure 35 : Variation in the detection statistic $\hat{\rho}$ when the time-dependent calibration parameters are adjusted for a non-spinning 30-30 M_{\odot} binary black hole merger simulated signal. The blue solid curve represents $\hat{\rho}$ averaged over 16 noise realizations in Advanced LIGO's second observing run. The orange dashed curve is a quadratic fit, and it represents the approximate behavior of $\hat{\rho}$ for a large population of simulated signals. The maximum $\hat{\rho}$ recovered over all 16 noise realizations is denoted as $\hat{\rho}_{\max}$. The black histogram represents the measured values of the time-dependent calibration parameters for times used in the analysis on January 19 and January 20, 2017. The change in the cavity pole frequency Δf_c is offset from the measured values of 360 Hz.

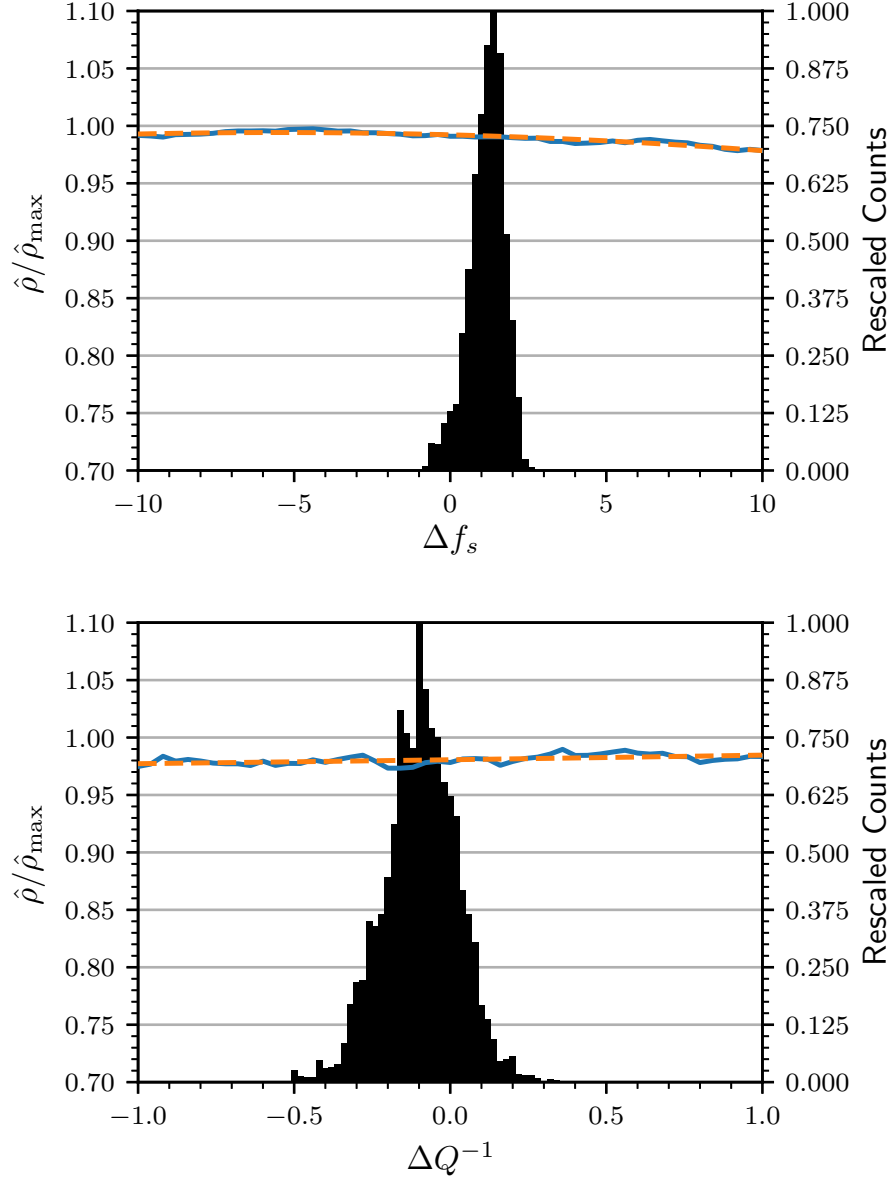


Figure 36 : Variation in the detection statistic $\hat{\rho}$ when the time-dependent calibration parameters are adjusted for a non-spinning 30-30 M_{\odot} binary black hole merger simulated signal. The blue solid curve represents $\hat{\rho}$ averaged over 16 noise realizations in Advanced LIGO's second observing run. The orange dashed curve is a quadratic fit, and it represents the approximate behavior of $\hat{\rho}$ for a large population of simulated signals. The maximum $\hat{\rho}$ recovered over all 16 noise realizations is denoted as $\hat{\rho}_{\max}$. The black histogram represents the measured values of the time-dependent calibration parameters for times used in the analysis on January 19 and January 20, 2017. The change in the optical spring frequency Δf_s , and inverse dimensionless quality factor ΔQ^{-1} are offset from their measured values of 6.9 Hz and 0.05 respectively.

Chapter 4

A parameter estimation pipeline for binary neutron star and black hole mergers in Advanced LIGO data

4.1 Introduction

The primary science product of the parameter estimation analyses is the posterior probability density function $p(\vec{\theta}|\{d_i(t)\}, H)$ which describes the probability of obtaining a set of astrophysical parameters $\vec{\theta}$ in a model of gravitational radiation from compact-object mergers H and a gravitational-wave observatory network dataset $\{d_i(t), 1 < i < N\}$ with N detectors. Processing binary neutron star and black hole mergers depend on 15 astrophysical parameters which can include: the component masses m_1 and m_2 (2 parameters), the component spins of the compact objects in three-dimensions (6 parameters), the luminosity distance d_L to the binary (1 parameter), the right ascension α and the declination δ of the binary (2 parameters), its polarization ψ (1 parameter), the binary inclination angle ι (1 parameter), the coalescence time t_c (1 parameter), and the phase at the time of coalescence ϕ_c (1 parameter). The domains of these 15 model parameters are shown in Table 4.

The posterior probability density function can be computed using Bayes' theorem

which describes the posterior probability density function as

$$p(\vec{\theta}|\{d_i(t)\}, H) = \frac{p(\vec{\theta}|H)p(\{d_i(t)\}|\vec{\theta}, H)}{p(\{d_i(t)\}|H)}, \quad (4.1)$$

where $p(\vec{\theta}|H)$ is the prior probability density function which describes our knowledge about the parameters before evaluating the posterior probability density function, $p(\{d_i(t)\}|\vec{\theta}, H)$ is the likelihood which is the probability of obtaining the dataset given the parameters, and $p(\{d_i(t)\}|H)$ is the evidence. The evidence is a normalization constant that does not affect estimating the parameters with a single model. However, the evidence allows us to compare different models [47, 124]. In this chapter, we do not explore Bayesian model selection and restrict our investigations to estimating the posterior probability density functions.

Stochastic sampling techniques, and in particular Markov-chain Monte Carlo methods, have been used to numerically evaluate the posterior probability density function of binary black hole mergers [47, 2]. In ensemble Markov chain Monte Carlo sampling algorithms, an ensemble of Markov chains move around the parameter space according to a set of rules. Markov chains are members of the ensemble which keep a record of where they have traveled in the parameter space. Eventually the ensemble of Markov chains converge to a distribution that is a sampling of the posterior probability density function. The astrophysical parameters $\vec{\theta}$ can then be estimated from histograms of the position of the Markov chains in the parameter space.

In this chapter, we present PyCBC Inference: a new Bayesian analysis framework for estimating the parameters of compact-object mergers. In Sec. 4.2 we explain our model of the likelihood function used in the calculation of the posterior probability density function for a candidate event. Section 4.3 describes how we evaluate and sample the choices of priors. PyCBC Inference is a flexible framework which allows the choice of multiple sampling algorithms. We have included methods to import two open-source, independent, ensemble Markov-chain Monte Carlo sampling algorithms. We describe ensemble Markov chain Monte Carlo sampling in Section 4.4. Then, in Sections 4.5 and 4.6, we summarize the two sampling algorithms that have been added. In Section 4.7, we present the similarities and differences between PyCBC Inference and the `LALInference` parameter estimation package which was used to publish the parameter estimates of the binary black hole mergers observed during Advanced LIGO’s first observing run. In Sec. 4.8 we use the binary black hole

Parameter	Symbol	Unconstrained Domain
Right ascension	α	$[0, 2\pi)$
Declination	δ	$[-\frac{\pi}{2}, \frac{\pi}{2}]$
Polarization angle	ψ	$[0, 2\pi)$
Primary mass	m_1	$>0 M_\odot$
Secondary mass	m_2	$>0 M_\odot$
Luminosity distance	d_L	$>0 \text{ Mpc}$
Inclination	ι	$[-\frac{\pi}{2}, \frac{\pi}{2}]$
Coalescence time	t_c	$(-\infty, \infty)$
Coalescence phase	ϕ_c	$[0, 2\pi)$
Dimensionless spin magnitude	χ_i	$[0, 1], i \in \{1, 2\}$
Dimensionless spin azimuthal angle	θ_i^a	$[0, 2\pi), i \in \{1, 2\}$
Dimensionless spin polar angle	θ_i^p	$[-\frac{\pi}{2}, \frac{\pi}{2}], i \in \{1, 2\}$

Table 4 : Table of model parameters. Note that not all waveform models include every parameter, and may only be valid for particular choices of mass and spin parameters. Spin parameters are expressed in spherical coordinates where $\theta_i^p = \frac{\pi}{2}$ is aligned with the angular momentum of the binary. Some models may choose to use mass or spin parameters that are functions of the component masses and spins as well. In this convention, $\iota = -\frac{\pi}{2}$ corresponds to a face-on binary (line of sight parallel to binary angular momentum), $\iota = 0$ corresponds to an edge-on binary (line of sight perpendicular to binary angular momentum), and $\iota = \frac{\pi}{2}$ corresponds to a face-away binary (line of sight anti-parallel to binary angular momentum).

mergers observed during Advanced LIGO’s first observing run to demonstrate PyCBC Inference. Finally, in Sec. 4.9 we suggest future development plans for PyCBC Inference.

4.2 Likelihood

In order to evaluate the posterior probability density function $p(\vec{\theta}|\{d_i(t)\}, H)$ we need a model of the likelihood $p(\{d_i(t)\}|\vec{\theta}, H)$ and a choice of prior $p(\vec{\theta}|H)$ probability density functions. Our model for the likelihood assumes that the noise in the dataset $\{d_i(t)\}$ is stationary and Gaussian [47]. The gravitational-wave strain time series for a single detector is $d_i(t)$, and the single-detector data can be decomposed into $d_i(t) = s_i(t) + n_i(t)$ where $s_i(t)$ is the astrophysical signal and $n_i(t)$ is detector noise. Since we do not know the true signal $s_i(t)$ we choose a model H to generate

$\tilde{h}_i(f, \vec{\theta})$ which is the frequency-domain gravitational waveform with parameters $\vec{\theta}$. The natural logarithm of the likelihood is

$$\log p(\{d_i(t)\}|\vec{\theta}) = -\frac{1}{2} \sum_{i=1}^N \langle \tilde{n}_i(f) | \tilde{n}_i(f) \rangle \quad (4.2)$$

$$= -\frac{1}{2} \sum_{i=1}^N \langle \tilde{d}_i(f) - \tilde{h}_i(f, \vec{\theta}) | \tilde{d}_i(f) - \tilde{h}_i(f, \vec{\theta}) \rangle, \quad (4.3)$$

where $\tilde{n}(f)$ denotes the Fourier transform of time series $n(t)$, and the inner product $\langle \tilde{a}(f) | \tilde{b}(f) \rangle$ is given by

$$\langle \tilde{a}(f) | \tilde{b}(f) \rangle = 4\Re \int_0^\infty \frac{\tilde{a}(f)\tilde{b}(f)}{S_n(f)} df. \quad (4.4)$$

Since the detectors are at different locations on Earth, we must account for the relative time delay and sensitivity to a particular sky position for each detector in Equation 4.2. The astrophysical gravitational-wave waveform $\tilde{h}_{i,\vec{\theta}}(f)$ generated with model H and astrophysical parameter set $\vec{\theta}$ in a particular detector can be written as

$$\tilde{h}_i(f, \vec{\theta}) = \left[F_{+,i}(\alpha, \delta, \psi) \tilde{h}_+(f, \vec{\theta}') + F_{\times,i}(\alpha, \delta, \psi) \tilde{h}_\times(f, \vec{\theta}') \right], \quad (4.5)$$

where $F_{+,i}(\alpha, \delta, \psi)$ and $F_{\times,i}(\alpha, \delta, \psi)$ are the antenna pattern of the detector which gives the amplitude response of the antenna to the two gravitational-wave polarizations $\tilde{h}_+(f, \vec{\theta}')$ and $\tilde{h}_\times(f, \vec{\theta}')$ [125]. The antenna patterns are known functions that depend on the Euler angles that transform from the detector frame to the radiation frame; physically these Euler angles are the sky position (right ascension α and declination δ) and the polarization ψ of the astrophysical source [125]. The two polarizations $h_+(t, \vec{\theta}')$ and $h_\times(t, \vec{\theta}')$ depend on the waveform model H that is selected to compute $\tilde{h}_i(f, \vec{\theta})$ where $\vec{\theta}' = \vec{\theta} \setminus \{\alpha, \delta, \psi\}$.

The likelihood from parameter estimation and the matched-filter signal-to-noise ratio are closely related quantities. The matched-filter search's goal is to maximize the likelihood ratio Λ [126]. The likelihood ratio comes from finding the ratio of the probability that a signal is present given the dataset $p(s(t)|\{d_i(t)\})$ and the probability there is no signal given the dataset $p(\{0|d_i(t)\}) = 1 - p(s(t)|\{d_i(t)\})$. We use Bayes'

theorem to find that [126]

$$p(\{d_i(t)\}|s(t)) = \frac{p(h)p(s(t)|h(t))}{p(s(t))} \quad (4.6)$$

$$= \frac{p(h(t))p(s(t)|h(t))}{p(h(t))p(s(t)|h(t)) + p(0)p(s(t)|0)} \quad (4.7)$$

$$= \frac{\frac{p(s(t)|h(t))}{p(s(t)|0)}}{\frac{p(s(t)|h(t))}{p(s(t)|0)} + \frac{p(0)}{p(h(t))}} \quad (4.8)$$

$$= \frac{\Lambda}{\Lambda + \frac{p(0)}{p(h(t))}} \quad (4.9)$$

where $\Lambda = p(s(t)|h(t))/p(s(t)|0)$ is the likelihood ratio. Now, we can find the ratio of the probabilities which is

$$\frac{p(\{s(t)|d_i(t)\})}{p(\{0|d_i(t)\})} = \frac{p(\{s(t)|d_i(t)\})}{1 - p(\{s(t)|d_i(t)\})} = \Lambda \frac{p(h(t))}{p(0)}, \quad (4.10)$$

since $p(h(t))/p(0)$ is a constant the search needs to find the maximums in the likelihood ratio.

We can evaluate the likelihood ratio using the probability of obtaining the interferometer output in the absence of signal $s(t) = n(t)$ and the probability density of obtaining $s(t)$ in the presence of a signal $s(t) = n(t) + h(t)$. We can write Λ in terms of $s(t)$ and $h(t)$ which is given by [126]

$$\Lambda = \frac{p(h(t)|s(t))}{p(0|s(t))} \quad (4.11)$$

$$= \frac{p(s(t) - h(t))}{p(n(t))} \quad (4.12)$$

$$= e^{-\frac{1}{2}\langle s(t)-h(t)|s(t)-h(t)\rangle} e^{\frac{1}{2}\langle s(t)|s(t)\rangle}, \quad (4.13)$$

and the natural logarithm of Λ is

$$\log(\Lambda) = -\frac{1}{2}\langle s(t) - h(t)|s(t) - h(t)\rangle + \frac{1}{2}\langle s(t)|s(t)\rangle. \quad (4.14)$$

If we compare Equations 4.2 we see that the likelihood from parameter estimation and likelihood ratio from the search are closely related quantities. If we simplify Equation 4.14 we find that

$$\log(\Lambda) = \langle s(t)|h(t)\rangle - \frac{1}{2}\langle h(t)|h(t)\rangle. \quad (4.15)$$

In practice, the search chooses to only compute $\langle s(t)|h(t)\rangle$ which is the matched-filter signal-to-noise ratio to maximize $\log(\Lambda)$.

4.3 Priors

The prior $p(\vec{\theta}|H)$ represents our knowledge about the parameters in model H before the dataset $\{d_i(t)\}$ is analyzed. The prior is a known set of probability distributions for each parameter in $\vec{\theta}$. Here, we treat each parameter independently such that

$$p(\vec{\theta}|H) = \prod_{i=1}^N p(\theta_i), \quad (4.16)$$

where N is the number of parameters in $\vec{\theta}$ and $p(\theta_i)$ is the prior probability density function for a single parameter θ_i .

We try to choose priors that make minimal assumptions about the distribution of the parameters. Models of precessing binary black hole mergers depend on 15 parameters: the component masses m_1 and m_2 , the component spins in three-dimensions, the luminosity distance d_L , the right ascension α , the declination δ , the polarization ψ , the binary inclination angle ι , the coalescence time t_c , and the phase at the time of coalescence ϕ_c . Here, we describe the distribution uniform in a power law, isotropic distributions, and distributions that are uniform in the logarithm. Specific choices for the bounds of distributions are described for their respective analysis in Section 4.8. For each distribution we find the probability density function to evaluate the prior in the computation of the posterior, and we show how to draw samples from each distribution. These distributions are used to generate distributions of simulated signals as well.

We choose a uniform prior for the component masses, coalescence time, and spin magnitudes, and a distribution that is uniform in volume for the distance. Both the uniform distribution and the distribution of the radial component in spherical coordinates that is uniform in volume are part of a family of probability density functions with the form

$$p(x) \sim x^n, \quad (4.17)$$

where n is a real number and x is bounded between a and b . We can find a general expression that describes both of these probability density functions which we have implemented in PyCBC Inference. We can use the cumulative distribution function to normalize the probability density function

$$p(x) = cx^n, \quad (4.18)$$

where c is an unknown constant. The cumulative distribution function is the integral of the probability density function which is given by

$$P(x) = \int_a^b cx^n dx = \frac{c}{n+1}x^{n+1} + k, \quad (4.19)$$

where k is a constant of integration. From the definition of the cumulative distribution function we know that $P(a) = 0$ and $P(b) = 1$. We can solve for c using the following system of equations

$$P(a) = 0 = \frac{c}{n+1}a^{n+1} + k \quad (4.20)$$

$$P(b) = 1 = \frac{c}{n+1}b^{n+1} + k, \quad (4.21)$$

to get

$$c = \frac{n+1}{b^{n+1} - a^{n+1}}. \quad (4.22)$$

If we substitute c into the expression for $P(a) = 0$, then we can solve for k where

$$k = -\frac{c}{n+1}a^{n+1} = -\frac{a^{n+1}}{b^{n+1} - a^{n+1}}. \quad (4.23)$$

Therefore the normalized probability density function is

$$p(x) = \frac{n+1}{b^{n+1} - a^{n+1}}x^n, \quad (4.24)$$

and the normalized cumulative distribution function is

$$P(x) = \frac{1}{b^{n+1} - a^{n+1}}x^{n+1} - \frac{a^{n+1}}{b^{n+1} - a^{n+1}}. \quad (4.25)$$

We also need the capability to sample these two distributions. Now we can use the probability integral transform method [127] to find a general expression that uses a uniform distribution of numbers u between 0 and 1 to sampling the distribution. The generalized expression can be found by finding $P^{-1}(u)$ which is the inverse of the cumulative probability density function evaluated for uniform numbers u on the interval between 0 and 1. To find $P^{-1}(u)$ we solve $P(x) = u$ for x . This gives

$$P(x) = u \quad (4.26)$$

$$\frac{1}{b^{n+1} - a^{n+1}}x^{n+1} - \frac{a^{n+1}}{b^{n+1} - a^{n+1}} = u \quad (4.27)$$

$$x = [(b^{n+1} - a^{n+1})u - a^{n+1}]^{\frac{1}{n+1}}. \quad (4.28)$$

This expression is used to sample the probability density function $p(x) = cx^n$ by drawing uniform numbers between 0 and 1 and then evaluating Equation 4.26.

The uniform distribution used for the component mass, coalescence time, and spin magnitude priors corresponds to the $n = 0$ case. We see the probability density function for the uniform distribution is

$$p(x) = \frac{1}{b-a}. \quad (4.29)$$

Sampling this uniform distribution is simply an offset from sampling the uniform distribution between 0 and 1 which is given by

$$x = (b-a)u + a. \quad (4.30)$$

Some analyses use uniform priors that are more complex than an n -sided cube of uniform distribution and we provide a method for properly normalizing these distributions. For example, the analysis of GW151226 [110] used a uniform prior in the component masses bounded by chirp masses between $9.5 M_\odot$ and $10.5 M_\odot$, and mass ratio between 1 and 18; however, using this more complex geometry requires us to carefully normalize the prior probability density function. If we have multidimensional uniform prior $p'(\vec{\theta})$ for parameters $\vec{\theta}$ with arbitrary bounds, then we can choose an n -sided cube of uniform prior $p(\vec{\theta})$ with bounds that encompass the entire parameter space of $p'(\vec{\theta})$. Then, we can perform rejection sampling which entails drawing points from $p(\vec{\theta})$ and rejecting all draws that lie outside the bounds of $p'(\vec{\theta})$. Now, the normalized uniform probability density function $p'(\vec{\theta})$ can be found evaluated from

$$p'(\vec{\theta}) = \xi p(\vec{\theta}), \quad (4.31)$$

where ξ is the fraction of samples accepted from rejection sampling $p'(\vec{\theta})$ with the bounds of $p(\vec{\theta})$. This method is applicable to uniform distributions, and for non-uniform, arbitrary distributions we have implemented a method that fits Gaussians to the distribution called Gaussian kernel-density estimation; however, we do not describe that method here since it is not used in this analysis.

The $n = 2$ case from this family of distributions can be used to sample a distribution uniform in volume where the distance is the radial component and the right ascension and declination are the angular components in spherical coordinates. In

the radial dimension, the cumulative distribution function of a distribution that is uniform in volume is the ratio of volumes

$$P(x) = \frac{V(x) - V(a)}{V(b)}, \quad (4.32)$$

where $V(x)$ is the volume of a sphere

$$V(x) = \frac{4}{3}\pi x^3, \quad (4.33)$$

therefore the cumulative distribution function is

$$P(x) \sim x^3. \quad (4.34)$$

This corresponds to the $n = 2$ case in Equations 4.24 and 4.26 which gives a probability density function

$$p(x) = \frac{3}{b^3 - a^3} x^2, \quad (4.35)$$

that can be sampled using

$$x = [(b^3 - a^3)u + a^3]^{1/3}. \quad (4.36)$$

Alternatively, we provide a method to use rejection sampling for sampling a sphere uniformly. We draw samples in a cube where each dimension is a uniform distribution, then discard samples that are outside the sphere. The fraction of samples discarded is found by calculating the probability a point is inside a sphere given the point is in inside a cube which is

$$p(\text{in sphere}|\text{in cube}) = \frac{\frac{4}{3}\pi x^3}{8x^3} = 0.52. \quad (4.37)$$

Note that we use $8x^3$ for the volume because we define the length of one side of the cube to be twice the radius of the sphere which is $2x$.

Models of binary neutron star and black hole mergers have a number of angular parameters which cannot be placed uniformly on the surface of a sphere with only the family of distributions described above. We use an isotropic prior which does place points uniform on a sphere for the angular sky position and orientation parameters which includes the right ascension, the declination, polarization, the inclination, the coalescence phase, and the component spin angles. We can follow the same prescription to determine the probability density function of the isotropic distribution

and how to draw points from the isotropic distribution. In spherical coordinates, we will need to determine these functions for the azimuthal and polar angles. The azimuthal angle in an isotropic distribution is simply a uniform distribution from 0 to 2π ; therefore, we use a uniform distribution for the right ascension, the polarization, the coalescence phase, and the azimuthal spin angles. The probability density function of the polar angle in spherical coordinates is

$$p(x) = c \sin(x), \quad (4.38)$$

where c is a constant and x is bounded between $a = -\pi/2$ and $b = \pi/2$. We use this probability density function for declination, inclination, and polar spin angles. From this we see that the cumulative distribution function is

$$P(x) = -c \cos(x) + k, \quad (4.39)$$

and solving for c and k using $P(a) = 0$ and $P(b) = 1$ gives

$$c = -\frac{1}{\cos(b) - \cos(a)}, \quad (4.40)$$

and

$$k = -\frac{\cos(a)}{\cos(b) - \cos(a)}. \quad (4.41)$$

Therefore we can evaluate the probability density function for declination and inclination as

$$p(x) = -\frac{1}{\cos(b) - \cos(a)} \sin(x) - \frac{\cos(a)}{\cos(b) - \cos(a)}, \quad (4.42)$$

and draw samples from the distribution with

$$x = \arccos \left((\cos(b) - \cos(a))u + \frac{\cos(a)}{\cos(b) - \cos(a)} \right). \quad (4.43)$$

One additional distribution used in Chapter 5 to draw distances for a population of simulated signals is a distribution uniform in the logarithm. This distribution was chosen instead of a uniform volume distribution of sources in the Universe because a uniform volume distribution has more probability of drawing further distances which results in more simulated signals with low signal-to-noise ratio. Here, we find the probability density function in base 10. We want the distribution that can be samples $\log_{10}(x) = u/c - k$ where c and k are constants and u is a sampling of uniform

numbers between 0 and 1. This corresponds to the cumulative distribution function $P(x) = c \log_{10}(x) + k$ with the system of equations where $P(a) = 0$ and $P(b) = 1$. We find that

$$c = \frac{1}{\log_{10}(b) - \log_{10}(a)}, \quad (4.44)$$

and

$$k = -\frac{\log_{10}(a)}{\log_{10}(b) - \log_{10}(a)}. \quad (4.45)$$

Using the fact that the probability density function is the derivative of the cumulative distribution function, $\frac{d}{dx}P(x) = p(x)$, we get

$$p(x) = \frac{1}{\log_{10}(b) - \log_{10}(a)} \frac{1}{\log(10)x}, \quad (4.46)$$

where $\log(10)$ denotes the natural logarithm of 10. This distribution can be sampled with

$$x = 10^{(\log_{10}(b) - \log_{10}(a))u + \log_{10}(a)}. \quad (4.47)$$

The probability density function that is uniform in the base 10 logarithm is the same as other probability density functions that are uniform in a different base. Here, we show that their probability density functions are equivalent. We can generalize Equation 4.47 to sample a uniform distribution in the base B logarithm as

$$x = B^{(\log_B(b) - \log_B(a))u + \log_B(a)}, \quad (4.48)$$

which has a cumulative distribution function of

$$P(x) = \frac{1}{\log_B(b) - \log_B(a)} \log_B(x) - \frac{\log_B(a)}{\log_B(b) - \log_B(a)}. \quad (4.49)$$

The probability density function is $p(x) = \frac{d}{dx}P(x)$ so we find that the probability density function is

$$p(x) = \frac{1}{\log_B(b) - \log_B(a)} \frac{d}{dx} (\log_B(x)) \quad (4.50)$$

$$= \frac{1}{(\log_B(b) - \log_B(a)) \log(B)} \frac{1}{x}. \quad (4.51)$$

We can rewrite Equation 4.50 using the identity

$$\log_A(B) \log_B(x) = \frac{\log(x)}{\log(A)}, \quad (4.52)$$

where A and B are two bases, and \log is the natural logarithm. In our case $A = e$ and Equation 4.52 reduces to

$$\log(B) \log_B(x) = \log(x). \quad (4.53)$$

Using Equation 4.53 we can reduce Equation 4.50 to

$$p(x) = \frac{1}{\log(b) - \log(a)} \frac{1}{x}. \quad (4.54)$$

Equations 4.46 and 4.54 are equivalent; however, in our analysis, we have chosen to evaluate the distribution in base 10.

4.4 Ensemble Markov-chain Monte Carlo sampling

Ensemble Markov-chain Monte Carlo sampling algorithms initialize a set of Markov chains in the parameter space. A simple choice to initialize the i -th Markov chain in the ensemble is to draw a set of parameters $\vec{\theta}_0^{(i)}$ from a given prior probability density function. The Markov chains move around the parameter space according to the following set of rules. At iteration n , the i -th Markov chain has the set of parameters $\vec{\theta}_n^{(i)}$. The sampling algorithm chooses a new proposed set of parameters $\vec{\theta}_k^{(i)}$ with probability $q(\vec{\theta}_n^{(i)}, \vec{\theta}_k^{(i)})$. When a new set of parameters is proposed the sampler computes an acceptance probability α which determines if the Markov chain should move to the proposed parameter set $\vec{\theta}_k^{(i)}$ such that $\vec{\theta}_{n+1}^{(i)} = \vec{\theta}_k^{(i)}$. If $\vec{\theta}_k^{(i)}$ is rejected, then $\vec{\theta}_{n+1}^{(i)} = \vec{\theta}_n^{(i)}$. Different sampling algorithms make particular choices for the proposal probability $q(\vec{\theta}_n^{(i)}, \vec{\theta}_k^{(i)})$ and acceptance probability α .

We would like a diagnostic statistic that tells us if our analysis has not yet converged; however, tests for convergence should not be accepted without further evaluation. The Gelman–Rubin convergence statistic [128] measures the potential to improve an estimate of the variance of the astrophysical parameter θ which could be achieved by continuing to advance the ensemble. When little improvement estimating the variance of the distribution of θ can be gained, then the ensemble is considered to be converged. This method compares the estimated between-chains variance B which accounts for variance between Markov chains, and within-chain variance W which accounts for the variance within each single Markov chain. Large differences

between these variances indicates that the ensemble has not converged yet. The between-chains variance is defined as

$$B = \frac{N}{M-1} \sum_{m=1}^M \left(\hat{\theta}^{(m)} - \hat{\theta} \right)^2, \quad (4.55)$$

where N is the length of the Markov-chains, M is the number of Markov-chains, $\hat{\theta}^{(m)}$ is the mean of parameter θ from the m -th Markov chain, and $\hat{\theta}$ is the mean of all within-chain means given by

$$\hat{\theta} = \frac{1}{M} \sum_{m=1}^M \hat{\theta}^{(m)}. \quad (4.56)$$

The within-chain variances is defined as

$$W = \frac{1}{M} \sum_{m=1}^M (\hat{\sigma}_a^{(m)})^2, \quad (4.57)$$

where $(\hat{\sigma}_a^{(m)})^2$ is the variance of the m -th Markov chain. The between-chains variance and within-chain variance are combined into a pooled variance \hat{V} such that it is an unbiased estimator of the variance of the posterior distribution for the astrophysical parameter θ [128]. This means that as the number of iterations $N \rightarrow \infty$ then \hat{V} is approximately the variance of the posterior distribution of our parameter $\text{var}(\theta)$. We define \hat{V} as [128]

$$\hat{V} = \frac{N-1}{N} W + \frac{M+1}{MN} B. \quad (4.58)$$

We see that \hat{V} overestimates $\text{var}(\theta)$ if the ensemble covers more of the parameter space than the posterior distribution since B will be large, and if the Markov chains are in the process of converging W will be large as well. Therefore, we use a statistic that measures reductions in \hat{V} . The ratio of the pooled variance \hat{V} and within-chain variances W is called the potential scale reduction factor \hat{R} which converges to 1 as the ensemble of Markov chains converge. \hat{R} is defined as [128, 129]

$$\hat{R} = \sqrt{\frac{d+3}{d+1} \frac{\hat{V}}{W}}, \quad (4.59)$$

where d is an estimate of the degrees of freedom in a Student's t distribution given by [128]

$$d = 2 \frac{\hat{V}}{\text{var}(\hat{V})}, \quad (4.60)$$

where $\text{var}(\hat{V})$ is the variance of \hat{V} given by [130]

$$\text{var}(\hat{V}) = \left(\frac{N-1}{N}\right)^2 \text{var}(W) + \left(\frac{M+1}{MN}\right)^2 \text{var}(B) + 2\frac{(M-1)(N-1)}{MN^2} \text{cov}(W, B), \quad (4.61)$$

where $\text{cov}(W, B)$ denotes the covariance between W and B . As the Markov chains advance, once the point scale reduction factor has passed an minimum number of iterations and \hat{R} goes below a threshold, then the ensemble is considered converged and the posterior probability density function can be sampled from the position of the Markov chains.

Since the Markov chains keep the history of their position in the parameter space, we can use that history to find more independent samples rather than just using only their current position in the parameter space. Since the Markov chains' position at iteration $n+1$ depends on their position at iteration n , then the points in the Markov chain are correlated. Therefore, not all iterations in the Markov chain can be used in constructing the histograms that estimate the posterior probability density function of the binary black hole merger. We need to select independent samples within a Markov chain that are not correlated with each other or the initial conditions. We compute the autocorrelation length (ACL) from the autocorrelation function of the Markov chain and use samples at least an ACL away from each other in the Markov chain to construct the histograms that sample the posterior probability density function. We can estimate the autocorrelation function $\hat{R}_\theta^{(i)}(k)$ of a single parameter θ from the i -th Markov chain using

$$\hat{R}_\theta^{(i)}(k) = \frac{1}{n\sigma^2} \sum_{t=1}^{n-k} \left[\theta_t^{(i)} - \mu \right] \left[\theta_{t+k}^{(i)} - \mu \right], \quad (4.62)$$

where n is the length of the i -th Markov chain, $\theta_t^{(i)}$ is the parameter θ from the i -th Markov chain at iteration t , σ^2 is the variance of $\{\theta_t^{(i)}, 1 < t < n\}$, and μ is the mean of $\{\theta_t^{(i)}, 1 < t < n\}$. Equation 4.62 normalizes $\hat{R}_\theta^{(i)}(k)$ such that $\hat{R}_\theta^{(i)}(0) = 1$. We can calculate the ACL for θ from $\hat{R}_\theta^{(i)}(k)$. The ACL is defined as

$$\text{ACL} = 1 + 2 \sum_{k=1}^l \hat{R}_\theta^{(i)}(k) < \frac{k}{m}, \quad (4.63)$$

where l is the length of the $\hat{R}_\theta^{(i)}(k)$ to use to compute ACL, and m controls the length

of the window that is summed to compute the ACL. A canonical choice for l is half the length of $\hat{R}_\theta^{(i)}(k)$ and $m = 5$.

The independent samples from all Markov chains are used to construct the one-dimensional histograms of each parameter that represents a sampling of the posterior probability density function. In results from Advanced LIGO’s first observing run, the parameters of binary black hole mergers are quoted in terms of the median and the bounds of 90% credible interval as x_{-b}^{+a} where x is the median, a is the difference between the median and the lower bound of the 90% credible interval, and b is the difference between the upper bound of the 90% credible interval and the median. The 90% credible interval is the interval that contains 90% percent of the probability from the probability density function. We find credible intervals from the histograms of independent samples. The 90% credible interval is calculated by finding the 5-th and 95-th percentile of the histograms. The percentile p is the value at $p/100$ of the way from the minimum to the maximum in a sorted list of the histogram values. The 50-th percentile corresponds to the median of the probability density function.

PyCBC Inference has two choices of ensemble Markov-chain Monte Carlo sampling algorithms: `emcee` [131] and `kombine` [132, 133]. The `emcee` sampling algorithm is an open-source project with a number of developers and it has already been used for many scientific studies [134]. We summarize the methods used in the `emcee` sampling algorithm in Sec. 4.5. The `kombine` sampling algorithm has been developed by Ben Farr and we summarize its methods in Sec. 4.6.

4.5 emcee sampling algorithm

PyCBC Inference has an interface to the `emcee` sampling algorithm [131]. The `emcee` sampling algorithm introduces tempering which modifies the likelihood function with a “temperature” parameter. The natural logarithm of a tempered likelihood $p_T(\{d_i(t)\}|\vec{\theta})$ has the form [131]

$$\log p_T(\{d_i(t)\}|\vec{\theta}) = -\frac{1}{2} \sum_{i=1}^N \left\langle \tilde{d}_i(f) - \tilde{s}_i(f, \vec{\theta}) | \tilde{d}_i(f) - \tilde{s}_i(f, \vec{\theta}) \right\rangle^{\frac{1}{T}}, \quad (4.64)$$

where T is the temperature and $T = 1$ corresponds to the original likelihood function. As T increases it broadens the maximums in the parameter space which reduces the contrast between modes the parameter space. At high T the posterior probability

density function is approximately the prior and ensembles with high T are more likely to explore the entire parameter space.

Markov chains can become isolated on a single mode in a multi-modal parameter space and parallel-tempering is implemented in the `emcee` sampling algorithm to avoid these cases. Parallel-tempering advances multiple ensembles with a different temperatures; however, only samples from the ensemble with $T = 1$ are used to construct the posterior probability density function. Parallel tempering helps prevent Markov chains in the $T = 1$ ensemble from becoming isolated on a single mode in a multi-modal parameter space. Ensembles with $T > 1$ are only used to inform the $T = 1$ ensemble and to calculate the evidence [131]. The $T > 1$ ensembles are not used to construct the histograms that estimate the posterior probability density function.

Ensembles with high temperatures explore more of the parameter space and inform the $T = 1$ ensemble by periodically switching the position of their Markov chains. The swap between an ensemble with temperature T_i and another with temperature T_j is accepted at a rate $r_s = \min(1, \omega_{ij})$ where

$$\omega_{ij} = \left[\frac{p_{T_j}(\{d_i(t)\}|\vec{\theta}_j)}{p_{T_i}(\{d_i(t)\}|\vec{\theta}_i)} \right]^{\frac{1}{T_i} - \frac{1}{T_j}}, \quad (4.65)$$

where $T_i < T_j$.

The `emcee` sampling algorithm uses the parallel stretch move [131] to propose a new set of parameters. The parallel stretch move splits an ensemble of K Markov chains into two sets defined as $S^{(0)} = \{X_k, 1 \leq k \leq K/2\}$ and $S^{(1)} = \{X_k, K/2 + 1 < k < K\}$. Then for the i -th Markov chain $\vec{\theta}_a^{(i,0)}$ in $S^{(0)}$ another Markov chain $\vec{\theta}_b^{(j,1)}$ in the complementary set is randomly chosen and the new set of proposed parameters $\vec{\theta}_c^{(i,0)}$ is [131]

$$\vec{\theta}_c^{(i,0)} = \vec{\theta}_a^{(i,0)} + z \left[\vec{\theta}_b^{(j,1)} - \vec{\theta}_a^{(i,0)} \right], \quad (4.66)$$

where z is drawn from the probability density function $p(z) \sim z^{-\frac{1}{2}}$ on the interval a^{-1} to a where a is a tunable parameter; canonically, this is set to 2 [131, 135]. Finally, the point is accepted with probability

$$\alpha = \min \left(1, z^{n-1} \frac{\vec{\theta}_c^{(i,0)}}{\vec{\theta}_a^{(i,0)}} \right), \quad (4.67)$$

where n is the number of astrophysical parameters. The parallel stretch move can

be parallelized for all Markov chains in a single set. Once the new position for $S^{(0)}$ Markov chains have been decided, then the Markov chains from $S^{(1)}$ are updated.

4.6 kombine sampling algorithm

PyCBC Inference is a flexible framework that allows the use of multiple sampling algorithms to estimate the parameters of binary neutron star and black hole mergers. We include methods to import the `kombine` sampling algorithm which uses a clustered kernel-density estimate to construct its proposal distribution [132, 133]. Proposals are accepted then using the Metropolis-Hastings acceptance condition [136] which is a common choice for the acceptance probability α [137]. The Metropolis-Hastings acceptance condition is [136]

$$\alpha = \min \left\{ 1, \frac{p(\{d_i\}|\vec{\theta}_k^{(i)}) q(\vec{\theta}_k^{(i)}, \vec{\theta}_n^{(i)})}{p(\{d_i\}|\vec{\theta}_n^{(i)}) q(\vec{\theta}_n^{(i)}, \vec{\theta}_k^{(i)})} \right\}, \quad (4.68)$$

where $q(\vec{\theta}_k^{(i)}, \vec{\theta}_n^{(i)})$ is the probability of the i -th Markov chain moving from the proposed set of parameters $\vec{\theta}_k^{(i)}$ to the current set of parameters $\vec{\theta}_n^{(i)}$ using the parallel stretch move. In this section, we summarize the methods that the `kombine` sampling algorithm uses to construct the clustered kernel-density estimator.

The `kombine` sampling algorithm models the current position of all Markov chains in the parameter space and uses that model as the proposal distribution. It uses a Gaussian kernel density estimator which effectively fits a set of Gaussians to the Markov chain positions to estimate the posterior probability density function. In general, an estimate of the probability density function $p(\vec{y})$ at point \vec{y} within a set of n points $\{\vec{x}_i, 1 < i < N\}$ is found using the kernel density estimator which is defined as

$$p(\vec{y}) = \sum_{i=1}^N K(\vec{y} - \vec{x}_i, h), \quad (4.69)$$

where $K(\vec{x}, h)$ is the kernel which is a non-negative function that integrates to one and has a mean equal to zero and h is the bandwidth parameter which scales the size of the kernel. The standard choice in the `kombine` sampling algorithm is to use a multi-variate Gaussian kernel which is given by

$$K(\vec{x}, h) \sim e^{-\frac{|\vec{x}|^2}{2h^2}}, \quad (4.70)$$

and the bandwidth parameter h is set using

$$h = n^{-1/(n+4)}\Sigma^{1/2}, \quad (4.71)$$

where n is the number of parameters and Σ is the covariance matrix of the astrophysical parameters in \vec{x} .

The posterior probability density function for binary black hole mergers has complex correlations between parameters, therefore we need more than a single kernel to describe the parameters' distributions. The `kombine` sampling algorithm uses k-means clustering [133, 138] to create a set of Gaussian kernel-density estimators from the position of the Markov chains; the set of Gaussian kernel-density estimators are used to evaluate the proposal probability $q(\vec{\theta}_k^{(i)})$. The k-means clustering is a two-step, iterative procedure. First, k points are placed in the parameter space; these points are referred to as centroids. Each Markov chain is assigned to the nearest centroid using the Euclidean distance. The second step is to update the value of each centroid with the arithmetic mean of the Markov chains clustered to it. The set of all current Markov chains positions $S_t^{(i)}$ associated with the i -th centroid on the t -th iteration is

$$S_t^{(i)} = \left\{ \vec{x}_p : |\vec{x}_p - \vec{m}_t^{(i)}|^2 < |\vec{x}_p - \vec{m}_t^{(j)}|^2 \forall j, 1 < j < k \right\}, \quad (4.72)$$

where $m_t^{(i)}$ is the i -th centroid on the t -th iteration and $\{\vec{x}_p\}$ is the set of all current Markov chain positions in the ensemble. This process continues until the value of the centroids stop changing.

The k-means clustering requires knowing the number of centroids to initialize in the parameter space. It is possible to increase the likelihood by adding many free parameters but doing so will result in overfitting. The `kombine` sampling algorithm uses the Bayesian information criterion (BIC) to select the number of centroids to use in its kernel-density estimation model. The BIC is a commonly used method in model selection that attempts to resolve the problem of overfitting by introducing a penalty term for the number of parameters in the model. For determining the number of centroids to use the `kombine` sampling algorithm uses

$$\text{BIC} = \log(p_{\max}(\{d_i(t)\}|\vec{\theta})) - \frac{d_m}{2} \log(N), \quad (4.73)$$

where d_m is the number of dimensions (or centroids) of the kernel-density estimation model, $p_{\max}(\{d_i(t)\}|\vec{\theta})$ is the maximized likelihood function of the model, and N is the total number of Markov chains being fit.

The proposal distribution is then estimated by combining the individual kernel-density estimator from each mean, weighted by the fraction of samples assigned to each cluster. This proposal distribution is used to draw new proposals and to evaluate the Metropolis-Hastings acceptance condition.

4.7 The state of parameter estimation pipelines in Advanced LIGO’s first and second observing runs

In Advanced LIGO’s first and second observing runs, the `LALInference` pipeline [47, 139] was used to publish the measured parameters of observed binary black hole mergers [110, 140, 75]. `PyCBC Inference` has not been used to publish parameter estimates of observations in Advanced LIGO’s first or second observing runs. At a high-level abstraction, both `LALInference` and `PyCBC Inference` use the same concepts to estimate the parameters of binary black hole merger. Both pipelines provide a thin layer of code that allows the choice from multiple sampling algorithms to compute the posterior probability density functions. The likelihood function from Section 4.2 and the choice of priors in Section 4.3 are implemented in `LALInference` and `PyCBC Inference`, and both pipelines provide choices of ensemble Markov-chain Monte Carlo sampling algorithms. In this section, we describe some techniques implemented in `LALInference` which are used in the published Advanced LIGO parameter estimation results but are not included in the `PyCBC Inference` analyses presented in this dissertation. This includes: nested sampling, cycling through different proposal distributions, and marginalizing over calibration uncertainties.

There are other methods aside from ensemble Markov-chain Monte Carlo sampling algorithms to estimate the posterior probability density function. Nested sampling [141] is a Monte Carlo method to efficiently calculate the evidence $p(d_i(t)|H)$. Nested sampling has the benefit that the the posterior probability density function for model parameters can be estimated from the results of the analysis. The results from Markov-chain Monte Carlo sampling algorithms and nested sampling algorithms should agree, and both stochastic sampling methods have been presented in the parameter estimation results from Advanced LIGO’s first observing run [142]. `LALInference` has a couple choices of nested sampling algorithms described in Refs. [47, 143, 144, 145].

If the likelihood has isolated modes, then a Markov chain must take improbable draws from the proposal distribution across regions with a low acceptance probability. One optimization for multi-modal parameter spaces which is used with ensemble Markov-chain Monte Carlo sampling algorithms is the parallel tempering technique described in Section 4.5. There is another optimization for parameters which are strongly correlated, if the proposal distributions are constructed along these correlations [47]. `LALInference` includes choices of proposal distributions to more efficiently sample the parameter space by taking into account these correlations that shape the structure of the likelihood function. The set of proposal distributions in `LALInference`, which is listed in Ref. [47], includes distributions that are specific to the binary black hole merger parameters. At the beginning of an analysis, the set of proposal distributions are randomly ordered, and as the Markov chains advance `LALInference` cycles through the proposal distributions. A single method for constructing the proposal distribution is used in each iteration. This is referred to as “jump proposal cycling” and `LALInference` provides jump proposal cycling for Markov-chain Monte Carlo and nested sampling algorithms. In contrast, `PyCBC Inference` uses the same method for constructing the proposal distribution for all iterations in a single analysis.

In Chapter 3 we assessed the impact of calibration errors on the search. Calibration errors will affect the parameter estimation analyses as well. `LALInference` has the option to marginalize over calibration errors; however, `LALInference` does not use the physical model of the calibration errors described in Chapter 3. In `LALInference`, the calibration errors are modeled in the frequency domain as [146]

$$\tilde{h}_m(f) = [1 + \delta A(f)] \tilde{h}_t(f) e^{i\delta\phi(f)} \quad (4.74)$$

$$= [1 + \delta A(f)] \tilde{h}(f) \frac{2 + i\delta\phi(f)}{2 - i\delta\phi(f)}, \quad (4.75)$$

where $\delta A(f)$ is the change in amplitude due to calibration errors, $\delta\phi(f)$ is the change in phase due to calibration errors, $\tilde{h}_t(f)$ is the gravitational-wave strain waveform without errors, and $\tilde{h}_m(f)$ is the gravitational-wave strain waveform with errors. In Equation 4.74, the Taylor expansion of the phase change to third order is

$$e^{i\delta\phi(f)} = 1 + i\delta\phi(f) - \frac{(\delta\phi(f))^2}{2} + \mathcal{O}((\delta\phi(f))^3), \quad (4.76)$$

and since the Taylor expansion

$$\frac{2 + i\delta\phi(f)}{2 - i\delta\phi(f)} = 1 + i\delta\phi(f) - \frac{(\delta\phi(f))^2}{2} + \mathcal{O}((\delta\phi(f))^3), \quad (4.77)$$

is equivalent to third order, if we assume the calibration errors are small then $(2 + i\delta\phi(f))/(2 - i\delta\phi(f))$ may substituted into Equation 4.74. This is a more efficient implementation since it includes only algebraic expressions [146]. `LALInference` uses a spline model to evaluate the calibration errors in $\delta A(f)$ and $\delta\phi(f)$. The change in amplitude is

$$\delta A(f) = p_s(f, \{f_i, \delta A_i\}), \quad (4.78)$$

and the change in phase is

$$\delta\psi(f) = p_s(f, \{f_i, \delta\psi_i\}), \quad (4.79)$$

and where $p_s(f, \{f_i, \delta A_i\})$ and $p_s(f, \{f_i, \delta\psi_i\})$ represent cubic spline polynomials of N nodes $\{f_i, \delta A_i, \delta\psi_i, 1 < i < N\}$, f_i are the nodes of the polynomial in frequency, and δA_i and $\delta\psi_i$ are the values of the spline at those nodes. Each detector will have an independent set of calibration parameters and the total number of calibration parameters sampled for a single detector is $2N$ (one for each δA_i and $\delta\psi_i$).

4.8 Parameter estimation of binary black hole mergers from Advanced LIGO's first observing run

In this section, we use PyCBC Inference to infer the source parameters of GW150914, GW151226, and LVT151012 assuming that the signals each originate from a compact-object binary coalescence as described by general relativity. This analysis uses the `IMRPhenomPv2` effective precessing spin waveform model [44, 45]. Our choices of priors and data selection for each event is chosen to match the choices in Ref. [75] which presents the parameter estimation results of the binary black hole mergers observed in Advanced LIGO's first observing run. We analyze the frequency band between 20 Hz and 2048 Hz from 8 s of data around the time of GW150914 and GW151226, and 24 s of data around LVT151012. We choose uniform priors in the coalescence time ± 2 s around each event and spin magnitude. We use isotropic priors for sky position and orientations, and we assume a uniform distribution of sources in the Universe.

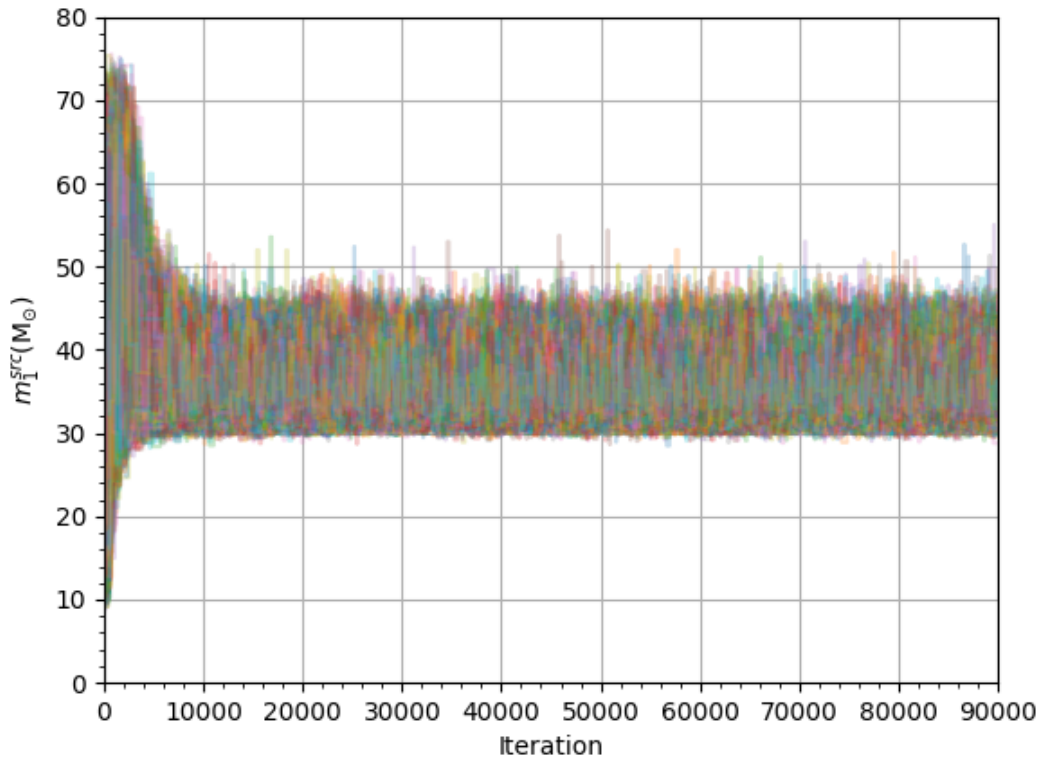


Figure 37 : An ensemble of 5,000 Markov chains while estimating the source-frame component mass of the larger black hole m_1^{src} . Initially the Markov chains are distributed according to the prior and as the Markov chains advance they converge.

Astrophysical parameters for the three events obtained using the `kombine` sampling algorithm with an ensemble of 5,000 Markov chains are included in Table 5.

In Figure 37 we show a demonstration of an ensemble of 5,000 Markov chains converging while estimating the source-frame primary mass m_1^{src} of GW150914. The position of the Markov chains are drawn from the prior, and eventually they converge as the sampling algorithm iteratively advances the ensemble of Markov chains. In Figure 38 shows the Gelman-Rubin convergence statistic for this ensemble which shows convergences as the ensemble advances as well. In this section, we only select independent samples from the last iteration of each Markov chain.

Posterior probability density functions of the mass parameters are shown in Figs. 39 and 40. The component masses for each event are constrained above the maximum

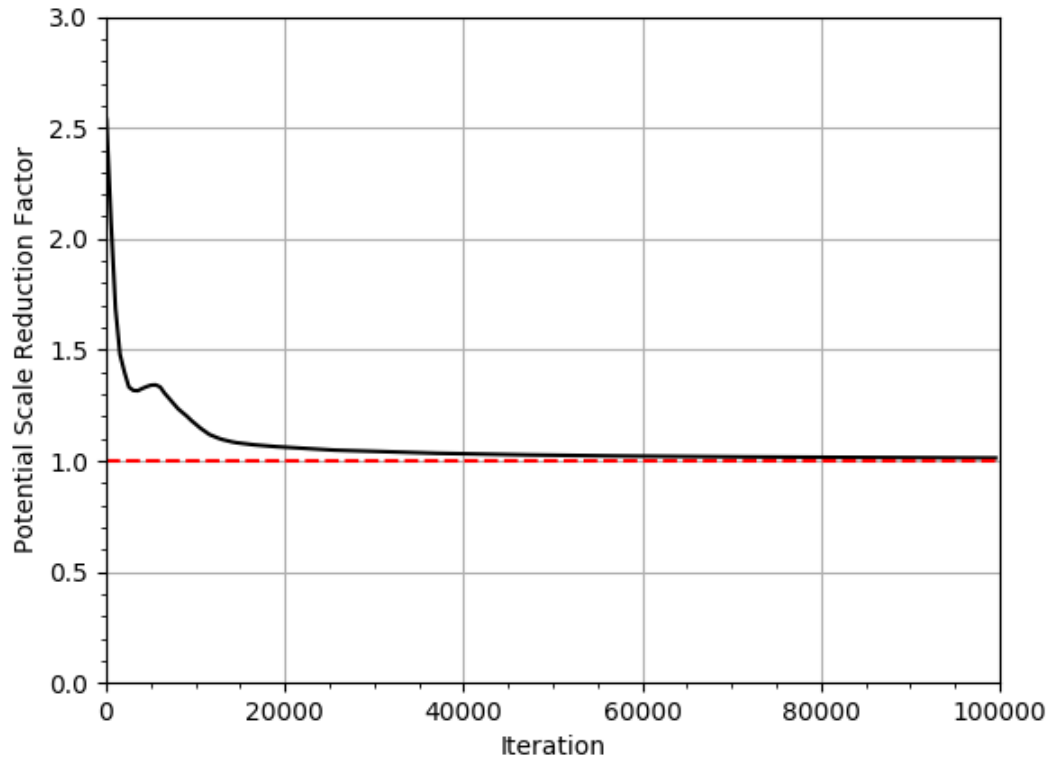


Figure 38 : The Gelman-Rubin convergence statistic (Point Scale Reduction Factor) for an ensemble of 5,000 Markov chains while estimating the source-frame component mass of the larger black hole m_1^{src} . The red dashed line corresponds to 1 which indicates the ensemble has converged.

mass of a neutron star masses which is $\sim 3 M_\odot$ [147, 148]. The black holes observed in Advanced LIGO’s first observing run cover a mass range between $8.4_{-1.86}^{+1.52} M_\odot$ and $35.0_{-3.0}^{+5.1} M_\odot$. The component masses inferred from the Advanced LIGO events are in a region of the mass space ($>25 M_\odot$) that has previously not been explored by stellar-mass black holes measured through X-ray observations [52, 149, 150]. Our observations extend beyond the X-ray observations into an area of the mass distribution of black holes not previously observed.

For the range of binary black hole masses observed we expect qualitative differences in the 90% credible interval contours of the posterior probability density functions of in the m_1^{src} and m_2^{src} plane. Since higher mass binaries merge at lower frequencies, then the ringdown has a larger contribution to the signal-to-noise ratio.

The inspiral predominantly constrains the chirp mass, and the ringdown is predominantly constrains the total mass. In Figure 39 we see that the posterior probability density functions for GW151226 and LVT15102 follow contours of constant chirp mass, and GW150914 follows a constant total mass contour.

We can only weakly constrain the component spins. The effects of the components' spins on the waveform are weaker in comparison to the masses. We are able to constrain the spin of the primary black hole more easily, since the spin of the primary black hole has a greater impact than the spin of the secondary black hole on the waveform during the inspiral. Figure 40 shows the posterior probability density function of χ_{eff} for each event. We can rule out spin configurations where both component spins are large and aligned, or large and anti-aligned to the angular momentum of the binary. We are able to rule out these configurations since all three events are consistent with $|\chi_{\text{eff}}| < 0.28$. Component spins misaligned with the orbital angular momentum cause orbital precession, therefore in Figure 42, we show the posterior probability density functions of the spin magnitude and polar spin angle. The inferred spins are similar to the prior probability density functions and therefore we cannot see indications of precession. Either the binaries do not have much precession or the orientation of the binary is either face-on or face-away (when the angular momentum is parallel or anti-parallel to the line of sight with respect to the Earth) with respect to the Earth which makes observing the effects of precession difficult; however, the inclination is only weakly constrained as well.

Information about the distance and the inclination of the binary is also encoded into the waveform. The inclination is weakly constrained; however, the posterior probability density functions do have maximums near face-on or face-off orientations. These orientations produces larger gravitational-wave amplitude than inclinations that are edge-on (when the angular momentum is perpendicular to the line of sight with respect to the Earth) which corresponds to further distances. In Figure 41 we show the posterior probability density function of the distance. We see that the binary black hole mergers observed by Advanced LIGO have distances constrained to less than 2 Gpc.

Since the sky location is predominantly determined by triangulating the arrival times in the detector, a two-detector network has a characteristic ring-shaped posterior probability density function. An astrophysical signal will also have a phase

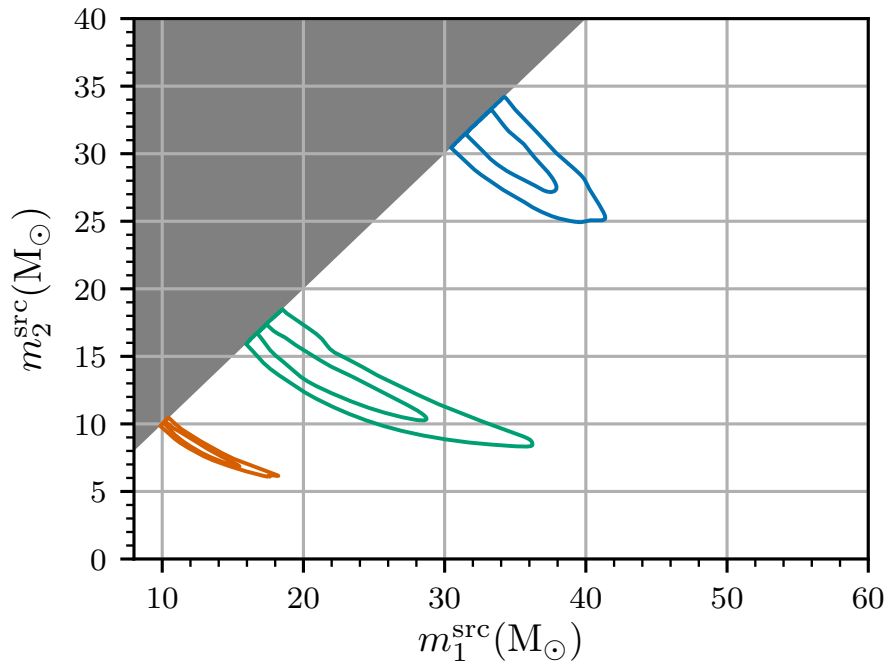


Figure 39 : The posterior probability density function of the source-frame primary mass m_1^{src} and secondary mass m_2^{src} for GW150914 (blue), GW151226 (orange), and LVT151012 (green).

difference because of the orientation of the detectors with respect to each other which factors into the sky localization as well. Adding more detectors improves the sky localization. The sky localizations of GW150914, GW151226, and LVT151012 are shown in Figures 43, 44, and 45 respectively.

4.9 Conclusions

We have presented PyCBC Inference which is a parameter estimation analysis for compact-object mergers and we demonstrated the methods using the three candidate events from Advanced LIGO's first observing run. We find that the black hole masses range between $8.4_{-1.86}^{+1.52} M_\odot$ and $35.0_{-3.0}^{+5.1} M_\odot$ which encompasses a previously unobserved region of the black hole mass distribution. The spins of the black holes are weakly constrained but we can rule out large aligned or large anti-aligned spin configurations. Our results are in general agreement with the published results for the parameters in Ref. [2]. Future development work will focus on more

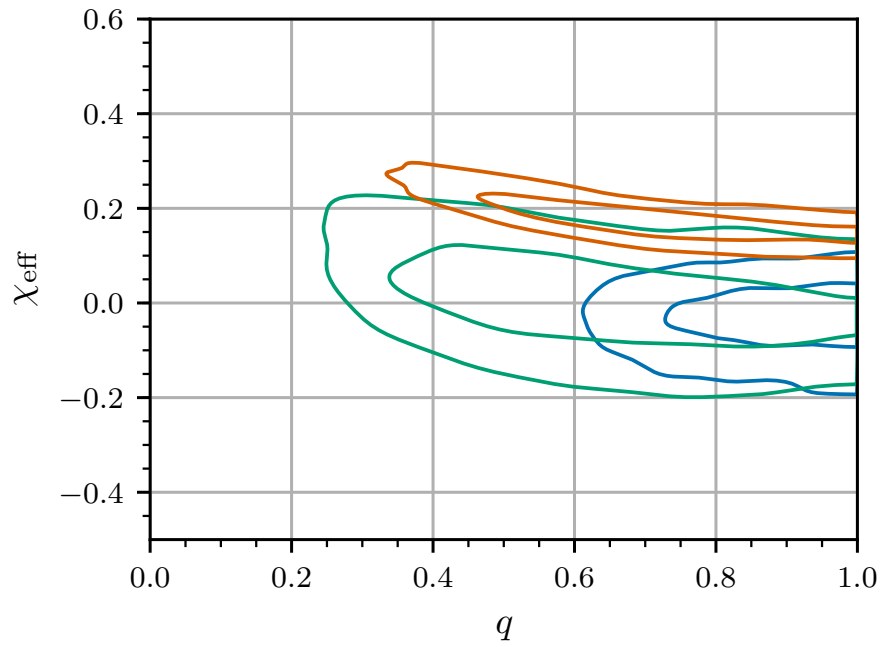


Figure 40 : the posterior probability density function of mass ratio $q = m_1/m_2$ where $m_1 > m_2$, and effective spin χ_{eff} for GW150914 (blue), GW151226 (orange), and LVT151012 (green).

detailed comparisons between the sampling methods between PyCBC Inference and the LALInference parameter estimation analysis used in Ref. [2].

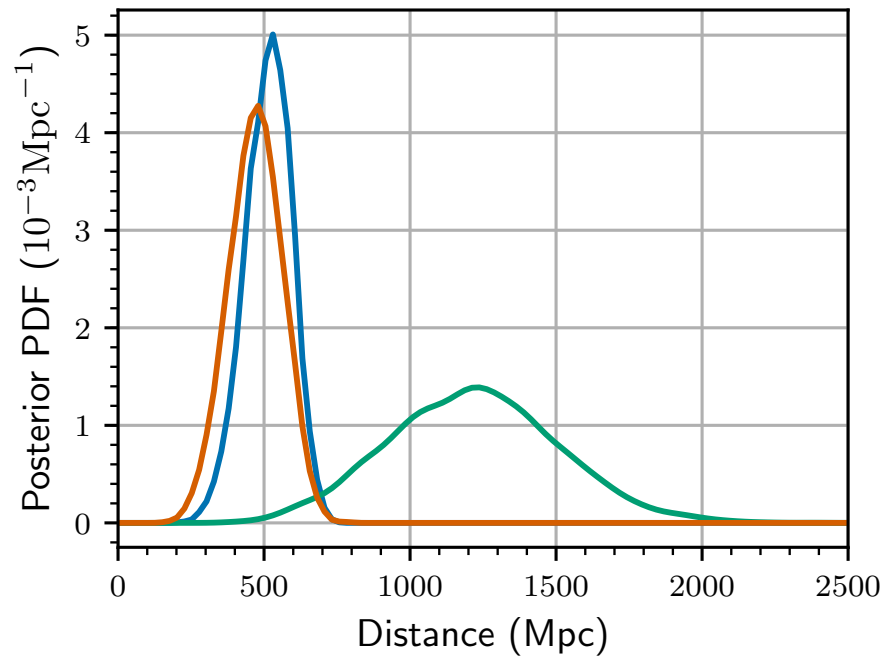


Figure 41 : The posterior probability density function (PDF) of distance for GW150914 (blue), GW151226 (orange), and LVT151012 (green).

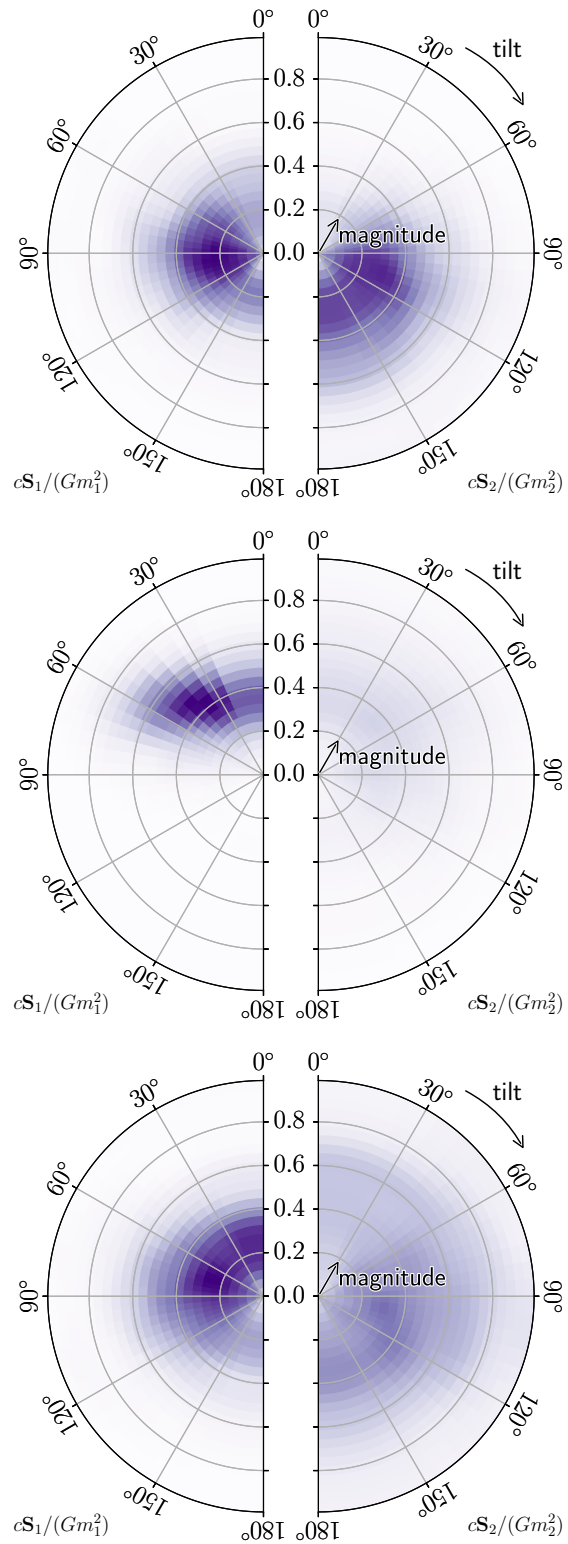


Figure 42 : The posterior probability density functions of the dimensionless spin magnitude as a function of the polar spin angle. The first row shows GW150914, the second row shows GW151226, and the third row shows LVT151012.

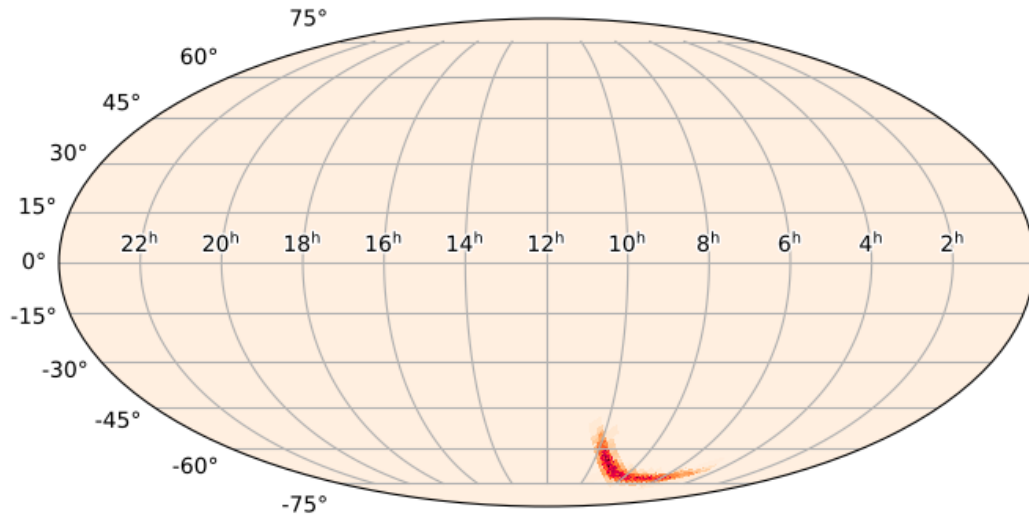


Figure 43 : The sky localization of GW150914 in celestial coordinates.

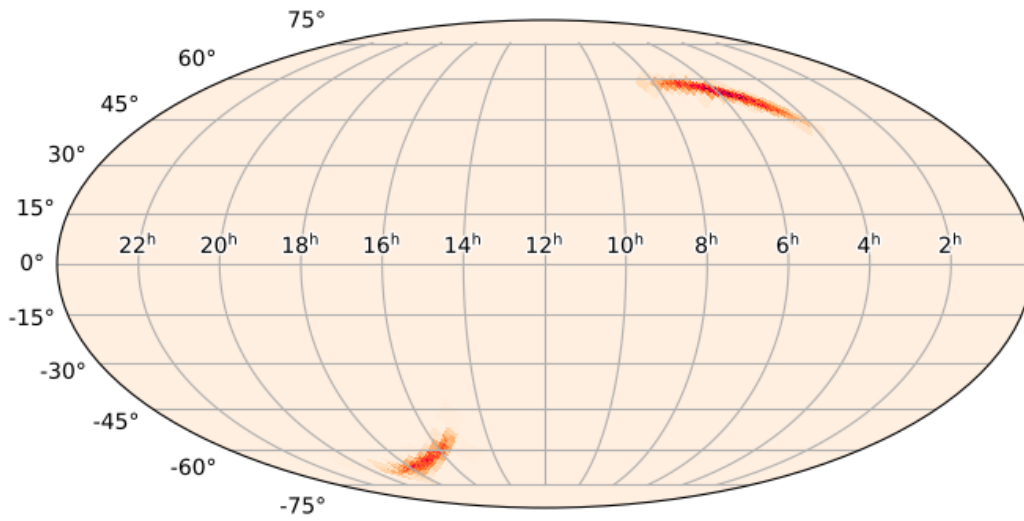


Figure 44 : The sky localization of GW151226 in celestial coordinates.

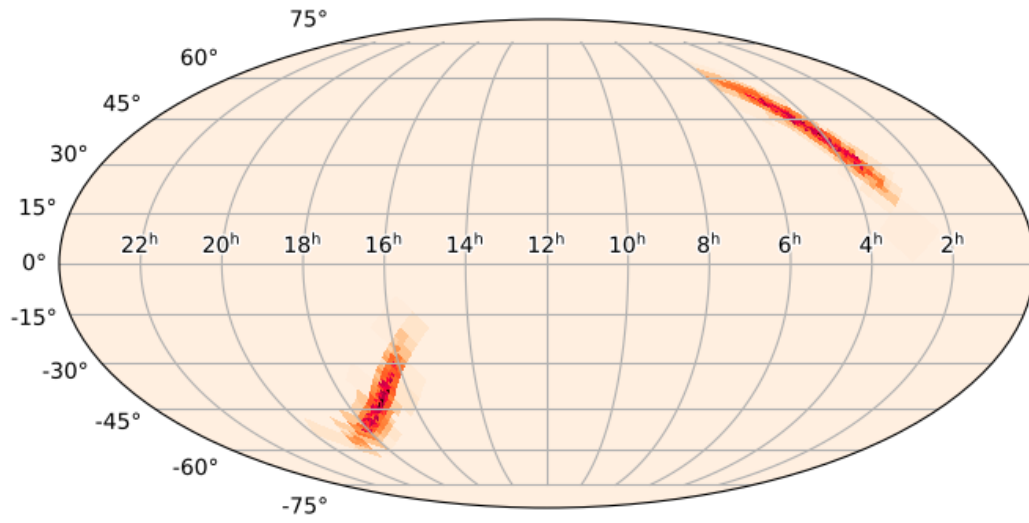


Figure 45 : The sky localization of LVT151012 in celestial coordinates.

Parameter (Units)	Symbol	90% Credible Interval		
		GW150914	GW151226	LVT151012
Source-frame primary mass (M_{\odot})	m_1^{src}	$35.0_{-3.0}^{+5.1}$	$12.3_{-2.0}^{+4.2}$	$21.5.3_{-4.3}^{+8.7}$
Source-frame secondary mass (M_{\odot})	m_2^{src}	$29.7_{-4.0}^{+2.9}$	$8.4_{-1.86}^{+1.52}$	$13.5_{-3.8}^{+3.4}$
Source-frame total mass (M_{\odot})	M^{src}	$64.8_{-3.1}^{+3.3}$	$20.8_{-0.8}^{+2.3}$	$35.4_{-3.0}^{+5.2}$
Source-frame chirp mass (M_{\odot})	\mathcal{M}^{src}	$28.0_{-1.3}^{+1.4}$	$8.83_{-0.22}^{+0.26}$	$14.7_{-1.0}^{+1.2}$
Detector-frame primary mass (M_{\odot})	m_1^{det}	$38.8_{-3.3}^{+5.5}$	$13.5_{-2.1}^{+4.6}$	$26.5_{-5.1}^{+10.4}$
Detector-frame secondary mass (M_{\odot})	m_2^{det}	$32.8_{-4.5}^{+3.2}$	$9.25_{-2.05}^{+1.68}$	$16.7_{-4.7}^{+4.0}$
Luminosity distance (Mpc)	d_L	521_{-139}^{+111}	477_{-154}^{+145}	$1.22_{-0.47}^{+0.49} \times 10^3$
Redshift	z	$0.108_{-0.027}^{+0.021}$	$0.100_{-0.031}^{+0.028}$	$0.0234_{-0.083}^{+0.081}$
Effective spin	χ_{eff}	$-0.03_{-0.12}^{+0.11}$	$0.18_{-0.06}^{+0.10}$	$0.01_{-0.17}^{+0.18}$

Table 5 : Table of inferred astrophysical parameters using PyCBC Inference for GW150914, GW151226, and LVT151012. Muplitply the detector-frame parameters by $(1 + z)$ to convert to the source-frame, where z is redshift.

Chapter 5

The capability of gravitational-wave observatories to probe the black hole mass gap due to pair-instability supernovae

5.1 Introduction

It has been known for some time that stars with core masses greater than about $30 M_{\odot}$ become dynamically unstable due to electron-positron pair production [151, 152, 153, 154]. The conversion of energy to rest mass, rather than thermal energy alters the equation of state of the core and hydrostatic equilibrium cannot be maintained. If a sufficiently large amount of the core is in the pair formation regime (adiabatic index $\Gamma_1 < 4/3$), then the core will become dynamically unstable. The resulting explosive oxygen burning can create pulses that drive off the outer layers of the star before eventual core collapse, called pulsation-pair instability supernovae (PPISN), or destroy the star entirely before a black hole can be formed, called pair-instability supernova (PISN).

Ref. [155] has explored the compact-object remnant masses of black holes in PPISN and PISN using the KEPLER code and claimed that no black holes between $52 M_{\odot}$ and $133 M_{\odot}$ are expected from stellar evolution in close binaries. Since no remnant of the massive star is formed, then there is an expected gap in the black hole

mass distribution between $52 M_{\odot}$ and $133 M_{\odot}$ [156, 24, 157].

All gravitational-wave signals from binary black hole mergers detected by Advanced LIGO to date have been produced from binary black hole mergers below the PISN mass gap. GW150914 and GW151226 were produced from binary black holes with component masses $36 M_{\odot}$ and $29 M_{\odot}$, and $14 M_{\odot}$ and $8 M_{\odot}$ respectively [76, 77]. A third possible signal, LVT151012, was also identified with component masses $23 M_{\odot}$ and $13 M_{\odot}$ with a lower significance [158]. Over the next three years, the Advanced LIGO and Advanced Virgo observatories will be commissioned to design sensitivity and signals may be expected daily [6]. In this era of gravitational-wave astronomy, the population of detected sources could be used to resolve the black hole mass distribution and to determine the existence of the PISN mass gap.

In this chapter, we assess the capability of an Advanced LIGO and Advanced Virgo network at design sensitivity to unambiguously constrain the mass of a black hole between $52 M_{\odot}$ and $133 M_{\odot}$, and their ability to observe the PISN mass gap. Section 5.2 describes the analysis of a population of binary black hole mergers that encompasses the PISN mass gap. Sec. 5.3 details the recovery of the component masses. Finally, in Sec. 5.4 we summarize the capability of the Advanced LIGO and Advanced Virgo network to probe the PISN mass gap.

5.2 Methods

Astrophysical properties of binary black hole mergers in Advanced LIGO data have been constrained using Bayesian inference [47, 76, 77]. We use the PyCBC Inference parameter estimation analysis described in Chapter 4 to measure the source component masses for a population of simulated binary black hole mergers. Here, we use the `kombine` sampling algorithm to sample the posterior probability density function.

The simulated signals were generated with the `SEOBNRv4` waveform model [159] which parameterizes binary black hole mergers by the masses, spins aligned with the angular momentum of the binary, distance, sky location, and orientation of the binary. We use the `SEOBNRv4_ROM` reduced-order waveform model [159] to generate the waveform in the likelihood function. This waveform model belongs to one of the waveform families that has been used to measure the parameters of GW150914 and GW151226 [76, 77].

Above 10 Hz, this mass region has waveforms that have time durations from a fraction of a second up to ~ 10 s. Using more time series data from the detectors in the likelihood function increases the computational time of the analysis. Therefore, we split the region into two mass regions based on the time duration of the waveforms. The two regions are divided based on the source-frame chirp mass \mathcal{M}^{src} : $25 M_{\odot} \leq \mathcal{M}^{\text{src}} \leq 52 M_{\odot}$ and $52 M_{\odot} < \mathcal{M}^{\text{src}} < 133 M_{\odot}$. Our likelihood function uses 16 s of data between 10 Hz and 2048 Hz around the time of the simulated signal for binaries where $\mathcal{M}^{\text{src}} \leq 52 M_{\odot}$. These systems are recovered with a uniform prior in component mass bounded by the detector-frame chirp mass $\mathcal{M}^{\text{det}} > 20$, mass ratio $1 < q < 10$ where $m_1^{\text{src}} > m_2^{\text{src}}$, and detector-frame total mass $M_T^{\text{det}} < 500 M_{\odot}$. Since higher mass systems have shorter waveforms we use 8 s of data between 10 Hz and 2048 Hz for the analysis of simulated signals where $\mathcal{M}^{\text{src}} > 52 M_{\odot}$. These systems are recovered with a uniform prior in component mass bounded by $\mathcal{M}^{\text{src}} > 35$, $1 < q < 10$, and $M_T^{\text{det}} < 500 M_{\odot}$. All simulated signals use uniform priors for the coalescence time ± 0.2 s around the time of the simulated signal, component spins aligned with the angular momentum of the binary between -0.9895 and 0.9895, and isotropic priors in sky position and orientation.

The simulated signals are coherently added to a gravitational-wave strain data from a gravitational-wave observatory network comprised of three interferometers: two Advanced LIGO and one Advanced Virgo observatory. The observatories' data were simulated with Gaussian noise recolored using the design amplitude spectral densities [6]. Figure 46 shows the design amplitude spectral densities.

The entire population of simulated signals is shown in Fig. 47. We generate simulated signals with a source-frame chirp mass \mathcal{M}^{src} between $25 M_{\odot}$ and $113 M_{\odot}$, and $1 < q < 8$. We generate a total of 2,407 simulated signals distributed isotropically in sky position and orientation. Black holes formed from metal poor massive stars through the pulsation pair-instability supernova are expected to have low spins < 0.15 ; however, black holes can be produced with spins up to 0.7 from more metal-rich massive stars which experience chemically homogeneous evolution [156]. We generate all simulated signals with component spins aligned with the angular momentum of the binary drawn from a uniform distribution between ± 0.7 . In Fig. 47, we show the effective spin χ_{eff} of the population of simulated signals. The simulated signals were drawn from several distributions of mass and distance.

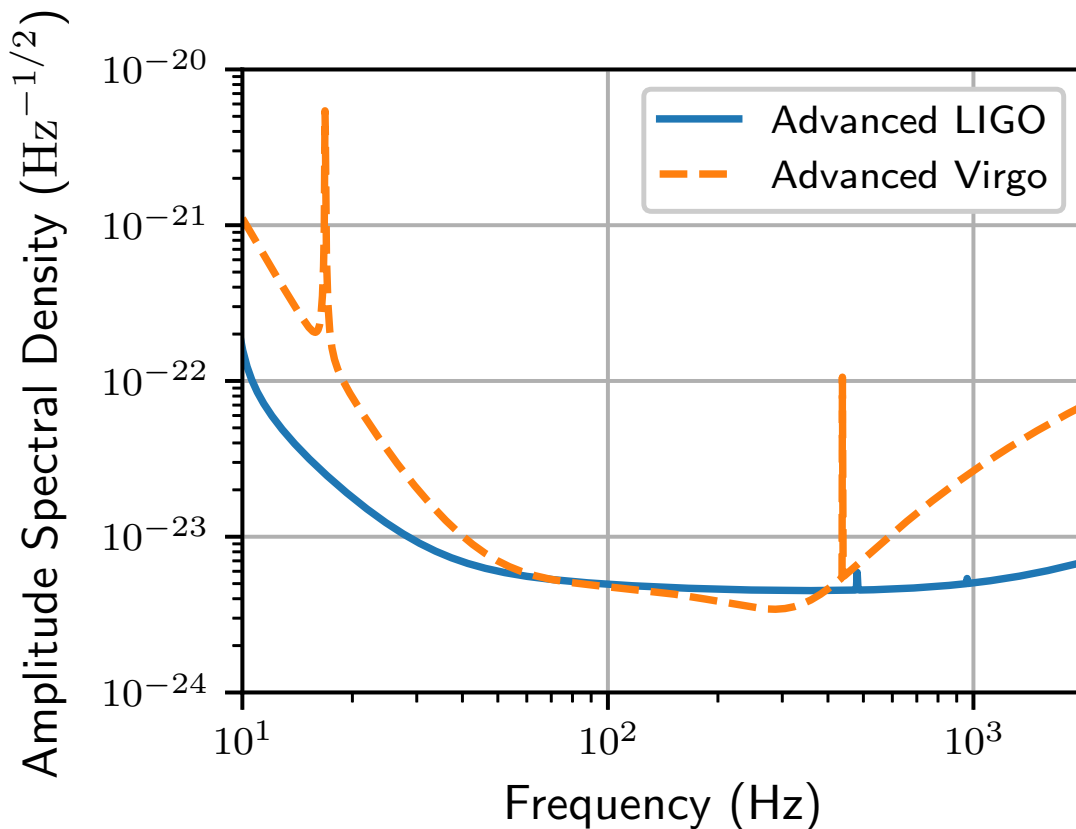


Figure 46 : The amplitude spectral density of Advanced LIGO and Advanced Virgo at design sensitivity [6].

We analyze 743 simulated signals whose distance is distributed uniformly in the logarithm. The distance scales the network signal-to-noise (SNR) of the simulated signals; the network SNR distribution for this sub-population of simulated signals is shown in Figure 48. In this sub-population there are: 100 simulated signals with $25 M_{\odot} \leq \mathcal{M}^{\text{src}} < 52 M_{\odot}$, 112 simulated signals with $52 M_{\odot} \leq \mathcal{M}^{\text{src}} < 113 M_{\odot}$, 198 signals with $m_1^{\text{src}} = 52 M_{\odot}$ and $25 M_{\odot} \leq \mathcal{M}^{\text{src}} < 52 M_{\odot}$, 134 signals with $m_1^{\text{src}} = 133 M_{\odot}$ and $25 M_{\odot} \leq \mathcal{M}^{\text{src}} < 52 M_{\odot}$, and 199 signals with $m_1^{\text{src}} = 133 M_{\odot}$ and $52 M_{\odot} \leq \mathcal{M}^{\text{src}} < 113 M_{\odot}$. These simulated signals are recovered with a distance prior that assumed a uniform volume distribution of sources in the Universe; this corresponds to a prior probability density function $p(d_L) \sim d_L^2$.

We analyze 832 simulated signals whose network SNR is distributed around 29.

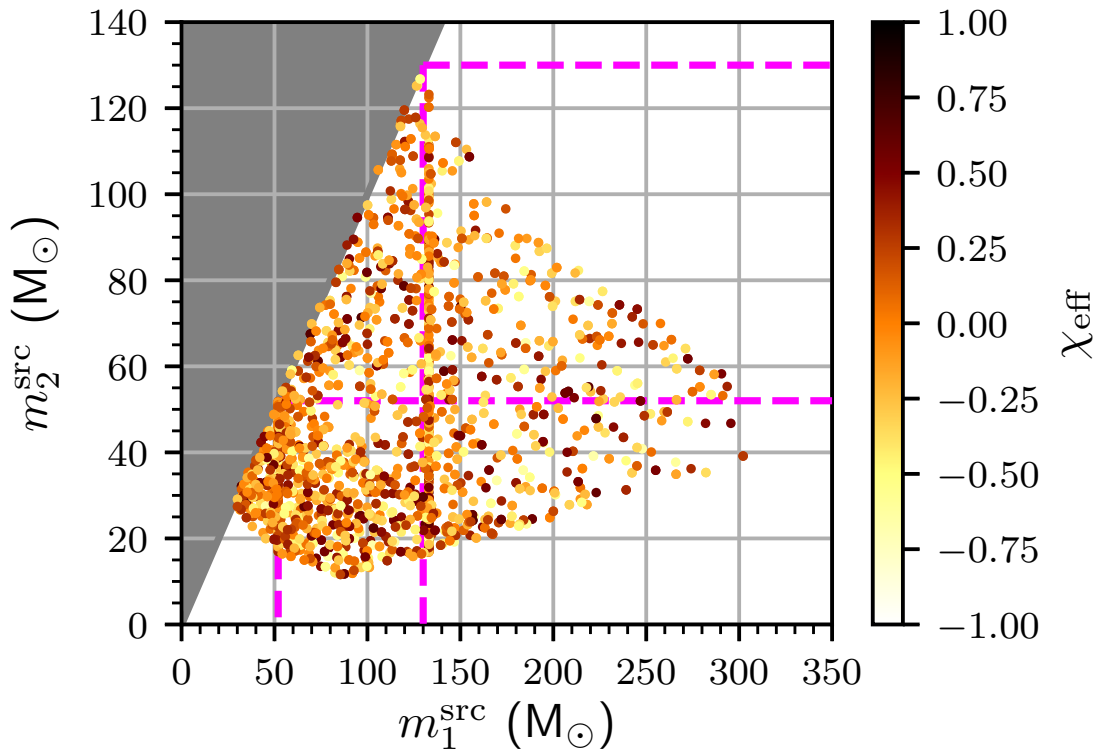


Figure 47 : The component masses m_1^{src} and m_2^{src} of all 2,407 simulated signals colored by the effective spin χ_{eff} . The dashed magenta lines represent the PISN mass gap between $52 M_\odot$ and $113 M_\odot$.

The network SNR distribution of this sub-population is shown in Figure 48. This sub-population of 832 simulated signals are drawn from two mass regions: 431 simulated signals with component masses uniform between $25 M_\odot \leq \mathcal{M}^{\text{src}} < 52 M_\odot$, and 401 simulated signals with component masses uniform between $52 M_\odot \leq \mathcal{M}^{\text{src}} < 113 M_\odot$. We create another sub-population of 832 simulated signals by scaling each simulated signal's distance by a factor of 2. These two sub-populations contain 1,664 simulated signals which we recover with a uniform prior for distance.

5.3 Results

In this section, we present the 90% credible interval of the component masses obtained with PyCBC Inference from the 2,407 simulated signals described in Sec. 5.2.

Figures 49 and 50 show the 90% credible intervals of m_1^{src} and m_2^{src} versus the injected mass. In Figures 49 and 50, we see that the width of the 90% credible intervals of m_1^{src} and m_2^{src} from simulated signals in the PISN mass gap (m_i^{src} between $52 M_\odot$ and $133 M_\odot$) can be smaller than $81 M_\odot$ which is the width of the PISN mass gap. Therefore, it is possible to unambiguously observe a binary black hole inside the PISN mass gap with the Advanced LIGO and Advanced Virgo network.

If the widths of the 90% credible intervals of m_1^{src} are sufficiently small, then the measurements of the component masses should show a distinct gap for a population of binaries with no black hole masses in the PISN mass gap. The width of the 90% credible intervals shrink as a function of network SNR as seen in Figure 49. Therefore, we show in Figure 51 the 90% credible interval of m_1^{src} for simulated signals generated with m_1^{src} outside the PISN mass gap boundaries versus the network SNR. At network SNR $\lesssim 27.5$ we see that the 90% credible intervals of m_1^{src} from the population can cover the full range of the PISN mass gap. At network SNR > 27.5 , we are able to resolve a distinct gap where the 90% credible intervals from simulated signals generated with $m_1^{\text{src}} > 133 M_\odot$ do not overlap with the 90% credible intervals from simulated signals generated with $m_1^{\text{src}} < 52 M_\odot$. This gap widens as the network SNR increases. This suggests that it may be possible to resolve the mass gap with a population of binary black holes that have a network SNR > 27.5 . We focus only on m_1^{src} since we did not simulate any signals with m_2^{src} above the PISN mass gap.

The Advanced LIGO and Advanced Virgo network is capable of distinguishing m_1^{src} inside the PISN mass gap; however, we caution against claiming that a single detection challenges the existence of the PISN mass gap if m_1^{src} does not fall in the region identified in Figure 51. Since we used several different distance distributions for priors and generating our population of simulated signals, we expect our analysis to have a lower efficiency and provide more conservative results than if we have generated and recovered with the same distributions. We found our analysis was able to recover the simulated signals' m_1^{src} within the 90% credible interval for 81% of the simulated signals, m_2^{src} within the 90% credible interval for 84% of the simulated signals, and both m_1^{src} and m_2^{src} within the 90% credible interval for 69% of the simulated signals. In particular, simulated signals with black hole masses near the PISN mass gap boundaries could incorrectly be identified as a source from within the PISN mass gap; we found 5% of the simulated signals were incorrectly identified as a

source from within the PISN mass gap. The simulated signals with either m_1^{src} or m_2^{src} not recovered in the 90% credible interval are colored gray in Figures 49, 50, and 51. We see from Figure 51 that our ability to constrain the network SNR at which we can claim a detection unambiguously inside the PISN mass gap is predominantly limited due to this subset of the simulated signals.

The source-frame masses are strongly influenced by uncertainties and errors from inferring the detector-frame masses and redshift since $m_i^{\text{src}} = m_i^{\text{det}}/(1+z)$ where z is the redshift. Recovering a larger redshift underestimates the source-frame mass since $m_i^{\text{src}} \sim 1/(1+z)$. We found most of these simulated signals have recovered a larger redshift. Figure 52 shows the 90% credible interval of redshift versus the injected redshift only for the simulated signals where either the m_1^{src} or m_2^{src} used to generate the simulated signal was not contained within the 90% credible interval.

We can find the regions of the parameter space most able to distinguish that a black hole is in the PISN mass gap, if there is a formation channel that produces black holes with masses between $52 M_\odot$ and $133 M_\odot$. Figures 53 and 54 show the fraction of simulated signals across the mass space where the 90% credible interval of m_1^{src} is constrained unambiguously inside the PISN mass gap. We repeat this procedure for m_2^{src} . Figures 55 and 56 show the fraction of simulated signals across the mass space where the 90% credible interval of m_2^{src} is constrained unambiguously inside the PISN mass gap.

5.4 Conclusions

In this chapter, we explored the capability of the Advanced LIGO and Advanced Virgo network to resolve the PISN mass gap between $52 M_\odot$ and $133 M_\odot$. We measured the component masses for 2,407 simulated, aligned-spin binary black holes with \mathcal{M}^{src} between $25 M_\odot$ and $113 M_\odot$. We find that the Advanced LIGO and Advanced Virgo network is able to unambiguously distinguish black hole masses inside the PISN mass gap. We find that a population of signals with network SNR >27.5 may be able to resolve the mass gap, and a signal observed in this mass region above network SNR 27.5 could challenge the existence of PISN mass gap. Finally, we present the mass regions our analysis was most able to constrain at least one black hole mass between $52 M_\odot$ and $133 M_\odot$.

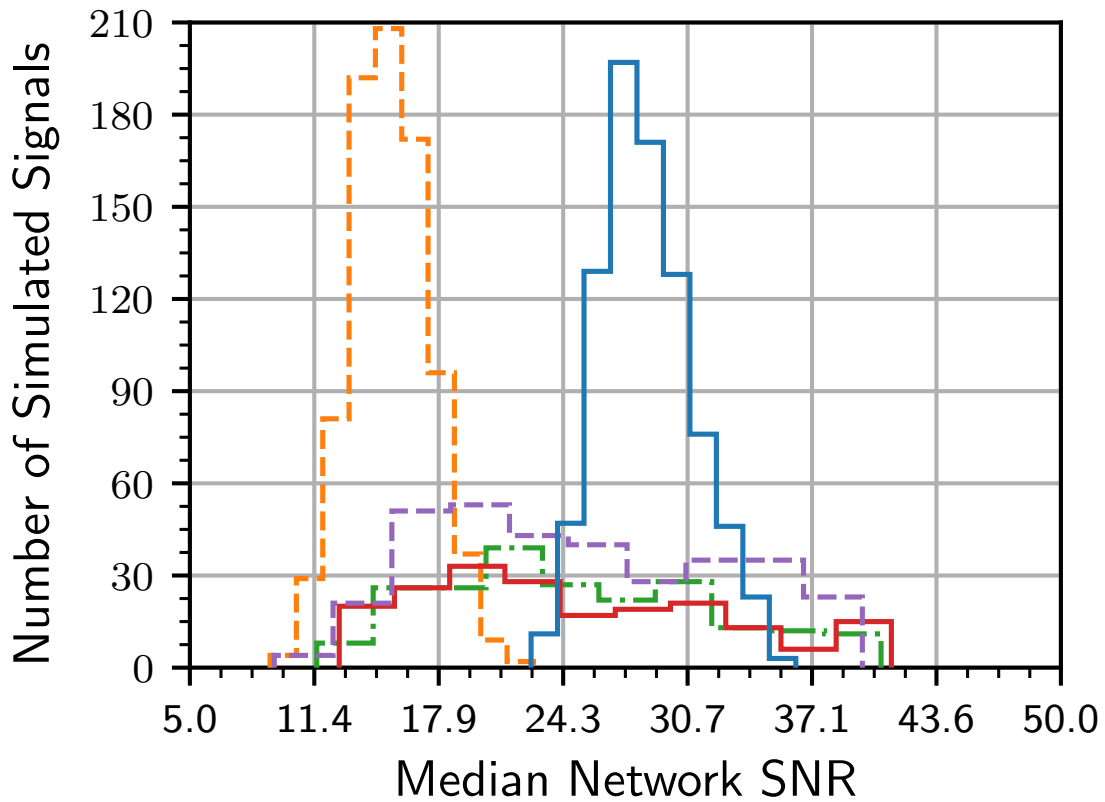


Figure 48 : Histogram of the simulated signals' median network signal-to-noise ratio (SNR) from the posterior distributions. The solid red histogram represents the simulated signals with their distance distributed uniformly in the logarithm. The dashed purple histogram represents the simulated signals with $m_1 = 52 M_\odot$. The dashed-dotted green histogram represents the simulated signals with $m_1 = 133 M_\odot$. The solid blue histogram represents the 832 simulated signals with their network SNR distributed around 29. The dashed orange histogram represents the 832 simulated signals from the blue histogram with their distance scaled by a factor of 2.

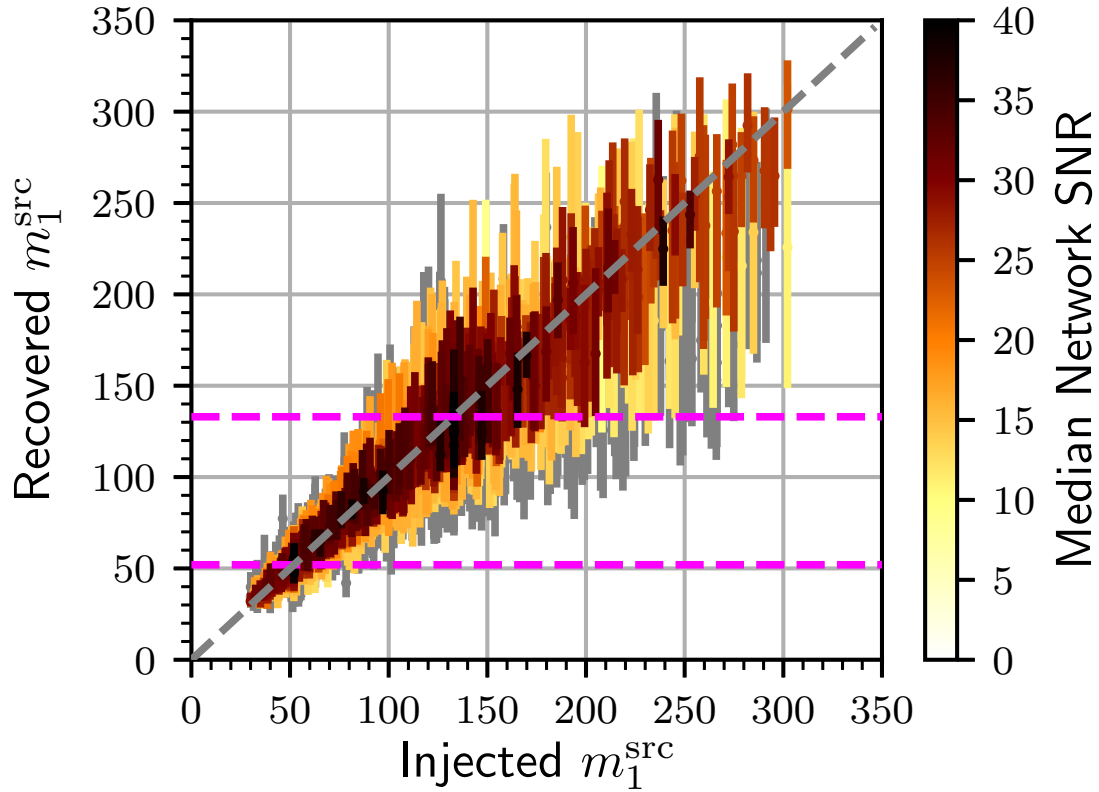


Figure 49 : The 90% credible interval of the source-frame primary mass m_1^{src} versus the m_1^{src} used to generate the simulated signal. The dashed magenta lines represent the PISN mass gap between $52 M_\odot$ and $113 M_\odot$. The dashed gray line represent the 1:1 ratio which is an exact match. Simulated signals with either m_1^{src} or m_2^{src} not recovered in the 90% credible interval are colored gray.

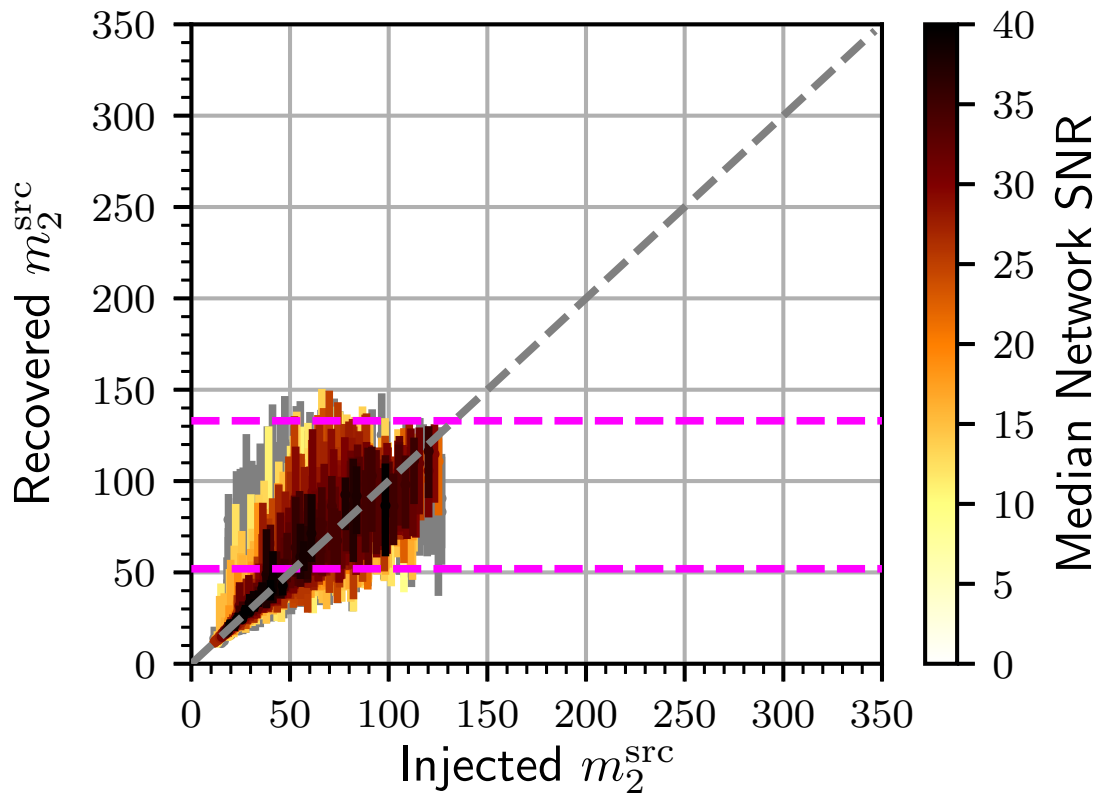


Figure 50 : The 90% credible interval of the source-frame secondary mass m_2^{src} versus the m_2^{src} used to generate the simulated signal. The dashed magenta lines represent the PISN mass gap between $52 M_{\odot}$ and $113 M_{\odot}$. The dashed gray line represent the 1:1 ratio which is an exact match. Simulated signals with either m_1^{src} or m_2^{src} not recovered in the 90% credible interval are colored gray.

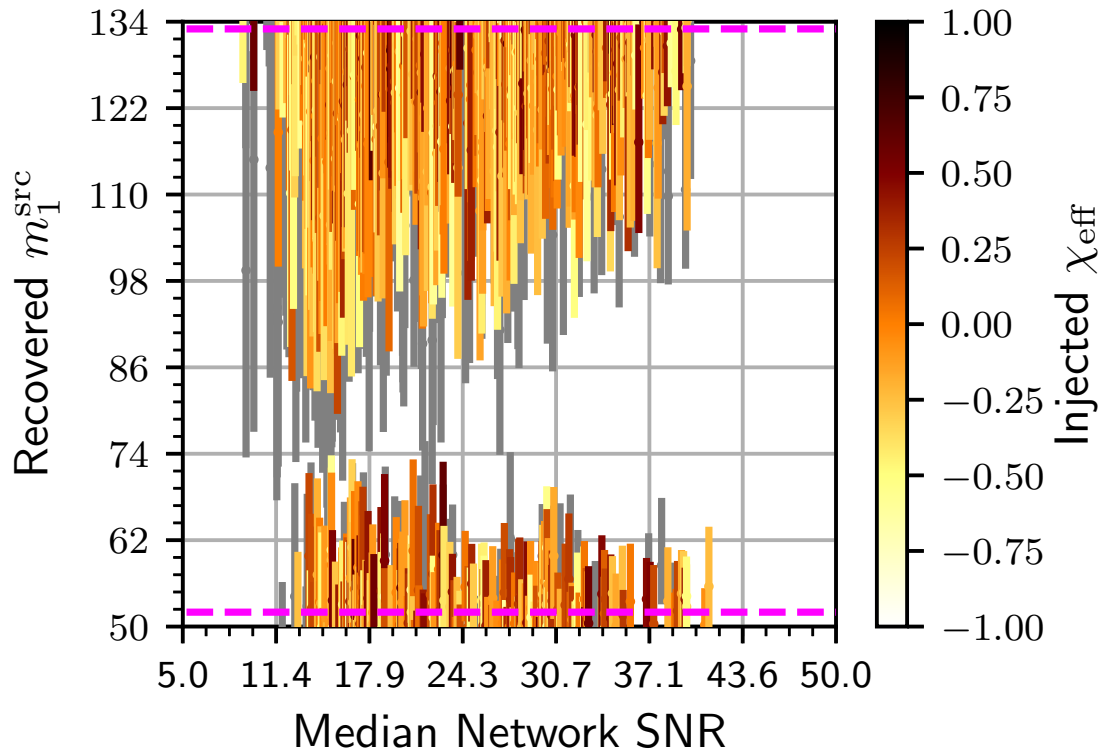


Figure 51 : The 90% credible interval of m_1^{src} from simulated signals generated with m_1^{src} outside the PISN mass gap versus the median network signal-to-noise ratio (SNR) from the posterior distributions. The points are colored by effective spin χ_{eff} . The dashed magenta lines represent the PISN mass gap between $52 M_{\odot}$ and $113 M_{\odot}$. Simulated signals with either m_1^{src} or m_2^{src} not recovered in the 90% credible interval are colored gray.

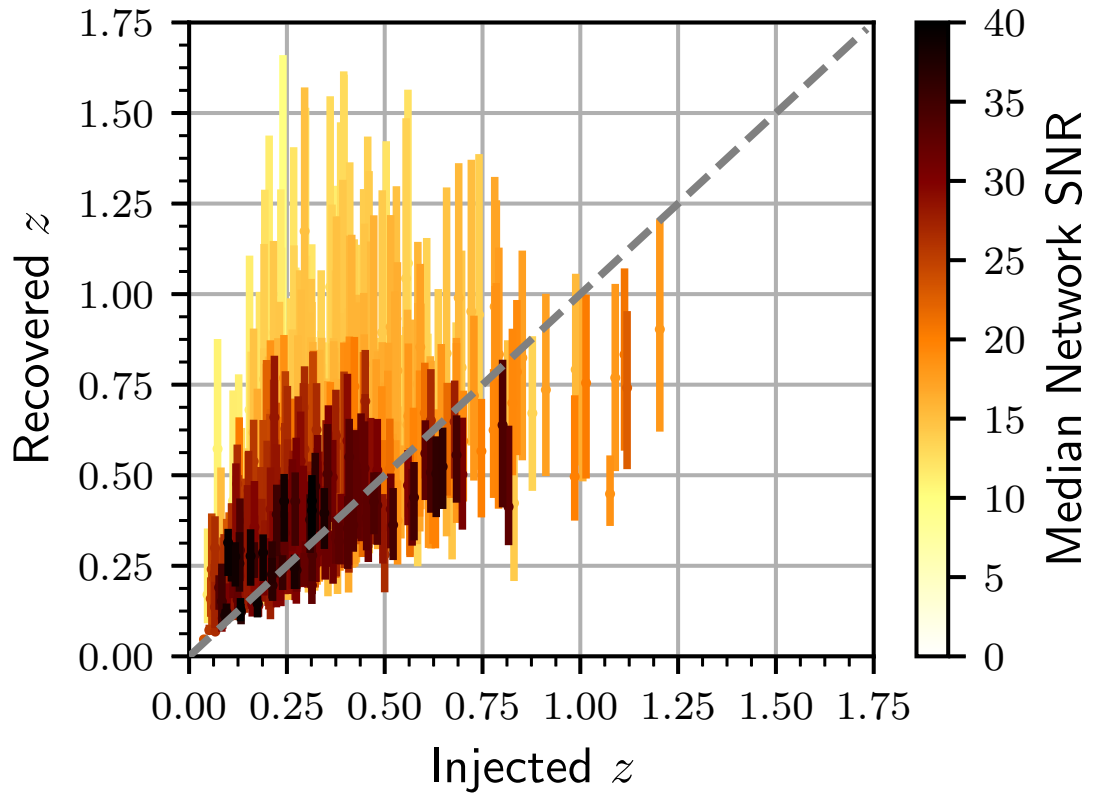


Figure 52 : The 90% credible interval of redshift z for simulated signals generated with m_1^{src} outside the PISN mass gap ($52 < m_1^{\text{src}} < 133$) but recovered with $52 < m_1^{\text{src}} < 133$.

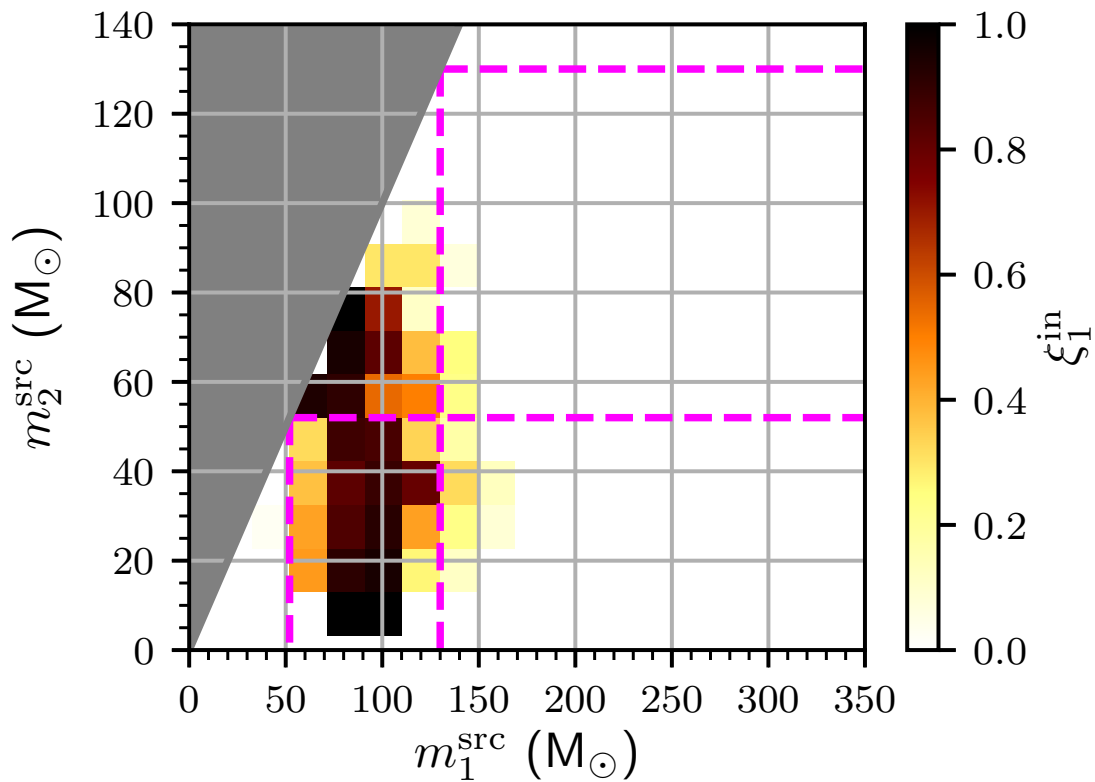


Figure 53 : The fraction of simulated signals generated in the mass bin that have their 90% credible interval for the primary mass m_1^{src} contained entirely inside the PISN mass gap; this is labeled as ξ_1^{in} . Results for simulated signals recovered with a median network SNR ≤ 22 . The dashed magenta lines represent the PISN mass gap between 52 M_\odot and 113 M_\odot .

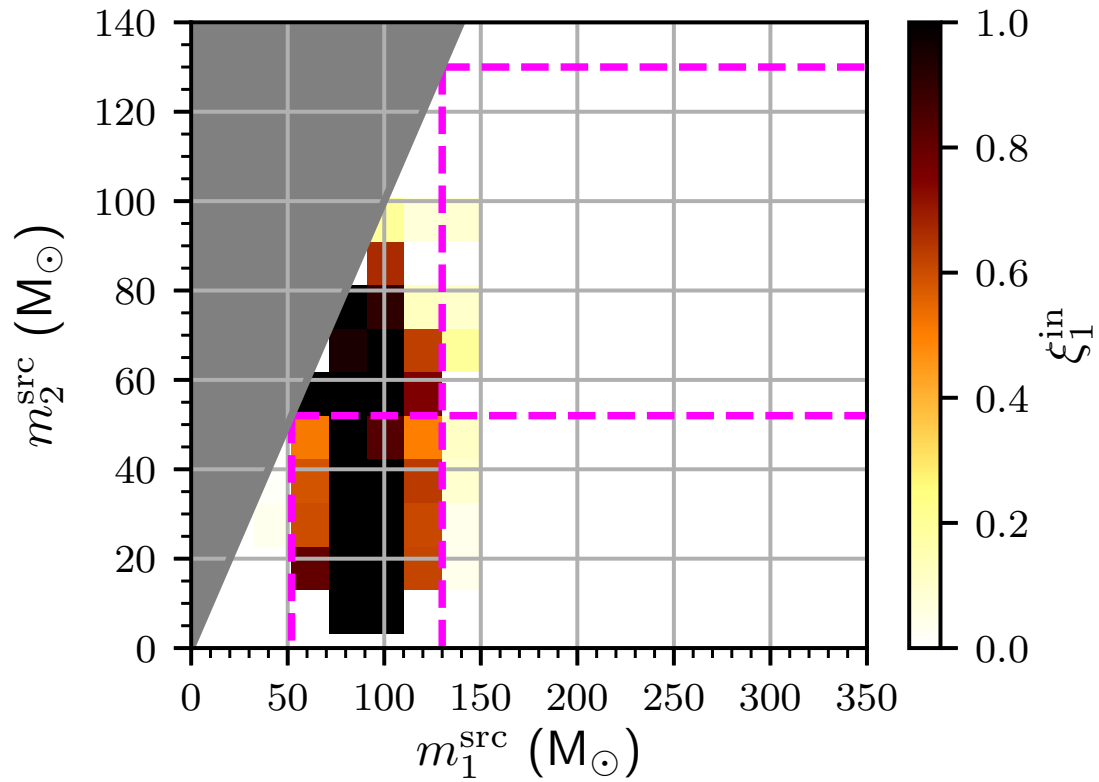


Figure 54 : The fraction of simulated signals generated in the mass bin that have their 90% credible interval for the primary mass m_1^{src} contained entirely inside the PISN mass gap; this is labeled as ξ_1^{in} . Results for simulated signals recovered with a median network SNR > 22 . The dashed magenta lines represent the PISN mass gap between 52 M_\odot and 113 M_\odot .

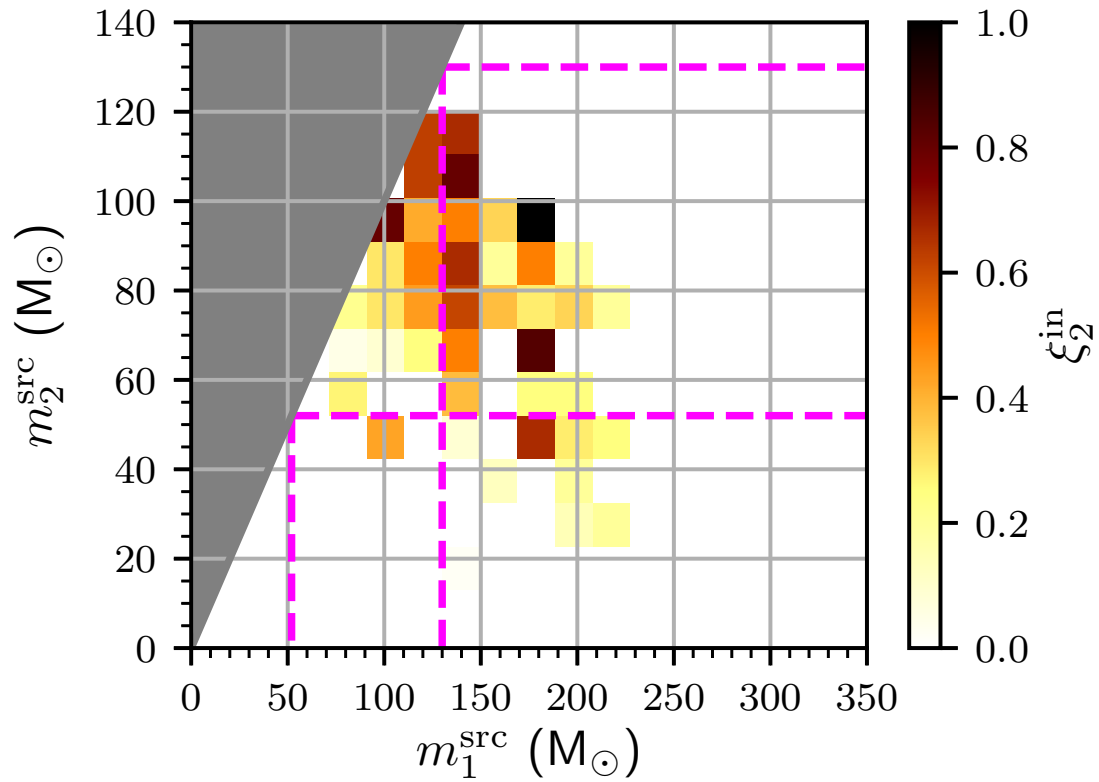


Figure 55 : The fraction of simulated signals generated in the mass bin that have their 90% credible interval for the secondary mass m_2^{src} contained entirely inside the PISN mass gap; this is labeled as ξ_2^{in} . Results for simulated signals recovered with a median network SNR ≤ 22 . The dashed magenta lines represent the PISN mass gap between 52 M_\odot and 113 M_\odot .

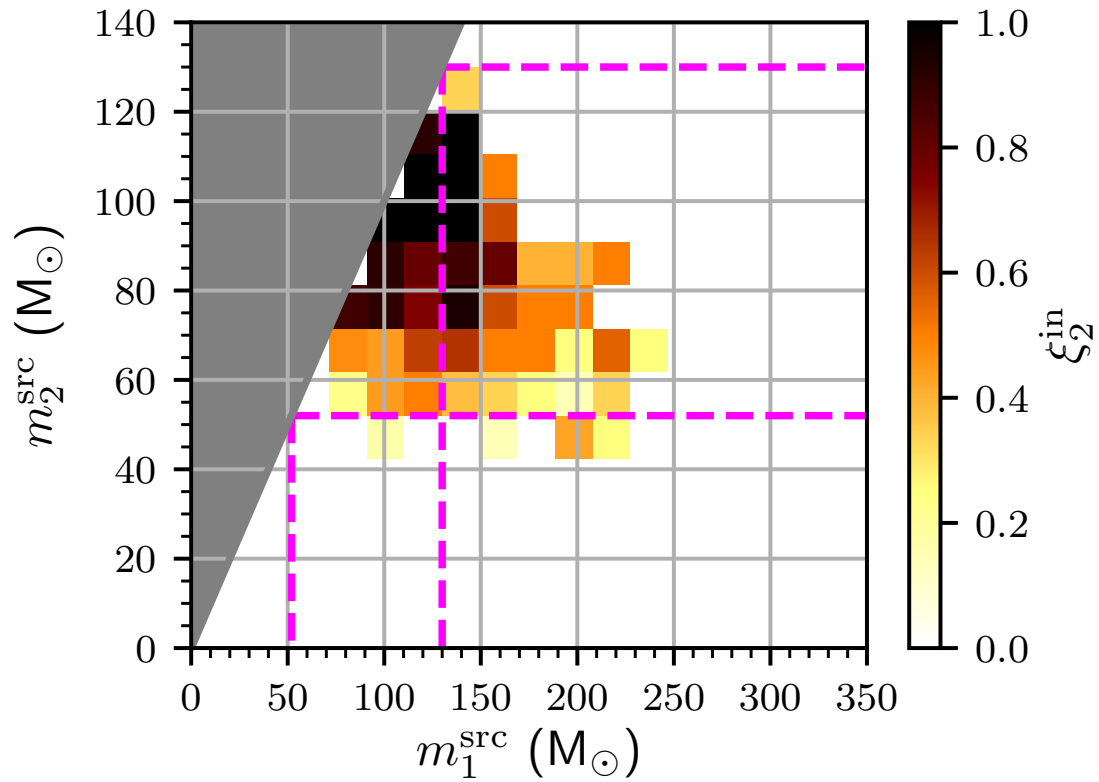


Figure 56 : The fraction of simulated signals generated in the mass bin that have their 90% credible interval for the secondary mass m_2^{src} contained entirely inside the PISN mass gap; this is labeled as ξ_2^{in} . Results for simulated signals recovered with a median network SNR > 22 . The dashed magenta lines represent the PISN mass gap between $52 M_\odot$ and $113 M_\odot$.

Chapter 6

The Advanced LIGO hardware injection system

6.1 Introduction

In order to understand the response of the Advanced LIGO detectors to gravitational waves, we perform “hardware injections” in which we simulate the detectors’ response to a gravitational-wave signal. To simulate the response we apply a force to one of the interferometer mirrors which moves the mirror in a pattern as if it were caused by a gravitational wave. Hardware injections are used to validate both detector characterization analyses and astrophysical searches. For example, hardware injections are used to validate “software injections”, where simulated signals are added to the data as part of an analysis pipeline without any physical actuation occurring; software injections are used for high-statistics evaluation of the performance of analyses. Another use for hardware injection in Initial LIGO were “blind injections” which were hardware injections known only to a small team [160, 161]. Blind injections simulate the detection and characterization of a real astrophysical signal. No blind injections were carried out during Advanced LIGO’s first observing run. There are no plans to perform blind injections in future observing runs.

Hardware injections have several other uses. Following a detection candidate, we study simulated gravitational-wave signals with parameters similar to the event through the use of hardware injections. These hardware injections provide an end-to-end check of the search and parameter estimation analyses to recover signals in the

detectors’ data. The recovery of hardware injections provides an additional check of the sign of the calibration between the Advanced LIGO detectors using astrophysical waveforms; however, the calibration of the detectors is verified by other means as well [162, 111]. The recovery of hardware injections also measures the time delay of the signal in the controls system.

To create a hardware injection we physically displace the detectors’ test masses. The mirrors in the arms act as “freely falling” test masses [163]. Advanced LIGO measures the differential displacement along the two arms $\Delta L = L_x - L_y$, and the output channel to analyses is gravitational-wave strain $h = \Delta L/L$ where $L = (L_x + L_y)/2$ [163]. The differential displacement of the test masses mimics the detectors’ response to a gravitational-wave signal.

Hardware injections are also used to can check for instrumental and environmental channels that respond to changes in differential arm length variations. The detectors’ response to a true gravitational-wave is not exactly the same as the detectors’ response to physically displacing the test masses [164, 165], and the actuators apply a force to the test masses in their suspensions whereas a true gravitational-wave does not. However, the difference is well understood, and it is only relevant at high frequencies [164, 165].

Advanced LIGO uses different actuators to control the test masses than Initial LIGO. In Initial LIGO, the test masses were displaced using magnets mounted on the optic itself, however, these actuators are no longer mounted on the test masses due to displacement noise [166, 167]. In Advanced LIGO’s first observing run, hardware injections were realized with two different actuation methods: electrostatic drive systems [121] and photon radiation pressure actuators referred to as “photon calibrators” [168]. Starting in December 2015 the photon calibrators have been the only actuator used to perform hardware injections since their actuation range available for hardware injections is larger.

During Advanced LIGO’s first observing run a wide variety of waveforms were injected. Advanced LIGO is sensitive to astrophysical sources of gravitational waves including: binary black hole and/or neutron star mergers [169, 75], the stochastic gravitational-wave background [170], and spinning neutron stars [171]. Hardware injections for each of these astrophysical sources were performed. In addition, detector characterization studies injected series of sine-Gaussians across the Advanced LIGO

frequency range.

This chapter describes how we inject signals into the Advanced LIGO detectors with the photon calibrators in Section 6.2. Sections 6.3 and 6.4 describe results from analyses that used hardware injections in Advanced LIGO’s first observing run. We focus the recovery of binary black hole merger signals in Section 6.3 and the detector characterization analysis to check the response of instrumental and environmental changes to differential displacement of the test masses in Section 6.4. Finally, Section 6.5 summarizes the hardware injections from Advanced LIGO’s first observing run.

6.2 Hardware injection procedure

Each different type of astrophysical source has different signal characteristics and properties, and hence different technical requirements for the hardware injection system. In particular, the astrophysical sources are observable in the Advanced LIGO frequency band for a wide range of time durations.

Compact-object binary mergers can last a fraction of a second to minutes depending on the component masses in Advanced LIGO’s frequency range. The signal enters Advanced LIGO’s most sensitive frequency range at 20 Hz, and as the two component masses inspiral closer together they sweep upward in frequency [110]. The merger’s termination frequency and waveform length are determined by the masses of the two objects. For example, GW150914 terminates at 250 Hz after about 0.2 s above 35 Hz [110], whereas the inspiral-only portion of a binary neutron star waveform with both component masses equal to $1.4 M_{\odot}$ terminates at 1527 Hz after about 36 s above 35 Hz.

The two other modeled sources of gravitational waves that are added to the detectors’ data through the Advanced LIGO hardware injection system are spinning neutron stars and the stochastic gravitational wave background. These sources persist in Advanced LIGO’s most sensitive frequency band for longer time durations than the compact-object binary mergers. Spinning neutron stars emit continuous gravitational waves at an almost constant frequency which is Doppler modulated by Earth’s motion [171], and the gravitational-wave frequency slowly evolves as the pulsar spins down [171]. Therefore, gravitational waves from a spinning neutron star

will be present in the data for the full duration of an observing run. The stochastic background is the superposition of many events that combine to create a low-level, broadband, non-deterministic signal [170]. Therefore, the stochastic gravitational-wave background will persist in the data throughout the observing run as well.

We also add non-astrophysically motivated injections to the detectors' data for detector characterization studies. These studies use a succession of short duration (< 1 s) sine-Gaussians across Advanced LIGO's frequency range.

We categorize hardware injections into two classes: “transient injections” that are localized in time, and “continuous-wave injections” that are active throughout the duration of the observing run. Examples of transient injections include simulated binary black hole and/or neutron star mergers, sine-Gaussians, and stochastic background signals. These signals have a waveform that is finite duration. The simulated stochastic background is included as a transient injection since we increase the amplitude of the waveform in order to limit it to a short segment of data. Continuous-wave injections simulate a synthetic population of rapidly spinning neutron stars (which we designate in shorthand as pulsars, although such a source need not emit electromagnetic pulsations detectable at the Earth).

Separate automation processes control transient and continuous-wave injections. Fig. 57 shows a schematic of the two pathways that generate and transmit gravitational-wave strain time series to the photon calibrator. In this section we work through Fig. 57, beginning at the top-left and working clockwise, in order to describe the processes that control the transient and continuous-wave injections.

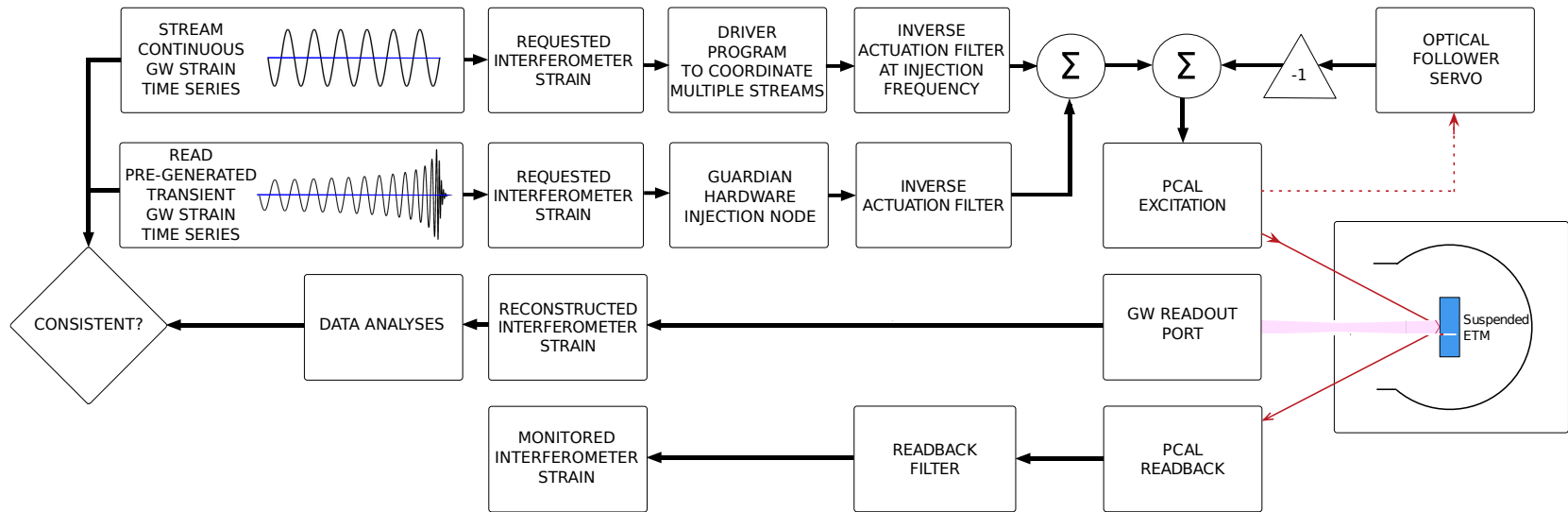


Figure 57 : Block overview of the Advanced LIGO hardware injection system. Time series for transient and continuous-wave injections are generated and sent to the photon calibrator (PCAL). The signal modulates the laser power of the photon calibrator to displace the end test mass (ETM) in a way that mimics a gravitational wave (GW) passing through the detector. The optical follower servo has its own pick-off of the light that is sent towards the ETM indicated by a dashed line. The gravitational-wave strain of the detector is analyzed and checked for consistency by the analysis' developers. A photodetector that receives the light reflected from the test mass is used to monitor and verify the injected signal.

We generate the simulated gravitational waveforms for transient injection signals prior to injection. The system for managing the automated processes of the Advanced LIGO detector subsystems is known as Guardian [172]. Guardian manages the transient hardware injections, it reads the next scheduled injection’s time series and transmits the data to the digital control system of the detector at the scheduled time.

Continuous-wave injections are generated in real-time. A streaming time series of simulated gravitational waves from a synthetic population of spinning neutron stars, described by astrophysical parameters, including the strain amplitude, sky location, and initial frequency, is transmitted to the digital controls system of the detector. A driver program called `psinject` (“pulsar injection”) coordinates the simultaneous generation and buffering of multiple streams of signals representing pulsars [139].

The transient and continuous-wave signals in the digital controls system of the detector are sent to an actuator that displaces the test masses to simulate the detector’s response to a gravitational wave signal. In Advanced LIGO’s first observing run, we used the electrostatic drive systems [121] and photon calibrators [168] as actuators for hardware injections. Each actuator has its own actuation pathway in the controls system; however, in Fig. 57 we show only the photon calibrators’ pathway.

Hardware injections are carried out by actuating one of the end test masses (ETM) of the interferometer and thus inducing differential interferometer strain variations that simulate the response to an incident gravitational wave. We only need to apply a force on one ETM to induce differential strain variations in the interferometer. The common arm length degree of freedom of the interferometer, $(L_x + L_y)/2$, is controlled by its own servo. If an actuator lengthens the x -arm by applying a force on the ETM, then the common arm length servo will promptly shorten the y -arm length to suppress the change in the common arm length degree of freedom. This creates differential interferometer strain variations that are partially suppressed by the differential arm length feedback servo.

The differential arm length degree of freedom of the interferometer is controlled by a feedback servo loop that actuates the longitudinal position of one of the ETMs [111]. The differential arm length feedback control loop suppresses apparent ETM displacements resulting from noise sources, signal injections, and gravitational waves. Because this servo suppresses the injected waveform, reconstructing the unsuppressed

injected strain requires correcting for the action of this servo. The correction for the response of the common and differential arm length servos used in reconstructing the gravitational-wave strain is described in [111].

The actuators for the servo that controls the differential arm length degree of freedom are electrostatic drive systems. These actuators apply forces via fringing field gradients from electrodes patterned onto a reaction mass separated by a few millimeters from the back surface of the ETM [121]. The electrostatic drive systems were used at the beginning of Advanced LIGO’s first observing run for injecting simulated signals. They successfully injected the waveforms for the GW150914 and stochastic background hardware injection analyses. However, the actuation range available for hardware injections is restricted because they are part of the differential arm length servo which consumes a significant fraction of its total actuation range in maintaining stable servo operation.

In order to inject a larger parameter space of waveforms, for example binary black hole and/or neutron star mergers at closer distances, we transitioned to photon calibrators for hardware injections. Since December 2015, we use a photon calibration system to displace the ETM in a way that simulates the effect of a gravitational wave signal. This is depicted on the right of Fig. 57.

A photon calibrator system uses an auxiliary, power-modulated laser with two beams impinging on the ETM located at the end of the x -arm of the interferometer. The photon calibrator on the other arm, the y -arm, is used for calibrating the detector output [168]. The two beams are diametrically opposed on the surface of the ETM, adjusted to have equal powers, and positioned to minimize unintended torques and deformations of the surface which could cause errors in the expected displacement. The Advanced LIGO photon calibrators employ a feedback control system referred to as the “optical follower servo” [168, 173]. This servo, with a bandwidth of ~ 100 kHz, facilitates simulated signal injection via ETM actuation. This ensures that the laser output power modulation closely follows the analog voltage waveform injected at the servo input.

Digital infinite impulse response (IIR) compensation filters, called the “inverse actuation filters,” convert the requested interferometer strain signal (a digital signal) into an estimate of the photon calibrator optical follower servo input signal (an analog signal) required to achieve the desired length actuation. There is an analogous set of

filters for the electrostatic drive system; however, we focus on the photon calibrators here. These filters are designed to compensate for several factors. There is compensation for: (i) the force-to-length transfer function of the suspended ETM, (ii) the signal conditioning electronics that includes a digital anti-imaging filter, the digital to analog converter gain, and an analog anti-imaging filter, and (iii) the optical follower servo transfer function. Phase delays of the anti-imaging filters and physical time delays of the digital control system cannot be compensated by the inverse actuation filters because the digital IIR filters allowed by the Advanced LIGO control system must be causal. These delays, on the order of $240 \mu\text{s}$, are taken into account during injection recovery.

The digital signals from the transient and continuous-wave injection pathways are passed through the inverse actuation filters, summed, and sent to the photon calibrator; see Fig. 57. Sporadic, unintended interruptions occurred in the Hanford injection system during Advanced LIGO's first observing run, in which the buffering failed to keep up with real-time injection. The cause was not tracked down because the interruptions occurred at apparently random times, but the drop-outs may be related to periods of high traffic on the controls system computer network. The sudden termination introduces a step function to the inverse actuation filters that has a large response at high frequencies. The effect of these dropouts, should they recur, will be mitigated by the use of point-by-point, Fourier-domain inverse actuation functions, using a separate, constant coefficient for each of the injected spinning neutron stars, all of which are extremely narrowband. This is shown in the continuous-wave injection pathway in Fig. 57. Transient injections were not affected. Guardian sets the gain after the inverse actuation filters to zero while there is no active transient injection so unintended signals do not propagate into the detector data.

The strain actually injected into the interferometer is determined using the photon calibrator read-back signal generated by a power sensor that monitors the laser light reflected from the ETM, as shown at the bottom of Fig. 57. The output of this sensor is converted to injected interferometer strain using the read-back filter that compensates for the force-to-length transfer function as well as digital and analog filters in the signal read-back pathway. In the case of hardware injections, however, the excitation channel is calibrated by taking a transfer function measurement between the excitation channel and the read-back photodetectors. This transfer function is

then incorporated within the inverse actuation filters. This provides a calibration accuracy on the order of a few percent, sufficient for the hardware injection analysis. For better calibration, however, we can compare the recovered signal and the injected signal as measured by the read-back photodetector.

There are some limitations to the photon calibrator system. First, the photon calibrator has a limited actuation strength. Fig. 58 shows the maximal displacement of the ETM using the photon calibrator system. The photon calibrator can provide up to ~ 1 W of peak power, but the force-to-length response of the ETM transfer function scales as the inverse-square of frequency [174]. Thus, the photon calibrator is limited in the amount of induced ETM displacement, especially at higher frequencies. Second, signal fidelity above 1 kHz is limited due to the shape of the anti-imaging filters and the desire to roll off the compensation filters close to the Nyquist frequency such that the compensation filters remain stable. Nonetheless, the photon calibrator is able to provide precise, calibrated displacements of the ETM in response to many astrophysical waveforms.

6.3 Binary black hole merger hardware injections

Advanced LIGO observed two binary black hole mergers (GW150914 and GW151226) and a third detection candidate (LVT151012) during its first observing run [110, 140]. After each detection was made, hardware injections were used to simulate gravitational-wave sources with similar parameters to each event in the detector. Verifying that these hardware injections were recovered by the search and parameter estimation analyses was part of the validation of each detection. Compact binary coalescence searches use matched filtering to correlate Advanced LIGO data with a bank of gravitational-wave templates [94]. Here we consider hardware injections analyzed by the PyCBC search for gravitational waves [8, 175] described in [4, 75]. Parameter estimation analyses were used to analyze the hardware injections and check for consistency with GW150914 and GW151226. We ran the same code used to characterize the detected events [47, 84]. We show the recovery of hardware injections with parameters taken from posterior distributions of parameter estimation results for GW150914 [84] and GW151226 [140, 75].

For GW150914 and GW151226, we injected ten waveforms coherently into the

two detectors. The waveforms were injected into the detectors' data after collecting enough data to measure a false-alarm rate to $6.0 \times 10^{-7} \text{ yr}^{-1}$ or significance greater than 5σ after each detection. The GW150914 hardware injections were generated with the SEOBNRv2 waveform approximant and included systems with component spins aligned with the angular momentum of the binary [7]. The GW150914 waveforms had a total mass from $[68 M_\odot, 79 M_\odot]$ in the source frame, mass ratios from 1 to 1.8, and distances from $[250 \text{ Mpc}, 530 \text{ Mpc}]$. Mass ratio is defined as m_1/m_2 where $m_1 > m_2$. These signals were injected October 2 to October 6, 2015. The GW151226 hardware injections were generated with the precessing waveform approximant IMRPhenomPv2 [44, 45] and injected on January 11, 2016. The GW151226 waveforms had a total mass from $[25 M_\odot, 30 M_\odot]$ in the source frame, mass ratios from 1 to 4.3, and distances from $[240 \text{ Mpc}, 580 \text{ Mpc}]$. For both the GW150914 and GW151226 waveforms the sky positions were selected to be on the same triangulation ring as the corresponding astrophysical event.

Figure 59 shows the reported PyCBC matched-filter signal-to-noise ratio ρ versus the expected ρ . The normalization of ρ implies that the ρ measured for a population of identical signals in different realizations of the detector noise will be $\int df |\tilde{h}(f)|^2 / S_h(f)$ [94]. We test this with software injections in which signals are added to the data without any physical actuation. We added the same software injection waveform into 47 noise realizations and compute the matched-filter signal-to-noise ratio. The recovered software injections were found to be consistent with the expectation. In Figure 59 we show the expected ρ computed from our population of software injections.

Fig. 59 includes 19 of the 20 hardware injections performed for GW150914 and GW151226. Detector data within hours of the hardware injections was selected for adding software injections since the sensitivity of the detectors does not significantly vary on these timescales [176].

Hanford and Livingston have their own angular sensitivity and noise spectra that affects the matched-filter SNR for an event [163]. All of the hardware injections are coherent but an astrophysical signal can have a different matched-filter SNR in each detector. Analysis of one of the simulated GW150914 hardware injections reported $\rho < 5.5$ in Livingston. In order to manage computational considerations, the analysis requires a single-detector signal-to-noise ratio of at least 5.5. Thus, this injection

was not “detected.” A signal-to-noise ratio < 5.5 for this injection, with an expected signal-to-noise ratio of 6, is consistent with the variation of the matched-filter output in Gaussian noise [94].

In Fig. 59 there is one GW150914 hardware injection that was recovered with a signal-to-noise ratio of 16.1 and 10.9 in Hanford and Livingston respectively; however, the injection had an expected signal-to-noise ratio of 22.1 and 13.4. This injection was recovered with a lower signal-to-noise ratio because a loud transient noise artifact was present in the Livingston data shortly after the hardware injection.

While hardware injections are an important end-to-end test, software injections are useful because a large number can be performed without disturbing the detector or significantly reducing the duty cycle of the detectors. Fig. 59 shows the software injections to be consistent with the recovery of signals that propagate through the detectors, therefore we can generate large populations of software injections that are used in other studies to evaluate the search efficiency [8], detections [4], and binary merger rates [75, 169].

Fig. 60 shows the PyCBC signal-consistency test [177] value χ_r^2 versus the matched-filter SNR ρ for hardware injections, a large population of software injections, and noise transients. Astrophysical events are indicated with stars. Hardware injections are indicated with squares. Software injections are denoted by pluses. These software simulations repeat the analysis many times to test the search across a large parameter space. The software injections in Fig. 60 were generated from a population of aligned-spin binaries with source-frame component masses between 2 to 98 M_\odot using the SEOBNRv2 waveform approximant [7]. The population of software injections is randomly distributed in sky location, orientation, distance, and time. The injection times are within the 39 day period around GW150914 reported in [4].

In Fig. 60 a highly significant astrophysical signal should be clearly separated from the background distributions. We see a separation of the software injections with high significance (false-alarm rate $< 1/100 \text{ yr}^{-1}$) and background distributions. All ten GW150914 hardware injections are recovered with high significance. Although the GW151226 Livingston hardware injections are not visibly distinguishable from the background distribution in Fig. 60, seven hardware injections have a highly significant false-alarm rate ($< 1/100 \text{ yr}^{-1}$) since we combine data from both detectors. Two hardware injections were recovered with $1/10 \text{ yr}^{-1} > \text{false-alarm rate} > 1/100 \text{ yr}^{-1}$,

a significance comparable to the gravitational-wave candidate LVT151012 ($1/2\text{yr}^{-1}$) reported in Advanced LIGO’s first observing run [110]. The software and hardware injections with similar parameters to GW150914 and GW151226 found with high significance validates the search’s ability to detect similar systems.

Following the detection of a candidate event the parameters are estimated using Bayesian inference methods [47, 76, 77]. If a detection candidate is a true gravitational wave, we should be able to reproduce the morphology of the posterior distributions using the hardware injections as well as with software injection. Conversely any significant differences have the potential to highlight discrepancies between the observation and our waveform models, or errors in our data analysis. Here we focus on two parameters: chirp mass and sky location.

The chirp mass \mathcal{M} is typically the best estimated parameter of a compact binary coalescence signal, since it dominates the phase evolution during inspiral. In Fig. 62 we show for all the simulated GW151226-like hardware injections the posterior distributions of the chirp mass minus the respective injected values, using the precessing waveform approximant IMRPhenomPv2 [44, 45]. Most posteriors have comparable width. Hardware injections with low signal-to-noise ratio have broader distributions and in one case shows bimodality. The width of the 90% credible interval for the detector-frame chirp mass for GW151226 is $\sim 0.12 M_{\odot}$ [75], which is comparable to that found with the hardware injections. Verifying that the width and shape of the posterior distribution for the chirp mass of the candidate events is similar to those of the hardware injection analyses has been part of validating the parameter estimation results for each detection.

Sky maps from the parameter estimation analysis of GW150914 and GW151226 were shared with electromagnetic observatories [178, 179] and are shown in [75, 180]. In Fig. 61, we show a reconstructed Earth-bound coordinate sky map for GW151226 along with sky maps for two hardware injections. One of the two hardware injections (at GPS time 1136588346) has low signal-to-noise ratio and thus spans a larger sky area, although still near to the same triangulation ring. The other injection (at GPS time 136592747) is instead representative of the typical map: all other maps look similar to this and are not shown to avoid overcrowding.

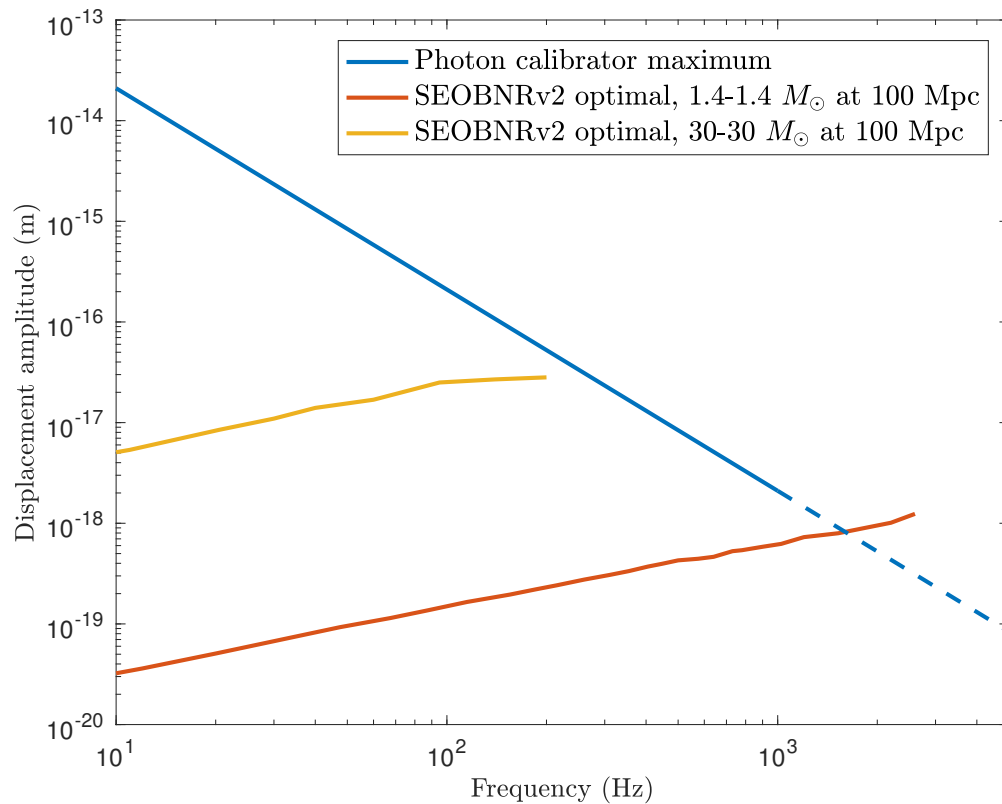


Figure 58 : The maximum displacement of an ETM using the photon calibrator (blue). For the sinusoidal force induced by sinusoidally power modulated laser beams, $F = mA$ implies that the induced displacement is given by $x = -F/(m\omega)^2$. The dashed blue curve indicates that the fidelity of the induced displacements degrades above 1kHz due to the need to roll off the inverse actuation filters to maintain stability near the Nyquist frequency. The maximum displacement of the ETM required for two optimally-oriented compact binary waveforms that contain an inspiral, merger, and ringdown are shown for reference. A 3-30 M_{\odot} binary at 100 Mpc (yellow) and 1.4-1.4 M_{\odot} binary at 100 Mpc (red) were generated using the SEOBNRv2 approximant [7]. Note that the required displacement for the 1.4-1.4 M_{\odot} binary exceeds the maximal photon calibrator displacement at high frequencies.

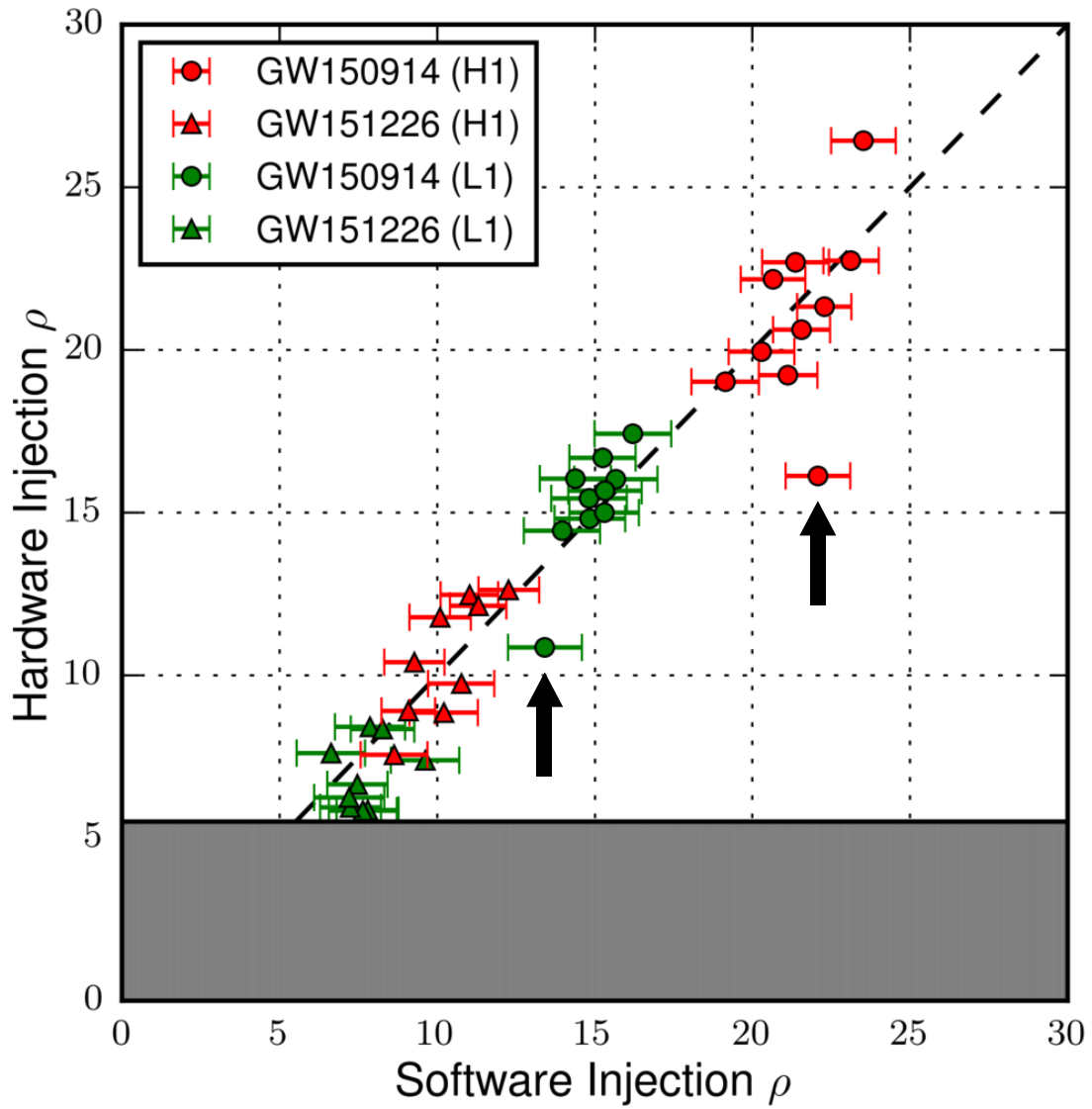


Figure 59 : A comparison of the signal-to-noise ratio ρ from software injections and the recovered signal-to-noise ratio of the hardware injection. Parameters for the hardware injections were drawn from the posterior distributions for GW150914 (circles) and GW151226 (triangles). The software injection ρ is the mean and 1σ error from the recovery of 50 software injections filtered with the injected waveform near the time of the injection. The threshold on ρ is indicated by the gray region. The arrows indicate the coherent injection affected by a nearby noise transient.

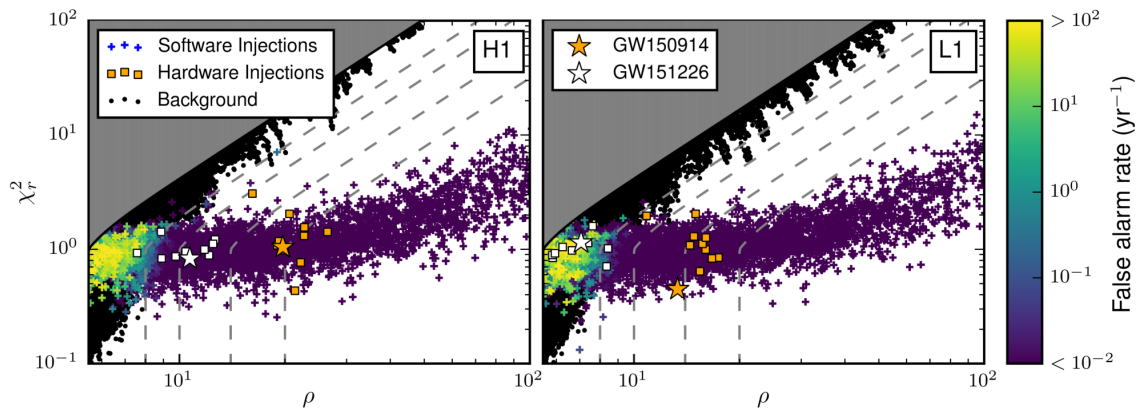


Figure 60 : PyCBC χ_r^2 statistic versus matched-filter signal-to-noise ratio ρ for each detector. Software injections are represented as pluses that are colored by false-alarm rate. The false-alarm rate is calculated using the time-slide algorithm described in [8]. The gravitational-wave events GW150914 and GW151226 are shown as stars. Hardware injections for GW150914 and GW151226 are represented as boxes. These are coherent software and hardware injections, therefore the H1 and L1 plots are dependent on each other. Single-detector background distributions (black dots) are plotted; there was a threshold applied indicated by the gray region. Lines of constant detection statistic $\hat{\rho}$ are shown (gray dashed lines); plotted are $\hat{\rho} = \{8, 10, 14, 20\}$.

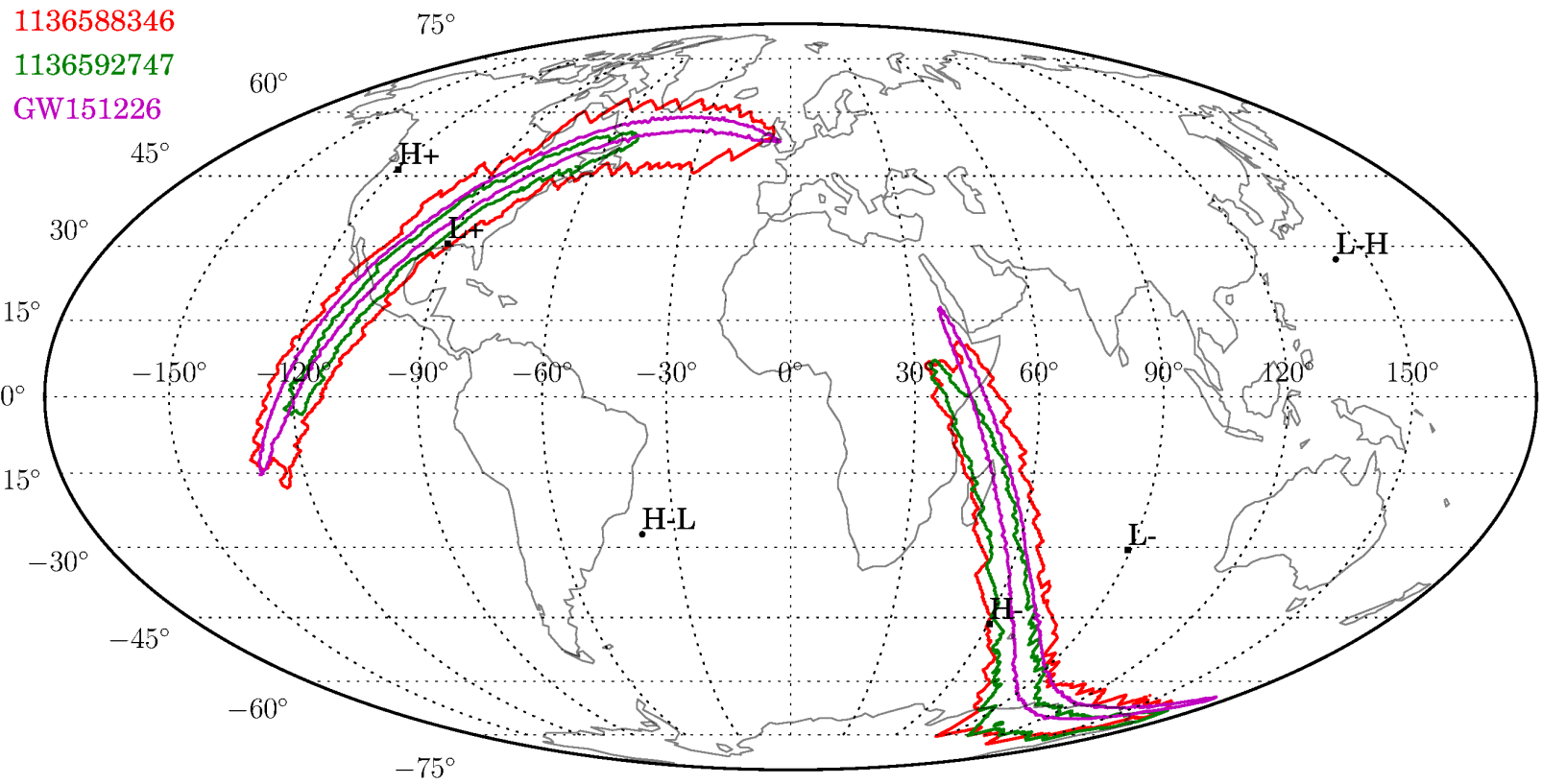


Figure 61 : The 90% confidence interval skymaps for two hardware injection (red and green) and GW151226 (magenta). The skymaps are shown in Earth-bound coordinates. H+ and L+ mark the Hanford and Livingston sites, and H- and L- indicate antipodal points; H-L and L-H mark the poles of the line connecting the two detectors (the points of maximal time delay). The two hardware injections are chosen to be representative of an average event (green) and a sub-threshold event (red). We notice how all sky maps have support near the same ring of equal time delay between the two Advanced LIGO detectors.

6.4 Loud hardware injections for detector characterization

Noise artifacts in Advanced LIGO data adversely affect the output of gravitational-wave search analyses [176, 162]. In searches for transient gravitational waves, some periods of time are excluded from the analysis to remove periods of poor data quality and known transient noise. These are known as “data quality vetoes” [176, 162]. Removing periods of time with excess noise improves the performance of gravitational-wave searches [176, 162]. Some of these data quality vetoes are derived from information recorded in auxiliary channels. Auxiliary channels include instrumental channels that record degrees of freedom of the interferometer and its isolation systems as well as channels that monitor the environmental conditions around the instrument [181]. The environmental monitoring system includes seismic, acoustic, and electromagnetic data.

To avoid discarding true gravitational-wave signals, any auxiliary channels used for vetoes are first checked to ensure that they do not respond to gravitational-wave-like signals; i.e., changes in differential arm length. This process is referred to as a “safety check,” since a channel that has no sensitivity to gravitational waves is considered “safe” for use when constructing a veto. To test whether auxiliary channels respond to differential arm length changes, three sets of 12 loud (matched-filter signal-to-noise ratios > 100) transient hardware injections were performed at both detectors, and the auxiliary channel data were examined both qualitatively and quantitatively for signs of coupling.

Spectrograms were manually inspected at the time of hardware injections. These signals were very strong and clear, with high signal-to-noise ratio, in channels that were expected to record differential displacement, e.g. interferometer differential sensing and actuation, and closely related degrees of freedom. No signs of coupling were found in thousands of other auxiliary channels, indicating that they may be used to construct vetoes. Hundreds of time-frequency representations of auxiliary channels were also inspected at the times of GW150914 and GW151226 with the same outcome [176].

Loud hardware injections were used to statistically assess the coupling. An algorithm based on a transformation using sine-Gaussians [182] was used to identify and parameterize noise transients by their time, frequency, and signal-to-noise ratio. The

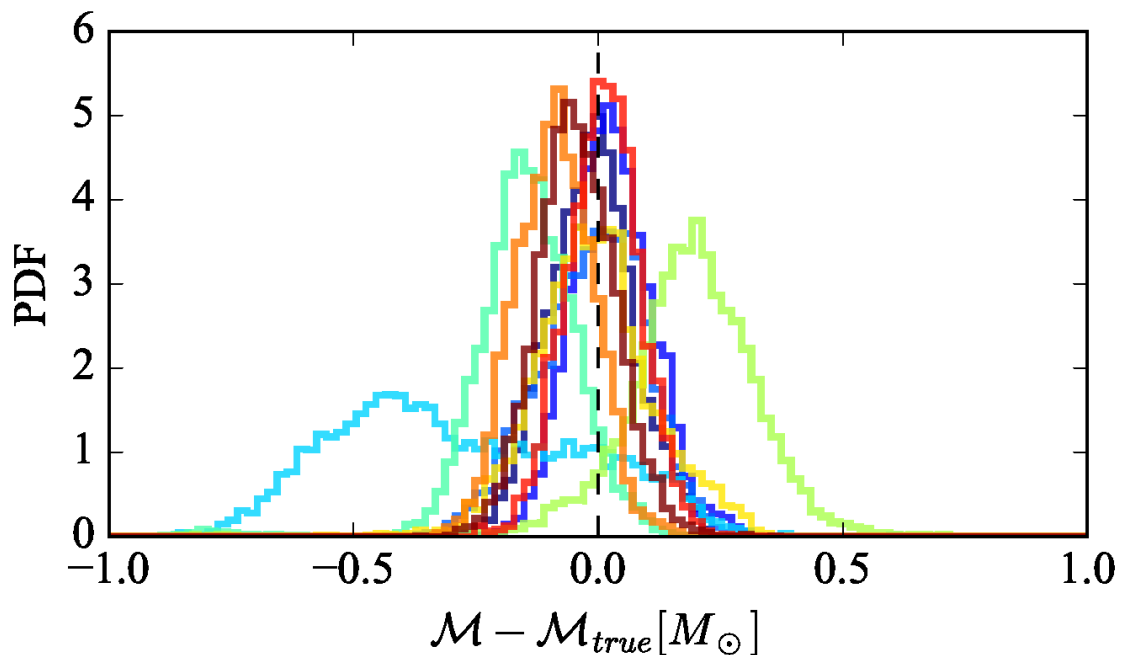


Figure 62 : Posterior probability density functions (PDF) for the chirp mass inferred from GW151226 hardware injections. The true value has been removed to center all distributions around zero. Hardware injections with very low signal-to-noise ratio show large width and in one case bimodality. The bimodal distribution comes from the injection at GPS time 1136588346 which is also shown in Fig. 61.

time of noise transient is compared with the times of the loud hardware injections.

For each channel, the number of noise transients that occurred within 100 ms of loud injections are counted and compared to the number that would be expected based on chance [183]. For any channel exhibiting a higher number of overlaps than expected by chance, the time-frequency behavior of the raw data is further investigated to see if there is a plausible connection. We find that only obviously related channels, such as those in the sensing and actuation chain for the differential length control loop, were sensitive to the loud hardware injections.

6.5 Conclusions

This chapter presents the Advanced LIGO hardware injection system infrastructure for injecting simulated gravitational-wave signals into the detectors by displacing

the test masses, and results from Advanced LIGO's first observing run. Hardware injections were used for validating analyses after a gravitational-wave detection, as an additional check of the calibration, and characterizing the detectors' response to differential arm length variations.

After the detection of GW150914 and GW151226, sets of binary black hole merger waveforms with similar parameters were injected to validate the search and parameter estimation analyses. The recovered signals were checked for consistency with the parameters of the injected waveforms, including signal-to-noise ratio, chirp mass, and sky position. Similarly, the stochastic background and continuous-wave searches used simulated waveforms as an end-to-end test.

In order to detect and estimate the parameters of astrophysical signals the calibration must be correct, and the hardware injections provided an additional check of the calibration sign. The overall sign of the calibration is important in order to detect and estimate the parameters of astrophysical signals correctly. An incorrect sign on the calibration would invert the signal in one detector and the parameter estimates would be incorrect. The binary black hole merger hardware injections were used to check the sign of the electrostatic drive and photon calibrator pathways. The continuous-wave injections were used as an additional check on the sign of the calibration between the Advanced LIGO detectors. We found the sign of the calibration to be correct.

Data quality vetoes are used to increase the performance of search analyses, and detector characterization hardware injections were used to identify output channels in the control system that can be used to construct data quality vetoes. After each gravitational-wave detection, we carried out a study to check for cross-couplings with the detectors' output gravitational-wave strain channel. Channels that contained a trace of the injected signal were considered unsafe and excluded from data quality veto studies.

In the future, we plan to exclusively use the photon calibrators to inject simulated gravitational waves.

Chapter 7

A pipeline for validating the Advanced LIGO hardware injection state information

7.1 Introduction

It is critical for Advanced LIGO to maintain a record of all hardware injections so searches can exclude data containing a hardware injection. Since hardware injections can pollute the results from background estimation methods or falsely claim a hardware injection as a new astrophysical detection. Advanced LIGO will also publicly release its observing run data [184]. As part of this data release, it is important to provide a comprehensive list of hardware injections in the data sets for the gravitational-wave astronomy community; since hardware injections may adversely affect their analyses.

Advanced LIGO monitors the state of the hardware injection system. Since analyses have different requirements, information about the state of the hardware injection system is transmitted and stored in several locations. For example, low-latency searches need to receive a continuous stream that describes the state of the Advanced LIGO hardware injection system to prevent hardware injections from initiating the process that sends an alert to electromagnetic observatories. In contrast, offline searches such as the PyCBC search are run on the order of weeks, therefore offline searches can use a processed version of the output of monitoring systems in

the interferometers' control system which more concisely summarize the state of the hardware injection system.

In this chapter, we describe a pipeline that was used in Advanced LIGO's first observing run to validate that accurate state information about the Advanced LIGO hardware injection system is provided to the searches. The output of this pipeline is an exhaustive list of hardware injections that was used to inform the LIGO Open Science Center which is responsible for Advanced LIGO's public data releases. Section 7.2 describes how the state of the Advanced LIGO hardware injection system is tracked and how the state information is provided to the searches. In Sec. 7.3 we present the details of the pipeline that validates the state information about the hardware injection system. Finally, in Sec. 7.4 we summarize the application of the pipeline to validate the state of the Advanced LIGO hardware injection system in Advanced LIGO's first observing run and improvements made after the observing run.

7.2 Hardware injection state information

There are two independent processes that transmit hardware injection time series data to the actuators; one process for transient hardware injections and another process for continuous hardware injections [185]. In this section, we focus on transient hardware injections and follow Figure 63 which depicts a block diagram that describes the locations where state information about the transient hardware injections injected through Advanced LIGO hardware injection system is stored.

During Advanced LIGO's first observing run, a continuously running script called `tinj` controlled when a transient hardware injection was added to the data. Transient hardware injections were scheduled at a designated time by appending a schedule file which contains the time and path to the time-domain gravitational-wave strain waveform data to be injected. Once it was time to perform a scheduled hardware injection, `tinj` would read and transmit the time series data to the controls system. As part of the validation process, we check that each transient hardware injection in Advanced LIGO's first observing run was scheduled.

Prior to injecting a signal, the team that schedules hardware injections manually creates an entry in the database that collects candidate events called Gravitational-wave Candidate Event Database (GraCEDb) [186]. We use database queries to check

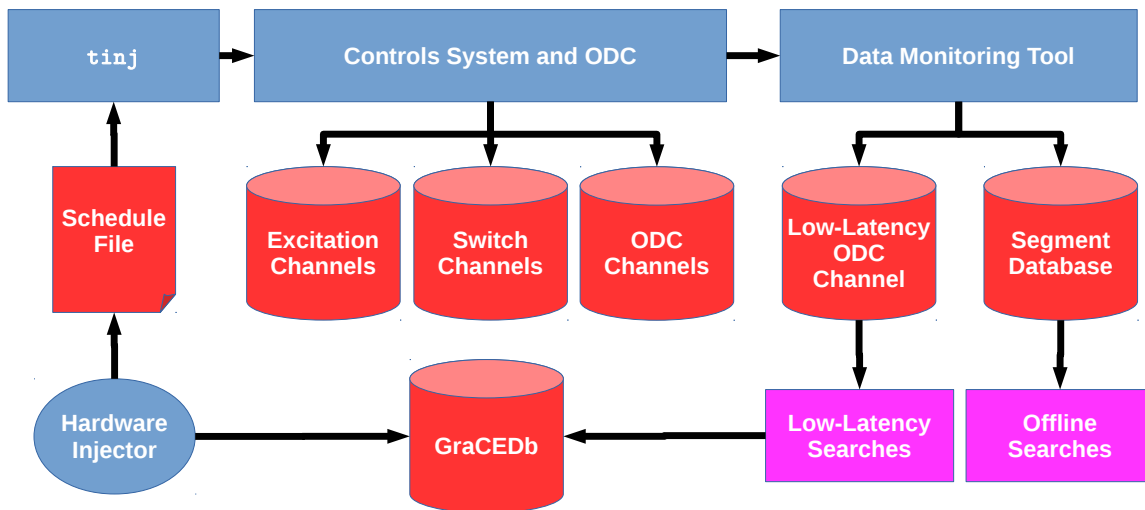


Figure 63 : Block diagram depicting the flow of state information about the hardware injection during Advanced LIGO’s first observing run. A team of hardware injectors schedule hardware injections using `tinj` and upload entries to the Gravitational-wave Event Candidate Database (GraCEDb). The scheduling program `tinj` transmits the hardware injection time-domain waveform data to the controls system. The controls system stores the injected time series into excitation channels and the state of the inverse actuation filters to the switch channels. The Online Data Characterization (ODC) system monitors these channels in the controls systems and produces bit vectors that indicate if a hardware injection has occurred. The Data Monitoring Tool receives the ODC bit vectors and records them to the data files that low-latency searches read and the segment database that offline searches query for state information about the hardware injection system.

that an entry exists for all hardware injections during Advanced LIGO’s first observing run.

The time series data is sent to an excitation channel which is continuously recorded to disk. Instrumental channels are test points in the controls system that record the time series of a readout from the detector, for example a photodiode, seismometer, or digital signal. The excitation channel is the entry point of the hardware injection time series data into the interferometers’ controls system. There were two actuators used to inject hardware injections during Advanced LIGO’s first observing run [185], the electrostatic drive systems [121] and the photon calibrators [168]. Therefore we search the electrostatic drive systems transient hardware injection excitation channel (`CAL-INJ_TRANSIENT_OUTPUT`) and the photon calibrator transient hardware injection excitation channel (`CAL-PINJX_TRANSIENT_OUTPUT`). The excitation channels are zero

except when a hardware injection is present, therefore we search each excitation channel and record the start and end times of contiguous samples with a non-zero value.

After the transient hardware injection is recorded to the excitation channel, it is summed with the continuous hardware injection time series and then the combined signal passes through the inverse actuation filters [185]. This is described in Chapter 6. The inverse actuation filters have switches to turned the filters “off.” If a filter is off, then the output from the filter is a time series of zeros; therefore, no hardware injection signal goes to the actuator. We search the electrostatic drive inverse actuation filter switch channels (`CAL-INJ_TRANSIENT_SWSTAT` and `CAL-INJ_HARDWARE_SWSTAT`) and the photon calibrator inverse actuation filter switch channels (`CAL-PINJX_TRANSIENT_SWSTAT` and `CAL-PINJX_HARDWARE_SWSTAT`) for all contiguous sets of samples where the switches were on. We record the start time and the end times of each contiguous set.

Searches receive meta-data about the state of the hardware injection system from monitoring systems in the detectors’ controls system. The hardware injection excitation channels and filtered time series channels are monitored and logged within the Online Detector Characterization (ODC) system [187]. The ODC system is conducted in real-time within the detectors’ controls system. The ODC system produces meta-data that indicates whether there is any non-zero signal in the excitation and filtered time series channels for more than two samples. If there is an active hardware injection signal, then a bit is flipped to indicate that a hardware injection is actively being injected. The ODC system organizes bits into bit vectors that summarizes the state of a subsystem in the interferometer. Each ODC bit vector is written to disk as a time series and a bitmask is used to resolve an individual bit in the bit vector. The hardware injection system has its own bit vector in the ODC system. Additional bits in the hardware injection bit vector are set to indicate which type of injection is being injected; the types of injections include compact-object binaries, burst, continuous, detector characterization, and stochastic gravitational-wave signals [187]. Figure 64 shows the state of the hardware injection system’s ODC bit vector during January 16, 2016.

Since two different actuators were used during Advanced LIGO’s first observing run to inject hardware injection signals there is a hardware injection ODC bit

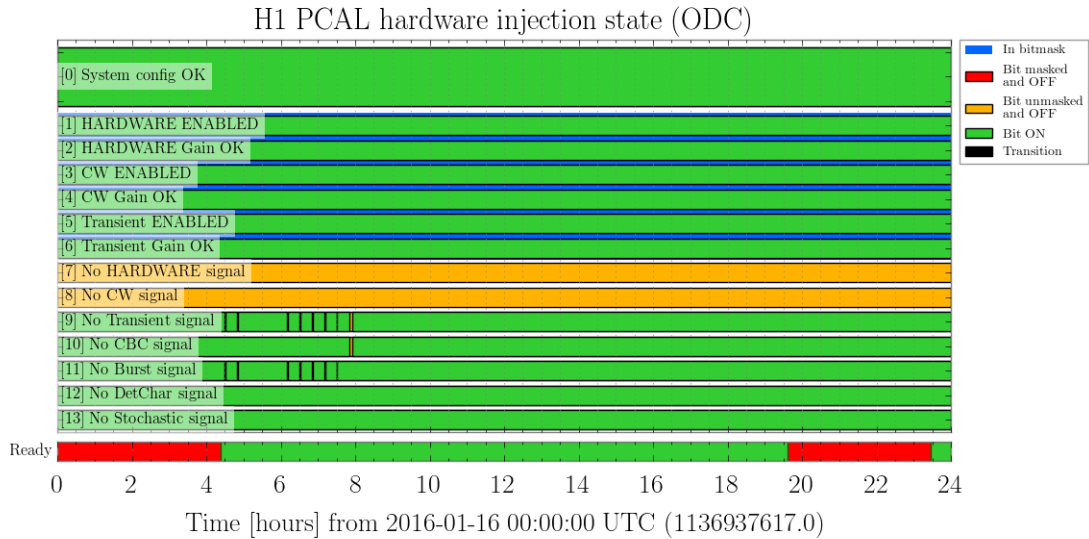


Figure 64 : The hardware injection ODC bit vector for the Hanford detector on January 16, 2016. At the top, the 0-th bit is the summary bit that describes if the hardware injection system is operating in its nominal state. Green indicates that it is. Bits 1 through 6 indicate that the filters, filter gains, and switches are in their nominal state. Bits 7 and 8 indicate that the continuous hardware injections are active. Bits 9 through 13 describe when and what type of transient injection was injected throughout the day. At the bottom is a bit time series that indicates if the detector was observing; green indicates that the detector was observing and red indicates that the detector was not observing.

vector for both actuators. These two bit vectors are each recorded as a separate channels (`CAL-INJ_ODC_CHANNEL_OUT_DQ` and `CAL-PINJX_ODC_CHANNEL_OUT_DQ`). We cross-check bits in the ODC bit vector with times when there is a non-zero signal in the excitation channels, switch channels, and the schedule file to validate that ODC is properly monitoring the state of the hardware injection system.

The ODC system has a bit vector that describes the overall state of the detector called ODC Master. The ODC Master bit vector contains a bit for the state of the hardware injection system as well as which type of injection is being injected; the bit is set to 1 if there is an active hardware injection. The hardware injection bits in ODC Master are consumed by software run in the Data Monitoring Tool [188] infrastructure in low-latency, and the bits that indicate whether each type of injection are active are copied into files sent to low-latency analyses. Low-latency analyses use this bit time series channel (`DCS-CALIB_STATE_VECTOR_C02`) to determine whether or not each type

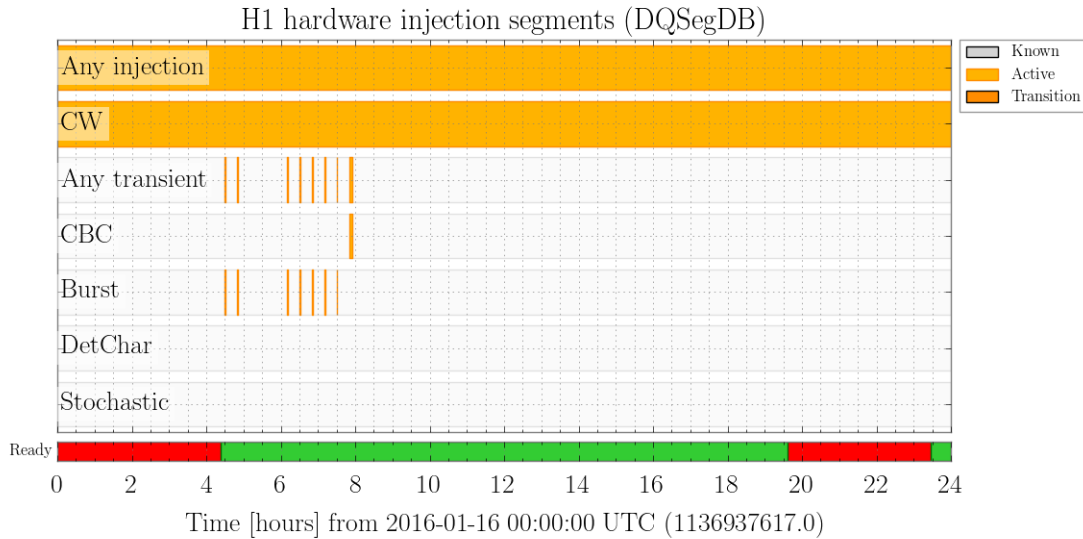


Figure 65 : The state of each hardware injection segment in the segment database for the Hanford detector on January, 16, 2016. This plot shows that the continuous hardware injections were active the entire day, there were seven burst hardware injections, and there was one compact binary coalescence hardware injection. At the bottom is a bit time series that indicates if the detector was observing; green indicates that the detector was observing and red indicates that the detector was not observing.

of injection is occurring.

The Data Monitoring Tool infrastructure also generates integer second segments that indicate whether or not each type of injection is occurring. There is a segment name for each injection type: compact binary coalescence hardware injections (ODC-INJECTION_CBC), burst hardware injections (ODC-INJECTION_BURST), stochastic hardware injections (ODC-INJECTION_STOCHASTIC), and detector characterization hardware injections (ODC-INJECTION_DETCHAR). These segments are padded from the higher sampling rate of the ODC system outward such that each second that contains any portion of an active injection is marked as having that injection active. These segments are then published to the segment database which is queried by the offline searches to determine when hardware injections occurred. Figure 65 shows the segments added to the segment database on January, 16, 2016.

7.3 Pipeline topology

In Sec. 7.2 we described seven sources that store information about the state information about the hardware injection system: the transient hardware injection schedule file, GraCEDb, the two excitation channels, the four inverse actuation switch channels, the two ODC bit vector channels, the low-latency ODC bit vector channel, and the segment database. Most of these sources contain bit vectors sampled ≥ 16 Hz that need to be searched with several bitmasks over four months; however, this is a naturally parallelizable problem since searching a finite time series for changes does not need to communicate with other processes. We have implemented a pipeline that parallelizes searching each source and then associates records from different sources with overlapping timestamps together as a single hardware injection event.

The continuous hardware injections were validated with other methods; however, the pipeline described here is flexible and could be used to validate continuous hardware injections as well.

Figure 66 shows a block schematic of the pipeline. We split the observing run data into 2048 s segments and search each source independently. Reading the transient hardware injection schedule file, querying GraCEDb, and querying the segment database are done independently at the beginning. The set of ODC bit vector channels, low-latency ODC bit vector channel, and switch channels are searched with bitmasks for times when a bit indicates a hardware injection has been added to the data. The excitation channels are searched for times when there is a non-zero value. After all channels and databases have been searched, we find coincidences between the sources of state information. When a contiguous series of samples is found in at least one source, then it is saved as a hardware injection event which contains the start time of the set of contiguous samples, the end time of the set of contiguous samples, and the set of sources that indicate an active hardware injection during the samples. A hardware injection should have a record from each source.

7.4 Conclusions

We presented the flow of information describing the state of transient hardware injections from Advanced LIGO's hardware injection system and a pipeline to validate

the state information. The pipeline described in Sec. 7.3 was used to document the hardware injections added to the data during Advanced LIGO's first observing run. The results from this pipeline is a hardware injections which was presented to members of the LIGO Open Science Center. The pipeline was automated to validate the state information as hardware injections are added during Advanced LIGO's second observing run.

After Advanced LIGO's first observing run, the transient hardware injections controls were integrated into Guardian which is the automation framework for the Advanced LIGO interferometers [172]. Guardian continuously records its state which describes what task its currently executing. There is a state that designates that a hardware injection is actively being sent to the controls system. Beginning in Advanced LIGO's second observing run, the Guardian state channels should be searched as well.

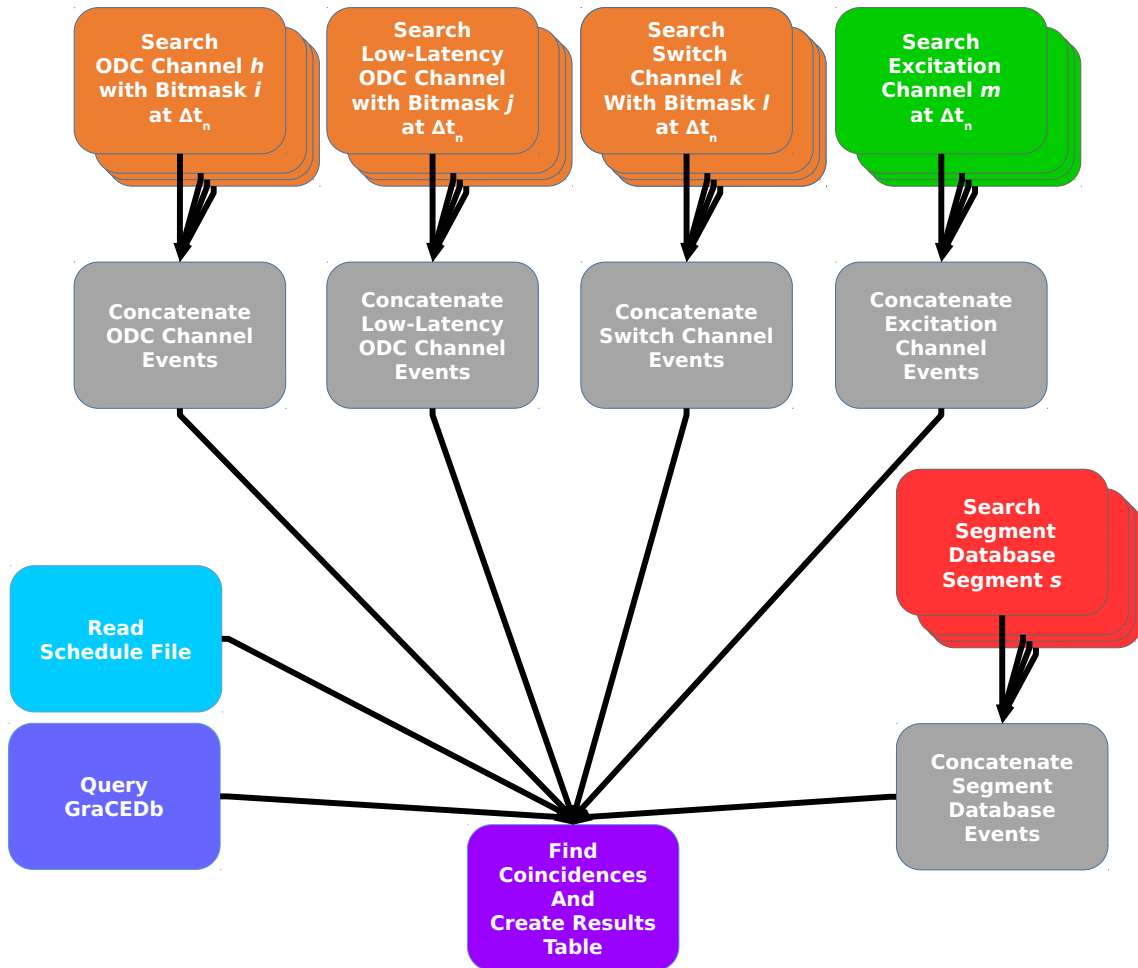


Figure 66 : Block diagram of the pipeline. The observing run is split into n 2048 s segments. The ODC bit vector channels, the low-latency ODC bit vector channel, and switch channels use bitmasks to check the state of individual bits in each 2048 s segment. There are h ODC bit vector channels that are searched with i bitmasks, the low-latency ODC bit vector is searched with j bitmasks, and there are k switch channel that are searched with l bitmasks. There are m excitation channels that are searched for non-zero samples in each 2048 s. There are s segment names queried in the segment database. The list of events found in each 2048 s segments are concatenated and combined with the schedule file and GraCEDb entries to find coincidences. A results table is rendered at the end that lists all coincidences.

Chapter 8

Conclusions

In this dissertation, we have reported the detection of gravitational waves from two binary black hole mergers (GW150914 and GW151226) and a detection candidate (LVT151012) consistent with a binary black hole merger. These are the first observed binary black hole system and the individual black hole masses are larger than other stellar-mass black holes previously observed. This search enabled many other analyses including measuring the rates of binary black hole mergers [2], testing the strong field dynamics of gravity [2], and bounding the rates of binary neutron star and neutron star-black hole mergers [105]. In the future, with a population of detections Advanced LIGO could begin to determine the mass and spin distributions of black holes, and possibly use more precise measurements of the spins, as the sensitivity of the detectors increase, to infer formation channels for events.

We determined the impact of calibration errors on the detection of binary black hole mergers. For GW150914, we find the loss in the detection statistic averaged over many noise realizations is $<3\%$ and applying corrections for time-dependent changes to the calibration would not have strongly impacted the detection of GW150914. Across a template bank with total mass up to $100 M_{\odot}$ we see the loss in the matched-filter signal-to-noise ratio for typical operating conditions is $< 1\%$. Future studies can focus on quantifying the loss in the detection statistic across the bank, as well as the impact calibration errors have on parameter estimation. Uncertainties in the gravitational-wave strain from calibration can increase the uncertainties in parameter estimation analyses [189]. The current parameter estimation analysis (LALInference [47]) Advanced LIGO uses to publish results do marginalize over

calibration uncertainties; however, it does not use a physical model of the calibration. Interesting studies could be done evaluating the impact of calibration on parameter estimation using a physical model of the detector. It is important to understand the impact calibrations errors have on sky localization since electromagnetic observatories will rely on the Advanced LIGO to decide where to direct their observations. Alerts are sent to electromagnetic observatories for complementary observations on much shorter timescales than the final, carefully-checked calibration is produced. The sky localization of a signal is impacted by changes in the timing and phase. Therefore, its important to understand how changes in the timing and phase impact the sky localization results sent to electromagnetic observations.

We have presented a Bayesian parameter estimation analysis called PyCBC Inference. PyCBC Inference uses ensemble Markov-chain Monte Carlo methods to estimate the posterior probability density functions of the astrophysical parameters. We demonstrate the method on GW150914, GW151226, and LVT151012. We find that the black hole masses range between $8.4_{-1.86}^{+1.52} M_{\odot}$ and $35.0_{-3.0}^{+5.1} M_{\odot}$. The spins of the black holes are weakly constrained but we can rule out large aligned or large anti-aligned spin configurations. It is difficult to measure the precession effects of the binary and we have already begun investigating how the choice of prior for the component spins impacts the spin measurement. These results agree with the published results in Ref. [2], and in the future, we plan to carry out a more detailed comparison of the two parameter estimation analyses. As far as new developments in parameter estimation of binary black hole mergers, we have already begun to explore how our choice of priors impacts our spin measurements.

We assess the capability of the Advanced LIGO and Advanced Virgo network at design sensitivity to observe the gap in the black hole mass distribution due to pair-instability supernovae. This is the first large-scale analysis with PyCBC Inference. We find the network is able to constrain the component masses of a population of simulated signals within the mass gap due to pair-instability supernovae which is between $52 M_{\odot}$ and $133 M_{\odot}$. We find that a population of detections with network $\text{SNR} > 29$ may observe the mass gap, and on the contrary, if a signal is observed with a network $\text{SNR} > 29$ inside the mass gap it could challenge the theory of the mass gap. The detection of binary black hole mergers with higher total mass are more strongly affected by noise transients, and a natural progression of this work would

be to predict the feasibility to detect these binaries, and how many detections would Advanced LIGO need before we confidently observe the mass gap.

Bibliography

- [1] L. K. Nuttall et al. Improving the Data Quality of Advanced LIGO Based on Early Engineering Run Results. *Class. Quantum Grav.*, 32(24):245005, 2015.
- [2] B. P. Abbott et al. Observation of Black Hole Binary Mergers in Advanced LIGO's First Run. 2016. <https://dcc.ligo.org/LIGO-P1600088/public/main>.
- [3] B. P. Abbott, R. Abbott, T. D. Abbott, et al. Calibration of the Advanced LIGO detectors for the discovery of the binary black-hole merger GW150914. 2016. <https://dcc.ligo.org/LIGO-P1500248/public/main>.
- [4] B. P. Abbott et al. GW150914: First results from the search for binary black hole coalescence with Advanced LIGO. *Phys. Rev.*, D93(12):122003, 2016.
- [5] S. Babak, R. Balasubramanian, D. Churches, T. Cokelaer, and B. S. Sathyaprakash. A template bank to search for gravitational waves from inspiralling compact binaries. I: Physical models. *Class. Quantum Grav.*, 23:5477–5504, 2006.
- [6] B. P. Abbott et al. Prospects for Observing and Localizing Gravitational-Wave Transients with Advanced LIGO and Advanced Virgo. *Living Rev. Relat.*, 19:1, 2016.
- [7] Andrea Taracchini, Yi Pan, Alessandra Buonanno, Enrico Barausse, Michael Boyle, Tony Chu, Geoffrey Lovelace, Harald P. Pfeiffer, and Mark A. Scheel. Prototype effective-one-body model for nonprecessing spinning inspiral-merger-ringdown waveforms. *Phys. Rev.*, D86:024011, 2012.

- [8] Samantha A. Usman et al. The PyCBC search for gravitational waves from compact binary coalescence. *Class. Quantum Grav.*, 33(21):215004, 2016.
- [9] A. Einstein. Approximative Integration of the Field Equations of Gravitation. *Sitzungsber. K. Preuss. Akad. Wiss.*, 1:688, 1916.
- [10] A. Einstein. Über Gravitationswellen. *Sitzungsber. K. Preuss. Akad. Wiss.*, 1:154–167, 1918.
- [11] Albert Einstein and N. Rosen. On Gravitational waves. *J. Franklin Inst.*, 223:43–54, 1937.
- [12] D. Kennefick. *Traveling at the Speed of Thought: Einstein and the Quest for Gravitational Waves*. Princeton University Press, 2007.
- [13] Peter R. Saulson. Josh goldberg and the physical reality of gravitational waves. *General Relativity and Gravitation*, 43(12):3289–3299, 2011.
- [14] A. Tutukov and L. Yungelson. Evolution of massive close binaries. *Nauchnye Informatsii*, 27:70, 1973.
- [15] Vassiliki Kalogera, K. Belczynski, C. Kim, Richard W. O’Shaughnessy, and B. Willems. Formation of Double Compact Objects. *Phys. Rept.*, 442:75–108, 2007.
- [16] Krzysztof Belczynski, Daniel E. Holz, Tomasz Bulik, and Richard O’Shaughnessy. The first gravitational-wave source from the isolated evolution of two 40-100 Msun stars. *Nature*, 534:512, 2016.
- [17] S. Sigurdsson and L. Hernquist. Primordial black holes in globular clusters. *Nat.*, 364:423–425, July 1993.
- [18] M. C. Miller and V. M. Lauburg. Mergers of Stellar-Mass Black Holes in Nuclear Star Clusters. *Astrophysical J.*, 692:917–923, February 2009.
- [19] C. L. Rodriguez, M. Morscher, B. Pattabiraman, S. Chatterjee, C.-J. Haster, and F. A. Rasio. Binary Black Hole Mergers from Globular Clusters: Implications for Advanced LIGO. *Physical Review Letters*, 115(5):051101, July 2015.

- [20] Fabio Antonini, Sourav Chatterjee, Carl L. Rodriguez, Meagan Morscher, Bharath Pattabiraman, Vicky Kalogera, and Frederic A. Rasio. Black hole mergers and blue stragglers from hierarchical triples formed in globular clusters. *Astrophys. J.*, 816:65, 2016.
- [21] Carl L. Rodriguez, Sourav Chatterjee, and Frederic A. Rasio. Binary Black Hole Mergers from Globular Clusters: Masses, Merger Rates, and the Impact of Stellar Evolution. *Phys. Rev.*, D93(8):084029, 2016.
- [22] I. Mandel and S. E. de Mink. Merging binary black holes formed through chemically homogeneous evolution in short-period stellar binaries. *Mon. Not. Roy. Astr. Soc.*, February 2016.
- [23] S. E. de Mink and I. Mandel. The chemically homogeneous evolutionary channel for binary black hole mergers: rates and properties of gravitational-wave events detectable by advanced LIGO. *Mon. Not. Roy. Astron. Soc.*, 460(4):3545–3553, 2016.
- [24] Pablo Marchant, Norbert Langer, Philipp Podsiadlowski, Thomas M. Tauris, and Takashi J. Moriya. A new route towards merging massive black holes. *Astron. Astrophys.*, 588:A50, 2016.
- [25] Tilman Hartwig, Marta Volonteri, Volker Bromm, Ralf S. Klessen, Enrico Barausse, Mattis Magg, and Athena Stacy. Gravitational Waves from the Remnants of the First Stars. *MNRAS*, 460:L74–78, 2016.
- [26] K. Inayoshi, K. Kashiyama, E. Visbal, and Z. Haiman. Strong gravitational wave background from Population III binary black holes consistent with cosmic reionization. *ArXiv e-prints*, March 2016.
- [27] P. C. Peters. Gravitational Radiation and the Motion of Two Point Masses. *Phys. Rev.*, 136:B1224–B1232, 1964.
- [28] K. Schwarzschild. On the gravitational field of a mass point according to Einstein’s theory. *Sitzungsber. K. Preuss. Akad. Wiss.*, 1:189–196, 1916.
- [29] David Finkelstein. Past-future asymmetry of the gravitational field of a point particle. *Phys. Rev.*, 110:965–967, May 1958.

- [30] M. D. Kruskal. Maximal extension of schwarzschild metric. *Phys. Rev.*, 119:1743–1745, Sep 1960.
- [31] Roy P. Kerr. Gravitational field of a spinning mass as an example of algebraically special metrics. *Phys. Rev. Lett.*, 11:237–238, Sep 1963.
- [32] P. C. Peters and J. Mathews. Gravitational radiation from point masses in a Keplerian orbit. *Phys. Rev.*, 131:435–439, 1963.
- [33] W. H. Press. Long Wave Trains of Gravitational Waves from a Vibrating Black Hole. *ApJL*, 170:L105+, December 1971.
- [34] S. Chandrasekhar and S. Detweiler. The quasi-normal modes of the schwarzschild black hole. *Proceedings of the Royal Society of London A: Mathematical, Physical and Engineering Sciences*, 344(1639):441–452, 1975.
- [35] C. V. Vishveshwara. Scattering of Gravitational Radiation by a Schwarzschild Black-hole. *Nature*, 227:936–938, 1970.
- [36] Luc Blanchet, Thibault Damour, Bala R. Iyer, Clifford M. Will, and Alan G. Wiseman. Gravitational-radiation damping of compact binary systems to second post-newtonian order. *Phys. Rev. Lett.*, 74:3515–3518, May 1995.
- [37] Luc Blanchet. Gravitational radiation from post-Newtonian sources and inspiralling compact binaries. *Living Rev. Rel.*, 5:3, 2002.
- [38] A. Buonanno and T. Damour. Effective one-body approach to general relativistic two-body dynamics. *Phys. Rev. D*, 59:084006, 1999.
- [39] Frans Pretorius. Evolution of binary black hole spacetimes. *Phys. Rev. Lett.*, 95:121101, 2005.
- [40] Manuela Campanelli, C. O. Lousto, and Y. Zlochower. Spinning-black-hole binaries: The orbital hang up. *Phys. Rev. D*, 74:041501, 2006.
- [41] John G. Baker, James R. van Meter, Sean T. McWilliams, Joan Centrella, and Bernard J. Kelly. Consistency of post-Newtonian waveforms with numerical relativity. *Phys. Rev. Lett.*, 99:181101, 2007.

- [42] Andrea Taracchini, Alessandra Buonanno, Yi Pan, Tanja Hinderer, Michael Boyle, et al. Effective-one-body model for black-hole binaries with generic mass ratios and spins. *Phys.Rev.*, D89:061502, 2014.
- [43] Michael Pürrer. Frequency domain reduced order model of aligned-spin effective-one-body waveforms with generic mass-ratios and spins. *Phys. Rev. D*, 93:064041, Mar 2016.
- [44] Patricia Schmidt, Frank Ohme, and Mark Hannam. Towards models of gravitational waveforms from generic binaries II: Modelling precession effects with a single effective precession parameter. *Phys. Rev.*, D91(2):024043, 2015.
- [45] Mark Hannam, Patricia Schmidt, Alejandro Bohè, Lela Haegel, Sascha Husa, Frank Ohme, Geraint Pratten, and Michael Pürrer. Simple Model of Complete Precessing Black-Hole-Binary Gravitational Waveforms. *Phys. Rev. Lett.*, 113(15):151101, 2014.
- [46] Samantha A. Usman et al. An improved pipeline to search for gravitational waves from compact binary coalescence. 2015.
- [47] J. Veitch, V. Raymond, B. Farr, W. Farr, P. Graff, S. Vitale, B. Aylott, K. Blackburn, N. Christensen, M. Coughlin, W. Del Pozzo, F. Feroz, J. Gair, C.-J. Haster, V. Kalogera, T. Littenberg, I. Mandel, R. O’Shaughnessy, M. Pitkin, C. Rodriguez, C. Röver, T. Sidery, R. Smith, M. Van Der Sluys, A. Vecchio, W. Vousden, and L. Wade. Robust parameter estimation for compact binaries with ground-based gravitational-wave observations using the lalinference software library. *Phys. Rev. D*, 91:042003, Feb 2015.
- [48] R. A. Hulse and J. H. Taylor. Discovery of a pulsar in a binary system. *Astroph. J. Lett.*, 195:L51–L53, January 1975.
- [49] J. M. Weisberg and J. H. Taylor. Relativistic binary pulsar b1913+16: Thirty years of observations and analysis. 2004.
- [50] B. Louise Webster and Paul Murdin. Cygnus X-1-a Spectroscopic Binary with a Heavy Companion ? *Nature*, 235:37–38, 1972.

- [51] D.R. Gies and C.T. Bolton. Optical spectrum of hde 226868 = cygnus x-1. ii. spectrophotometry and mass estimates. *Astrophys. J.; (United States)*, 304, May 1986.
- [52] J. Casares and P. G. Jonker. Mass measurements of stellar and intermediate-mass black holes. *Space Science Reviews*, 183(1):223–252, 2014.
- [53] J. Weber. Detection and generation of gravitational waves. *Phys. Rev.*, 117:306–313, Jan 1960.
- [54] P. Astone, L. Baggio, M. Bassan, M. Bignotto, M. Bonaldi, P. Bonifazi, G. Cavallari, M. Cerdonio, E. Coccia, L. Conti, S. D’Antonio, M. di Paolo Emilio, M. Drago, V. Fafone, P. Falferi, S. Foffa, P. Fortini, S. Frasca, G. Giordano, W. O. Hamilton, J. Hanson, W. W. Johnson, N. Liguori, S. Longo, M. Maggiore, F. Marin, A. Marini, M. P. McHugh, R. Mezzena, P. Miller, Y. Minenkov, A. Mion, G. Modestino, A. Moleti, D. Nettles, A. Ortolan, G. V. Pallottino, G. Pizzella, S. Poggi, G. A. Prodi, V. Re, A. Rocchi, F. Ronga, F. Salemi, R. Sturani, L. Taffarello, R. Terenzi, G. Vedovato, A. Vinante, M. Visco, S. Vitale, J. Weaver, J. P. Zendri, and P. Zhang. Igec2: A 17-month search for gravitational wave bursts in 2005~2007. *Phys. Rev. D*, 82:022003, Jul 2010.
- [55] F. A. E. Pirani. *Acta Physica Polonica*, 15:389, 1956.
- [56] M. E. Gertsenshtein and V. I. Pustovoit. On the Detection of Low Frequency Gravitational Waves. *Sov. Phys. JETP*, 16:433, 1962.
- [57] G. E. Moss, L. R. Miller, and R. L. Forward. Photon-noise-limited laser transducer for gravitational antenna. *Appl. Opt.*, 10(11):2495–2498, Nov 1971.
- [58] R Weiss. Electromagnetically coupled broadband gravitational wave antenna. *Quarterly Progress Report, Research Laboratory of Electronics of MIT*, 105:54, April 1972.
- [59] K. S. Thorne R. Vogt R. W. P. Drever, F. J. Raab and R. Weiss. Laser interferometer gravitational-wave observatory (ligo) technical report. Technical Report LIGO-M890001, 1989.

- [60] A. Giazotto A. Brillet and othersw. Virgo project technical report. Technical Report LIGO-P720002, 1989.
- [61] J. Hough et al. Proposal for a joint german-british interferometric gravitational wave detector. Technical report, 1989.
- [62] Alex Abramovici et al. LIGO: The laser interferometer gravitational wave observatory. 256:325, 1992.
- [63] M. Ando et al. Stable operation of a 300-m laser interferometer with sufficient sensitivity to detect gravitational-wave events within our galaxy. 86:3950–3954, 2001.
- [64] H. Grote. The GEO 600 status. *Class. Quantum Grav.*, 27:084003, 2010.
- [65] B. Abbott et al. LIGO: The Laser Interferometer Gravitational-Wave Observatory. *Rept. Prog. Phys.*, 72:076901, 2009.
- [66] F. Acernese et al. Status of VIRGO. *Class. Quantum Grav.*, 22:S869–S880, 2005.
- [67] B. Abbott et al. Search for gravitational waves from binary black hole inspirals in LIGO data. *Phys. Rev. D*, 73:062001, 2006.
- [68] B. Abbott et al. Search of S3 LIGO data for gravitational wave signals from spinning black hole and neutron star binary inspirals. *Phys. Rev.*, D78:042002, 2008.
- [69] B. Abbott et al. Search for gravitational waves from binary inspirals in S3 and S4 LIGO data. *Phys. Rev.*, D77:062002, 2008.
- [70] J. Abadie et al. Search for Gravitational Waves from Compact Binary Coalescence in LIGO and Virgo Data from S5 and VSR1. *Phys. Rev.*, D82:102001, 2010.
- [71] J. Aasi et al. Search for Gravitational Waves from Binary Black Hole Inspiral, Merger and Ringdown in LIGO-Virgo Data from 2009-2010. *Phys.Rev.*, D87:022002, 2013.

- [72] J. Aasi et al. Advanced LIGO. *Class. Quantum Grav.*, 32:074001, 2015.
- [73] B. P. Abbott, R. Abbott, T. D. Abbott, et al. GW150914: The Advanced LIGO Detectors in the Era of First Discoveries. *Phys. Rev. Lett.*, 116:131103, 2016.
- [74] J. Aasi et al. Advanced LIGO. *Class. Quantum Grav.*, 32:074001, 2015.
- [75] B. P. Abbott et al. Binary Black Hole Mergers in the first Advanced LIGO Observing Run, 2016.
- [76] B. P. Abbott, R. Abbott, T. D. Abbott, et al. Observation of gravitational waves from a binary black hole merger. *Phys. Rev. Lett.*, 116:061102, 2016.
- [77] B.P. Abbott et al. GW151226: Observation of Gravitational Waves from a 22-Solar-Mass Binary Black Hole Coalescence. *Phys. Rev. Lett.*, 116(24):241103, 2016.
- [78] B. P. Abbott, R. Abbott, T. D. Abbott, et al. The Rate of Binary Black Hole Mergers Inferred from Advanced LIGO Observations Surrounding GW150914. *Astrophys. J. Lett.*, 833(1), 2016.
- [79] Tito Dal Canton et al. Implementing a search for aligned-spin neutron star-black hole systems with advanced ground based gravitational wave detectors. *Phys. Rev.*, D90(8):082004, 2014.
- [80] Ian W. Harry, Bruce Allen, and B.S. Sathyaprakash. A Stochastic template placement algorithm for gravitational wave data analysis. *Phys. Rev. D*, 80:104014, 2009.
- [81] Duncan A. Brown, Ian Harry, Andrew Lundgren, and Alexander H. Nitz. Detecting binary neutron star systems with spin in advanced gravitational-wave detectors. *Phys.Rev.*, D86:084017, 2012.
- [82] Stephen Privitera, Satyanarayan R. P. Mohapatra, Parameswaran Ajith, Kipp Cannon, Nickolas Fotopoulos, Melissa A. Frei, Chad Hanna, Alan J. Weinstein, and John T. Whelan. Improving the sensitivity of a search for coalescing binary black holes with nonprecessing spins in gravitational wave data. *Phys. Rev.*, D89(2):024003, 2014.

- [83] Collin Capano, Thomas Dent, Yi-Ming Hu, Martin Hendry, Chris Messenger, and John Veitch. Systematic errors in estimation of gravitational-wave candidate significance. 2016.
- [84] B. P. Abbott, R. Abbott, T. D. Abbott, et al. Properties of the binary black hole merger GW150914. *Phys. Rev. Lett.*, 116(24):241102, 2016.
- [85] D. V. Martynov, E. D. Hall, et al. Sensitivity of the advanced ligo detectors at the beginning of gravitational wave astronomy. *Phys. Rev. D*, 93:112004, Jun 2016.
- [86] Peter R. Saulson. Thermal noise in mechanical experiments. *Phys. Rev. D*, 42:2437–2445, Oct 1990.
- [87] B. P. Abbott et al. Characterization of the advanced ligo detectors for binary merger searches. 2016.
- [88] Eanna E. Flanagan and Scott A. Hughes. Measuring gravitational waves from binary black hole coalescences: 1. Signal-to-noise for inspiral, merger, and ring-down. *Phys. Rev. D*, 57:4535–4565, 1998.
- [89] L A Wainstein and V D Zubakov. *Extraction of signals from noise*. Prentice-Hall, Englewood Cliffs, NJ, 1962.
- [90] Alexander H. Nitz, Ian W. Harry, Joshua L. Willis, Christopher M. Biwer, Duncan A. Brown, Larne P. Pekowsky, T. Dal Canton, Andrew R. Williamson, Thomas Dent, Collin D. Capano, Thomas J. Massinger, Amber K. Lenon, Alex B. Nielsen, and Miriam Cabero. PyCBC Software. <https://github.com/ligo-cbc/pycbc>, 2016.
- [91] Luc Blanchet. Gravitational radiation from post-Newtonian sources and inspiralling compact binaries. *Living Rev. Rel.*, 9:3, 2006.
- [92] Luc Blanchet, Alessandra Buonanno, and Guillaume Faye. Higher-order spin effects in the dynamics of compact binaries II. Radiation field. *Phys. Rev. D*, 74:104034, 2006.

- [93] C. W. Helmstrom. *Statistical Theory of Signal Detection, 2nd edition*. Pergamon Press, London, 1968.
- [94] Bruce Allen, Warren G. Anderson, Patrick R. Brady, Duncan A. Brown, and Jolien D. E. Creighton. FINDCHIRP: An Algorithm for detection of gravitational waves from inspiraling compact binaries. *Phys. Rev. D*, 85:122006, 2012.
- [95] C Cutler and E Flanagan. Gravitational waves from merging compact binaries: How accurately can one extract the binary’s parameters from the inspiral waveform? *Phys. Rev. D*, 49:2658, 1994.
- [96] Luc Blanchet, Bala R. Iyer, Clifford M. Will, and Alan G. Wiseman. Gravitational wave forms from inspiralling compact binaries to second postNewtonian order. *Class. Quantum Grav.*, 13:575–584, 1996.
- [97] Luc Blanchet, Thibault Damour, Bala R. Iyer, Clifford M. Will, and Alan. G. Wiseman. Gravitational-radiation damping of compact binary systems to second post-Newtonian order. *Phys. Rev. Lett.*, 74:3515–3518, 1995.
- [98] Thibault Damour. Coalescence of two spinning black holes: An effective one-body approach. *Phys. Rev. D*, 64:124013, 2001.
- [99] Etienne Racine. Analysis of spin precession in binary black hole systems including quadrupole-monopole interaction. *Phys. Rev.*, D78:044021, 2008.
- [100] P. Ajith, M. Hannam, S. Husa, Y. Chen, B. Brügmann, N. Dorband, D. Müller, F. Ohme, D. Pollney, C. Reisswig, L. Santamaría, and J. Seiler. Inspiral-merger-ringdown waveforms for black-hole binaries with nonprecessing spins. *Phys. Rev. Lett.*, 106(24):241101, Jun 2011.
- [101] L. Santamaría, F. Ohme, P. Ajith, B. Brügmann, N. Dorband, M. Hannam, S. Husa, P. Moesta, D. Pollney, C. Reisswig, E. L. Robinson, J. Seiler, and B. Krishnan. Matching post-newtonian and numerical relativity waveforms: systematic errors and a new phenomenological model for non-precessing black hole binaries. *Phys. Rev. D*, 82:064016, 2010.

- [102] Alex B. Nielsen. Compact binary coalescence parameter estimations for 2.5 post-Newtonian aligned spinning waveforms. *Class. Quant. Grav.*, 30:075023, 2013.
- [103] Frank Ohme, Alex B. Nielsen, Drew Keppel, and Andrew Lundgren. Statistical and systematic errors for gravitational-wave inspiral signals: A principal component analysis. *Phys. Rev.*, D88(4):042002, 2013.
- [104] I.W. Harry, S. Privitera, A. Bohe, and A. Buonanno. *In preparation*, 2016.
- [105] B. P. Abbott et al. Upper limits on the rates of binary neutron star and neutron-star–black-hole mergers from Advanced LIGO’s first observing run. 2016.
- [106] Bruce Allen. A χ^2 time-frequency discriminator for gravitational wave detection. *Phys. Rev. D*, 71:062001, 2005.
- [107] B. P. Abbott, R. Abbott, T. D. Abbott, et al. GW150914: First results from the search for binary black hole coalescence with Advanced LIGO. *Phys. Rev. D*, 93:122003, 2016.
- [108] B. P. Abbott, R. Abbott, T. D. Abbott, et al. Characterization of transient noise in Advanced LIGO relevant to gravitational wave signal GW150914. *Class. Quantum Grav.*, 33:134001, 2016.
- [109] A. Effler, R. M. S. Schofield, V. V. Frolov, G. Gonzalez, K. Kawabe, J. R. Smith, J. Birch, and R. McCarthy. Environmental Influences on the LIGO Gravitational Wave Detectors during the 6th Science Run. *Class. Quantum Grav.*, 32(3):035017, 2015.
- [110] B. P. Abbott et al. Observation of Gravitational Waves from a Binary Black Hole Merger. *Phys. Rev. Lett.*, 116(6):061102, 2016.
- [111] B. P. Abbott et al. Calibration of the Advanced LIGO detectors for the discovery of the binary black-hole merger GW150914. 2016.
- [112] Duncan A Brown. *Search for gravitational radiation from black hole MACHOs in the Galactic halo*. PhD thesis, University of Wisconsin–Milwaukee, 2004.

- [113] Bruce Allen. LIGO calibration accuracy. Technical Report LIGO-T960189-00-Z, LIGO Project, 1996.
- [114] D. A. Brown (for the LIGO Scientific Collaboration). Testing the LIGO inspiral analysis with hardware injections. *Class. Quantum Grav.*, 21:S797–S800, 2004.
- [115] L. S. Finn and D. F. Chernoff. Observing binary inspiral in gravitational radiation: One interferometer. *Phys. Rev. D*, 47:2198–2219, March 1993.
- [116] J. Abadie et al. Predictions for the rates of compact binary coalescences observable by ground-based gravitational-wave detectors. *Class. Quantum Grav.*, 27:173001, March 2010.
- [117] Xavier Siemens, Bruce Allen, Jolien Creighton, Martin Hewitson, and Michael Landry. Making $h(t)$ for LIGO. *Class. Quantum Grav.*, 21:S1723–S1736, 2004.
- [118] D. Tuyenbayev et al. Improving LIGO calibration accuracy by tracking and compensating for slow temporal variations. *Class. Quantum Grav.*, 34(1):015002, 2017.
- [119] Alessandra Buonanno and Yanbei Chen. Signal recycled laser-interferometer gravitational-wave detectors as optical springs. *Phys. Rev. D*, 65:042001, Jan 2002.
- [120] E. Hall. *Long-baseline laser interferometry for the detection of binary black-hole mergers*. PhD thesis, California Institute of Technology, 2017.
- [121] L. Carbone et al. Sensors and Actuators for the Advanced LIGO Mirror Suspensions. *Class. Quantum Grav.*, 29:115005, 2012.
- [122] Bruce Allen. A χ^2 time-frequency discriminator for gravitational wave detection. *Phys. Rev. D*, 71:062001, 2005.
- [123] Marta Burgay et al. An increased estimate of the merger rate of double neutron stars from observations of a highly relativistic system. *Nature.*, 426:531–533, 2003.

- [124] John Veitch and Alberto Vecchio. Assigning confidence to inspiral gravitational wave candidates with Bayesian model selection. *Class. Quantum Grav.*, 25:184010, 2008.
- [125] J. Whelan. Laser interferometer gravitational-wave observatory (ligo) technical report. Technical Report LIGO-T1100431, 2012.
- [126] Duncan A. Brown. *Searching for gravitational radiation from binary black hole MACHOs in the galactic halo*. PhD thesis, Wisconsin U., Milwaukee, 2004.
- [127] John E. Angus. The probability integral transform and related results. *SIAM Review*, 36(4):652–654, 1994.
- [128] Andrew Gelman and Donald B. Rubin. Inference from Iterative Simulation Using Multiple Sequences. *Statist. Sci.*, 7:457–472, 1992.
- [129] Stephen P. Brooks and Andrew Gelman. General methods for monitoring convergence of iterative simulations. *Journal of Computational and Graphical Statistics*, 7(4):434–455, 1998.
- [130] A. Gelman and D. B. Rubin. Inference from iterative simulation using multiple sequences. *Statistical Science*, 7:457–472, 1992.
- [131] Daniel Foreman-Mackey, David W. Hogg, Dustin Lang, and Jonathan Goodman. emcee: The MCMC Hammer. *Publ. Astron. Soc. Pac.*, 125:306–312, 2013.
- [132] B. Farr and W. M. Farr. kombine: a kernel-density-based, embarrassingly parallel ensemble sampler. 2015. in prep.
- [133] Benjamin Farr, Vicky Kalogera, and Erik Lijten. A more efficient approach to parallel-tempered Markov-chain Monte Carlo for the highly structured posteriors of gravitational-wave signals. *Phys. Rev.*, D90(2):024014, 2014.
- [134] emcee testimonials. <http://dan.iel.fm/emcee/current/testimonials/>. Accessed: 2017-07-27.
- [135] Jonathan Goodman and Jonathan Weare. Ensemble samplers with affine invariance. *Comm. App. Math. and Comp. Sci.*, 5:1, 2010.

- [136] W. K. Hastings. Monte Carlo Sampling Methods Using Markov Chains and Their Applications. *Biometrika*, 57:97–109, 1970.
- [137] Siddhartha Chib and Edward Greenberg. Understanding the metropolis-hastings algorithm. *The American Statistician*, 49(4):327–335, 1995.
- [138] Jörg Sander, Xuejie Qin, Zhiyong Lu, Nan Niu, and Alex Kovarsky. Automatic extraction of clusters from hierarchical clustering representations. In *Proceedings of the 7th Pacific-Asia Conference on Advances in Knowledge Discovery and Data Mining*, PAKDD '03, pages 75–87, Berlin, Heidelberg, 2003. Springer-Verlag.
- [139] LSC Data Analysis Software Working Group. LALSuite. <https://www.lsc-group.phys.uwm.edu/daswg/projects/lalsuite.html>.
- [140] B. P. Abbott et al. GW151226: Observation of Gravitational Waves from a 22-Solar-Mass Binary Black Hole Coalescence. *Phys. Rev. Lett.*, 116(24):241103, 2016.
- [141] J. Skilling. Nested sampling for general Bayesian computation. *Bayesian Analysis*, 1(4):833–860, 2006.
- [142] B. P. Abbott et al. Properties of the Binary Black Hole Merger GW150914. *Phys. Rev. Lett.*, 116(24):241102, 2016.
- [143] F. Feroz and M. P. Hobson. Multimodal nested sampling: an efficient and robust alternative to Markov Chain Monte Carlo methods for astronomical data analyses. *Mon. Not. Roy. Astr. Soc.*, 384:449–463, February 2008.
- [144] F. Feroz, M. P. Hobson, and M. Bridges. MULTINEST: an efficient and robust Bayesian inference tool for cosmology and particle physics. *Mon. Not. Roy. Astr. Soc.*, 398:1601–1614, October 2009.
- [145] F. Feroz, M. P. Hobson, E. Cameron, and A. N. Pettitt. Importance Nested Sampling and the MultiNest Algorithm. *ArXiv e-prints*, June 2013.
- [146] B. Farr and W. Farr. Modelling Calibration Errors In CBC Waveforms, 2014.

- [147] N. Chamel, P. Haensel, J. L. Zdunik, and A. F. Fantina. On the Maximum Mass of Neutron Stars. *Int. J. Mod. Phys.*, E22:1330018, 2013.
- [148] Blent Kiziltan, Athanasios Kottas, Maria De Yoreo, and Stephen E. Thorsett. The Neutron Star Mass Distribution. *Astrophys. J.*, 778:66, 2013.
- [149] Corral-Santana, J. M., Casares, J., Muoz-Darias, T., Bauer, F. E., Martnez-Pais, I. G., and Russell, D. M. Blackcat: A catalogue of stellar-mass black holes in x-ray transients. *A&A*, 587:A61, 2016.
- [150] B. E. Tetarenko, G. R. Sivakoff, C. O. Heinke, and J. C. Gladstone. Watchdog: A comprehensive all-sky database of galactic black hole x-ray binaries. *The Astrophysical Journal Supplement Series*, 222(2):15, 2016.
- [151] Z. Barkat, G. Rakavy, and N. Sack. Dynamics of Supernova Explosion Resulting from Pair Formation. *Physical Review Letters*, 18:379–381, March 1967.
- [152] G. Rakavy and G. Shaviv. Instabilities in Highly Evolved Stellar Models. *Astrophysical J.*, 148:803, June 1967.
- [153] G. Rakavy and G. Shaviv. Isentropic Models for Final Stages of Stellar Evolution. *Ap&SS*, 1:429–441, June 1968.
- [154] G. S. Fraley. Supernovae Explosions Induced by Pair-Production Instability. *Ap&SS*, 2:96–114, August 1968.
- [155] S. E. Woosley. Pulsational Pair-instability Supernovae. *Astrophysical J.*, 836:244, February 2017.
- [156] S. E. Woosley. Pulsational Pair-Instability Supernovae. *Astrophys. J.*, 836(2):244, 2017.
- [157] K. Belczynski et al. The Effect of Pair-Instability Mass Loss on Black Hole Mergers. 2016.
- [158] B. P. Abbott et al. *Phys. Rev. X*, 6:041015, Oct 2016.
- [159] Alejandro Bohé et al. Improved effective-one-body model of spinning, non-precessing binary black holes for the era of gravitational-wave astrophysics with advanced detectors. *Phys. Rev.*, D95(4):044028, 2017.

- [160] J. Abadie et al. Search for Gravitational Waves from Low Mass Compact Binary Coalescence in LIGO's Sixth Science Run and Virgo's Science Runs 2 and 3. *Phys. Rev.*, D85:082002, 2012.
- [161] J. Abadie et al. All-sky search for gravitational-wave bursts in the first joint LIGO-GEO-Virgo run. *Phys.Rev.*, D81:102001, 2010.
- [162] S6 Detector Characterization Paper; in preparation for publication.
- [163] B. P. Abbott et al. GW150914: The Advanced LIGO Detectors in the Era of First Discoveries. *Phys. Rev. Lett.*, 116(13):131103, 2016.
- [164] Keita Kawabe. *Development of a 3-meter Fabry-Perot-Michelson Interferometer for Gravitational Wave Detection*. PhD thesis, University of Tokyo, 1998.
- [165] M. Rakhmanov, J. D. Romano, and J. T. Whelan. High-frequency corrections to the detector response and their effect on searches for gravitational waves. *Class. Quantum Grav.*, 25:184017, 2008.
- [166] R Weiss. Various Reports of Experiments Conducted on the Barkhausen Noise Research, 2009.
- [167] Joshua R Smith. The Path to the enhanced and advanced LIGO gravitational-wave detectors. *Class. Quantum Grav.*, 26:114013, 2009.
- [168] S. Karki et al. The Advanced LIGO Photon Calibrators. 2016.
- [169] Benjamin P. Abbott et al. Upper limits on the rates of binary neutron star and neutron-star-black-hole mergers from Advanced LIGO's first observing run. 2016.
- [170] Michele Maggiore. Gravitational wave experiments and early universe cosmology. *Phys. Rept.*, 331:283-367, 2000.
- [171] J. Aasi et al. Gravitational waves from known pulsars: results from the initial detector era. *Astrophys. J.*, 785:119, 2014.
- [172] J. Rollins. Advanced LIGO Guardian Documentation, 2015.

- [173] L Canete. Implementation of an Optical Follower Servo for the aLIGO Pcal, 2014.
- [174] E Goetz, P Kalmus, S Erickson, R L Savage, G Gonzalez, K Kawabe, M Landry, S Marka, B O'Reilly, K Riles, D Sigg, and P Willems. Precise calibration of LIGO test mass actuators using photon radiation pressure. *Class. Quantum Grav.*, 26:245011, 2009.
- [175] Alex Nitz, Ian Harry, Christopher M. Biwer, Duncan A. Brown, Josh Willis, Larne Pekowsky, Tito Dal Canton, Thomas Dent, Andrew R. Williamson, Collin Capano, Prayush Kumar, Soumi De, Miriam Cabero, Amber Lenon, Thomas Massinger, Stephen Fairhurst, Alex Nielsen, Bernd Machenschalk, Steven Reyes, Stanislav Babak, Leo Singer, Duncan Macleod, John Veitch, Peter Couvares, Lorena Magana Zertuche, Brian Bockelman, Vaibhav Tewari, and Sebastian Khan. Pycbc software, December 2016.
- [176] B. P. Abbott et al. Characterization of transient noise in Advanced LIGO relevant to gravitational wave signal GW150914. *Class. Quantum Grav.*, 33(13):134001, 2016.
- [177] Bruce Allen. A χ^2 time-frequency discriminator for gravitational wave detection. *Phys. Rev.*, D71:062001, 2005.
- [178] L. Singer et al., 2015.
- [179] L. Singer et al., 2015.
- [180] LIGO Scientific Collaboration and the Virgo Collaboration, 2016.
- [181] A. Effler, R. M. S. Schofield, V. V. Frolov, G. Gonzalez, K. Kawabe, J. R. Smith, J. Birch, and R. McCarthy. Environmental Influences on the LIGO Gravitational Wave Detectors during the 6th Science Run. *Class. Quantum Grav.*, 32(3):035017, 2015.
- [182] S. Chatterji, L. Blackburn, G. Martin, and E. Katsavounidis. Multiresolution techniques for the detection of gravitational-wave bursts. *Class. Quantum Grav.*, 21:S1809–S1818, 2004.

- [183] Joshua R. Smith, Thomas Abbott, Eiichi Hirose, Nicolas Leroy, Duncan Macleod, Jessica McIver, Peter Saulson, and Peter Shawhan. A Hierarchical method for vetoing noise transients in gravitational-wave detectors. *Class. Quantum Grav.*, 28:235005, 2011.
- [184] Stuart Anderson and Roy Williams. Ligo data management plan: August 2016. Technical Report M1000066, LIGO and Virgo Scientific Collaborations, <https://dcc.ligo.org/LIGO-M1000066>, 2016.
- [185] C. Biwer et al. Validating gravitational-wave detections: The Advanced LIGO hardware injection system. *Phys. Rev.*, D95(6):062002, 2017.
- [186] GraCEDb. <https://www.lsc-group.phys.uwm.edu/daswg/projects/gracedb.html>.
- [187] R. Fisher, D. Macleod, A. Mullavey, E. Thrane, and J. Betzwieser. CAL-INJ ODC documentation, 2015.
- [188] LSC Data Analysis Software Working Group. Data monitoring tool. <https://www.lsc-group.phys.uwm.edu/daswg/projects/dmt.html>.
- [189] Salvatore Vitale, Walter Del Pozzo, Tjonnie G. F. Li, Chris Van Den Broeck, Ilya Mandel, Ben Aylott, and John Veitch. Effect of calibration errors on Bayesian parameter estimation for gravitational wave signals from inspiral binary systems in the Advanced Detectors era. *Phys. Rev.*, D85:064034, 2012.

Christopher M. Biwer

Postal Address Department of Physics
Syracuse University
Syracuse, NY 13244-1130, USA

Telephone +1 414-858-8414

E-mail christopher.biwer@ligo.org

Citizenship United States of America

Employment

- 2013 – Present **Research Assistant**, Department of Physics, Syracuse University.
- 2012 – 2013 **Teaching Assistant**, Department of Physics, Syracuse University.
- 2009 – 2012 **Research Assistant**, Center for Gravitation, Cosmology, and Astrophysics, University of Wisconsin-Milwaukee.

Education

- 2012 – Present **Ph.D. Candidate in Physics**, Syracuse University.
Expected completion: Summer 2017
Supervisor: Prof. Duncan Brown
- 2011 **B.S. in Applied Mathematics and Physics**, University of Wisconsin-Milwaukee.

Experience

Teaching Experience

- 2013 **AST 101 Astronomy Laboratory Teaching Assistant**, Department of Physics, Syracuse University.
- 2012 – 2013 **PHY 221 Physics Laboratory Teaching Assistant**, Department of Physics, Syracuse University.

Computing Experience

Programming languages: Python, C, and Java.

High-throughput computing: Open Science Grid, Pegasus, and Condor.

Web application frameworks: Django.

Professional Development

- 2016 **Open Science Grid User School**, Department of Computer Science, University of Wisconsin-Madison.

Honors, Awards, and Scholarships

- 2016 Breakthrough Prize in Fundamental Physics - as part of the LIGO Scientific Collaboration
- 2016 Gruber Cosmology Prize - as part of the LIGO Scientific Collaboration
- 2016 Open Science Grid User School Travel Grant

- 2016 LIGO-Hanford Observatory Visitor
- 2016 American Physical Society Travel Grant
- 2015 LIGO-Hanford Observatory Fellow
- 2013 Syracuse University College of Letters and Science Summer Fellowship
- 2013 Syracuse University Physics Department Levinstein Fellowship
- 2012 North American Nanohertz Observatory for Gravitational Waves Scholarship
- 2012 University of Wisconsin-Milwaukee Physics Department James Martin Scholarship for the best performance in Modern Physics
- 2011 LIGO-Caltech Summer Undergraduate Research Fellow
- 2011 National Science Foundation Fellowship in Biological Mathematics

Outreach Activities

- 2016 LIGO Open Science Center - I developed a high-throughput pipeline that was used to record hardware injections in preparation for a public data release.
- 2013, 2014 Syracuse University Summer Scholars Enrichment Program - I organized a week-long program of physics demonstrations for local high school students.
- 2011 – 2012 Alliance School of Milwaukee - I was an algebra and geometry mentor for high school students at an anti-bullying charter school.

Presentations

- Talk ‘*Status of searches for compact binaries in aLIGO with PyCBC*’
April 2016 American Physical Society April Meeting, Salt Lake City, USA
- Plenary Talk ‘*Hardware injections of simulated gravitational-wave signals*’
March 2016 LIGO-Virgo Collaboration Meeting, Pasadena, USA
- Poster ‘*Review progress of the PyCBC offline search*’
March 2016 LIGO-Virgo Collaboration Meeting, Pasadena, USA
- Plenary Talk ‘*Update on daily ihope analysis of L1 lock stretches*’
August 2014 LIGO-Virgo Collaboration Meeting, Stanford University, USA
- Poster ‘*Offline ihope analysis during ER5*’
March 2014 LIGO-Virgo Collaboration Meeting, Nice, France
- Poster ‘*Detector characterization with daily ihope during ER5*’
March 2014 LIGO-Virgo Collaboration Meeting, Nice, France

Publications

Publications (including LIGO Scientific Collaboration papers) to which I have made a significant contribution.

C. Biwer et al., ‘*Validating gravitational-wave detections: The Advanced LIGO hardware injection system*’, to be submitted to Phys. Rev. D (2016)

B. P. Abbott et al. (**LIGO Scientific Collaboration**) ‘*Upper limits on the rates of binary neutron star and neutron-star–black-hole mergers from Advanced LIGO’s first observing run*’, arXiv:1607.07456 (2016)

B. P. Abbott et al. (**LIGO Scientific Collaboration**) ‘*The Rate of Binary Black Hole Mergers Inferred from Advanced LIGO Observations Surrounding GW150914*’, arXiv:1602.03842, accepted by ApJL (2016)

B. P. Abbott et al. (**LIGO Scientific Collaboration**), ‘*Binary Black Hole Mergers in the First Advanced LIGO Observing Run*’, Phys. Rev. X., 6, 041015 (2016)

B. P. Abbott et al. (**LIGO Scientific Collaboration**), ‘*GW151226: Observation of Gravitational Waves from a 22-Solar-Mass Binary Black Hole Coalescence*’, Phys. Rev. Lett., 116, 241103 (2016)

B. P. Abbott et al. (**LIGO Scientific Collaboration**), ‘*GW150914: First results from the search for binary black hole coalescence with Advanced LIGO*’, Phys. Rev. D 93, 122003 (2016)

B. P. Abbott et al. (**LIGO Scientific Collaboration**), ‘*Observation of Gravitational Waves from a Binary Black Hole Merger*’, Phys. Rev. Lett., 116, 061102 (2016)

S. A. Usman, A. H. Nitz, I. W. Harry, **C. M. Biwer** et al., ‘*The PyCBC search for gravitational waves from compact binary coalescence*’, Class. Quantum Grav. 33, 215004 (2016)

A. R. Williamson, **C. Biwer**, S. Fairhurst, I. W. Harry, E. Macdonald, D. Macleod, and V. Predoi, ‘*Improved methods for detecting gravitational waves associated with short gamma-ray bursts*’, Phys. Rev. D 90, 122004 (2014)

K. Stovall, R. S. Lynch, S. M. Ransom, A. M. Archibald, S. Banaszak, **C. M. Biwer** et al., ‘*The Green Bank Northern Celestial Cap Pulsar Survey - I: Survey Description, Data Analysis, and Initial Results*’, ApJ 791, 67 (2014)

R. S. Lynch, A. M. Archibald, S. Banaszak, A. Becker, A. Berndsen, **C. Biwer** et al. ‘*The hunt for new pulsars with the Green Bank Telescope*’, IAU Symp. 291 (2013)

Other Publications

As an active member of the LIGO Scientific Collaboration and former student working in the NANOGrav Collaboration the following publications are those for which I hold authorship rights.

B. P. Abbott et al. (**LIGO Scientific Collaboration**) ‘*All-sky search for short gravitational-wave bursts in the first Advanced LIGO run*’, arXiv:1611.02972 (2016)

B. P. Abbott et al. (**LIGO Scientific Collaboration**) ‘*Exploring the Sensitivity of Next Generation Gravitational Wave Detectors*’, arXiv:1607.08697 (2016)

B. P. Abbott et al. (**LIGO Scientific Collaboration**) ‘*Search for continuous gravitational waves from neutron stars in globular cluster NGC 6544*’, arXiv:1607.02216 (2016)

B. P. Abbott et al. (**LIGO Scientific Collaboration**) ‘*Supplement: The Rate of Binary Black Hole Mergers Inferred from Advanced LIGO Observations Surrounding GW150914*’, arXiv:1606.03939, accepted by ApJS (2016)

B. P. Abbott et al. (**LIGO Scientific Collaboration**) ‘*The basic physics of the binary black hole merger GW150914*’, Annalen Phys. (2016)

B. P. Abbott et al. (**LIGO Scientific Collaboration**) ‘*Directly comparing GW150914 with numerical solutions of Einstein’s equations for binary black hole coalescence*’, Phys. Rev. D 94, 064035 (2016)

B. P. Abbott et al. (**LIGO Scientific Collaboration**) ‘*An improved analysis of GW150914 using a fully spin-precessing waveform model*’, Phys. Rev. X 6, 041014 (2016)

B. P. Abbott et al. (**LIGO Scientific Collaboration**) ‘*Comprehensive All-sky Search for Periodic Gravitational Waves in the Sixth Science Run LIGO Data*’, Phys. Rev. D 94, 042002 (2016)

B. P. Abbott et al., (**LIGO Scientific Collaboration**) ‘*Results of the Deepest All-Sky Survey for Continuous Gravitational Waves on LIGO S6 Data Running on the Einstein@Home Volunteer Distributed Computing Project*’, arXiv:1606.09619 (2016)

- B. P. Abbott et al. (**LIGO Scientific Collaboration**) ‘*A First Targeted Search for Gravitational-Wave Bursts from Core-Collapse Supernovae in Data of First-Generation Laser Interferometer Detectors*’, Phys. Rev. D 94, 102001 (2016)
- B. P. Abbott et al., (**LIGO Scientific Collaboration**) ‘*Calibration of the Advanced LIGO Detectors for the Discovery of the Binary Black-Hole Merger GW150914*’, arXiv:1602.03845 (2016)
- B. P. Abbott et al. (**LIGO Scientific Collaboration**) ‘*Search for transient gravitational waves in coincidence with short duration radio transients during 2007-2013*’, Phys. Rev. D 93, 122008 (2016)
- B. P. Abbott et al., (**LIGO Scientific Collaboration**) ‘*Observing Gravitational-Wave Transient GW150914 with Minimal Assumptions*’, Phys. Rev. D., 93, 122004 (2016)
- B. P. Abbott et al., (**LIGO Scientific Collaboration**) ‘*Tests of General Relativity with GW150914*’, Phys. Rev. Lett., 116, 221101 (2016)
- B. P. Abbott et al., (**LIGO Scientific Collaboration**) ‘*GW150914: The Advanced LIGO Detectors in the Era of First Discoveries*’, Phys. Rev. Lett., 116, 131103 (2016)
- B. P. Abbott et al., (**LIGO Scientific Collaboration**) ‘*GW150914: Implications for the Stochastic Gravitational Wave Background from Binary Black Holes*’, Phys. Rev. Lett., 116, 131102 (2016)
- B. P. Abbott et al., (**LIGO Scientific Collaboration**) ‘*Astrophysical Implications of the Binary Black Hole Merger GW150914*’, ApJL, 818, 2 (2016)
- B. P. Abbott et al., (**LIGO Scientific Collaboration**) ‘*Characterization of Transient Noise in Advanced LIGO relevant to Gravitational Wave Signal GW150914*’, Class. Quantum Grav. 33, 134001 (2016)
- D. V. Martynov, ..., **C. Biwer** et al. ‘*The Sensitivity of the Advanced LIGO Detectors at the Beginning of Gravitational Wave Astronomy*’, Phys. Rev. D 93, 112004 (2016)
- B. P. Abbott et al. (**LIGO Scientific Collaboration**) ‘*Supplement: Localization and broadband follow-up of the gravitational-wave transient GW150914*’, ApJS 255, 8 (2016)
- B. P. Abbott et al. (**LIGO Scientific Collaboration**) ‘*Localization and broadband follow-up of the gravitational-wave transient GW150914*’, ApJ 826, L13 (2016)
- B. P. Abbott et al. (**LIGO Scientific Collaboration**) ‘*High-energy Neutrino follow-up search of Gravitational Wave Event GW150914 with ANTARES and IceCube*’, Phys. Rev. D 93, 122010 (2016)
- B. P. Abbott et al. (**LIGO Scientific Collaboration**) ‘*Properties of the Binary Black Hole Merger GW150914*’, Phys. Rev. Lett. 116, 241102 (2016)
- B. P. Abbott et al. (**LIGO Scientific Collaboration**) ‘*Prospects for Observing and Localizing Gravitational-Wave Transients with Advanced LIGO and Advanced Virgo*’, Living Reviews in Relativity 19, 1 (2016)
- B. P. Abbott et al. (**LIGO Scientific Collaboration**) ‘*All-sky search for long-duration gravitational wave transients with LIGO*’, Phys. Rev. D 93, 042005 (2016)
- J. Aasi et al. (**LIGO Scientific Collaboration**) ‘*First low frequency all-sky search for continuous gravitational wave signals*’, Phys. Rev. D 93, 042007 (2016)
- J. Aasi et al. (**LIGO Scientific Collaboration**) ‘*A search of the Orion spur for continuous gravitational waves using a "loosely coherent" algorithm on data from LIGO interferometers*’, Phys. Rev. D 93, 042006 (2016)
- J. Aasi et al. (**LIGO Scientific Collaboration**) ‘*Searches for continuous gravitational waves from nine young supernova remnants*’, ApJ 813, 39 (2015)

- J. Aasi et al., (**LIGO Scientific Collaboration**) ‘*Advanced LIGO*’, *Class. Quantum Grav.*, 32, 074001 (2015)
- J. Aasi et al. (**LIGO Scientific Collaboration**) ‘*A directed search for gravitational waves from Scorpius X-1 with initial LIGO*’, *Phys. Rev. D* 91, 062008 (2015)
- J. Aasi et al. (**LIGO Scientific Collaboration**) ‘*Narrow-band search of continuous gravitational-wave signals from Crab and Vela pulsars in Virgo VSR4 data*’, *Phys. Rev. D* 91, 022004 (2015)
- M. G. Aartsen et al. (**LIGO Scientific Collaboration**) ‘*Multimessenger Search for Sources of Gravitational Waves and High-Energy Neutrinos: Results for Initial LIGO-Virgo and IceCube*’, *Phys. Rev. D* 90, 102002 (2014)
- J. Aasi et al. (**LIGO Scientific Collaboration**) ‘*Methods and results of a search for gravitational waves associated with gamma-ray bursts using the GEO600, LIGO, and Virgo detectors*’, *Phys. Rev. D* 89, 122004 (2014)
- J. Aasi et al. (**LIGO Scientific Collaboration**) ‘*Search for gravitational waves associated with gamma-ray bursts detected by the InterPlanetary Network*’, *Phys. Rev. Lett.* 113, 011102 (2014)
- W. W. Zhu, A. Berndsen, E. C. Madsen, M. Tan, I. H. Stairs, A. Brazier, P. Lazarus, R. Lynch, P. Scholz, K. Stovall, S. M. Ransom, S. Banaszak, **C. M. Biwer** et al. ‘*Searching for pulsars using image pattern recognition*’, *ApJ* 781, 117 (2014)
- K. J. Lee, K. Stovall, F. A. Jenet, J. Martinez, L. P. Dartez, A. Mata, G. Lunsford, S. Cohen, **C. M. Biwer** et al. ‘*PEACE: Pulsar Evaluation Algorithm for Candidate Extraction – A software package for post-analysis processing of pulsar survey candidates*’, *Mon. Not. Roy. Astron. Soc.* 433, 688 (2013)
- D. L. Kaplan, K. Stovall, S. M. Ransom, M. S. E. Roberts, R. Kotulla, A. M. Archibald, **C. M. Biwer** et al. ‘*Discovery of the Optical/Ultraviolet/Gamma-ray Counterpart to the Eclipsing Millisecond Pulsar J1816+4510*’, *ApJ* 753, 174 (2012)